THEORETICAL DEVELOPMENTS AND PRACTICAL ASPECTS OF DYNAMIC SYSTEMS IN WIND ENERGY APPLICATIONS

A Dissertation

by

BRIAN CHRISTOPHER OWENS

Submitted to the Office of Graduate and Professional Studies of
Texas A&M University
in partial fulfillment of the requirements for the degree of

DOCTOR OF PHILOSOPHY

Chair of Committee,	John E. Hurtado
Committee Members,	Junuthula N. Reddy
	Thomas W. Strganac
	Ramesh Talreja
Head of Department,	Rodney D. W. Bowersox

December 2013

Major Subject: Aerospace Engineering

ABSTRACT

The availability of offshore wind resources in coastal regions along with a high concentration of load centers in these areas makes offshore wind energy an attractive opportunity. Infrastructure costs and operation and maintenance costs for offshore wind technology, however, are significant obstacles that need to be overcome to make offshore wind a viable option. Vertical-axis wind turbines (VAWTs) are potentially ideal candidates for large offshore wind energy applications, and may provide a means to significantly reduce life-cycle costs associated with offshore wind energy. This has motivated the development of a flexible and extensible modular analysis framework for investigating VAWT designs. The Offshore Wind Energy Simulation toolkit contains a modular analysis framework that provides a general interface to external modules such as aerodynamics, hydrodynamics/platform dynamics, and generator/drive-train modeling software.

Theoretical developments in dynamic systems are also presented in this work. Implicit time integration methods are investigated for their applicability to Gyric systems (flexible systems undergoing general rotational motion). An energy conserving integration method for conventional flexible systems are considered and proven to be energy preserving for Gyric systems. A new, efficient procedure for developing linearized representation of discrete dynamic systems is also presented. Two existing approaches for developing linear representations are combined to arrive at a new, more efficient linearization procedure that overcomes the pitfalls of the individual approaches alone. Furthermore, aeroelastic stability is a known issue for large, flexible

structures under aerodynamic loads, and aeroelastic analysis was considered in the development of wind energy design tools. Finally, an investigation of the structural dynamics of offshore VAWT structure is conducted. A fundamental understanding of a resonance in VAWT configurations is sought, and the effects of support conditions on dynamic response of VAWT configurations is explored.

ACKNOWLEDGEMENTS

First, I wish to express my gratitude to my advisor Dr. John Hurtado for his guidance and support. I am grateful for him giving me the opportunity to work with him and for him sharing his knowledge, experience, and expertise with me. His emphasis on developing quality relationships in addition to performing quality technical work is one of the things I appreciated most while working with him. Dr. Hurtado's enthusiasm, patience, and helpful insights made our weekly meetings something to look forward to. His advisement extended beyond my technical development, with a genuine interest in the well-being of all facets of my life. I don't know that words can adequately convey what it's like to be one of his students or the impact he has had on me. I'll always be grateful for him believing in me and for everything he has taught me.

I would also like to thank Drs. Junuthula Reddy, Thomas Strganac, and Ramesh Talreja for serving on my committee. Each has had a significant academic impact on me in their respective areas of expertise. I am also appreciative of Dr. Vikram Kinra for serving as a substitute committee member when scheduling conflicts arose. I am grateful to my Master's advisor Dr. John Whitcomb for supporting me during my early years in graduate school. His guidance and the opportunity to work in his research group shaped my research interests in finite elements and software development for engineering applications. Furthermore, I would like to thank the Texas A&M Aerospace Department staff, especially Mrs. Karen Knabe and Mrs. Rose Sauser, for their every day assistance during my graduate studies.

I would like to acknowledge members of the Wind and Water Power Technologies organization at Sandia National Laboratories for their assistance in this work. In particular, Matt Barone and Josh Paquette for providing me the opportunity to work on the project that has supported me during my doctoral studies. I'd also like to thank managers Dave Minster and Daniel Laird for the opportunity to work closely with their organizations through internships at Sandia over the past few summers. I'm appreciative to my Sandia mentors Todd Griffith and Brian Resor for their technical assistance and insight throughout this work. I'm also grateful to Lenore Boulton, Alyssa Archibeque, Jan Snow, and Natalie Pitcher for their administrative assistance and morning coffee discussions.

I am thankful to all my friends for their support outside of my academic life, especially Kurt, Jamie, Kelley, Kevin, Forrest, David, Tom, Ross, Ruth, and Jade. I would also like to thank my parents, grandparents, brothers, and sisters for their lifelong support and encouragement. My nephews and niece have encouraged me to strive to be my best and to be an uncle worth looking up to.

This work was funded by a research grant from Sandia National Laboratories (Sandia Technical Monitors Matthew F. Barone and D. Todd Griffith). Sandia National Laboratories is a multi-program laboratory managed and operated by Sandia Corporation, a wholly owned subsidiary of Lockheed Martin Corporation, for the U.S. Department of Energy's National Nuclear Security Administration under contract DE-AC04-94AL85000.

TABLE OF CONTENTS

Page

ABSTRACT ii

ACKNOWLEDGEMENTS iv

TABLE OF CONTENTS vi

LIST OF FIGURES xii

LIST OF TABLES xxii

CHAPTER

I INTRODUCTION 1

I.A. Motivation 2
I.B. Literature review 5
I.B.1. Overview of previous VAWT technology 6
I.B.2. Previous design tools and investigations 10
I.B.3. External load models/modules 17
I.B.4. Analysis strategies 25
I.C. Outline 30

II THE OFFSHORE WIND ENERGY SIMULATION TOOLKIT FOR VERTICAL AXIS WIND TURBINES 34

II.A. Design tool features 35
II.B. Model formulation 37
II.B.1. Basic formulation concepts 38
II.C. Analysis framework 44
II.D. Coupling strategies 48
II.D.1. Demonstration of coupling approaches 51
II.D.2. Data flow between external modules and analysis framework 57
II.E. Mesh generation 63
II.F. Beam element 70
II.G. Constraints 72

CHAPTER Page

II.G.1. Constraints between nodes of two beam elements . . . 73
II.G.2. Single-axis hinge constraint . . . 75
II.H. Rotor speed update . . . 77
II.I. Generator modeling . . . 78
II.J. Drive-shaft modeling . . . 79
II.K. Conclusion . . . 80

III AN ENERGY PRESERVING TIME INTEGRATION METHOD FOR GYRIC SYSTEMS . . . 82

III.A. Gyric systems . . . 83
III.A.1. Lagrangian development of equations of motion for a conservative Gyric system . . . 84
III.A.2. Lagrangian development of equations of motion for a non-conservative Gyric system . . . 86
III.B. Energy considerations for Gyric systems . . . 87
III.B.1. Energy of a Gyric system . . . 88
III.B.2. The energy function $\mathscr{H}^*$ of a Gyric system . . . 89
III.C. Time integration of Gyric systems . . . 90
III.C.1. An energy preserving time integration method for conservative Gyric systems . . . 91
III.C.2. Considerations for Gyric systems with circulatory effects and non-conservative forces . . . 94
III.C.3. Implementation of time integration method . . . 96
III.D. An illustrative Gyric problem . . . 97
III.D.1. Formulation of equations of motion . . . 97
III.D.2. Establishing a reference solution . . . 99
III.D.3. Time integration studies using a simple conservative Gyric system . . . 100
III.D.4. Time integration studies using a simple Gyric system with circulatory effects . . . 103
III.E. Energy preservation of Newmark-β method with respect to conservative Gyric systems . . . 105
III.F. Conclusions . . . 108

IV DIRECT LINEARIZATION VIA A METHOD OF QUADRATIC MODES . . . 110

IV.A. Flow charts of various methods . . . 112
IV.A.1. Flow chart of direct linearization . . . 112

IV.A.2. Flow chart of a method of quadratic modes . . . 113
IV.A.3. Flow chart of proposed method 114
IV.B. Overview of direct linearization of rheonomic systems . 116
IV.C. Employing a method of quadratic modes representation 117
IV.D. Direct linearization of discrete rheonomic systems via a method of quadratic modes 120
IV.D.1. Equilibrium configuration solution 121
IV.D.2. Linearized mass matrix 123
IV.D.3. Linearized Gyric matrix 124
IV.D.4. Linearized stiffness matrix 125
IV.D.5. Linearized $\dot{M}_{ij}$ matrix 128
IV.D.6. Linearized Circulatory matrix 129
IV.E. Simple examples of employing linearization procedures 130
IV.E.1. Rotating beam 130
IV.E.2. Linearly accelerating beam 134
IV.F. Conclusions 137

V FINITE ELEMENT FORMULATION FOR A GYRIC BEAM IN A FLOATING FRAME 139

V.A. Quadratic modes representation of Timoshenko beam displacements 139
V.B. Finite element mass matrix 141
V.C. Finite element spin softening matrix 144
V.D. Finite element Gyric matrix 145
V.E. Finite element Circulatory matrix 146
V.F. Finite element stiffness matrix 148
V.G. Finite element load vector 151
V.H. Reduced order modeling of a finite element assembly . 152
V.I. Conclusions 158

VI CONSIDERATIONS OF AEROELASTIC STABILITY IN WIND ENERGY SYSTEMS 159

VI.A. Aeroelastic formulation 160
VI.A.1. Finite element formulation for a complex valued aeroelastic representation 163
VI.A.2. Finite element formulation for a real valued aeroelastic representation 165

CHAPTER Page

VI.B. BLade Aeroelastic Stability Tool (BLAST) 168
VI.B.1. Analysis procedures 169
VI.B.2. Demonstration of BLAST 170
VI.C. Time-domain modeling of unsteady aerodynamics and aeroelastic stability 177
VI.C.1. Overview of Leishman unsteady aerodynamics model 179
VI.C.2. Application of modeling approaches to a simplified example 181
VI.D. Conclusions 186

VII DEMONSTRATION OF FEATURES AND COUPLING TO EXTERNAL MODULES IN THE OFFSHORE WIND ENERGY SIMULATION TOOLKIT 189

VII.A. Demonstration and verification of reduced order model for VAWT configurations 190
VII.A.1. Linear reduced order model verification 191
VII.A.2. Nonlinear reduced order model verification . . . 204
VII.B. Demonstration of rotor operation modes 208
VII.B.1. Demonstration of specified rotor speed mode . . 209
VII.B.2. Demonstration of generator start up mode . . . 211
VII.B.3. Demonstration of self starting turbine mode . . 219
VII.C. Demonstration of two-way coupling to platform dynamics software 221
VII.C.1. Configuration 221
VII.C.2. Demonstration and baseline verification procedures 225
VII.D. Demonstration of coupling to aerodynamics software . 240
VII.E. Conclusions 242

VIII STRUCTURAL DYNAMICS OF VERTICAL-AXIS WIND TURBINES 245

VIII.A. Understanding critical per-rev excitations for tower resonance 247
VIII.A.1. Development of an analytical expression for tower forcing frequency content for a VAWT with an arbitrary number of blades . . . 248

CHAPTER Page

VIII.A.2. Validation of analytical per-rev tower excitation expressing using CACTUS aerodynamics software . . . 252
VIII.A.3. Interpretation of critical per-rev excitations . . 256
VIII.B. Initial system design studies on support structure influence of the Sandia 34-meter VAWT 258
VIII.B.1. Monopile support structure 258
VIII.B.2. Barge/floating support structure 264
VIII.C. Initial system design studies on support structure influence of a 5MW VAWT configuration 268
VIII.C.1. Configuration 268
VIII.C.2. Land-based configuration 268
VIII.C.3. Monopile configuration 272
VIII.C.4. Floating configuration 274
VIII.D. Initial aeroelastic stability analysis of 5MW VAWT configuration 277
VIII.D.1. Aeroelastic analysis of an isolated blade 277
VIII.D.2. Aeroelastic analysis of land-based configuration 278
VIII.E. Conclusions 283

IX CONCLUSION 286

IX.A. Chapter summary 286
IX.B. Future work 289

REFERENCES 291

APPENDIX A: VERIFICATION AND VALIDATION OF STRUCTURAL DYNAMICS ANALYSIS CAPABILITY IN THE OFFSHORE WIND ENERGY SIMULATION TOOLKIT 305

A.1. Modal analysis analytical verification procedures . . . 306
A.1.a. Verification of uncoupled vibration 307
A.1.b. Whirling shaft verification exercise 311
A.2. Modal and static analysis numerical verification procedures 322
A.2.a. Code-to-code verification exercise 322
A.2.b. Assumed modes verification exercise 336
A.3. Transient analysis verification 342
A.4. Validation procedures 349
A.4.a. Parked modal analysis 349

CHAPTER Page

A.4.b. Rotating modal analysis 351
A.5. Conclusions 354

APPENDIX B: AN EXAMPLE DYNAMIC SYSTEM WITH A COMPLEX REPRESENTATION 356

APPENDIX C: RESONANCE OF RIGID BODY MODES OF A FLOATING WIND TURBINE 360

APPENDIX D: APPROXIMATE TREATMENT OF RIGID BODY MODES IN MODAL ANALYSIS USING A GYRIC FORMULATION 362

D.1. An approach for incorporating rigid body modes into an existing flexible structural dynamics framework 362
D.2. An extension of approach to Gyric system analysis . . 366

LIST OF FIGURES

FIGURE		Page
I.1	Life-cycle cost breakdown for an offshore wind project	3
I.2	Comparison of VAWTs and HAWTs for offshore applications	5
II.1	Illustration of frames, position vectors, and angular velocities	39
II.2	Analysis framework for the OWENS toolkit	45
II.3	Illustration of loose coupling approach	49
II.4	Illustration of Gauss-Seidel coupling approach	50
II.5	Illustration of two degree-of-freedom gantry crane	52
II.6	Gantry translation $x(t)$ for various coupling approaches, $\Delta t = 0.01s$.	54
II.7	Payload rotation $\theta(t)$ for various coupling approaches, $\Delta t = 0.01s$ . .	55
II.8	Gantry translation $x(t)$ for various coupling approaches, $\Delta t = 0.2s$.	56
II.9	Payload rotation $\theta(t)$ for various coupling approaches, $\Delta t = 0.2s$ . . .	56
II.10	General framework for network socket interface of core analysis code to external module	62
II.11	Basic types of VAWT configurations	63
II.12	Wireframe of swept Darrieus configuration generated with VAWTGen	65
II.13	Finite element mesh of swept Darrieus configuration generated with VAWTGen	66
II.14	Flowchart of VAWTGen input and output	67
II.15	Wireframe of V-VAWT configuration generated with VAWTGen . . .	68
II.16	Wireframe of H-VAWT configuration generated with VAWTGen . . .	69

FIGURE Page

II.17 Wireframe of strutted Darrieus configuration generated with VAWTGen 69

II.18 Illustration of hinge-frame coordinate system between two elements . 75

II.19 Torque vs. speed curve for simple induction generator 79

III.1 Illustration of simplified Gyric system 98

III.2 Time integration comparison for a simple conservative Gyric system ($\Delta t = 0.01\ s$) 101

III.3 Time integration comparison for a simple conservative Gyric system ($\Delta t = 0.1\ s$) 102

III.4 Time integration comparison for a simple conservative Gyric system ($\Delta t = 1.0\ s$) 102

III.5 Time integration comparison for a simple Gyric system with circulatory terms($\Delta t = 0.01\ s$) 104

III.6 Time integration comparison for a simple Gyric system with circulatory terms($\Delta t = 0.1\ s$) 105

IV.1 Flowchart describing the direct linearization procedure 113

IV.2 Flowchart describing the method of quadratic modes linearization procedure 115

IV.3 Flowchart describing the proposed linearization procedure 115

VI.1 Schematic of two-dimensional airfoil section 162

VI.2 Frequency and damping ratio vs. rotor speed complex valued BLAST predictions for WindPACT 1.5MW blade 172

VI.3 Flutter mode shape for the WindPACT 1.5MW blade predicted using complex valued BLAST 173

VI.4 Frequency and damping ratio vs. rotor speed real valued BLAST predictions for WindPACT 1.5MW blade 174

VI.5 WindPACT 1.5MW flutter mode shape predicted using real valued BLAST 174

VI.6 Frequency and damping ratio vs. rotor speed BLAST predictions for SNL100-00 blade 176

VI.7 Frequency and damping ratio vs. rotor speed real valued BLAST predictions for SNL100 blade 177

VI.8 SNL100-00 flutter mode shape predicted using real valued BLAST . . 177

VI.9 Frequency and damping ratio vs. rotor speed complex valued BLAST predictions for 2 element uniform blade 182

VI.10 Frequency and damping ratio vs. rotor speed real valued BLAST predictions for 2 element uniform blade 183

VI.11 Blade tip plunging and pitching vs. time at 48 RPM with Leishman unsteady aerodynamics model loads 184

VI.12 Blade tip plunging and pitching vs. time at 48.8 RPM with Leishman unsteady aerodynamics model loads 185

VI.13 Frequency and damping trends for aeroelastic Timoshenko beam implementation (dashed lines extrapolating) 186

VII.1 Schematic of idealized 34-meter VAWT with inertial (n_i) and hub-fixed (h_i) coordinate systems 191

VII.2 VAWT blade midpoint u displacement history for various reduced order models (rigid body translation, linear analysis) 192

VII.3 VAWT blade midpoint v displacement history for various reduced order models (rigid body translation, linear analysis) 193

VII.4 VAWT blade midpoint w displacement history for various reduced order models (rigid body translation, linear analysis) 193

VII.5 VAWT blade midpoint θ_x displacement history for various reduced order models (rigid body translation, linear analysis) 194

VII.6 VAWT blade midpoint θ_y displacement history for various reduced order models (rigid body translation, linear analysis) 194

VII.7 VAWT blade midpoint θ_z displacement history for various reduced order models (rigid body translation, linear analysis) 195

VII.8 Prescribed angular velocity profiles employed in reduced order model verification procedures. 196

VII.9 VAWT blade midpoint u displacement history for various reduced order models (rigid body rotation, linear analysis) 197

VII.10 VAWT blade midpoint v displacement history for various reduced order models (rigid body rotation, linear analysis) 197

VII.11 VAWT blade midpoint w displacement history for various reduced order models (rigid body rotation, linear analysis) 198

VII.12 VAWT blade midpoint θ_x displacement history for various reduced order models (rigid body rotation, linear analysis) 198

VII.13 VAWT blade midpoint θ_y displacement history for various reduced order models (rigid body rotation, linear analysis) 199

VII.14 VAWT blade midpoint θ_z displacement history for various reduced order models (rigid body rotation, linear analysis) 199

VII.15 VAWT blade midpoint u displacement history for various reduced order models (full rigid body motion, linear analysis) 200

VII.16 VAWT blade midpoint v displacement history for various reduced order models (full rigid body motion, linear analysis) 201

VII.17 VAWT blade midpoint w displacement history for various reduced order models (full rigid body motion, linear analysis) 201

VII.18 VAWT blade midpoint θ_x displacement history for various reduced order models (full rigid body motion, linear analysis) 202

VII.19 VAWT blade midpoint θ_y displacement history for various reduced order models (full rigid body motion, linear analysis) 202

VII.20 VAWT blade midpoint θ_z displacement history for various reduced order models (full rigid body motion, linear analysis) 203

VII.21 VAWT blade midpoint u displacement history for various reduced order models (full rigid body motion, nonlinear analysis) . . . 205

VII.22 VAWT blade midpoint v displacement history for various reduced order models (full rigid body motion, nonlinear analysis) . . . 205

VII.23 VAWT blade midpoint w displacement history for various reduced order models (full rigid body motion, nonlinear analysis) . . . 206

VII.24 VAWT blade midpoint θ_x displacement history for various reduced order models (full rigid body motion, nonlinear analysis) . . 206

VII.25 VAWT blade midpoint θ_y displacement history for various reduced order models (full rigid body motion, nonlinear analysis) . . 207

VII.26 VAWT blade midpoint θ_z displacement history for various reduced order models (full rigid body motion, nonlinear analysis) . . 207

VII.27 Prescribed rotor speed profile 210

VII.28 Prescribed rotor acceleration profile 210

VII.29 Blade midspan u displacement for prescribed rotor speed profile . . . 212

VII.30 Blade midspan v displacement for prescribed rotor speed profile . . . 212

VII.31 Generator torque vs. speed curve used in demonstration and verification procedures 213

VII.32 Rotor speed vs. time for generator start up mode 214

VII.33 Generator power vs. time for generator start up mode 214

VII.34 Rotor acceleration vs. time for generator start up mode 215

VII.35 Blade midspan u displacement vs. time for generator start up mode . 216

VII.36 Blade midspan v displacement vs. time for generator start up mode . 217

VII.37 Angular velocity vs. time of rotor and drive-shaft for generator start up mode 218

VII.38 Azimuth vs. time of rotor and drive-shaft for generator start up mode 219

VII.39 Rotor speed vs. time for self starting turbine mode 220

VII.40 Generator power vs. time for self starting turbine mode 221

VII.41 Schematic of configuration employed for demonstration of coupling to platform dynamics module 222

VII.42 Platform sway motion as a result of platform sway step relaxation . . 228

VII.43 FFT of platform sway motion as a result of platform sway step relaxation 229

VII.44 Platform roll motion as a result of platform sway step relaxation . . 229

VII.45 FFT of platform roll motion as a result of platform sway step relaxation 230

VII.46 Tower top motion as a result of platform sway step relaxation 230

VII.47 FFT of tower top motion as a result of platform sway step relaxation 231

VII.48 Platform sway motion as a result of tower forcing 233

VII.49 FFT of platform sway motion as a result of tower forcing 234

VII.50 Platform roll motion as a result of tower forcing 234

VII.51 FFT of platform roll motion as a result of tower forcing 235

VII.52 Tower top motion as a result of tower forcing 235

VII.53 FFT of tower top motion as a result of tower forcing 236

VII.54 Platform surge motion as a result of wave excitation 238

VII.55 FFT of platform surge motion as a result of wave excitation 238

VII.56 Tower top motion as a result of wave excitation 239

VII.57 FFT of tower top motion as a result of wave excitation 239

VII.58 Normal and tangential force history at blade midspan generated with CACTUS 241

VII.59 Radial and edgewise displacement history of blade midspan under CACTUS loads 242

VIII.1 Illustration of various coordinate systems considered in blade/tower forcing 249

VIII.2 Effective radial force on a single blade vs. normalized azimuth 253

VIII.3 FFT of effective radial force on a single blade vs. normalized azimuth 254

VIII.4 Effective edgewise force on a single blade vs. normalized azimuth . . 254

VIII.5 FFT of effective edgewise force on a single blade vs. normalized azimuth 255

VIII.6 Illustration of 34-meter VAWT on monopile 259

VIII.7 Tower mode Campbell diagrams: 34-meter VAWT on monopile . . . 261

VIII.8 Flatwise mode Campbell diagrams: 34-meter VAWT on monopile . . 263

VIII.9 Edgewise mode Campbell diagrams: 34-meter VAWT on monopile . . 263

VIII.10 1st Tower mode and rigid body mode Campbell diagrams for 34-meter VAWT with various support conditions 265

VIII.11 Parked 34-meter VAWT tower mode frequencies for various support conditions 266

VIII.12 Rigid body mode Campbell diagrams for 34-meter VAWT on floating barge platform 267

VIII.13 Illustration of 5MW VAWT configuration 269

VIII.14 Campbell diagram for 5MW land-based VAWT 271

VIII.15 Campbell diagram for 5MW VAWT on 30-meter monopile 273

VIII.16 Parked 5MW VAWT tower mode frequencies for various support conditions 275

VIII.17 Campbell diagram for 5MW VAWT on barge platform 276

VIII.18 Frequency and damping vs. rotor speed for isolated 5MW blade aeroelastic stability analysis 279

VIII.19 Mode shape of isolated blade 9.2 RPM flutter mode (red: in-phase shape, blue: out-of-phase shape) 280

VIII.20 Frequency and damping vs. rotor speed for land-based 5MW VAWT configuration 281

VIII.21 Mode shape of 8.1 RPM VAWT 1st flatwise flutter mode (red: in-phase shape, blue: out-of-phase shape) 282

VIII.22 Mode shape of 4 RPM VAWT "1st edgewise" flutter mode (red: in-phase shape, blue: out-of-phase shape) 282

A.1 Uniaxial rod 1st mode shape (100 elements) 308

A.2 Uniaxial rod 2nd mode shape (100 elements) 309

A.3 Uniaxial rod 3rd mode shape (100 elements) 309

A.4 Uniaxial rod 4th mode shape (100 elements) 309

A.5 Uniaxial rod 5th mode shape (100 elements) 310

A.6 Beam deflection 1st mode shape (10 elements) 312

A.7 Beam deflection 2nd mode shape (10 elements) 312

A.8 Illustration of whirling shaft 313

A.9 Mode shapes for stationary shaft 318

A.10 Whirling shaft coupled mode shape (n=1) 319

A.11 Whirling shaft coupled mode shape (n=2) 319

A.12 Whirling shaft coupled mode shape (n=3) 320

A.13 Whirling shaft coupled mode shape (n=4) 320

A.14 Whirling shaft coupled mode shape (n=5) 321

A.15 Sandia 34-meter VAWT ANSYS configuration mesh 324

A.16 1st anti-symmetric flatwise (FA) mode 325

A.17 1st symmetric flatwise (FS) mode 325

A.18 1st propeller (PR) mode 326

A.19 1st butterfly (blade edgewise - BE) mode 326

A.20 2nd anti-symmetric flatwise (FA) mode 327

A.21 2nd symmetric flatwise (FS) mode 327

A.22 2nd butterfly (blade edgewise - BE) mode 328

A.23 2nd propeller (PR) mode 328

A.24 3rd anti-symmetric flatwise (FA) mode 329

A.25 3rd symmetric flatwise (FS) mode 329

A.26 Deformed mesh for acceleration in h_1 (scale factor = 76.78) 331

A.27 Deformed mesh for acceleration in h_2 (scale factor = 13.61) 331

A.28 Deformed mesh for acceleration in h_3 (scale factor = 8.12) 332

A.29 llustration of beam with arbitrary orientation in the hub frame . . . 337

A.30 Tower flatwise displacement history for transient verification exercise . . . 344

A.31 Tower edgewise displacement history for transient verification exercise . . . 344

A.32 FFT of tower flatwise displacement history for transient verification exercise . . . 345

A.33 FFT of tower edgewise displacement history for transient verification exercise . . . 345

A.34 Blade midspan flatwise displacement history for transient verification exercise . . . 346

A.35 Blade midspan edgewise displacement history for transient verification exercise . . . 346

A.36 FFT of blade midspan flatwise displacement history for transient verification exercise . . . 347

A.37 FFT of blade midspan edgewise displacement history for transient verification exercise . . . 347

A.38 Campbell diagram for the SNL 34-meter VAWT test bed (experimental data and numerical predictions) . . . 352

A.39 Campbell diagram for the SNL 34-meter VAWT test bed with guy-wires (experimental data and numerical predictions) . . . 353

D.1 Schematic of rigid body and flexible motion within a single frame . . . 363

LIST OF TABLES

TABLE Page

VII.1 Generator properties for idealized 34-meter VAWT 213

VII.2 Drive-shaft properties for idealized 34-meter VAWT 217

VII.3 Spar buoy platform properties 224

VII.4 Flexible structure properties 225

VII.5 Platform sway/roll and tower frequency content (Hz) as a result of sway step relaxation 228

VII.6 Platform sway/roll and tower frequency content (Hz) as a result of tower forcing 233

VIII.1 Numerical validation of per-rev tower forcing 256

VIII.2 Critical per-rev tower resonance design sensitivities (hub-frame) . . . 257

VIII.3 Rigid body mode frequencies of platform/scaled barge system 265

A.1 Frequencies (Hz) for uniaxial rod as predicted by Petyt, OWENS, and analytical solution 308

A.2 Frequencies (Hz) for beam bending as predicted by Petyt, OWENS, and analytical solution 311

A.3 Whirling shaft beam properties 313

A.4 Whirling shaft frequencies (Hz) from analytical solution 314

A.5 Whirling shaft frequencies (Hz) predicted using finite element analysis 315

A.6 Whirling shaft frequencies predicted percent error relative to analytical solution 315

A.7 Parked natural frequencies (Hz) for 34m VAWT via ANSYS and OWENS tools 330

A.8 Relative difference norms for displacements between ANSYS and OWENS results for acceleration body forces 331

A.9 Frequencies (Hz) for 34m VAWT with rotational effects about h_1 via ANSYS and OWENS tools 333

A.10 Frequencies (Hz) for 34m VAWT with rotational effects about h_2 via ANSYS and OWENS tools 334

A.11 Frequencies (Hz) for 34m VAWT with rotational effects about h_3 via ANSYS and OWENS tools 335

A.12 Frequencies (Hz) for 34m VAWT with rotational effects and stress stiffening via ANSYS and OWENS tools 335

A.13 Uniform beam properties 336

A.14 Comparison of modal analysis for case 1 339

A.15 Comparison of modal analysis for case 2 340

A.16 Comparison of modal analysis for case 3 340

A.17 Comparison of modal analysis for case 4 341

A.18 Comparison of modal analysis for case 5 342

A.19 Comparison of frequency content of transient analysis predictions to modal analysis predictions 348

A.20 Relative error of frequency content of transient analysis predictions to modal analysis predictions 348

A.21 Comparison of OWENS modal analysis frequencies (Hz) to parked modal tests for Sandia 34m VAWT 350

A.22 Comparison of OWENS modal analysis frequencies (Hz) to parked modal tests for Sandia 34m VAWT with guy wire modeling . 351

CHAPTER I

INTRODUCTION

This dissertation presents theoretical developments and practical aspects of dynamic systems with applications to wind energy systems. The primary motivation of this work is the development of a robust design tool for offshore vertical-axis wind turbines (VAWTs). VAWTs are potentially ideal candidates for large offshore wind energy applications, and may provide a means to significantly reduce life-cycle costs associated with offshore wind energy. A flexible and extensible modular analysis framework for investigating VAWT designs has been developed. The Offshore Wind ENergy Simulation (OWENS) toolkit contains a modular analysis framework that provides a general interface to external modules such as aerodynamics, hydrodynamics/platform dynamics, and generator/drive-train modeling software. At the core of this design tool is a robust VAWT mesh generator and finite element structural dynamics analysis package capable of considering arbitrary VAWT configurations under a wide variety of scenarios. Verification and demonstration of the features implemented in OWENS are presented in this dissertation.

Theoretical developments of dynamic systems are also presented in this work. Implicit time integration methods are investigated for their applicability to Gyric systems (flexible systems undergoing general rotational motion). An energy conserving integration method for flexible systems is considered and proven to be energy preserving for Gyric systems. Energy preserving properties are also proven for certain schemes of the Newmark-β implicit integration method. A new, efficient procedure

for developing linearized representation of discrete dynamic systems is also presented. Two existing approaches for developing linear representations are combined to arrive at a new, more efficient linearization procedure that overcomes the pitfalls of the individual approaches alone. Furthermore, aeroelastic stability is a known issue for large, flexible structures under aerodynamic loads, and aeroelastic analysis was considered in the development of wind energy design tools. As a result, choice of aeroelastic representation in a conventional structural dynamics analysis framework was explored and findings are discussed. Finally, an investigation of the structural dynamics of offshore VAWT structure is conducted. A fundamental understanding of the dynamics of VAWT designs is sought, and the effects of support conditions and fundamental design choices on resonance are explored.

This chapter begins with a detailed discussion of the motivation for considering VAWTs for offshore wind energy applications. A literature review follows, examining previous VAWT technology and design tools. Potential external modules for aerodynamics and hydrodynamics loads calculation are also reviewed to assess interfaces to a core structural dynamics design tool. Analysis strategies including structural dynamics of flexible bodes, the finite element method, aeroelastic stability, and linearization techniques are also reviewed. This chapter concludes with a chapter outline of this dissertation.

I.A. Motivation

The availability of offshore wind resources in coastal regions along with a high concentration of load centers in these areas makes offshore wind energy an attractive

opportunity. Infrastructure costs and operation and maintenance (O&M) costs for offshore wind technology, however, are significant obstacles that need to be overcome to make offshore wind a viable option. It has been estimated that a greater than 20% decrease in cost of energy (COE) will be required to ensure the viability of offshore wind energy [1]. This reduction in COE is likely to come from decreases in installation costs and O&M, while increasing energy production. Rotor design has a significant impact on all three of these areas, and therefore is critical in reducing the COE. Whereas it is estimated that the entire turbine contributes nearly 28% of the life-cycle cost (see Figure I.1), the actual rotor is only estimated to contribute about 7% of this cost. Therefore, it is more important to consider design configurations that lower the installation, logistics, and O&M costs while increasing energy capture rather than trying to decrease the cost of the rotor itself.

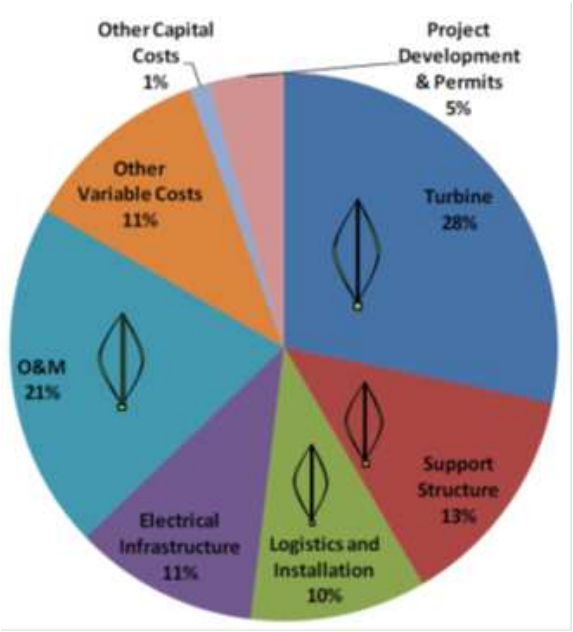

Figure I.1. Life-cycle cost breakdown for an offshore wind project

Horizontal-axis wind turbines (HAWTs) have gained much popularity for land-based wind energy. HAWT designs have undergone much development over the past 15 years, which has led to lowered COE. As a result, further significant reduction in COE, which is necessary for future offshore wind energy, is not likely in the foreseeable future with HAWT configurations. Moreover, the high center of gravity together with gearbox and generator placement at the top of the tower exacerbates installation, logistics, and other O&M cost concerns of offshore wind. Generally speaking, these contributions to COE are often considered to have the greatest potential for lowering COE for offshore wind.

Vertical-axis wind turbines held significant interest in the earlier days of wind energy technology during the 1980s. In the early 1990s, this configuration lost its popularity and the HAWT was adopted as the primary wind turbine configuration. The VAWT configuration, however, can significantly complement the need for lower COE for offshore applications. Areas on Figure I.1 with a VAWT symbol show aspects of life-cycle cost than can be benefited by a VAWT configuration. Figure I.2 illustrated potential advantages of a VAWT configuration over a HAWT configuration for offshore applications. This is primarily due to the placement of the gearbox and generator at the bottom of the tower. This not only reduces platform cost by lowering the center of gravity of the turbine, but also reduces O&M costs by having components readily accessible near water level. The simplicity of the VAWT configuration compared to the HAWT can also lower rotor costs. The insensitivity of the VAWT to wind direction and the ability to scale the machines to large sizes will increase energy production and further reduce COE. To remain a viable option

for offshore wind energy, however, VAWT technology will need to undergo significant development in coming years. Thus, the Offshore Wind Energy Simulation Toolkit is being developed to assess VAWT designs for offshore environments.

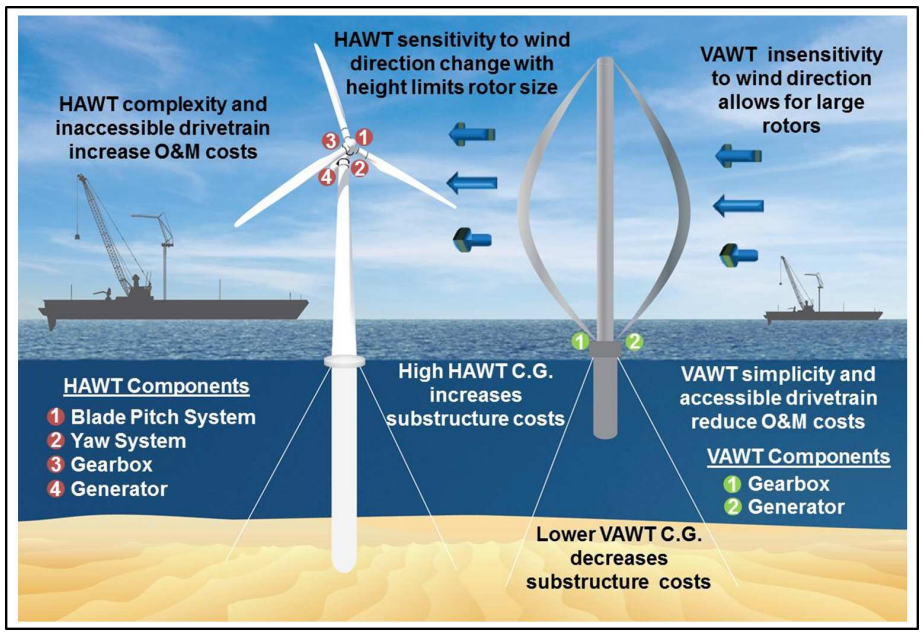

Figure I.2. Comparison of VAWTs and HAWTs for offshore applications

I.B. Literature review

In the 1980s, vertical-axis wind turbines were undergoing significant research and development. Later, in the 1990s, the horizontal-axis wind turbines gained much popularity, and future research efforts were primarily concerned the HAWT turbine configuration. For multiple reasons, however, VAWTs are poised to become a leading configuration in the offshore wind arena. Given the relative maturity of HAWT

configurations, VAWT technology will need to undergo significant development to maximize the potential of this configuration in an offshore environment. Accordingly, a literature review has been conducted to examine previous VAWT technology and research efforts.

I.B.1. Overview of previous VAWT technology

Sutherland et al. [2] have compiled an invaluable report documenting the previous VAWT related research at Sandia National Laboratories. Primary advantages of VAWTs are6 an increased reliability and lower costs due to the simpler hardware associated with their omnidirectional wind capturing capability. This eliminated the yaw system present on HAWTs, and allowed for the VAWT to be scaled to large watt configurations without the need to develop costly yaw systems for larger scales. This inherently decreases the hardware and O&M costs associated with a VAWT compared to a HAWT. It was noted that the VAWT requires blades twice as long as a HAWT to have an equivalent swept area. While this may raise the blade cost of a VAWT, the overall simpler hardware configuration may prove less costly than a HAWT in addition to the higher HAWT O&M costs that accrue over the service life of a turbine.

VAWT research at Sandia National Laboratories primarily focused on a Darrieus configuration [3] for its high efficiency. A troposkein (Greek for "the shape of a spun rope") shape was a popular blade geometry for Darrieus turbines. This shape theoretically eliminates bending stresses in a blade at a certain rotor speed. In reality, the manufacturing process seeks near zero bending stresses by approximating the

troposkein shape. Such a shape also eliminates compressive loading in the blade, resulting in a tensile stress state that is preferable for composite materials. While early prototypes showed fatigue problems with aluminum Darrieus blades, the blades were no more prone to fatigue than HAWT blades. Tower-to-blade struts could be employed to provide extra stiffening to the blades. Unfortunately, struts reduce aerodynamic efficiency of a turbine by interfering with the flow through the rotor.

The nature of a VAWT can also require a more complicated gearbox/drive-train system. VAWTs require a starting system, which necessitates a bi-directional gear box. VAWTs also produce a variable torque as a result of wind flow over the spinning rotor. Variable torque issues can be remedied by adding compliance to the drive train. Furthermore, land-based Darrieus VAWTs typically made use of guy cables for stability. This resulted in structural components and hardware being designed for guy cable loads. Guy cables also significantly increased the footprint of a VAWT. The use of guy wires to stabilize offshore floating platform is unlikely, and innovative design concepts will be needed to ensure the stability of a floating VAWT. Sutherland et al. also noted the difficulty of active aerodynamic control on VAWT configurations. Passive control via load shedding airfoils and variable speed operation could, however, be a viable means for controlling the aerodynamic loads on a turbine.

Sandia National Laboratories developed a 34m VAWT test bed [4–6] for experimental investigations and to provide data for the validation of design tools. The test bed was of modular design, capable of operation with a single blade. Blades were of troposkein shaped blade with stall regulated airfoils. No struts were utilized, and

each blade had four blade-to-blade joints to preserve the troposkein shape and minimize stresses. Resonances for the rotor were measured at 32 revolutions per minute (RPM) and just above 40 RPM. The lower resonance was narrow/weak and wasn't a major concern during the test program. The second resonance was potentially catastrophic, and the rotor speed was limited to 38 RPM. Modal response of the turbine was examined and indicated guy cable natural frequencies were an important consideration. A guy cable resonance at 25 RPM was avoided by using a controller to pass the rotor speed through this frequency quickly. Fatigue comparisons [7–10] between aluminum and fiberglass blades were also conducted, indicating that fiberglass blades had better fatigue characteristics. Other aerodynamic experiments indicated vortex generators [11] had no noticeable effect on operation, and dirty blades could significantly affect the rotor aerodynamics.

FloWind Corporation sought to commercialize the Darrieus VAWT design [12] developed by the Sandia "Point Design" [13]. The commercial "Point Design" was developed out of a variation of the VAWT test bed project. FloWind replaced the rotors on an existing 19-meter VAWT fleet with a rotor based off the "Point Design". Three pultruded fiberglass blades were utilized in the FloWind rotors, with a V-shaped "deep strut" design. A non troposkein blade shape resulted in increased bending stresses for the FloWind rotor. It was determined that the use of three blades allowed the torque tube and other structural components to be reduced. Three bladed designs also reduce "torque ripple" compared to two bladed designs, thus requiring less compliance in the gearbox. Therefore, while the total blade cost in a three bladed design is more, costs are reduced in other areas of the turbine.

The Darrieus configuration was the leading design due to its efficiency, but other cantilevered designs were also considered. H-configuration VAWTs were examined, some with fixed-geometry [14] and others with variable-geometry [15]. H-configurations were rather large and expensive and had relatively low aerodynamic efficiency. To eliminate the need for guy cables, a spindle configuration Darrieus VAWT was considered in the Pioneer I design [16]. This design had a 15-meter rotor and was never scaled to larger sizes. The spindle configuration may be of interest for future designs of offshore VAWTs where use of guy cables in not likely.

Sutherland et al. identified key areas for future VAWT research. The impact of blade roughness due to dirty blades should be considered to ensure optimum efficiency of a turbine. Appropriate airfoils or blade coatings/textures to remedy this concern should be utilized in future VAWT designs. Struts can significantly improve the stability of a rotor, but with adverse effects on aerodynamics. Increasing the aerodynamic efficiency of strut designs or using thick airfoils to eliminate the need for struts could ensure the efficiency and stability of VAWT designs. Use of modern composite material technology could reduce the weight of structural components (thereby reducing cost of other hardware components). Composite materials also provide a means for aeroelastic tailoring to be explored through couplings that result from composite layups. As shown with the FloWind rotor, three blade designs may reduce the structural components needed on a turbine as well as provide a better torque balance on the generator. With respect to offshore technology, a three-bladed design will need to have blades affixed to the tower on-site while a two-bladed design can be assembled off-site. These considerations would directly affect the installation

costs of an offshore turbine.

I.B.2. Previous design tools and investigations

To study the dynamic behavior of VAWTs, Lobitz and Sullivan [17] developed the VAWTDYN numerical dynamic analysis package in 1980. Dynamic analysis is key to understanding resonance of a VAWT configuration and modifying the design or operating conditions to avoid catastrophic failure. Furthermore, the dynamic behavior of a VAWT is also crucial for predicting the fatigue of the rotor. Initial VAWT configurations were designed using quasi-static finite element analysis. This may be sufficient if the resonance frequency is above the excitation frequency, thereby avoiding a significant dynamic response. As a result of the lack of reliable dynamic tools, early VAWT designs had significant factors of safety. The original VAWTDYN package which was capable of modeling two bladed rotors, sought to provide an avenue for improved structural dynamics analysis of VAWTs. Motions of the rotors were assumed to be those most observed in existing research systems. Therefore, a limited possibility of turbine motions is considered in the analysis package. The VAWTDYN package includes aerodynamic loads, structural damping, gyroscopic effects, and the ability to consider generator dynamics. At the time of the 1980 SAND report describing VAWTDYN, gravity loads were not considered. Flexibility with respect to the aerodynamics model was considered in the design of VAWTDYN.

VAWTDYN represents the turbine as a collection of masses, springs, dashpots, and joints. The tower has a relatively simple representation of two links connected together by a U-joint. The stiffness/damping of the tower is represented by

springs/dashpots at the U-joint. The blades are affixed to the tower at their ends via ball joints, permitting rotations but not translations. Blade motions are allowed independent of one another and lead-lag stiffness and damping in the blades is modeled by springs and dashpots. No motion is allowed perpendicular to the chord of the blade in the rotating coordinate system affixed to the VAWT. While there are clear limitations in the structural representation of the turbine, it was believed that the predominant motions of the VAWT were being captured. In deriving the equations of motion for the VAWTDYN package, small motions are assumed to eliminate higher order terms. Therefore, VAWTDYN is not expected to accurately predict large deformations of a VAWT configuration. Angular motion about the tower base is also considered and used in modeling the effects of guy cables.

Transient dynamic analysis of a VAWT was performed by integrating the equations of motion using a "canned" ODE solver with variable time stepping capabilities. Frequency content of a VAWT may be explored via a fast Fourier transform (FFT). With these capabilities developed, a number of verification and validation procedures were performed on the VAWTDYN package. Considering the nutation and precession of a spinning top verified the implementation of gyroscopic effects. The vibrational characteristics of a turbine were examined by displacing and releasing the top of the turbine to excite the vibrational modes for a "parked" turbine. Results from a "hand calculation" of a simple mass-spring model were compared for agreement to further verify the VAWTDYN implementation. Validation or "qualification" was also performed by comparing VAWTDYN results to experimental data. Predicted results of low-speed drive-shaft torque were in decent agreement with experimental

data. Measured stress amplitudes at the trailing edge of a blade were compared to those predicted by VAWTDYN, and the predicted values were in general agreement considering the amount of spread in the experimental data. The authors indicated that better agreement may be obtained by "fine-tuning" the model. The above verification and validation procedures could serve as useful references for the verification and validation of future tools.

Original VAWT dynamic analysis had been conducted using a version of Sandia's SAP IV FEA code, modified for centrifugal stiffening. Some resonance predictions from the modified SAP IV code, however, were not in agreement with the observations of Alcoa's ALVAWT 6342 turbine [18]. Simple verification of the SAP IV FEA against a "whirling shaft" problem emphasized the need to include all rotational effects in the model formulation. It was observed that the simpler VAWTDYN package which accounts for the rotational effects has noticeably different trends compared to the SAP IV code. The VAWTDYN package could actually predict certain resonances in the ALVWAWT 6342 turbine, despite its relatively crude representation of the VAWT. This further emphasized the importance of including rotational effects in the formulation. Nevertheless, certain blade resonances were not predicted accurately by the VAWTDYN software regardless of how model parameters were adjusted. This indicated clear limitations of the VAWTDYN model. Accordingly, a more accurate finite element model (capable of including all rotational effects) and aerodynamic loads was considered. Coriolis and spin softening matrices were developed form Hamilton's principle and appended to the structural element matrices generated by NASTRAN® [19, 20] using the FEVD processing tool. This new

analysis tool resulted in a more accurate characterization of the ALVAWT turbine, being able to capture the resonance the other analysis tools could not predict. The NASTRAN tool performed a modal analysis of the turbine in the frequency domain. At the time of the report, future work for the tool would be concerned with transient analysis for examining forced response and implementing aerodynamic loading of the turbine.

In 1982, Carne et al. [21] further exercised the original Lobitz NASTRAN based tool with additional modifications for rotational effects. The finite element analysis tool was well suited for modeling the structure of a VAWT configuration. The linear nature of the analysis tool, however, continued to impose assumptions regarding small displacements of the rotor. At this time aeroelastic effects were not considered in the model. The beam element used in this analysis was developed from a less rigorous formulation that neglected the torsional rotational kinetic energy about the element's axis. This version of the tool also accounted for concentrated masses and the resulting mass and Coriolis matrices appropriately. The tool was further verified by considering a whirling shaft with pinned ends. This verification problem is likely to be of use in newly developed tools to ensure rotational effects are formulated and implemented correctly. In a validation effort, the model was "tuned" to the frequencies of a parked turbine and predicted modal frequencies at various rotor speeds were compared to experimental data. There was reasonable agreement given the relative coarseness of the experimental measurements. It was seen that the analysis results and experiment were in qualitative agreement when rotor speed was introduced. Couplings occurred between modes that were in and out of the rotor plane, (being

approximately ninety degrees out of phase). Possible sources of error were believed to be inadequate modeling of tower to blade connections. Therefore, future tools should consider the ability to accurately characterize structural connections/joints in the model formulation and implementation.

Around the same time, Popelka [22] examined the aeroelastic stability of a VAWT turbine using a NASTRAN based tool. Flutter instability was examined in scale testing of a Darrieus rotor, and this investigation sought to predict the stability of a full scale turbine. A simple straight beam element was used in the NASTRAN analysis with aerodynamics and masses being "lumped" at intermediate nodes on the beam elements. The tool allowed for a mass center offset with respect to the elastic axis, and included Coriolis and spin softening effects. The moments of inertia of the beam were not considered in the NASTRAN analysis. It would seem that the tool had a rather coarse representation of the mass distribution of the turbine, concerned only with translational motion of concentrated mass terms. Future research efforts could improve upon this formulation by including rotary inertial effects due to the bending and twisting of structural components. The formulation incorporated a relatively simple aerodynamic model, using unsteady Theodorsen theory [23]. Therefore, only two-dimensional flow was considered and no considerations were made for inflow, wake, or stall. Nevertheless, the Theodorsen unsteady aerodynamics model lends itself well to considering aerodynamic effects on the stability of a wind turbine through modal analysis. Good agreement was seen with the flutter speed observed in an experimental system, indicating that the less refined treatment of mass distribution may be sufficient for stability analysis of certain VAWTs. Popelka also observed

that small changes in the assumed structural damping have a large impact on the flutter speed. Therefore, future design tools should seek appropriate ways to model structural damping in order to alleviate flutter concerns. Popelka also determined that two blade modes need not be in resonance in order to produce flutter and that the tower and drive-train stiffness can affect the flutter speed of a turbine. Future development of the tool would focus on a more robust aerodynamics model capable of considering wind gust effects and inflow/wake and stall.

In 1984, Lobitz and Sullivan [24] continued work on the development of a finite element based VAWT analysis tool. This work primarily concerned implementation of aerodynamic models into the structural dynamics analysis, giving the tool aeroelastic analysis capabilities. The FFEVD software implemented an advanced steady state stream tube model with the option of double or single stream tubes. These aerodynamics models are implemented in the CARDAA and FORCE routines respectively. These models will be briefly discussed later. The FFEVD provided an interface to modify the NASTRAN matrices to account for aerodynamic effects. One key difference in this version of the tool was that nonlinearities in the structural stiffness matrix were also accounted for via a "spin up" procedure. A static analysis of the turbine was performed considering centrifugal loads, steady aerodynamic loads, gravity loads, and spin softening. A converged nonlinear stiffness matrix was then used in the modal analysis of the turbine. Results showed excellent agreement of turbine natural frequencies with experimental data. The tool also predicted reasonable agreement with centrifugal and gravity load response although additional nonlinearities were present. Potential sources of error were identified as inadequacies

in the aerodynamic model and steady wind assumption. The structural damping and aerodynamic damping were also identified as key factors that could significantly affect result predictions.

In 1988, Dohrmann and Veers [25] extended the tool to consider the time domain response of VAWTs. While a frequency domain analysis may be suitable for analysis in steady conditions, a transient analysis capability is crucial for investigating the fatigue of a VAWT rotor. A variety of transient conditions exist for a VAWT, including start up, shut down, and unsteady winds. With the limited computational power of the time, efficient techniques were needed to perform transient analysis while minimizing calculations. Therefore, Coriolis and spin softening matrices were scaled with respect to the rotor speed. A term for the rotor acceleration was implemented in the formulation, and was scaled with respect to rotor acceleration. This scaling routine provided an efficient means to perform transient analysis of varying rotor speed and acceleration without the need to recalculate system matrices. This methodology assumes no significant dynamic response results from varying centrifugal loads, and motions between pre-stressed states are quasi-steady. This tool used NASTRAN to perform the nonlinear static analysis or "spin up" procedure for a certain rotor speed, which resulted in a converged nonlinear structural stiffness matrix. Next, the system matrices were output to file from NASTRAN, and processed by the VSFEVD tool. VSFEVD scaled system matrices with respect to rotor speed/acceleration, and performed transient analysis via a Newmark-β implicit time integration procedure. To further increase efficiency, the system matrix used in the Newmark-β formulation is re-factorized only when rotor speed has changed by a certain amount. Therefore,

one of the most expensive steps of the solution procedure was performed less frequently. A torque control model was also considered in the VSFEVD tool. In the event of an emergency shutdown braking torques are applied, but the rotor acceleration may not be directly prescribed. The torque control model ensured that the shaft torque, generator torque, shaft motions, and generator motions are compatible before prescribing a rotor speed and acceleration for a particular time step.

I.B.3. External load models/modules

Environmental loadings are obviously a crucial aspect in the operation of wind turbines. Accordingly, dynamic analysis tools should be able to interface with aerodynamic models to facilitate aeroelastic analysis. For a turbine atop a floating platform, hydrodynamics and mooring systems need to be considered. Thus, the analysis tool should interface with the external modules for hydrodynamics and mooring dynamics. To understand the flow of information between a structural dynamics tool and external modules, a review of aerodynamic and hydrodynamic models/modules was conducted.

I.B.3.a. Aerodynamics modules

The aerodynamic module the analysis tool will interface with is more or less a "black box", and it is more important to understand the data flow between the analysis tool and module than it is to understand details of individual aerodynamic models. However, a basic understanding of the various aerodynamic modeling approaches is still beneficial to the developer and designer. Allet et al. [26] provided

a comprehensive review of aergodynamic models for VAWTs, including momentum, vortex, dynamic stall, and stochastic wind models [27]. An investigation by Veers [28] provided further motivation for robust aerodynamic models. Dynamic stall is likely to be a critical aspect given large rates of change in angle of attack for a VAWT, so a validated dynamic stall model is desirable. The investigation also emphasized the limitations of steady wind assumptions and the need to include turbulent winds. Turbulent winds contain all frequencies; therefore, the response of a turbine under turbulent wind loads is of particular interest.

Sullivan and Leonard [29] made and early attempt to apply aerodynamic loads on Darrieus VAWTs using a single stream tube model developed by Templin [30]. The numerical aerodynamic loading software was known as FORCE. The code required rotor geometry, rotor speed, wind speed, and blade chord as inputs, and normal and tangential forces on the blade section are output by FORCE. The single streamtube model assumes the flow inside the rotor is parallel to flow outside the rotor. The inflow velocity to the rotor is determined via a momentum balance parallel to the ambient wind direction. An effective angle of attack for a blade section is determined from wind velocity, rotor speed, and blade geometry. Unsteady effects due to the velocity and acceleration of blade deformations did not appear to be considered by FORCE, thus indicating a limited aeroelastic modeling capability.

More refined and computationally intensive vortex methods were considered in order to provide a better local representation of flow around a VAWT. While most momentum methods can predict the average or overall response of a rotor very efficiently, these sacrificed resolution of the aerodynamic loads acting on a VAWT.

Strickland et al. [31, 32] developed the VDART3 three-dimensional vortex code for VAWTs with curved blades to provide a more accurate representation of aerodynamic loading. The vortex methods implemented in VDART3 account for vortex shedding and convection and aerodynamic stall. Studies indicated very good agreement of aerodynamic loads with experimental data.

Strickland [33] also developed a multiple streamtube model that considered multiple adjacent stream tubes capable of variations in induced velocity in the horizontal and vertical directions of the turbine. While this method was an improvement in predicting the overall performance of a rotor, it lacked the ability to describe detailed blade loadings. Paraschivoiu [34] sought to improve upon the multiple streamtube model with a double-multiple streamtube model. This model considered two actuator disks in tandem, to consider effect of upstream and downstream flow. The model was implemented in the CARDAA software package. Inputs to CARDAA were similar to FORCE, and angle of attack, forces, torques, induced velocities, and power were output. CARDAA also provided a more efficient means for simulation than a three-dimensional vortex model. Paraschivoiu et al. [35] later extended CARDAA to CARDAAV to account for secondary effects such as detailed blade geometry, rotating tower effects, and struts/spoilers via interference factors. Dynamic stall was also considered in the CARDAAV implementation. Aerodynamic force data was quite acceptable, especially considering the extreme computational efficiency gains compared to the VDART3 code.

A dissertation by Ferreira [36] has provided an extensive study of VAWT aerodynamics. In this work, a fundamental understanding of VAWT aerodynamics was

sought. These included the relation between blade loading and energy conversion, the development of the near wake of a VAWT, and differences in the two-dimensional and three-dimensional wake descriptions. A better understanding of the near wake can produce better VAWT designs, and two-dimensional aerodynamic analysis at the blade and rotor scale were employed. Considering the rotor scale allowed the relation between energy exchange and wake expansion to be characterized, whereas considering the blade scale allowed for the bound circulation to be employed to characterize the shedding of wake. Two-dimensional aerodynamic studies by Ferreira revealed that the basic treatment of VAWT as upwind and downwind actuator systems results in inaccurate energy estimations.

An improvement on double multiple streamtube models is also suggested to allow for a better description of the flow and better predictions of induction and blade loadings. Furthermore, it is advocated that streamtube momentum models be replaced by more efficient and accurate vortex models [37]. Ferreira presents a number of experimental and numerical studies to support the proposed improved aerodynamic approaches. These studies included prediction of the near wake of a VAWT, including considerations for dynamic stall. Overall, this work emphasizes the merits of two-dimensional and three-dimensional aerodynamic approaches for gaining fundamental understanding of flow physics, as well as the relation of energy exchange to blade loading. These developed insights were employed to explore VAWT design optimization at various levels, including airfoil design and blade/rotor geometry.

The Sandia National Laboratories CACTUS (Code for Axial and Cross-flow TUrbine Simulation) [38] is a modern extension of the VDART3 code and may serve

as a viable aerodynamics module in an offshore VAWT simulation framework. Vortex methods can provide a mid-fidelity option to bridge the gap between high fidelity computational fluid dynamics (CFD) simulation and lower fidelity momentum methods. This method also supports the modeling of aerodynamics for general turbine geometries. In addition to the standard capabilities of a vortex method aerodynamics code, CACTUS has modernized the solution approach to enhance computational efficiency. The software is also capable of considerations for marine applications in the modeling of marine hydrokinetic (MHK) devices.

Primary outputs of CACTUS are overall turbine torque and power, wake vortex trajectories, and blade loads. The blade loads in CACTUS are calculated as a superposition of potential flow elements, free-stream flow elements, a wake vortex system, and a bound vortex system. This yields a more accurate local blade load calculation than momentum methods. Dynamic blade load modeling is also included, and the Boeing-Vertol [39] and Leishmann-Beddoes [40] dynamic stall models are implemented within CACTUS. In order to facilitate a two-way aeroelastic coupling between CACTUS and a structural dynamics code, CACTUS will need to be modified to account accept blade displacement and potentially blade velocity and acceleration information and calculate an effective angle of attack due to blade motions.

I.B.3.b. Hydrodynamics/mooring modules

Similar to aerodynamics modules, a detailed understanding of the theory of hydrodynamic and mooring models for a floating platform is not sought in this literature review. However, understanding the data flow from an analysis tool to a

hydrodynamics/mooring module and basic concepts about the model is beneficial. The National Renewable Energy Laboratory (NREL) has developed a hydrodynamics (HydroDyn) and mooring model for interface with HAWT dynamics codes [41]. Initially, these research efforts will be utilized to understand the interface of a hydrodynamics model to a wind turbine structural dynamics implementation.

Jonkman [42] sought to develop hydrodynamics and mooring models capable of considering various floating turbine configurations, including ballast stabilized turbines using a "spar buoy", mooring line stabilized platforms using, and buoyancy stabilized platform for a floating "barge" with mooring lines. The model also accounts for wave dynamics, including the radiation and diffraction of waves from a floating platform using the WAMIT [43] wave analysis software package. The platform is treated as a rigid body with six degrees of freedom. The rigid body assumption appears adequate given the greater flexibility of the VAWT rotor relative to the floating platform. The mooring lines are treated in a quasi-static nature, providing a restoring force given the displacements of the platform. Linearization of hydrodynamics allows the problems of radiation, diffraction, and hydrostatics to be analyzed separately and combined via superposition. Vibrations induced by sea currents and effects of floating debris or ice are ignored. These effects could be significant depending on the geographical location of the turbine. Furthermore, the linearization of the hydrodynamics does not allow for steep, breaking waves against the turbine/platform to be considered. Therefore, the model assumes the amplitude of an incident wave is much less than its wavelength.

Hydrodynamic analysis considers the force of incident waves, hydrostatic forces

such as buoyancy, wave radiation/diffraction, and an added mass term due to the dynamic movement of the platform. In addition to these hydrodynamic forces, restoring forces from a mooring system may be applied to the platform. The quasi-static nature of mooring system force calculations may be adequate if the inertia of the mooring system is negligible (which is often the case relative to the platform). The HydroDyn [41] hydrodynamic module accepts information regarding the platform geometry, wave data, and platform motions. The platform geometry is used in the WAMIT processor to calculate hydrostatic restoring, damping, and added mass matrices. This information is used by HydroDyn in conjunction with buoyancy calculations to output the hydrodynamic loads and an added mass of the platform to the turbine dynamics software. Overall, one can note the striking similarities to aerodynamics modules. Wave data is analogous to wind data, platform geometry analogous to blade geometry, and platform motions analogous to turbine motions/deformations. In addition to forces acting on a turbine the added mass of the platform is also considered. The mooring module is much simpler in nature, requiring only the platform position and mooring line properties as inputs and outputting restoring forces, as well as line and anchor tensions.

The WavEC hydrodynamics code [44] developed for wave energy converters (WEC) may serve as another viable option for a hydrodynamics module. This analysis software contains the necessary physics to model a floating platform, and requires minimal effort to account for an attached turbine structure that imparts an arbitrary force onto a floating platform modeling in WavEC. Three dimensional radiation and diffraction effects are accounted for by using the WAMIT processor. WavEC also has

the ability to consider a regular and irregular spectrum of wave histories applying forcing to the floating platform. This allows for structural dynamics analysis of the turbine to consider the effect of various wave loadings. Mooring restoring forces are currently calculated using a user-specified polynomial function that is dependent on platform position and velocity. Future developments could increase the robustness of the mooring model implemented in WavEC. Nevertheless, the WavEC hydrodynamics module is a viable option for modeling the rigid body motions of a offshore turbine/floating platform system.

Commercial analysis codes developed for offshore marine systems may also serve as a viable module for modeling platform dynamics, hydrodynamics, and mooring systems. Codes such as OrcaFlex® [45] are very capable of modeling a variety of offshore systems including risers, hose systems, towed systems, buoy systems, wave power systems, and floating platform systems. OrcaFlex features a robust, high fidelity mooring line modeling capability that includes fully coupled bending, torsion, and axial stiffness, sea-bed friction modeling, contact modeling, hydrodynamic loading, wake interference, and compressibility effects. Mooring line modeling is coupled to platform dynamics modeling within the OrcaFlex analysis software. Furthermore, platform motion modeling can accept arbitrary loads, such as thrusters, ice, or interaction forces of an attached wind turbine. A variety of environmental conditions such as wind, wave, and current conditions can also be specified. OrcaFlex is also packaged behind a convenient user interface to aid in model preparation and visualization of analysis results. For these reasons, design of future offshore wind energy tools should consider the interface of robust, third-party analysis software in addition

to custom research codes.

I.B.4. Analysis strategies

This sub-section presents a review of analysis strategies that may provide useful insight towards the development of an aeroelastic design tool for offshore vertical-axis wind turbines. A review of existing beam models will be given for consideration in the development of a structural dynamics formulation for VAWT configurations. Linearization procedures for efficiently arriving at linearized representations of flexible systems are also highlighted, and a review of aeroelastic stability of wind energy systems is also presented.

I.B.4.a. Beam models

Structural components of a VAWT are relatively slender compared to the length of a component, and may be adequately described by beam theory. Therefore, a review of previous beam structural dynamics research was conducted. Crespo da Silva [46] presented a formulation for the equations of motion of an Euler-Bernoulli beam with flexural-flexural-torsional-extensional deformation. This was an extension of previous work for flexural-flexural-torsional dynamics [47]. This formulation included nonlinearities resulting from midplane stretching, curvature, and inertia terms. The formulation also accounted for a variation in stiffness and mass properties along the beam axis. Hodges [48] formulated nonlinear equations of motion for a curved and twisted beam in a moving frame. The formulation also allowed for relatively simple shape functions to be utilized, making it an ideal candidate for a finite

element formulation/implementation. Freno and Cizmas [49] developed an efficient non-linear beam model for aeroelastic analysis. The formulation required a straight elastic axis, and employed an assumed modes method. Nonlinear aeroelastic analysis would be performed using an iterative approach between structural dynamics and aerodynamic loads analysis.

High fidelity beam theories such as Geometrically Exact Beam Theory (GEBT) [50] may provide a means for accurate modeling of structural motions beyond initial design study efforts. Such a theory employs local displacement measures, exact coordinate transformations, and orthogonal virtual rotations to arrive at a formulation capable of accurately predicting large rotations and large displacements in a flexible structure. The use of "energetically-conjugate" [51] stress and strain measures is central in the development of an accurate nonlinear beam theory. Warping functions [50,52] may also be employed to accurately characterize cross-sectional warping and behavior of composite structures. This more accurate modeling (due to the large degree of nonlinearities present in a GEBT model) comes at some computational expense. Thus, linear representations or models with limited nonlinearities may be of use for preliminary design studies while GEBT is employed for more detailed analysis studies.

The aforementioned research will serve as a valuable reference for the development of a nonlinear beam for use in modeling the aeroelastic response of VAWTs. Furthermore, it appears that the finite element method [51] is well poised to provide a flexible and robust beam formulation for aeroelastic VAWT analysis. Where necessary, extensions in formulations should include effects due to turbine rigid body

motion, as well as general orientations of beam structures to characterize arbitrary VAWT configurations. Furthermore, one should note that as robust beam models are formulated, it is also critical to have accurate methods for predicting effective section properties of a beam from the three-dimensional description of a structural component. The methods considered in variational asymptotic beam section analysis (VABS) [53], Sandia National Laboratories Beam Property Extraction (BPE) tool [54], or NREL PreComp [55] will likely be useful in obtaining sectional properties for VAWT structural components.

I.B.4.b. Linearization methods

Although linear representations do not fully embody the nature of a dynamic system, linearization can capture the dominant motions about a particular equilibrium condition. Furthermore, linear representations are extremely useful for gaining insight into system behavior as well as providing an efficient analysis capability for initial design studies. Thus, a linearized representation of a flexible beam in a floating frame are of interest. Accordingly, the method of quadratic modes developed by Segalman and Dohrmann [56, 57] may be useful to ensure the critical components of kinematics due to rotational motion are included. This method seeks to relieve the analyst of cumbersome linearization procedures by ensuring only a "bare minimum" of the kinematic description is included before linearization. Alternatively, direct linearization procedures developed by Parish et al. [58] may also be utilized to efficiently formulate linearized equations of motion. This procedure was developed for general rheonomic systems, including discrete and continuous systems.

I.B.4.c. Aeroelastic stability

Dynamic aeroelastic instability or "flutter" is a self-starting and potentially destructive vibration where aerodynamic forces on a lifting structure couple with the structure's natural modes, producing large-amplitude, diverging periodic motion. Flutter is a common consideration for aircraft which may be exposed to a variety of operating conditions. Historically, flutter has not been a design issue for utility-scale HAWTs, but as previously noted, flutter instability was observed on a small-scale VAWT design [22]. Furthermore, estimates of flutter speed for a variety of HAWTs have shown that as blades grow in length, the margin of estimated flutter speed relative to turbine operating speed decreases [59,60]. Thus, flutter may be a concern and may be a concern for very large VAWT designs. For this reason, aeroelastic stability analysis capability is being considered in the development of a design tool for offshore VAWTs.

Classical flutter [23, 61, 62] examines the effects of aerodynamic loads on the dynamic stability of a structure. Vortex shedding at the trailing edge of an oscillating lifting surface results in unsteady aerodynamic effects that depend on the motion of the structure. Examination of unsteady aerodynamic theory developed by Theodorsen [23] reveals that unsteady aerodynamic effects may be considered as aerodynamic mass, damping, and stiffness terms and combined with the structural coefficient matrices of a dynamic system. Thus, modal analysis may be employed to assess the stability of an elastic system under aerodynamic effects (aeroelastic system). Aeroelastic analysis of an aircraft may consider stability at particular operating conditions such as airspeed and altitude. A similar analogy exists for a wind

turbine, with the operating condition being rotor speed.

Previous work by Lobitz [59] considered the flutter analysis of an isolated wind turbine blade rotating in still air. The turbine blade was considered to be cantilevered at the root, and analysis was performed in a rotating frame. Such a system has been termed a "Gyric" system in the literature [63] in that it is a linear representation of a flexible structure under a prescribed angular velocity. Considering the system in the rotating frame allows for rotational effects such as "spin softening" and "Coriolis" effects to be considered in a straightforward manner. Accounting for centrifugal loads on the reference position of the blade allows for "stress stiffening" effects to be accounted for. These effects model the increased stiffness of a structure under load, and may significantly affect the modal response of a flexible system. The tool, which was originally developed for considering flutter in vertical-axis wind turbines, was applied to utility scale horizontal-axis wind turbine blades. This analysis tool was used to investigate the ramifications of using simplified aerodynamic theory (quasi-steady) in flutter analysis of wind turbine blades, as well as investigate the effects of flap-twist coupling on the flutter of turbine blade designs.

Hansen [64] also considered flutter of wind turbines, but considers stall induced vibration. This is a fundamentally different phenomenon from classical flutter. It should be noted that classical flutter tends to be more catastrophic in nature than stall induced vibrations. Furthermore, classical flutter is typically a concern for pitch regulated turbines while stall-induced vibrations tend to be a concern in stall regulated turbines. Hansen considered modeling of a complete turbine (tower and rotor) and the aeroelastic interaction of stall induced vibrations with the inflow/wake.

The aforementioned approaches make use of a modal analysis approach to investigate aeroelastic stability of wind turbines. Indeed, the frequency domain representation of Theodorsen unsteady aerodynamics are easily adapted in a modal analysis approach. Modal analysis, however, relies on the identification of some equilibrium condition such as a constant rotor speed. Transient aeroelastic stability analysis can allow for time-varying conditions such as start up, shut down, unsteady inflow and gusts to be considered. The transient unsteady aerodynamics model developed by Leishman [65, 66] may be useful in the development of transient aeroelastic stability analysis. In this model, unsteady aerodynamic loads due to shed wake are accounted for through a state-space realization that is easily adaptable to transient analysis. Under this approach, the structural matrices would not modified to account for aeroelastic effects. Instead, unsteady aerodynamic loads that are a function of structural displacements are simply applied to the structure.

I.C. Outline

Chapter II presents an overview of the modular analysis framework for the developed design tool. The Offshore Wind ENergy Simulation (OWENS) toolkit is a modular, extensible framework that will allow the interface of a core structural dynamics module (for characterizing the motion of a flexible turbine configurations), with various external modules including aerodynamics, hydrodynamics, generator, and drive-train modules. At the core of the structural dynamics modeling is a dynamic finite element beam formulation and implementation which includes gyroscopic effects. As part of this effort, a robust mesh generator capable of considering

arbitrary VAWT configurations has also been developed.

Chapter III presents the development of an energy preserving time integration method for Gyric systems. A previously developed integration method for flexible systems was extended to consider Gyric systems which include rotational effects. A discussion of Gyric systems is presented and these systems are contrasted to flexible/deformable systems without rotational effects. Energy in Gyric systems is also discussed. The unique energy properties of conservative Gyric systems are employed to develop a proof of unconditional stability and energy preservation for the Gyric time integration method. The formulation of the time integration method is discussed in detail, as well as the practical implementation of the method into a numerical framework. Furthermore, certain schemes of the popular Newmark-β implicit integration method are also proved and demonstrated to be energy preserving for conservative Gyric systems.

Chapter IV presents the basis for a new approach for efficiency developing linearized representations of dynamic systems. This process seeks to combine to developed strategies for developing linearized representations, while eliminating the drawbacks of each approach. The strengths of each approach are employed to arrive at a more powerful and efficient approach that will be elaborated on and demonstrated. This efficient approach is employed in Chapter V to develop linearized equations of motion for a Timoshenko finite beam element in a floating frame, undergoing general rotational motion. This chapter also presents an efficient means for developing a reduced order model of a VAWT structure represented as an assembly of finite elements.

Chapter VI presents considerations for aeroelastic stability analysis in wind energy systems. Aeroelastic instabilities have been observed in small-scale VAWT configurations and may be of concern for very large VAWT configurations. Thus, aeroelastic stability analysis has been considered in the development of the OWENS toolkit. Furthermore, the modular framework within the OWENS toolkit was employed to develop a new aeroelastic design tool for HAWT blades, and formulations for adding aeroelastic effects to modal analysis capability are discussed. Key differences between the newly developed tool and previously developed approaches are highlighted. Aeroelastic stability predictions from modal analysis are contrasted to time-domain approaches, and advantages of a transient aeroelastic analysis capability are discussed.

Chapter VII demonstrates and verifies a reduced order model of a VAWT structure. Other features are also demonstrated, including a variety of turbine rotor operation modes including specified rotor speed profiles, generator start up mode, and self starting turbine modes. This chapter also demonstrates a two-way coupling of the structural dynamics analysis capability to an external floating platform dynamics module using the coupling strategies discussed in Chapter II. Coupling to a VAWT aerodynamics code is also presented.

Chapter VIII presents initial design studies of large vertical-axis wind turbines for offshore deployment. Historically, tower resonance has been a concern for VAWTs, and this issue is explored further. Tower mode excitations are known to be sensitive to certain per-rev excitations dependent on the number of blades employed in the VAWT configurations. Previous "rules of thumb" have been generalized to analytical

expressions for identifying critical per-rev excitations capable of causing resonance for an n-bladed VAWT configuration. The effect of support conditions (e.g. land-based, monopile, floating platform) on resonance in rotating VAWT structures is also presented and the potential for resonance in rigid body modes of floating VAWT configurations is discussed. Aeroelastic stability analysis of a multi-megawatt VAWT configuration is also considered.

Appendix A presents verification and validation of the structural dynamics formulation and implementation in the OWENS toolkit. Initial verification exercises consist of comparison to analytical expressions for stationary as well as a rotating beam with gyroscopic effects by employing the known analytical solutions for a "whirling shaft" configuration. Results for both modal and transient analysis are presented. Numerical verification procedures are also considered, including the use an assumed modes approach as well as commercial finite element software. Validation exercises are conducted by comparing numerical predictions to experimental measurements of a parked and rotating utility scale turbine.

CHAPTER II

THE OFFSHORE WIND ENERGY SIMULATION TOOLKIT FOR VERTICAL AXIS WIND TURBINES

This chapter presents the analysis framework for the Offshore Wind Energy Simulation toolkit for vertical-axis wind turbines. First, the desired features for the analysis tool are identified. These features are necessary to consider preliminary design studies of innovative VAWT configurations, as well as ensure the tool will be extensible to future needs of the wind energy community. Fundamentals of the model formulation are discussed, and a modular framework for interfacing a core structural dynamics solver with various external modules is presented. The concept of a "loose" coupling strategy is presented and coupling methodologies are demonstrated on a simplified example. The practical implementation of data flow between a core analysis framework and external modules using network sockets is also discussed.

A robust mesh generator has been developed that is capable of considering arbitrary VAWT configurations, and the design and features of this mesh generator are discussed. An overview of the finite beam element that is central in the development of the analysis tool is given, and details of the formulation are given in a later chapter. The framework also allows for various constraints (i.e. fixed, ball joint, hinge) to be specified between turbine structural components. This chapter concludes with a discussion of various "internal modules" implemented into the analysis tool which include rotor speed update, generator, and drive-shaft modules.

II.A. Design tool features

The analysis tool has been designed per the envisioned needs of modeling efforts for large offshore vertical-axis wind turbines. This tool has been developed with the goal of maintaining a general framework for analyzing VAWTs of an arbitrary configuration. Furthermore, the formulation seeks to provide flexibility for future analysis needs. In particular the following features are central in the design and development of the analysis tool.

- The analysis tool can model the structural dynamics of a collection of beam structures prescribing an arbitrary path in space that rotates around a central, vertical axis. Potential VAWT configurations will include Darrieus rotors, H-rotors, and V-rotors. Blades may be affixed to the tower directly or through the use of struts, and rotor blades could be swept toward or against the direction of travel.

- The analysis tool can integrate the equations of motions in the time-domain as well as consider frequency domain analysis. Transient analysis is necessary to consider structural response under transient conditions such as start up, shut down, and irregular wave and wind loadings. A frequency domain analysis is desirable to facilitate stability analysis of a VAWT configuration and identify potential resonance issues.

- The analysis tool has a streamlined, modular framework that can account for various fidelity of structural dynamics analysis models. These models include linear beam representations with geometric nonlinearities in the form of stress

stiffening effects, efficient reduced order models, and future development of capability to include geometric nonlinearities due to large component deflections.

- The structural model can account for passive aeroelastic coupling mechanisms, including bend-twist, extension twist, and sweep-twist couplings. Thus, the blade must have a torsional degree of freedom.

- The structural formulation can accommodate jointed blade structures. This requires the ability to specify concentrated mass and stiffness terms.

- The boundary conditions for the blade connections as well as the platform/turbine base are general and can include fixed, free, and pinned conditions.

- The analysis tool enables general coupling with available VAWT aerodynamic models.

- The analysis tool enables general coupling to floating support structure, and mooring system hydrodynamic models.

- The analysis tool enables a general interface with a model for drive-train mass and dynamics.

- The analysis tool design considers the interface of a turbine control algorithm, as well as prescribed motion of the blades and tower, and prescribed braking torque on the tower.

- The analysis tool considers ease of interface with existing wind turbine design tools.

The following sections present a formulation for the aeroelastic modeling of offshore VAWTs while satisfying these desired features.

II.B. Model formulation

The fundamental requirements of the aeroelastic analysis tool for offshore VAWTs necessitates a flexible framework capable of considering arbitrary configuration geometries, arbitrary loading scenarios, and the ability to interface with various modules that account for the interaction of the environment and power generation hardware with the turbine structure. The finite element method provides a means to satisfy these general requirements. If a sufficiently robust element is developed, a mesh (collection of elements) of an arbitrary VAWT configuration may be constructed via a mesh generator. The ability to capture various couplings and provide an accurate representation of turbine behavior will depend on the robustness of the element formulation.

The finite element method requires boundary conditions to be imposed on the elements by specifying loads or displacements at discrete points (nodes) in the mesh. These boundary conditions provide a clear interface between aerodynamic and hydrodynamic modules that impart forces on the turbine. With boundary conditions specified, unspecified displacements and loads may be calculated. Next, displacement motions of the turbine and/or internal reaction forces may be provided to aerodynamic and hydrodynamic modules to calculate loads on the turbine. This gives rise to mutual causation because in reality loads and displacements are intricately connected. Iterative procedures and coupling methods that will be discussed in this

chapter, however, allow for convergence to be reached, eliminating this issue for all practical purposes.

The subsections that follow will present basic formulation concepts including the equations of motion and considerations for modal and transient analysis. Subsequent sections will present a modular analysis framework, along with coupling strategies. Details of a mesh generator for VAWTs, necessary features of a finite beam element formulation, and constraints are also discussed.

II.B.1. Basic formulation concepts

Basic formulation concepts will be discussed before describing components of the proposed formulation in detail. As stated earlier, the finite element method will be employed for its robustness and flexibility. A robust element formulation will become the foundation of the aeroelastic analysis tool. Analysis of the dynamic response of the turbine is challenging because of rotating components. Because almost all structural components of the turbine will be rotating at some rotor speed (Ω), it is convenient to perform the formulation in a rotating reference frame. Such a frame is capable of capturing rotational effects, including centrifugal stiffening/softening and Coriolis effects in a straightforward manner.

II.B.1.a. Equations of motion

Equations of motion for the platform are developed by treating the platform as a rigid body, whereas the turbine is treated as a rotating deformable body. Motions of discrete points on the turbine can be expressed as the sum of the turbine motion

(deformation and rigid rotor rotation) and the platform motion (rigid). Expressions for the velocities of the platform and for an arbitrary point on the turbine are shown below:

$$\vec{V}_{platform} = \frac{^{(N)}d}{dt}\vec{R}_{P/N} = \dot{U}_1\hat{n}_1 + \dot{U}_2\hat{n}_2 + \dot{U}_3\hat{n}_3 \tag{2.1}$$

$$\vec{\omega}_{platform} = \omega_1\hat{p}_1 + \omega_2\hat{p}_2 + \omega_3\hat{p}_3 \tag{2.2}$$

$$\vec{v} = \vec{V}_{platform} + \left[\left(\vec{\omega}_{platform} + \Omega\hat{h}_3\right) \times \left(\vec{R}_{offset} + \vec{r}\right)\right] + \frac{^{(H)}d}{dt}\vec{r} \tag{2.3}$$

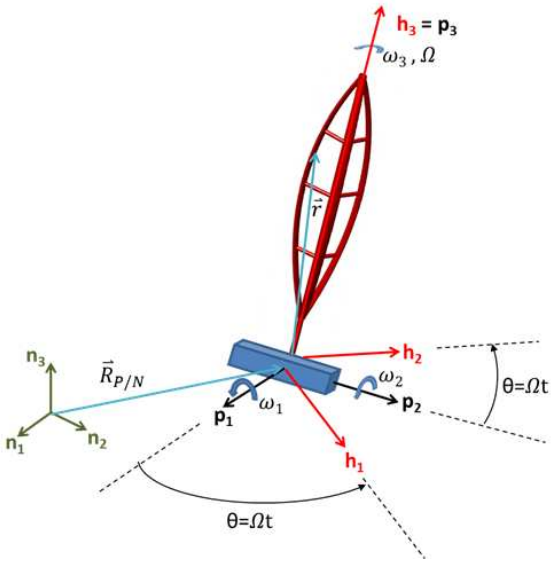

Figure II.1. Illustration of frames, position vectors, and angular velocities

Figure II.1 presents an illustration of the frames, angular velocities, and positions vectors that will be described. Here, U_i represents the displacement components of the platform center of mass, and ω_i represents the angular velocity of the platform. The inertial frame is represented by the $\hat{n}_i$ coordinate axes, the platform frame is represented by the $\hat{p}_i$ coordinate axes, and the rotating hub frame is represented by

the $\hat{h}_i$ coordinate axes. The operators $\frac{^{(N)}d}{dt}$ and $\frac{^{(H)}d}{dt}$ define derivatives with respect to the inertial and hub frames respectively. The vector r_i defines the position of an arbitrary point on the turbine with respect to the hub frame origin. The expression for velocity of a particle in this floating frame is arrived at through use of the Transport Theorem [67]. An offset between the platform frame origin and the hub-frame origin may be introduced through the vector $\vec{R}_{offset}$. The rigid nature of the platform enforces that $\dot{\vec{R}}_{offset} = 0$. Angular acceleration $\dot{\Omega}$ and $\dot{\omega}_i$ will become apparent when these velocities are used in conjunction with Hamilton's extended principle to formulate finite element equations of motion, but these details will not be elaborated on in this section. Hamilton's principle relates the variation of kinetic energy (T) and potential energy (V), and virtual work of non-conservative forces (δW_{np}) to formulate equations of motion. Hamilton's extended principle is written simply as:

$$\delta \int_{t_1}^{t_2} [T(t) - V(t)]\, dt + \int_{t_1}^{t_2} \delta W_{np} = 0 \tag{2.4}$$

The kinetic energy of the system may be written compactly as:

$$T_{system} = T_{platform} + T_{turbine} \tag{2.5}$$

$$T_{platform} = \frac{1}{2} M_{platform} \vec{V}_{platform} \cdot \vec{V}_{platform} + \frac{1}{2} \left(\vec{\omega}_{platform}\right)^T [J] \vec{\omega}_{platform} \tag{2.6}$$

$$T_{turbine} = \frac{1}{2} \int_V (\rho \vec{v} \cdot \vec{v})\, dV \tag{2.7}$$

The platform kinetic energy is decomposed into two parts, translational kinetic energy and rotational kinetic energy (where $[J]$ is the moment of inertia tensor for the platform). The turbine (which will be represented by a collection of elements) kinetic energy is expressed in terms of the volume integral of the structural component den-

sity at infinitesimal points and the velocity of the infinitesimal points in the turbine (as developed earlier).

Note that the quantities described above may be represented or "coordinatized" in any frame. Indeed, some vectors were expressed in the inertial ($\hat{n}_i$) frame, and others in the rotating hub ($\hat{h}_i$) frame. Because the rotating turbine represents the bulk of the modeling effort, the implementation of the equations of motion will be coordinatized in the hub frame. Platform motions and forces, however, are likely to be described in the inertial frame. Therefore, transformations between the inertial and hub frame are performed where necessary.

In the development of equations of motion, one can choose to retain the rotor angular velocity/acceleration (Ω / $\dot{\Omega}$) and platform angular velocity/acceleration (ω_i / $\dot{\omega}_i$) as degrees of freedom in the resulting system of equations or as specified motion parameters. Retaining these terms as degrees of freedom is undesirable because it adds significant complexity to the formulation and introduces a significant number of nonlinear terms. More critically, however, is that the analysis tool must be interfaced with independent modules for aerodynamics, hydrodynamics, and generator dynamics that will affect these rotational motion quantities. Therefore, the advantage of retaining this term as a degree of freedom instead of a prescribed parameter is diminished. Accordingly, these variables will be retained as specified motion parameters. The value of these parameters will be updated by post-processing routines after gathering information from the aforementioned modules and turbine motions. Beam theory will be employed to represent the structural motions of the turbine, and a derivation of equations of motion for a beam element are presented in a later

chapter.

The resulting equations of motion for a floating turbine structure will be of the following form (hyperbolic):

$$[M]\{\ddot{q}\} + [C]\{\dot{q}\} + [K]\{q\} = \{F\} \tag{2.8}$$

This can be decomposed to show contributions from the turbine and platform and show couplings between the two:

$$\begin{bmatrix} M_{TT} & M_{TP} \\ M_{PT} & M_{PP} \end{bmatrix} \begin{Bmatrix} \ddot{q}_T \\ \ddot{q}_P \end{Bmatrix} + \begin{bmatrix} C_{TT} & C_{TP} \\ C_{PT} & C_{PP} \end{bmatrix} \begin{Bmatrix} \dot{q}_T \\ \dot{q}_P \end{Bmatrix} + \begin{bmatrix} K_{TT} & K_{TP} \\ K_{PT} & K_{PP} \end{bmatrix} \begin{Bmatrix} q_T \\ q_P \end{Bmatrix} = \begin{Bmatrix} F_T \\ F_P \end{Bmatrix} \tag{2.9}$$

Such that M, C, and K represent the system mass, damping, and stiffness matrices respectively. The terms q_T and q_P denote the generalized displacements of the turbine and platform respectively. The terms F_T and F_P denote the forces acting on the turbine and platform respectively. Terms with subscript "TT" denote influence of the turbine forces on the turbine response. Whereas, terms with subscript "TP" denote influence of turbine forces on the platform response, and terms with subscript "PT" denote influence of the platform forces on the turbine response. Finally, terms with subscript "PP" denote the influence of platform forces on the platform response. Although not explicitly shown here, the rotor angular velocity/acceleration and platform angular velocity/acceleration are incorporated in the turbine damping and stiffness matrices through gyroscopic effects. Effects related to translational acceleration of the hub-frame (due to platform rigid body motion) are manifested in

the turbine force vector through body forces. These details will be expanded on in the finite element formulation presented in Chapter V.

As will be shown in a later section, the ability to consider a modular framework will require this coupled system to be partitioned into two sub-systems with interaction terms. That is, the turbine equations of motion in Eq. 2.9 become

$$[M_{TT}]\ddot{q}_T + [C_{TT}]\dot{q}_T + [K_{TT}]q_T = F_T + F_{TP} \tag{2.10}$$

Such that,

$$F_{TP} = -[M_{TP}]\ddot{q}_P - [C_{TP}]\dot{q}_P - [K_{TP}]q_P \tag{2.11}$$

Similarly, the platform equations of motion in Eq. 2.9 become

$$[M_{PP}]\ddot{q}_P + [C_{PP}]\dot{q}_P + [K_{PP}]q_P = F_P + F_{PT} \tag{2.12}$$

Such that,

$$F_{PT} = -[M_{PT}]\ddot{q}_T - [C_{PT}]\dot{q}_T - [K_{PT}]q_T \tag{2.13}$$

II.B.1.b. Modal/Transient Analysis

Modal analysis may be performed on the above turbine system of equations to examine the stability of the turbine configuration. Whereas understanding the stability of a turbine to avoid potential resonance issues is critical, transient conditions such as rotor start-up, turbulent/unsteady winds, and unsteady waves require a transient analysis capability. Explicit time integration of the ordinary differential equations (ODEs) is convenient due to its simplicity and the availability of commercial ODE integrators. Unfortunately, explicit time integration typically requires the time domain to be highly discretized (small time steps). This concern is exacerbated

by the high frequencies that can be present in the finite element representation of the turbine configuration. Therefore, implicit time integration methods have been considered for their ability to reduce time step restriction and maintain efficiency. The Newmark-β [68] method as well as another time integration method developed by Dean et al. [69] have been employed in the analysis framework. A subsequent chapter discusses the energy conserving properties of these integration methods can be generalized to rotational or *Gyric* [63] systems.

II.C. Analysis framework

The proposed analysis framework will allow a convenient coupling of the structural dynamics finite element analysis to aerodynamic, hydrodynamic/mooring/platform dynamics, and generator modules. Figure II.2 shows an illustration for the framework of the Offshore Wind Energy Numerical Simulation (OWENS) toolkit indicating data flow among the analysis tool and various modules. In this figure analysis components surrounded in the purple boxes are independent modules that will interface with the VAWT simulation tool. The proposed analysis tool will provide and receive data to and from these modules. The implementation of these modules, however, are "as is" and cannot be modified by the developer. Components outlined in the blue boxes are components of the analysis tool that are under direct development by the developer. Data flow is illustrated by various colored arrows. Orange arrows denote an internal data flow from one segment of OWENS analysis components to another. Red arrows denote flow of information from the core analysis tool to external modules. Green arrows represent flow of information from external modules to the core analysis tool

components. Blue arrows denote flow of information from one external module to another or external data to an external module.

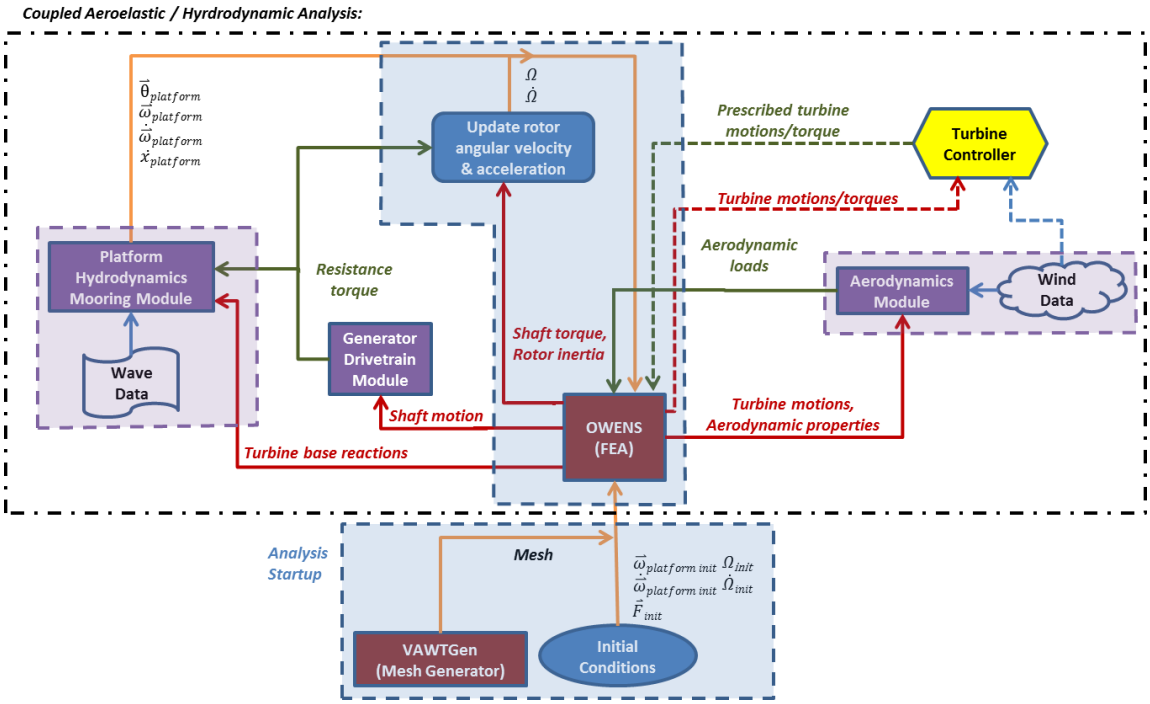

Figure II.2. Analysis framework for the OWENS toolkit

The proposed framework begins with start up procedures. These include creation of the VAWT configuration mesh using the mesh generator VAWTGen, and specification of initial conditions. VAWTGen produces a finite element mesh (a collection of beam elements and concentrated masses/springs) representative of the VAWT turbine. Initial conditions such as the initial forces acting on the turbine/platform, initial rotor angular velocity/acceleration, and initial platform angular velocity/acceleration must be provided. With these specifications complete, the

coupled aeroelastic/hydrodynamic analysis begins, involving the components outlined in the black box.

The mesh and initial conditions are provided to the OWENS toolkit. By performing a transient analysis via the aforementioned time integration procedures, turbine and platform motions are calculated. The turbine motions along with aerodynamic properties of the turbine are provided to an aerodynamics module. Wind field data is also considered along with the motions to calculate aerodynamic loads on the turbine. The aerodynamic loads are provided back to the OWENS toolkit as boundary conditions for the next time step or iteration. This interface is analogous to the interface between NREL's FAST analysis tool [70] and the AeroDyn aerodynamics module [71, 72].

The motion of the turbine shaft is provided to a generator/drive-train model, which considers the relative motions of the shaft and generator to calculate a resistance torque provided by the generator. By considering the resistance torque along with the shaft torque and rotor inertia, an updated rotor angular velocity/acceleration may be calculated. This interface is modeled after the generator interface in NREL's FAST analysis tool [70].

Turbine base reactions are provided to the hydrodynamics/mooring/platform dynamics module. This serves as external forcing on the platform in addition to wave excitation and hydrodynamic/mooring restoring forces. Within the platform module, a dynamics solver predicts the rigid body motion (translation and rotation) of the floating platform and the rigid body motion is returned to the structural dynamics solver. Translational acceleration, angular acceleration, and angular velocity

are used to apply body forces to the flexible structure as well as update the rotational effects that are inherent in the finite element formulation system matrices. The attitude description of the platform is also used to perform coordinate transformations between the platform an inertial frames. This along with the transforms related to the rotor azimuth ensures that effects coordinatized in the inertial frame (such as gravity) are correctly applied to the rotating structure that is represented in the hub frame.

The above description fully outlines the proposed analysis framework and interface of the core analysis tool with various modules. In the development of this framework, a one-way coupling is inherent in that typically motions are provided to a module and loads are calculated and supplied back to the analysis tool. In reality such a clear flow of information does not exist, and the coupling is more complex with loads influencing motions in addition to the motions influencing loads. Therefore, at any given time step an iterative procedure will likely be considered to reach a convergence among the actual two-way coupling between the turbine structural dynamics and aerodynamics, hydrodynamics/platform dynamics, and generator dynamics. The framework can also account for a turbine controller algorithm, such as an applied breaking torque to control rotor speed.

As illustrated in Figure II.2, the turbine controller accepts turbine motions, rotor speed/torque, or wind data and provides prescribed motions or breaking torques. Details of the controller will not be elaborated on, but consideration for a controller algorithm has been made in the development of the proposed framework.

II.D. Coupling strategies

The OWENS toolkit has been designed with ability to interface with arbitrary modules that provide forcing during a structural dynamics simulation. There are a number of ways to consider incorporating external forcing in the analysis framework. One approach, which has been termed "monolithic" [73] incorporates the solution for both the external loads and the structural responses into a single system of equations to be solved at each time step. Whereas this potentially allows for structural dynamics and loading calculations to be performed simultaneously, the modularity of the framework is severely limited. This approach requires all details of loading calculations be implemented alongside the structural dynamics code under a single framework. Furthermore, this approach potentially requires more overhead in code management and limits the ease of collaboration. A monolithic code not only requires developers to understand the details and implementation of particular external loading calculations, but also requires understanding the intricacies of the monolithic framework design and implementation. This can potentially limit code development and collaboration efforts. Therefore, a monolithic framework has not been considered for the OWENS toolkit.

Another approach considers "loose" coupling of modules and provides a greater degree of flexibility and modularity in the framework. The framework is no longer monolithic and knowledge of details of external modules is not required by the core analysis framework. Instead, only the data flow between the module and core analysis framework must be defined. This approach has been illustrated in Figure II.2 for the OWENS toolkit. A specific example is that reaction force at the base of a turbine

will be provided to a platform/hydrodynamics module that calculates the rigid body motions (translational and rotational) of a floating platform under the influence of an attached, flexible turbine structure. The core analysis has no knowledge of the hydrodynamics calculations being performed, and only requires the rigid body motions of the platform system to perform the coupled simulation.

The drawback of the loosely coupled approach is that analysis occurs in a staggered manner with motions/forces at previous time steps being utilized to calculate solutions at a current time step(see FigureII.3). This can lead to potential stability concerns in the coupling procedure, and critical time step sizes must be considered to maintain a stable solution procedure. The stability limits of this approach are understood [74] and consequences of the inherent approximations in this approach can be eliminated for all practical purposes with sufficiently small time steps.

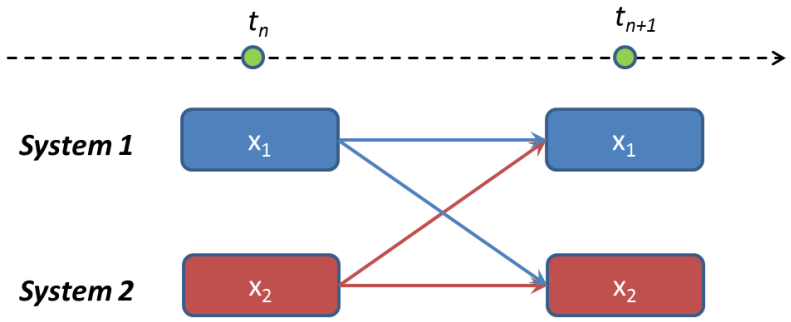

Figure II.3. Illustration of loose coupling approach

An improvement over the loose coupling procedure considers an iteration at each time step, using a "predictor-corrector" approach. A popular approach is the Gauss-Seidel method [75]. This approach is illustrated in Figure II.4, in which a coupling

of two sub-systems is considered. First, information from solutions established at a previous time is used to predict the solution of system 1. This is the "predictor" step of the method. Second, a substitution of the predicted system 1 solution is used to obtain a solution prediction for system 2. Thirdly, a correction to the solution of system 1 is obtained by using the most up to date estimates. The second and third steps may be iterated until some convergence criterion between current predictions and previous predictions is met. Although this simple discussion considered only two systems, the Gauss-Seidel iterative method is applicable to a modular framework composed of an arbitrary number of systems, such as that in the OWENS analysis framework.

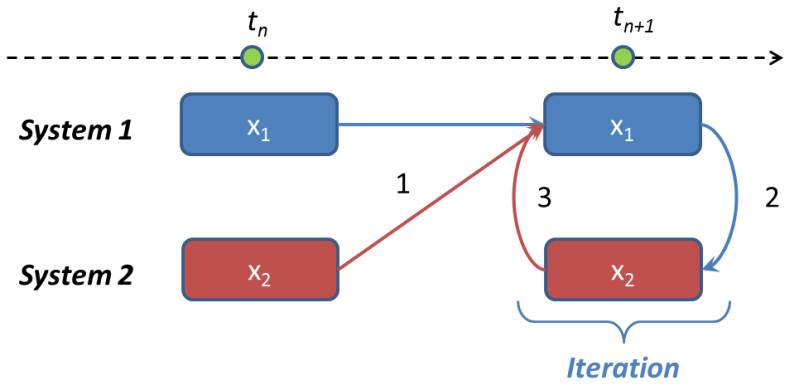

Figure II.4. Illustration of Gauss-Seidel coupling approach

A drawback of the Gauss-Seidel iterative approach requires more evaluations per time-step. For k iterations, the approach will require $1 + nk$ sub-system evaluations where n is the number of sub-systems in the modular framework. Thus, the iterative

approach comes at greater computational cost per time step compared to a loose coupled approach. Nevertheless, stability and accuracy concerns can exist for a loose coupled methodology. As will be shown, the Gauss-Seidel approach can relax stability concerns (allowing a larger time step size) and can allow for a more accurate solution. Such benefits can outweigh the increased computational cost per time step associated with the Gauss-Seidel approach.

II.D.1. Demonstration of coupling approaches

Previous work [73] has investigated various coupling approaches using simple spring-mass type systems. The simplified nature of this system allows for a "monolithic" coupling to be developed with relative ease. This also allows for modular sub-systems with interaction terms to be identified, and alternative coupling approaches to be explored. Herein, an alternative model is considered to demonstrate the coupling approach that is more analogous to a floating wind turbine.

Consider the classical dynamic system of a gantry crane as shown in Figure II.5. The gantry with mass M is constrained to translate a distance $x(t)$ in the horizontal direction. An attached pendulum with massless arm of length L with a payload represented by a concentrated mass m at the end of the bar can rotate through an angle $\theta(t)$ in-plane. Furthermore, a linear translational spring with stiffness k is attached to the gantry, and a linear rotational spring of stiffness κ is attached between the base of the crane and the rotating arm. This two degree-of-freedom system may be considered a simplified model of a swaying platform with some flexible structure (i.e. a turbine or tower) attached.

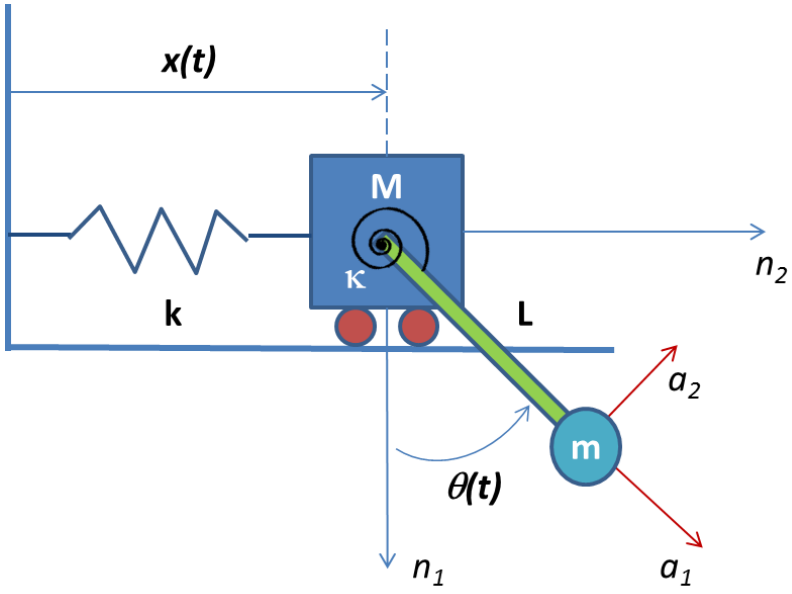

Figure II.5. Illustration of two degree-of-freedom gantry crane

The kinetic energy function of this system is

$$\mathscr{T}\left(\dot{x},\dot{\theta},\theta\right)=\frac{1}{2}\left[\left(M+m\right)\dot{x}^{2}+mL^{2}\dot{\theta}^{2}+2m\dot{x}\dot{\theta}L\sin\theta\right] \tag{2.14}$$

and the potential energy function of this system is

$$\mathscr{V}\left(x,\theta\right)=\frac{1}{2}\left[kx^{2}+\kappa\theta^{2}\right] \tag{2.15}$$

The Lagrangian of this system is

$$\mathscr{L}=\mathscr{T}-\mathscr{V}=\frac{1}{2}\left[\left(M+m\right)\dot{x}^{2}+mL^{2}\dot{\theta}^{2}+2m\dot{x}\dot{\theta}L\sin\theta-kx^{2}-\kappa\theta^{2}\right] \tag{2.16}$$

The governing equations of motion for this coupled two degree-of-freedom system can be obtained through a Lagrangian approach as

$$\left(M+m\right)\ddot{x}+\left(mL\cos\theta\right)\ddot{\theta}-\left(mL\sin\theta\right)\dot{\theta}^{2}+kx=F(t) \tag{2.17}$$

$$mL^{2}\ddot{\theta}+\left(mL\cos\theta\right)\ddot{x}+\kappa\theta=\tau(t) \tag{2.18}$$

This system may be subdivided into two sub-systems, representative of a modular approach.

System 1 ($x(t)$) Equations:

$$M\ddot{x} + kx = F(t) + F_{payload} \tag{2.19}$$

$$F_{payload} = -\left(mL\cos\theta\right)\ddot{\theta} + \left(mL\sin\theta\right)\dot{\theta}^2 - m\ddot{x} \tag{2.20}$$

System 2 ($\theta(t)$) Equations:

$$mL^2\ddot{\theta} + \kappa\theta = \tau(t) + \tau_{gantry} \tag{2.21}$$

$$\tau_{gantry} = -mL\cos\theta\ddot{x} \tag{2.22}$$

Here, $F_{payload}$ and τ_{gantry} represent the interaction terms between the two sub-systems.

The explicitly coupled and modular systems were used to demonstrate the loose and Gauss-Seidel coupling approaches. For this study, the following system values were used: $M = 3$, $m = 1$, $L = 1.5$, $k = 1$, $\kappa = 10$. Initial conditions of $x(0) = 1$, $\theta(0) = 0$, $\dot{x}(0) = 0$, and $\dot{\theta}(0) = 0$ were employed. External forces are specified to zero ($F(t) = 0$ and $\tau(t) = 0$). The solution for the monolithic approach is obtained using an explicit Runge-Kutta integration method with adaptive time-stepping (MATLAB® ode45). This is considered as the reference solution to which solutions obtained via alternative coupling approaches will be compared to.

The various coupling approaches were initially considered with an "update rate" of every 0.01 seconds. That is, each system/module performed time integration internally (using the MATLAB ODE45 solver), but exchanged interaction terms every 0.01 seconds. Figures II.6 and II.7 show the solution for the gantry translation and payload rotation vs. time respectively for the various coupling schemes. Again,

the monolithic solution is viewed as the reference to which loose and Gauss-Seidel coupling schemes are compared to. For this study, two iterations of the Gauss-Seidel approach were employed.

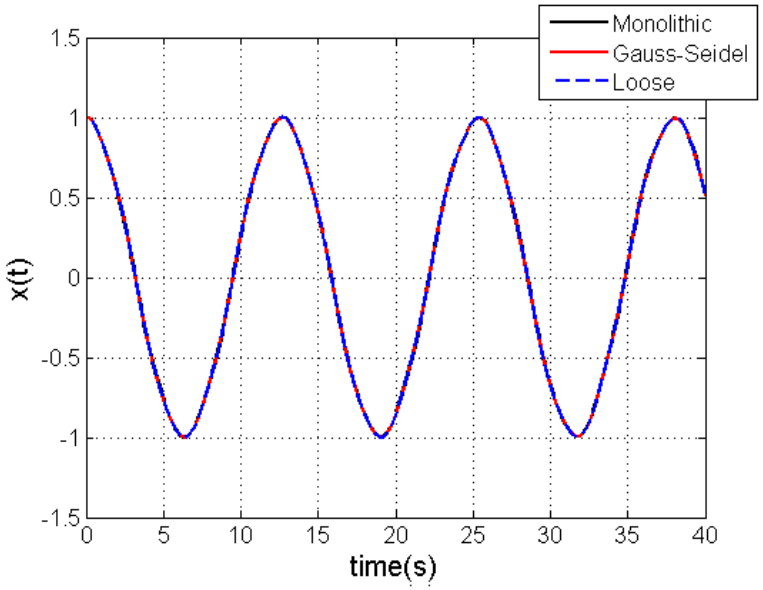

Figure II.6. Gantry translation $x(t)$ for various coupling approaches, $\Delta t = 0.01s$

Both loose and Gauss-Seidel approaches agree quite well with the monolithic solution for the low frequency motion in $x(t)$. Similar trends are seen for the higher frequency motion in $\theta(t)$, although some visible discrepancies between the monolithic and loose approach exist. This is a consequence of using only previously available information in the loose approach and making no use of available estimates of solutions at the current time step. Furthermore, this level of agreement comes at the cost of a relatively fine time step of 0.01 seconds.

Next, a larger update rate of 0.2 seconds is considered. Figures II.8 and II.9 show

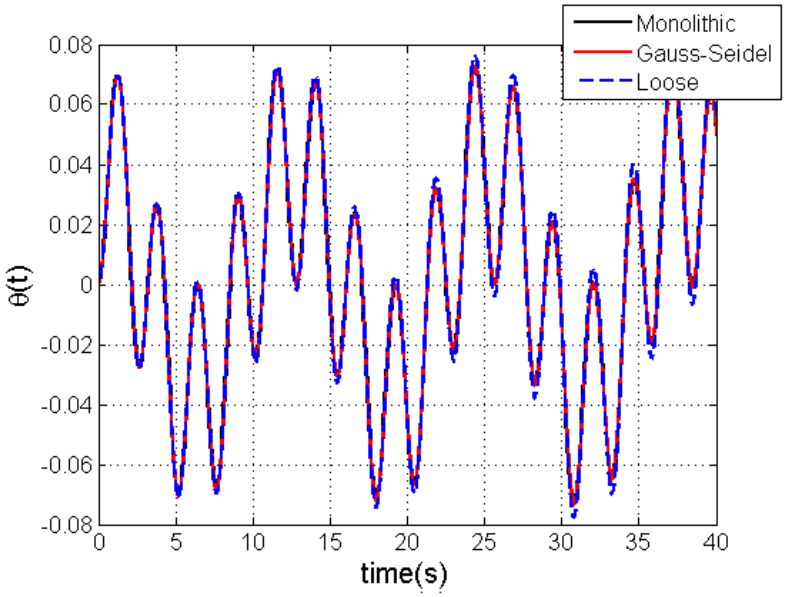

Figure II.7. Payload rotation $\theta(t)$ for various coupling approaches, $\Delta t = 0.01s$

the solution for the gantry translation and payload rotation vs. time respectively for the various coupling schemes. A clear instability is present in Figure II.9 for the loose coupling scheme, indicating a smaller time step is required for a stable solution procedure. This instability is also seen at later times in Figure II.8. It is also notable that the Gauss-Seidel approach with two iterations maintains reasonable agreement with the monolithic solution. Thus, a clear advantage of the Gauss-Seidel approach is evident in the ability to maintain stable solutions at coarser time steps than the loose coupling approach. This concludes the preliminary demonstration of coupling schemes on a representative sample problem. Coupling of the actual modules within the OWENS framework will be performed using the same coupling methodologies.

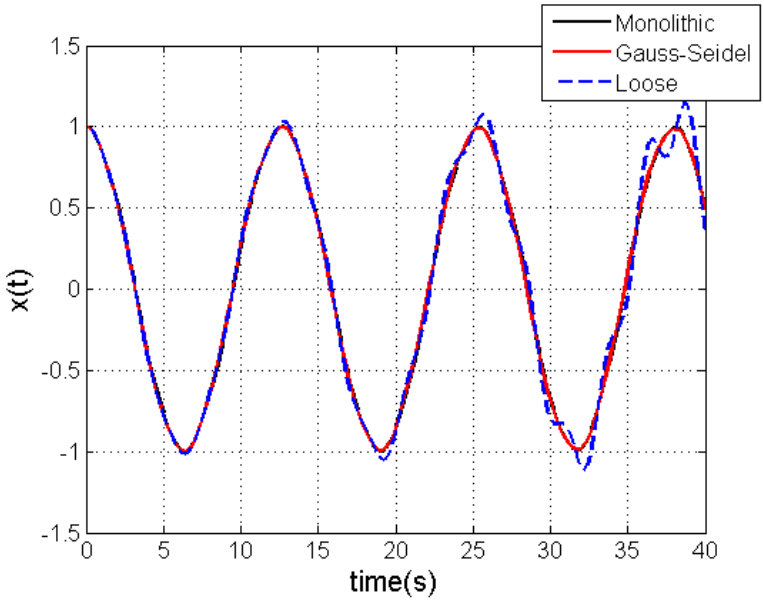

Figure II.8. Gantry translation $x(t)$ for various coupling approaches, $\Delta t = 0.2s$

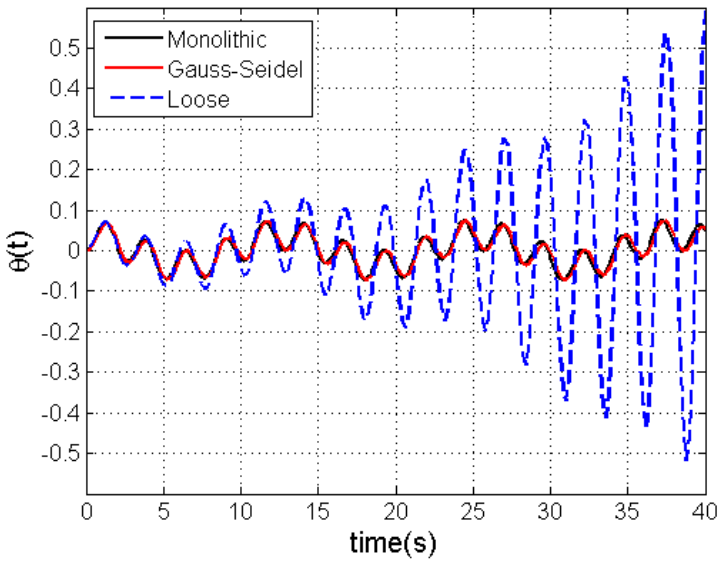

Figure II.9. Payload rotation $\theta(t)$ for various coupling approaches, $\Delta t = 0.2s$

II.D.2. Data flow between external modules and analysis framework

The previous subsection discussed the coupling schemes that may be employed between various external modules and the analysis framework developed in this chapter. It was shown that various coupling schemes can result in varying degrees of stability and accuracy in coupled analysis results. A practical issue still remains in identifying a means to actually implement an interface between the core analysis framework and an external module, facilitating data flow between the two pieces of software.

One approach for interfacing the two pieces of software would considers linking external software as a dynamic library [76] into the core analysis framework software. Such an approach would simply call the external module as a function call from the core analysis software. Although, this approach can result in a modular framework it may cause some redevelopment of external modules to integrate with the core analysis software as linkable libraries. The ability to use existing analysis capabilities as external modules without significant modification is a primary motivation for a modular framework which may be diminished by this interface approach. Furthermore, this approach requires a certain level of familiarity with the implementation of external modules, the core analysis framework, and the software languages they are written in which may serve as another obstacle for facilitating the coupling of external modules.

An obvious and rudimentary approach would be to use file input and output to write and read commands to facilitate data flow between external modules and the core analysis framework. Although this approach is easily understood and can

be easily implemented into the relevant pieces of software, efficiency is a significant concern since any write/read to/from disk requires more time than accessing data from internal memory. A similar but alternative approach is the use of memory-mapped files [77] to facilitate data flow. This approach associates segments of internal memory with a file identifier that may be accessed for read and write as any other file but without the associated efficiency concerns, This method, however, does require a certain degree of familiarity with memory addressing. The use of such an approach could potentially cause some complication in the development of modular frameworks and the associated interface depending on a developer's programming experience and abilities.

Yet another option would be to consider the use of network sockets [78]. This approach allows data packets to be sent across a network connection between a server and client. These data packets are constructed by a server, sent via a socket connection, and received by a client for processing. Although originally intended to provide a means of data flow between two computers on a network, this approach can also be used internally on a single computer. The ports on a computer's network card allow clients and servers to be initialized between various applications. This allows for convenient and efficient data flow between various applications such as the core analysis capability and external modules. Indeed, the analysis framework is treated as a network with the core analysis application and external modules being equivalent to servers and clients on a network.

An external module is truly treated as a "black box" in this approach just as the details of a computer on a network need not be known to send and receive infor-

mation. The defined input and output between these modules is accounted for in the format of the data packets being sent across the network. Thus, only the data packet format needs to be defined as well as a general framework for the interaction of an external module with the core analysis capability. With these defined, development of the core analysis framework and external modules may be made at the discretion of the independent developers. Figure II.10 shows this proposed framework for providing a general socket interface between a core analysis software and an external module.

The core analysis framework begins by defining ports for the client and server on the core analysis side. These port numbers will correspond to the server and client on the external module software and may be specified by an input file for each software application. The core analysis software can then launch the external module software application using a system call. After which, server and client initialization occurs within the core analysis software as well as within the external module software. At this point, a connection is created between the two applications, allowing two-way flow of data as required by the modular analysis framework. After connections are made, each software application can perform any required initialization, pre-processing, or start-up procedures. Next, the time step loop begins in the core analysis software. Required input is sent to the module, the module receives this data, and performs calculations before sending the required output back to the core analysis framework. The core analysis framework can then perform calculations or send/receive data to/from other modules as necessary. As discussed in the previous section, at each time step an iteration to converge the coupling between the two

modules may occur. The segments of the framework shown in Figure II.10 contained in the red dashed box may be repeated until convergence is reached. After this, the next time step may be considered performing the steps contained in the blue dashed box. At the end of the time step loop the coupled analysis is completed, and the core analysis module sends a termination message to the external module that prompts the end of analysis and termination of the external module client and server. The core analysis software client and server is also terminated.

This approach requires an external module to have the ability to start and stop analysis over a finite amount of simulation time before receiving and sending data to the core analysis software. This also requires the ability to consider whether calculations are occurring for a new time step or iterations are occurring for a single iteration. External modules may employ an algorithm that can account for this possibility, or the external module may simply be written to accept inputs and initial conditions before calculating a prediction at some later simulation time. In this approach, the core analysis software stores the states or degrees of freedom (DOFs) of the system, and provide them as initial conditions to the external module along with other input that is used to calculated an external module prediction at a later time step. In this approach, the external module is simply performing calculations over a prescribed time interval. The core analysis framework tracks the states of this simulation and determines whether iterations are necessary or the simulation may proceed to the next time step.

Admittedly, there is some programming overhead associated with sockets. Nevertheless, very general functions can be written in a variety of programming lan-

guages to initialize and terminate server-client connections, send data packets, and receive data packets. Such functions can be implemented and distributed with the OWENS toolkit for use by developers of external modules. Thus, developers of varying programming experience can create external modules with socket interfaces to the OWENS analysis framework without the need understand the details of socket programming. For these reasons, the initial development of the OWENS toolkit considers socket interfaces to provide data flow within the analysis framework.

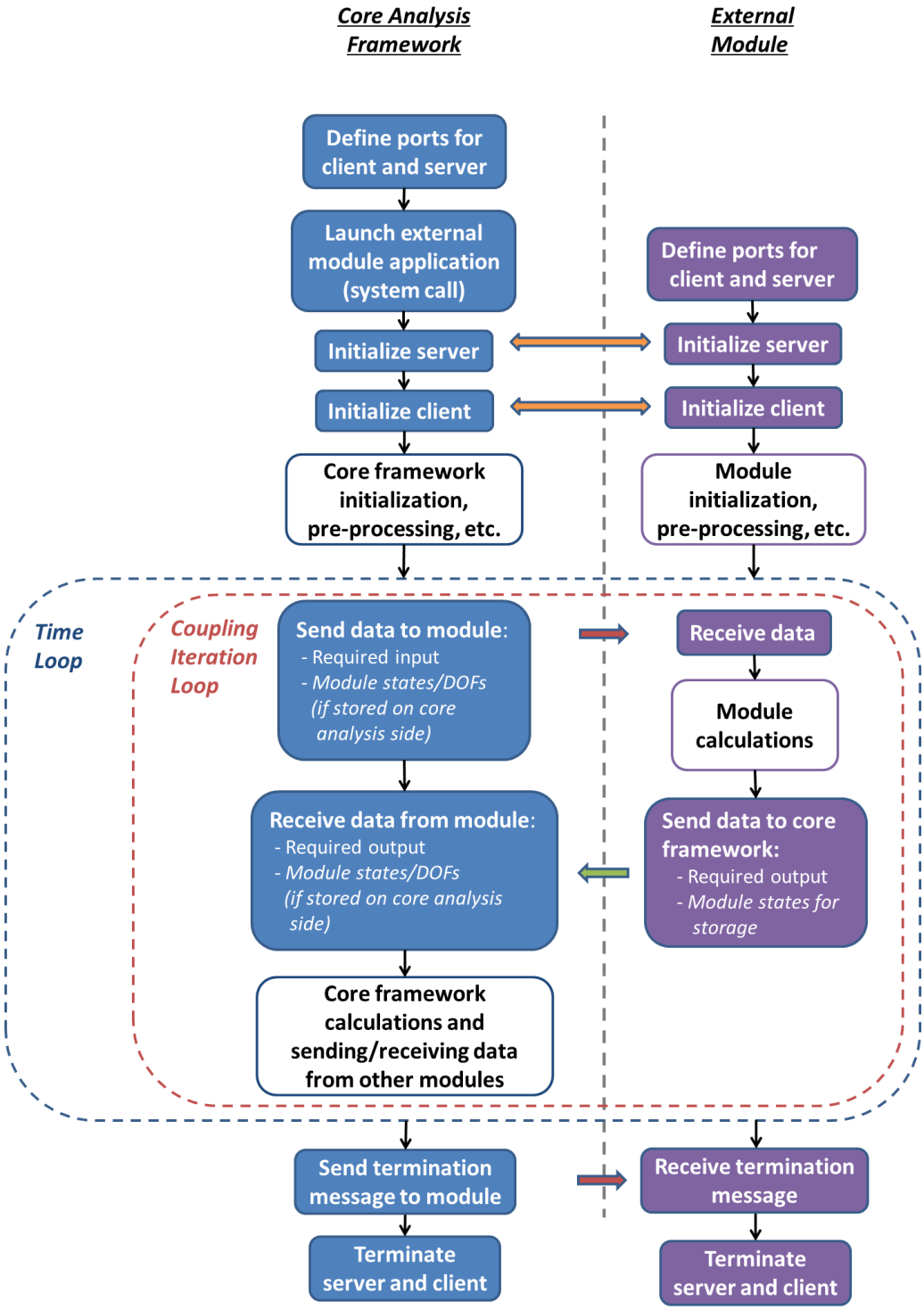

Figure II.10. General framework for network socket interface of core analysis code to external module

II.E. Mesh generation

A VAWT rotor primarily consists of a tower and blade components. The blades may be affixed to the tower at their ends as in the Darrieus and V-VAWT configurations or via struts (H-VAWT). Struts may also provide a connection between the tower and blades at any position along the tower and blade spans. Accordingly, a mesh generator (VAWTGen) has been created that is capable of generating VAWTs of arbitrary geometry, including H-type, V-type, and Darrieus configurations shown in Figure II.11. The VAWT configuration will be discretized from continuous structural components into a finite number of beam elements. Elements span between discrete points in the mesh, known as nodes. Finite element analysis will examine the motion of nodes as dictated by the deformation of the beam elements under prescribed boundary conditions. This collection of nodes and elements forms the mesh of the VAWT configuration.

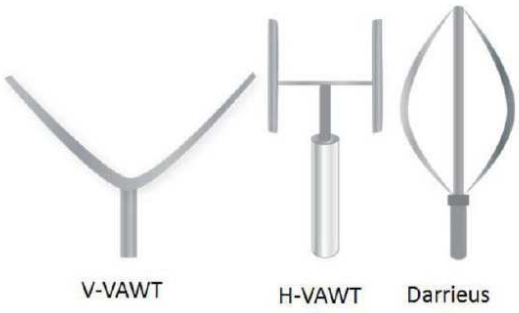

Figure II.11. Basic types of VAWT configurations

VAWTGen accepts data files containing the basic geometry of tower, blade,

and strut components. Other crucial configuration information is specified such as the elevation of the blade root from the tower root, as well as the radial distance the blade root is positioned from the tower. An arbitrary number of blades may be specified for the configuration. VAWTGen positions the blade roots in equal angular increments about the tower axis. The blades may be rotated into an arbitrary orientation per a sequence of Euler angles input by the user. If required, struts may be inserted between the tower and a blade by specifying a fraction of the tower span and the blade span the strut will span. VAWTGen will insert a straight strut of the appropriate length between the tower and blade components. The geometry of the strut component is specified by a file containing geometric data. The strut may be oriented at a certain pitch angle as described by user input.

With these relatively minimal set of inputs (as illustrated in Figure II.14) a VAWT of arbitrary configuration may be created. Therefore, a separate tool is not required for the various types of configurations. VAWTGen provides a convenient means to visualize the VAWT turbine as a wireframe (Figure II.12). This serves as a quick check for the user to ensure the VAWT has been constructed as intended, and shows the actual turbine configuration that the mesh of beam elements represents. VAWTGen also visualizes the finite element mesh (FigureII.13) to allow the user to visually inspect the refinement of the mesh. VAWTGen identifies points of intersection between the various components and inserts nodes accordingly. These node pairs at points of intersection (i.e. strut to tower, blade to strut, blade to tower) are recorded so appropriate constraint conditions at these joints may be imposed. Details of imposing constraints will be discussed later in this chapter. A mesh file is

generated that will be used by the analysis software. An elemental data file is also created, containing the structural and aerodynamic properties of the element, as well as the Euler angles representing the orientation of the element. By default, the mesh is discretized in the same manner as the geometric description of components. The user may further subdivide the mesh by specifying an integer factor to further discretize the geometric data into elements.

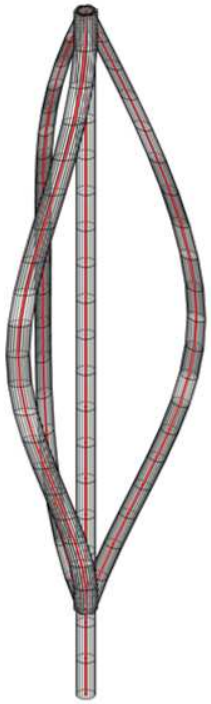

Figure II.12. Wireframe of swept Darrieus configuration generated with VAWTGen

VAWTGen requires data files be supplied to describe the geometry of the primary turbine components (blades, towers, and struts). The format of these data

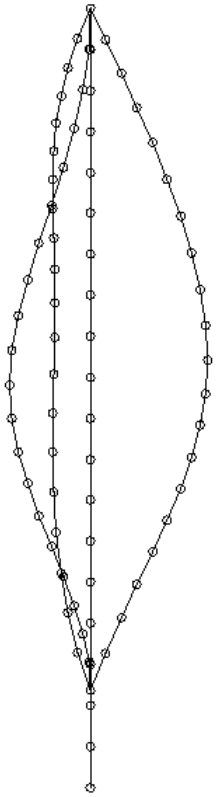

Figure II.13. Finite element mesh of swept Darrieus configuration generated with VAWTGen

files is the same as the component files for NREL's FAST code [70]. These files describe the geometry and aerodynamic properties of general turbine components, and there is nothing that restricts their use to HAWTs specifically. For example, even though a Darrieus blade is not likely be installed on a HAWT, it is easily described by the NREL blade geometry file format. This allows existing design tools such as the Sandia National Laboratories Numerical Manufacturing and Design Tool (NuMAD) for wind turbine blades [79], to be interfaced with the VAWT analysis tool without the need to consider new file formats. The NREL file format separates geometrical/structural properties of a blade and aerodynamic properties of a blade

into two files. This potentially allows one to segment structural dynamics analysis from aeroelastic analysis, depending on the design of the mesh generation and analysis tools. Also, a separation of information more readily facilitates parametric studies. If a user would like to change aerodynamic properties of a blade under the assumption that structural properties do not change significantly, there is no need to create two files with duplicate information (which is inherently prone to introducing errors in analysis files).

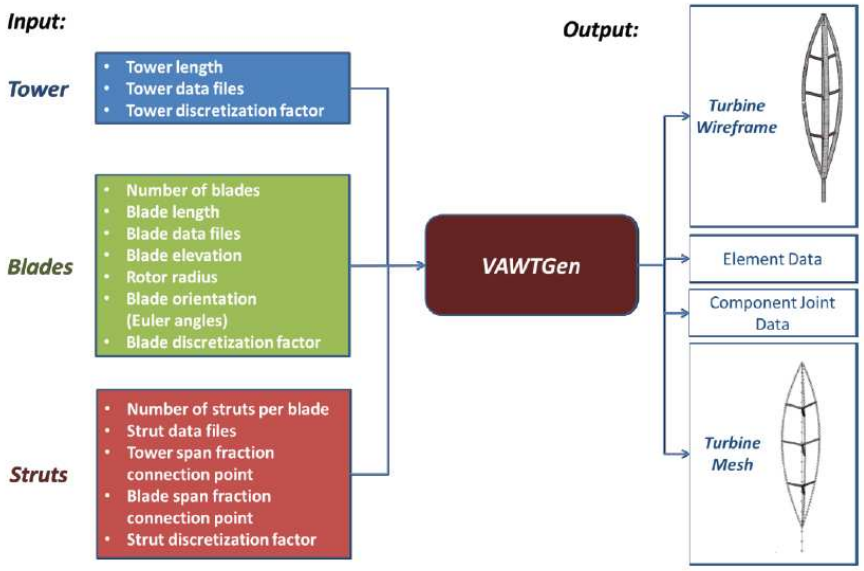

Figure II.14. Flowchart of VAWTGen input and output

Next, the mesh generation capabilities of the VAWTGen software are demonstrated. First a two bladed V-VAWT configuration is considered. Figure II.15 shows the wireframe visualization for this configuration. Note that the blades may be po-

sitioned at any orientation. The blades and top of the tower share a common point and can be joined together via whatever constraint appropriately models the joint. Next, a three bladed H-VAWT with multiple strut connections is considered. Figure II.16 shows the wireframe visualization for the H-VAWT configuration. The blades are oriented at an arbitrary orientation, and two strut connections per blade are specified. A Darrieus type configuration with swept blades is considered as shown in Figure II.12 can also be considered, as well as a strutted Darrieus configuration as shown in Figure II.17.

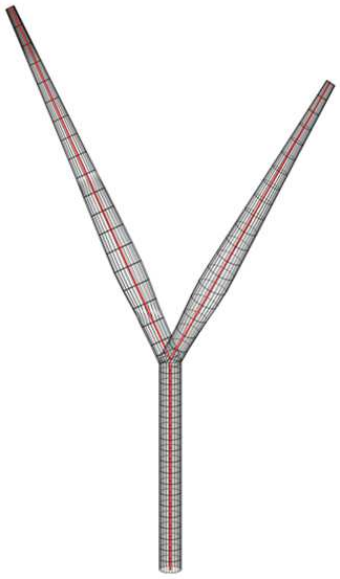

Figure II.15. Wireframe of V-VAWT configuration generated with VAWTGen

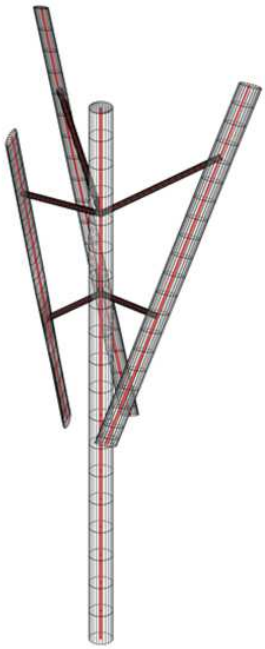

Figure II.16. Wireframe of H-VAWT configuration generated with VAWTGen

Figure II.17. Wireframe of strutted Darrieus configuration generated with VAWTGen

II.F. Beam element

To facilitate the aeroelastic analysis of a vertical axis wind turbine via a finite element approach, a three-dimensional Timoshenko beam element has been formulated. The beam is "three-dimensional" in the sense that it allows for deformations of the beam in all physical dimensions. Each node of the beam has three translational degrees of freedom and three rotational degrees of freedom. By retaining a torsional degree of freedom in the element passive aeroelastic tailoring concepts can be explored. An overview of the beam element will be given here, and details of the formulation are elaborated on in a later chapter.

The element has been formulated so that it may possess at an arbitrary orientation in the hub frame of the turbine. Furthermore, the constitutive relations of the beam element have been developed in a manner that allows for coupling terms to be introduced for bend-twist and extension-twist couplings that may arise due to cross-sectional shape or composite material usage. This allows more complex VAWT configurations to be constructed, and also allows the investigation of passive aeroelastic couplings through swept configurations. Inherent in the formulation of this Timoshenko beam is that deformations of the elastic axis are being modeled. For proper dynamics modeling, it was necessary to introduce mass center offsets from the elastic axis at each cross-section. Again, details of the element formulation including expression for element matrices are shown in a later chapter.

The existing beam formulation accounts for nonlinearities in the form of stress-stiffening effects. Such effects were known to be crucial for accurately predicting the stiffening behavior observed in modal tests of a rotating VAWT [2]. The beam for-

mulation also accounts for the ability to model concentrated masses, and stiffness at any point along the element. Imposing concentrated masses allows for one to account unsmooth mass distributions in the turbine, due to joints at tower/strut/blade connected or other installed hardware. Concentrated masses can also be used to model internal joints in a turbine blade that result in unsmooth mass distributions. Concentrated stiffness can model stiffness at component joints, or even at internal blade joints.

The beam formulation utilizes numerical integration to construct the element system matrices that will be assembled into the global system of equations. This allows flexibility in the shape functions that are used to describe the variation of a displacement along the length of an element. One would typically use higher order shape function to use less elements in the discretization of a component. This also facilitates the use of an assumed modes method. Such a method is utilized by NREL's FAST dynamics code for HAWTs [70]. Alternatively, a reduced order model may be constructed by selecting the dominant modes of a turbine and including these modes in a lower order analysis. Custom reduced order models may be developed for specific VAWT configurations that take into account geometry, mass and stiffness distributions, and joint constraints. Such a procedure may be automated and included as an efficient option for preliminary design studies. Reduced order modeling has been implemented into OWENS, and details of this analysis method are discussed in a later chapter.

II.G. Constraints

The turbine configuration will have various structural components connected together using joints, bearings, and other hardware. This hardware will impose constraints on the relative motion of the two components. Therefore, a flexible framework is needed to handle a variety of constraint conditions between structural components. In the case where structural components are fully constrained to each other or "fixed" (such as a welded connection), the constraint may be imposed via a coincident node in the mesh between the two structural components. If only selected degrees of freedom between two structural components are constrained, however, the method described by Craig [80] will be employed. Degrees of freedom in the model are decomposed into active (q_A) and dependent (q_D) degrees of freedom. The dependent degrees of freedom will be reduced from the model by imposing constraints. The dependent and active degrees of freedom are related through a transformation matrix $[T]$.

$$\vec{q} = \left\{ \begin{array}{c} q_A \\ \\ q_D \end{array} \right\} = [T] \{q_A\} \tag{2.23}$$

The original system of equations may be modified to eliminate dependent degrees of freedom and retain only active degrees of freedom:

$$[T]^T[M][T]\{\ddot{q}_A\} + [T]^T[C][T]\{\dot{q}_A\} + [T]^T[K][T]\{q_A\} = [T]^T\{F\} \tag{2.24}$$

As Craig has shown, constraint equations of the following form may be introduced

$$[R_{DA}\ R_{DD}] \left\{ \begin{array}{c} q_A \\ \\ q_D \end{array} \right\} = \{0\} \tag{2.25}$$

This expression is then useful in constructing the contraint transformation matrix. For example, for a system with k active degrees of freedom, and m dependent degrees of freedom, an $(k+m) \times k$ constraint transformation matrix may be specified such that

$$T_{DA} = -R_{DD}^{-1} R_{DA} \tag{2.26}$$

$$T = \begin{bmatrix} I_{k\times k} \\ T_{DA} \end{bmatrix} \tag{2.27}$$

II.G.1. Constraints between nodes of two beam elements

Consider a general constraint between two elements: element B and element C. For a beam element, a node has six degrees of freedom associated with it. Let these degrees of freedom be labeled $q_i^B, i = 1, 2, .., 6$ for element B, with a similar notation for element C. An arbitrary constraint can be imposed between the degrees of freedom q_i^B and q_i^C using the aforementioned transformation matrix. Herein, degrees of freedom associated with element C will be eliminated as dependent degrees of freedom while degrees of freedom associated with element B will be retained as active degrees of freedom.

II.G.1.a. Fully fixed constraint

For the case of a fully fixed constraint between two nodes, the following constraint relations exist.

$$\begin{bmatrix} -I_{3\times3} & 0_{3\times3} & I_{3\times3} & 0_{3\times3} \\ 0_{3\times3} & -I_{3\times3} & 0_{3\times3} & I_{3\times3} \end{bmatrix} \begin{Bmatrix} q_i^B \\ q_i^C \end{Bmatrix} = \{0_{6\times1}\} \tag{2.28}$$

For this constraint equation, the active and dependent degrees of freedom are

$$q_A = \left[q_1^B, q_2^B, q_3^B, q_4^B, q_5^B, q_6^B\right]^T \tag{2.29}$$

$$q_D = \left[q_1^C, q_2^C, q_3^C, q_4^C, q_5^C, q_6^C\right]^T \tag{2.30}$$

Using the following definitions of R_{DA} and R_{DD} from this constraint equation, T_{DA} is determined to be

$$R_{DA} = -I_{6\times 6} \tag{2.31}$$

$$R_{DD} = I_{6\times 6} \tag{2.32}$$

$$T_{DA} = I_{6\times 6} \tag{2.33}$$

II.G.1.b. Fully pinned constraint

For the case of a fully pinned constraint the following constraint relations exist

$$\left[\begin{array}{cccc} -I_{3\times 3} & 0_{3\times 3} & I_{3\times 3} & 0_{3\times 3} \end{array}\right] \left\{\begin{array}{c} q_i^B \\ \\ q_i^C \end{array}\right\} = \{0_{3\times 1}\} \tag{2.34}$$

For this constraint equation, the active and dependent degrees of freedom are

$$q_A = \left[q_1^B, q_2^B, q_3^B, q_4^B, q_5^B, q_6^B, q_4^C, q_5^C, q_6^C\right]^T \tag{2.35}$$

$$q_D = \left[q_1^C, q_2^C, q_3^C\right]^T \tag{2.36}$$

Using the definitions of R_{DA} and R_{DD} from this constraint equation, T_{DA} is determined to be

$$R_{DA} = -\left[I_{3\times 3}\ 0_{3\times 6}\right] \tag{2.37}$$

$$R_{DD} = I_{3\times 3} \tag{2.38}$$

$$T_{DA} = \left[I_{3\times 3}\ 0_{3\times 6}\right] \tag{2.39}$$

II.G.2. Single-axis hinge constraint

Consider a single-axis hinge with some attached local frame ($\hat{b}_i$) as shown in Figure II.18. This local frame may be positioned with respect to any orientation in some global frame ($\hat{g}_i$). This global frame represent the common frame a structural assembly is represented in (i.e. the hub-frame for a vertical-axis wind turbine finite element assembly).

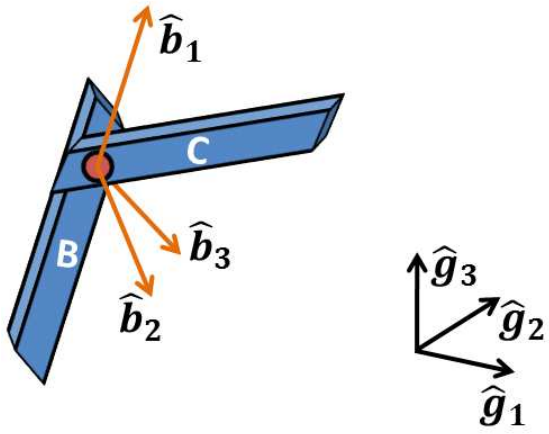

Figure II.18. Illustration of hinge-frame coordinate system between two elements

For the case of a single-axis hinge constraint about the local $\tilde{q}_5^B$ degree of freedom ($\hat{b}_2$ hinge-axis) the constraint equation is

$$\begin{bmatrix} -I_{3\times3} & 0_{3\times3} & I_{3\times3} & 0_{3\times3} \\ 0_{2\times3} & I_{2\times3} & 0_{2\times3} & I_{2\times3} \end{bmatrix} \begin{Bmatrix} \tilde{q}_i^B \\ \tilde{q}_i^C \end{Bmatrix} = \{0_{5\times1}\} \tag{2.40}$$

Here, the tilde signifies the quantity is coordinatized in the hinge fixed ($\hat{b}_i$) frame. Furthermore, let C_G^B represent the 3×3 transformation matrix from the global frame

the assembled finite element system will be coordinatized in to the local B element frame. Thus, the constraint equation may expressed in terms of degrees of freedom coordinatized in the global frame.

$$\begin{bmatrix} -I_{3\times3} & 0_{3\times3} & I_{3\times3} & 0_{3\times3} \\ 0_{2\times3} & I_{2\times3} & 0_{2\times3} & I_{2\times3} \end{bmatrix} \begin{bmatrix} C_G^B & 0_{3\times3} & 0_{3\times3} & 0_{3\times3} \\ 0_{3\times3} & C_G^B & 0_{3\times3} & 0_{3\times3} \\ 0_{3\times3} & 0_{3\times3} & C_G^B & 0_{3\times3} \\ 0_{3\times3} & 0_{3\times3} & 0_{3\times3} & C_G^B \end{bmatrix} \begin{Bmatrix} q_i^B \\ q_i^C \end{Bmatrix} = \{0_{5\times1}\} \tag{2.41}$$

For this constraint equation, the active and dependent degrees of freedom are

$$q_A = \left[q_1^B, q_2^B, q_3^B, q_4^B, q_5^B, q_6^B, q_5^C\right]^T \tag{2.42}$$

$$q_D = \left[q_1^C, q_2^C, q_3^C, q_4^C, q_6^C\right]^T \tag{2.43}$$

Using the definitions of R_{DA} and R_{DD} from this constraint equation, T_{DA} is determined to be

$$R_{DA} = \begin{bmatrix} -C_G^B & & 0_{3\times4} & & \\ & C_{G_{11}}^B & C_{G_{12}}^B & C_{G_{13}}^B & C_{G_{12}}^B \\ 0_{2\times3} & & & & \\ & C_{G_{31}}^B & C_{G_{32}}^B & C_{G_{33}}^B & C_{G_{33}}^B \end{bmatrix} \tag{2.44}$$

$$R_{DD} = \begin{bmatrix} C_G^B & & 0_{3\times2} \\ & C_{G_{11}}^B & C_{G_{13}}^B \\ 0_{2\times3} & & \\ & C_{G_{31}}^B & C_{G_{33}}^B \end{bmatrix} \tag{2.45}$$

$$T_{DA} = \begin{bmatrix} I_{3\times3} & & & 0_{3\times4} & & \\ & 1 & \frac{C_{G_{12}}^B C_{G_{33}}^B - C_{G_{13}}^B C_{G_{32}}^B}{C_{G_{11}}^B C_{G_{33}}^B - C_{G_{13}}^B C_{G_{31}}^B} & 0 & \frac{C_{G_{13}}^B C_{G_{32}}^B - C_{G_{12}}^B C_{G_{33}}^B}{C_{G_{11}}^B C_{G_{33}}^B - C_{G_{13}}^B C_{G_{31}}^B} \\ 0_{3\times3} & & & & \\ & 0 & \frac{C_{G_{11}}^B C_{G_{32}}^B - C_{G_{31}}^B C_{G_{12}}^B}{C_{G_{11}}^B C_{G_{33}}^B - C_{G_{13}}^B C_{G_{31}}^B} & 1 & \frac{C_{G_{12}}^B C_{G_{31}}^B - C_{G_{11}}^B C_{G_{32}}^B}{C_{G_{11}}^B C_{G_{33}}^B - C_{G_{13}}^B C_{G_{31}}^B} \end{bmatrix} \tag{2.46}$$

It is notable that a singularity exists in the constraint transformation matrix for

$$C^B_{G_{11}} C^B_{G_{33}} - C^B_{G_{13}} C^B_{G_{31}} = 0 \tag{2.47}$$

Nevertheless, an equivalent constraint may be imposed by choosing another b-frame axis to be the hinge axis and simply repeating the previously performed procedure to eliminate the local $\tilde{q}^C_4$ or $\tilde{q}_6 C$ constraint. Thus, this issue can be eliminated for all practical purposes. The procedure for these alternative constraints is identical to the one just carried out and will not be elaborated on.

II.H. Rotor speed update

The structural dynamics formulation has been formulated in a rotating frame that rotates about one axis with angular velocity (Ω), and angular acceleration ($\dot{\Omega}$). These quantities are not degrees of freedom in the simulation and must be updated at each time step or in an iterative manner. This treatment facilitates the interaction of the turbine with external modules. The angular motion of the rotor is dictated primarily by the aerodynamic loads acting on the turbine, and a resistance torque provided by the generator. The torque of the turbine shaft can be calculated by post-processing for the nodal reaction force at the turbine base. Information about the rotor speed and position at the current time step, as well as the generator angular velocity and position will be used to calculate the opposing resistance torque on the turbine shaft provided by the generator. The dynamic equilibrium equations for the turbine shaft motion may be expressed as:

$$\tau_{shaft} - \tau_{generator} = J_{turbine} \dot{\Omega} \tag{2.48}$$

Such that $J_{turbine}$ is the moment of inertia of the turbine about the tower axis. Calculation of the angular acceleration of the rotor allows the rotor velocity to be updated when considering the time step of the simulation. The angular position of the rotor can also be updated as required by the analysis tool and external modules.

II.I. Generator modeling

A simple induction generator module is implemented in the OWENS framework. The induction generator model is essentially the same approach considered in the FAST HAWT analysis tool [70]. More robust generator modules can be considered as required by future analysis needs. A simple generator torque vs. speed relationship (see Figure II.19) is considered. The generator modeling component of OWENS is very modular in nature and may be updated with more robust models with relatively minimal effort. The low speed shaft speed (turbine side) may be amplified by an appropriate gear ratio to account for the high speed shaft speed (generator speed). Options also exist to account for the drive-shaft/gearbox dynamics.

Key parameters in the specification of a simple induction generator model are:

- Rated torque (τ_{rated})
- Rated Slip Percentage (a_{slip})
- Zero torque generator speed ($\tilde{\Omega}_0$)
- Pull out ratio ($\bar{p}$)

The rated generator speed is calculated as follows

$$\tilde{\Omega}_R = \tilde{\Omega}_0 \frac{100 + a_{slip}}{100} \tag{2.49}$$

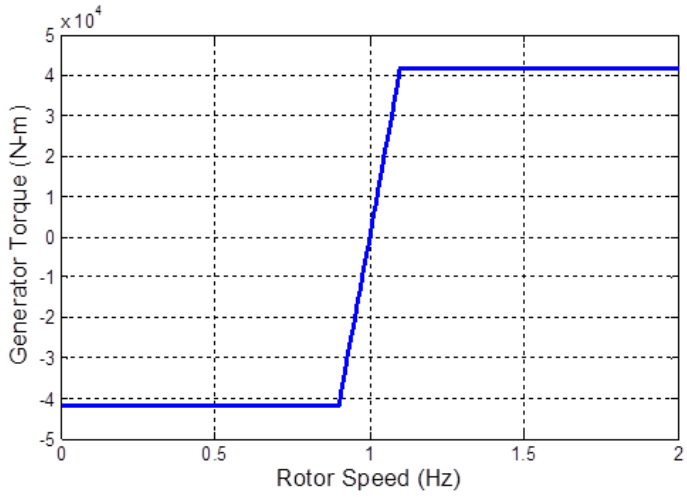

Figure II.19. Torque vs. speed curve for simple induction generator

The torque(τ) vs. speed($\tilde{\Omega}$) relations shown in Figure II.19 are generated using a piecewise defined function

$$\tau(\tilde{\Omega}) = \begin{cases} -\bar{p}\tau_{rated} & \tilde{\Omega} \leq \left[\tilde{\Omega}_0 - \bar{p}\left(\Omega_R - \tilde{\Omega}_0\right)\right] \\ \tau_{rated}\frac{\tilde{\Omega}-\tilde{\Omega}_0}{\tilde{\Omega}-\tilde{\Omega}_R} & \left[\tilde{\Omega}_0 - \bar{p}\left(\Omega_R - \tilde{\Omega}_0\right)\right] < \tilde{\Omega} < \left[\tilde{\Omega}_0 + \bar{p}\left(\Omega_R - \tilde{\Omega}_0\right)\right] \\ \bar{p}\tau_{rated} & \tilde{\Omega} \geq \left[\tilde{\Omega}_0 + \bar{p}\left(\Omega_R - \tilde{\Omega}_0\right)\right] \end{cases} \quad (2.50)$$

II.J. Drive-shaft modeling

Drive-shaft effects may be modeled by considering the torsional flexibility of a drive-shaft mechanism. Alternatively, a rigid shaft connection between turbine and generator may be assumed. As mentioned before, some gear ratio may be considered to amplify the low speed shaft speed and calculated a resulting high speed shaft speed/torque applied to the generator. If generator effects are to be included in the analysis, a simplified model that calculate drive-shaft reaction torque is implemented in OWENS. This torque accounts for stiffness and damping in the drive-shaft by

considering the difference in low speed shaft and gearbox azimuth angle and angular velocity.

$$\tau_{ds} = k_{ds}\left(\theta_{LSS} - \theta_{gb}\right) + c_{ds}\left(\Omega_{LSS} - \Omega_{gb}\right) \tag{2.51}$$

Such that k_{ds} and c_{ds} are the effective stiffness and damping of the drive shaft respectively, θ_{LSS} and θ_{gb} are the low speed shaft and gearbox azimuth respectively, and Ω_{LSS} and Ω_{gb} are the angular velocity of the low speed shaft and gearbox respectively. This is essentially the drive-train modeling approach employed by the FAST HAWT analysis tool [70].

The model for drive-shaft effects is implemented in a very modular fashion and can be replaced with higher fidelity drive shaft models as required with relatively minimal effort.

II.K. Conclusion

This chapter has presented the analysis framework for the Offshore Wind Energy Simulation toolkit for vertical-axis wind turbines. This framework was designed with the necessary features for a robust and extensible design tool for offshore vertical-axis wind turbines in mind. The fundamental model formulation was discussed and modular framework for interfacing a core structural dynamics solver with various external modules was developed. An iterative coupling strategy to allow for a "loose" coupling of external modules to the core analysis was presented, and the practical implementation of network sockets to facilitate data flow within the framework was discussed.

As part of this effort, a robust mesh generator was designed that is capable of

constructing VAWT configurations of arbitrary geometry. The necessary features of a beam element capable of modeling a general rotating, flexible structure were identified and the associated formulation is presented in a later chapter. Details of various modules such as rotor speed update, generator, and drive-shaft modules were also discussed.

CHAPTER III

AN ENERGY PRESERVING TIME INTEGRATION METHOD FOR GYRIC SYSTEMS

An energy preserving time integration method for Gyric systems is presented herein. A previously developed integration method for flexible systems was extended to consider Gyric systems which include rotational effects. A discussion of Gyric systems is presented and these systems are contrasted to flexible/deformable systems without rotational effects. Energy in Gyric systems is also discussed. While the energy of a Gyric system is not constant, the Jacobi integral is utilized to obtain an energy function (the Hamiltonian) which is conserved for conservative Gyric systems. This energy function is utilized to obtain a bound from which an unconditionally stable numerical time integration scheme is developed. The formulation of the time integration method is discussed in detail, as well as the practical implementation of the method into a numerical framework. It is shown that for conservative Gyric systems, energy is preserved regardless of time step size. This means that large time steps may be utilized to give a good approximation of motion.

The energy preserving integration method is demonstrated on a simplified two degree of freedom system and considerations are made for nonconservative systems. The energy preserving time integration method is compared to a reference solution obtained through analysis with very small time step sizes. The method is also compared to a Newmark-β integration method, a popular time integration scheme for structural dynamics analysis. This exercise also served as a reminder that certain

schemes of the Newmark-β time integration method are energy conserving. This work has extended the concept of an energy conserving Newmark-β integration scheme for flexible bodies to prove that the scheme conserves the Hamiltonian for a conservative Gyric system. Furthermore, the concept of a Hamiltonian conserving integration scheme is more general than an energy conserving one in that this energy function can encompass a broader set of systems, namely conservative Gyric systems.

III.A. Gyric systems

In general, the equations of motion for a flexible/deformable body may be represented in the following form

$$M\ddot{q} + C\dot{q} + Kq = Q \tag{3.1}$$

Such that M is a symmetric positive definite mass matrix, C is a positive semi-definite damping matrix, and K is a symmetric positive definite stiffness matrix. Q and q are generalized force and displacement vectors respectively. An over dot represents a time derivative of a quantity (i.e. $\dot{q} = \frac{\partial q}{\partial t}$).

Considerations for rotating systems are slightly different in that these systems consider linear representations that are subject to prescribed angular velocities $\vec{\omega}(t)$ about fixed axes. Such systems are commonly called *Gyric Systems* [63]. The resulting governing differential equations of motion are

$$M\ddot{q} + (C + G)\dot{q} + (K - S + H)q = Q_c + Q_{nc} \tag{3.2}$$

Here, M and K are defined as before. G is the *Gyric* or *Coriolis* matrix and is skew symmetric in nature. S is the *Spin Softening* matrix and is symmetric

positive definite in nature. H is the *Circulatory* matrix and is skew symmetric in nature. Q_c is a conservative force vector and Q_{nc} is the non-conservative vector resulting from external forces on the system. For Gyric systems, the conservative force vector consists of centrifugal forces resulting from rotational effects on reference position coordinates. Non-conservative forces are not derivable from potential or kinetic energy of the system, such as any externally applied forces.

For the interested reader, the following subsections present a rigorous development of the equations of motions. First, a conservative Gyric system (with non-conservative forcing) is considered followed by a non-conservative Gyric system.

III.A.1. Lagrangian development of equations of motion for a conservative Gyric system

An earlier section presented the equations of motion for a Gyric system, and contrasted the properties of a Gyric system with that of a non-rotating system. This section presents a rigorous derivation of equations of motion for a conservative Gyric system acted upon by non-conservative forces.

Consider a system with kinetic energy (T) separated into three parts as follows

$$T(q, \dot{q}) = T_2(\dot{q}) + T_1(q, \dot{q}) + T_0(q) \tag{3.3}$$

Such that T_2 is quadratic in generalized velocities ($\dot{q}$), T_1 is linear in generalized velocities, and T_0 is not velocity dependent. These contributions to total kinetic energy can be expressed as

$$T_2(\dot{q}) = \frac{1}{2}\dot{q}^T M \dot{q} \tag{3.4}$$

$$T_1(q, \dot{q}) = N^T(q)\dot{q} \tag{3.5}$$

$$T_0(q) = \frac{1}{2} q^T S q + Q_c^T q \tag{3.6}$$

The potential energy of the system may be defined as

$$V(q) = \frac{1}{2} q^T K q \tag{3.7}$$

As mentioned in a previous section, M, K, and S are the mass, stiffness, and spin softening matrices, and are assumed to be symmetric positive definite. For a conservative Gyric system, $N(q)$ is a vector proportional to a constant angular velocity of the system $\vec{\omega}$. Q_c is a conservative generalized force vector that is derived from T_0. In the preceding definitions of kinetic and potential energy it has been assumed that there is no explicit time dependence, and that no nonlinearities are present in the aforementioned matrices. The Lagrangian of the system is expressed as

$$\mathscr{L} = T - V = \frac{1}{2} \dot{q}^T M \dot{q} + \frac{1}{2} q^T S q + N^T(q) \dot{q} + Q_c^T q - \frac{1}{2} q^T K q \tag{3.8}$$

The equations of motion are readily derived from the Lagrangian

$$\frac{d}{dt} \left(\frac{\partial \mathscr{L}}{\partial \dot{q}} \right) - \frac{\partial \mathscr{L}}{\partial q} = Q_{nc} \tag{3.9}$$

Here, Q_{nc} represents nonconservative generalized forces acting on the system. Proceeding with development of the equations of motions from the above expression for the Lagrangian

$$\frac{\partial \mathscr{L}}{\partial \dot{q}} = M \dot{q} + N(q) \tag{3.10}$$

$$\frac{d}{dt} \left(\frac{\partial \mathscr{L}}{\partial \dot{q}} \right) = M \ddot{q} + \frac{\partial N(q)}{\partial q} \dot{q} \tag{3.11}$$

$$\frac{\partial \mathscr{L}}{\partial q} = \frac{\partial}{\partial q} \left(N^T \right) \dot{q} + S q + Q_c - K q \tag{3.12}$$

Let the following definition be introduced by assuming $N(q)$ is linear in generalized displacements q.

$$\frac{\partial N}{\partial q} = L \tag{3.13}$$

Thus, the resulting equations of motion are

$$M\ddot{q} + L\dot{q} - L^T\dot{q} - Sq + Kq - Q_c = Q_{nc} \tag{3.14}$$

Next, coefficient matrices may be grouped

$$M\ddot{q} + \left(L - L^T\right)\dot{q} + (K - S)\,q = Q_c + Q_{nc} \tag{3.15}$$

Introducing the definition of the "Gyric" matrix

$$G = L - L^T \tag{3.16}$$

The skew-symmetric nature of the Gyric matrix is clearly demonstrated

$$G^T = L^T - L = -\left(L - L^T\right) = -G \tag{3.17}$$

Thus, the resulting equations of motion for a Gyric system under non-conservative forces are

$$M\ddot{q} + G\dot{q} + (K - S)\,q = Q_c + Q_{nc} \tag{3.18}$$

III.A.2. Lagrangian development of equations of motion for a non-conservative Gyric system

Consider the previous Lagrangian development, but with the inclusion of dissipative forces by introducing the Rayleigh dissipation function $\mathscr{F}$ [63]. This function allows dissipative forces to be accounted for that are not derivable from the kinetic

and potential energy functions of the system. Examples of dissipative forces include damping and so called "Circulatory" effects. Circulatory effects are common in rotational systems, and can arise due to prescribed angular accelerations in Gyric systems.

For the non-conservative Gyric system under consideration the dissipation function may be expressed as

$$\mathscr{F} = \frac{1}{2}\dot{q}^T C\dot{q} + \dot{q}^T H q \tag{3.19}$$

Here, C is a positive definite damping matrix, and H is a skew symmetric Circulatory matrix. A modified form of Lagrange's equations with considerations for the dissipative function is shown below.

$$\frac{d}{dt}\left(\frac{\partial \mathscr{L}}{\partial \dot{q}}\right) - \frac{\partial \mathscr{L}}{\partial q} + \frac{\partial \mathscr{F}}{\partial \dot{q}} = Q_{nc} \tag{3.20}$$

Derivation of the equations of motion including the dissipative functions produces the form of equations of motion for a non-conservative Gyric system from the previous section.

$$M\ddot{q} + (C+G)\dot{q} + (K - S + H)\, q = Q_c + Q_{nc} \tag{3.21}$$

III.B. Energy considerations for Gyric systems

This section will discuss energy in Gyric systems. First, the total energy of a Gyric system will be discussed. It will be shown that the total energy of a conservative Gyric system is not constant. While the Lagrangian function $\mathscr{L}(q, \dot{q}, t) = T - V$ is important in developing the governing equations of motion, another energy function commonly used to characterize energy in rotational system will also be introduced.

It will be shown that for a conservative Gyric system this energy function is indeed constant.

III.B.1. Energy of a Gyric system

The energy of a system is defined as the sum of kinetic and potential energy, $\mathscr{E} = T + V$. Using the kinetic and potential energy of a Gyric system defined in the previous section, the energy of a Gyric system may be written as

$$\mathscr{E} = \frac{1}{2}\dot{q}^T M\dot{q} + \frac{1}{2}q^T Kq + \frac{1}{2}q^T Sq + Q_c^T q + N^T(q)\dot{q} \tag{3.22}$$

The energy rate equation is derived assuming the system matrices not time dependent and nonlinearities are absent. Also, the previous assumption that N(q) is linear in q ($N(q) = Lq$) is introduced.

$$\dot{\mathscr{E}} = \dot{q}^T \left(M\ddot{q} + Kq + Sq + Q_c + Q_{nc} + L^T\dot{q}\right) + q^T L^T\ddot{q} \tag{3.23}$$

Next, the equations of motion for a non-conservative Gyric system are inserted into the energy rate equation. The skew symmetric nature of G is used to eliminate this term from the energy rate equation.

$$\dot{\mathscr{E}} = \dot{q}^T \left(2(Sq + Q_c) - Hq - C\dot{q} + L^T\dot{q} + Q_{nc}\right) + q^T L^T\ddot{q} \tag{3.24}$$

Now consider the specific case of a conservative Gyric system with no dissipative forces ($C = 0$ and $H = 0$) acted upon by only conservative forces ($Q_{nc} = 0$).

$$\dot{\mathscr{E}} = \dot{q}^T \left(2(Sq + Q_c) + L^T\dot{q}\right) + q^T L^T\ddot{q} \tag{3.25}$$

Therefore, it is clearly demonstrated that even for a conservative Gyric system, energy is not constant.

III.B.2. The energy function $\mathscr{H}^*$ of a Gyric system

In addition to total energy, there is another important energy function known as the Hamiltonian, $\mathscr{H}^*$. As shown in (3.3), the kinetic energy of any finite dimensional system can be separated into three parts (T_0, T_1, T_2), and this function is defined as $\mathscr{H}^*(q, \dot{q}, t) = T_2 - T_0 + V$. One can readily note that if T_1 and T_0 are not present (i.e. kinetic energy consists of T_2 only) then $\mathscr{H}^*$ is identical to the energy of the system, $\mathscr{E} = T + V$.

Consider the energy function $\mathscr{H}^*$ generated from T_2, T_0, and V for a Gyric system.

$$\mathscr{H}^* = \frac{1}{2}\dot{q}^T M \dot{q} + \frac{1}{2} q^T K q - \frac{1}{2} q^T S q - Q_c^T q \tag{3.26}$$

The rate of change of $\mathscr{H}^*$ may be expressed as

$$\dot{\mathscr{H}}^* = \dot{q}^T M \ddot{q} + \dot{q}^T K q - \dot{q}^T S q - \dot{q}^T Q_c = \dot{q}^T \left(M \ddot{q} + (K - S)\, q - Q_c \right) \tag{3.27}$$

Next, introduce the equations of motion for a non-conservative Gyric system as shown in (3.21).

$$\dot{\mathscr{H}}^* = -\dot{q}^T (C + G) \dot{q} - \dot{q}^T H q + \dot{q}^T Q_{nc} \tag{3.28}$$

The skew symmetric nature of G $(\dot{q}^T G \dot{q} = 0)$ allows this term to be eliminated from the equation for $\dot{\mathscr{H}}^*$. Furthermore, let the rate of work of non-conservative forces be introduced $\dot{W}_{nc} = \dot{q}^T Q_{nc}$. The remaining terms may be thought of as the work rate of damping and Circulatory (dissipative) forces.

$$\dot{\mathscr{H}}^* = -\dot{q}^T C \dot{q} - \dot{q}^T H q + \dot{W}_{nc} \tag{3.29}$$

Thus, $\dot{\mathscr{H}}^*$ is proportional to the work rate of non-conservative/dissipative forces on

the system. For a conservative Gyric system ($C = 0$ and $H = 0$) under no external loading ($Q_{nc} = 0$) it is notable that $\dot{\mathscr{H}}^*$=0.

It is remarkable that there are situations when the energy function $\mathscr{H}^*$ is constant but the system energy is not. The conditions for $\mathscr{H}^*$ to be constant are that the Lagrangian $\mathscr{L}$ is not an explicit function of time and that there are no externally applied or dissipative forces, (i.e. $\mathscr{L} = \mathscr{L}(q, \dot{q})$, $Q_{nc} = 0$, and $\mathscr{F} = 0$). Such a configuration with a constant energy function is a subset of a general Gyric system, and will be useful in developing stable time integration methods that conserve $\mathscr{H}^*$.

III.C. Time integration of Gyric systems

Transient structural dynamics analysis requires time integration strategies to integrate second order differential equations of motion. A number of methods exist for time integration [81, 82], and may be explicit or implicit in nature. Explicit methods are inexpensive computationally, but require smaller time steps and numerical stability is often a significant concern. Implicit methods require more expense computationally, but allow for larger time steps. Furthermore, implicit methods can allow for unconditional stability when suitable integration parameters are chosen. Although stability of an implicit integration method may be ensured by selection of appropriate integration parameter, accuracy of the solution is not guaranteed. Indeed, without careful tuning of integration parameters, spurious energy trends may be observed in the motions of a system.

The implicit integration method developed by Dean et al. is well suited for the transient analysis of flexible structures [69]. This method is unconditionally

stable if an appropriate integration parameter is chosen, and has the ability to conserve the energy of a system if non-conservative forces are absent. Such properties are extremely desirable when performing structural dynamics analysis to ensure an accurate representation of motion; integration methods that accumulate numerical error can cause numerical instability or display spurious and artificial energy trends that can cloud any analysis of complex systems.

Using the original ideas of Dean et al., the scope of the original method has been extended to show that finite difference approximations utilized to construct the integration scheme lead to a constant energy function $\mathscr{H}^*$ for conservative Gyric systems regardless of the size of the time step Δt. This means that large time steps can provide a good representation of motion.

III.C.1. An energy preserving time integration method for conservative Gyric systems

. Consider the equations of motion for a conservative Gyric system with added damping pre-multiplied with the transpose of the generalized velocity vector ($\dot{q}^T$).

$$\dot{q}^T M\ddot{q} + \dot{q}^T(C+G)\dot{q} + \dot{q}^T(K-S)q - \dot{q}^T Q_c = 0 \tag{3.30}$$

The Gyric matrix terms are removed due to their skew symmetric nature.

$$\dot{q}^T M\ddot{q} + \dot{q}^T C\dot{q} + \dot{q}^T(K-S)q - \dot{q}^T Q_c = 0 \tag{3.31}$$

Next, the equations are discretized through a finite difference approach as shown by Dean et al. [69]. Here, the integration parameter α is limited to the values

$0 \leq \alpha \leq 1/2$.

$$\begin{aligned} 0 &= \frac{(q^{n+1}-q^{n-1})}{2\Delta t}\left\{M\left(\frac{q^{n+1}+q^{n-1}-2q^n}{\Delta t^2}\right)+C\left(\frac{(q^{n+1}-q^{n-1})}{2\Delta t}\right)\right. \\ &+ \left.(K-S)\left(\alpha q^{n+1}+(1-2\alpha)q^n+\alpha q^{n-1}\right)\right\}-\frac{(q^{n+1}-q^{n-1})}{2\Delta t}Q_c \end{aligned} \tag{3.32}$$

The following relations will be useful in relating the discretization to energy quantities

$$\begin{aligned} q^{n+1}+q^{n-1}-2q^n &= (q^{n+1}-q^n)-(q^n-q^{n-1}) \\ q^{n+1}+2q^n+q^{n-1} &= (q^{n+1}+q^n)+(q^n+q^{n-1}) \\ q^{n+1}-q^{n-1} &= (q^{n+1}-q^n)+(q^n-q^{n-1}) \\ &= (q^{n+1}+q^n)-(q^n+q^{n-1}) \end{aligned} \tag{3.33}$$

The discretized form of the equations of motion may be re-written as

$$\begin{aligned} 0 &= \frac{1}{2}\left(\frac{q^{n+1}-q^n}{\Delta t}\right)^T M\left(\frac{q^{n+1}-q^n}{\Delta t}\right) \\ &- \frac{1}{2}\left(\frac{q^n-q^{n-1}}{\Delta t}\right)^T M\left(\frac{q^n-q^{n-1}}{\Delta t}\right) \\ &+ \left(\frac{q^{n+1}-q^{n-1}}{2\Delta t}\right)^T C\left(\frac{q^{n+1}-q^{n-1}}{2\Delta t}\right) \\ &+ \frac{1}{2}\left(\frac{q^{n+1}+q^n}{2}\right)^T K\left(\frac{q^{n+1}+q^n}{2}\right) \\ &- \frac{1}{2}\left(\frac{q^n+q^{n-1}}{2}\right)^T K\left(\frac{q^n+q^{n-1}}{2}\right) \\ &- \frac{1}{2}\left(\frac{q^{n+1}+q^n}{2}\right)^T S\left(\frac{q^{n+1}+q^n}{2}\right) \\ &+ \frac{1}{2}\left(\frac{q^n+q^{n-1}}{2}\right)^T S\left(\frac{q^n+q^{n-1}}{2}\right) \\ &- Q_c^T\left(\frac{q^{n+1}+q^n}{2}\right)+Q_c^T\left(\frac{q^n+q^{n-1}}{2}\right) \\ &+ \left(\alpha-\frac{1}{4}\right)\left[\left(q^{n+1}-q^n\right)^T(K-S)\left(q^{n+1}-q^n\right)\right] \\ &- \left(\alpha-\frac{1}{4}\right)\left[\left(q^n-q^{n-1}\right)^T(K-S)\left(q^n-q^{n-1}\right)\right] \end{aligned} \tag{3.34}$$

These discrete terms can be expressed as energy components at the mid steps $n+\frac{1}{2}$ and $n-\frac{1}{2}$. The assumed semi-positive definiteness of the damping matrix C also allows for a semi-positive valued constant ($\bar{C}$) to be introduced

$$\bar{C} = \left(\frac{q^{n+1} - q^{n-1}}{2\Delta t}\right)^T C \left(\frac{q^{n+1} - q^{n-1}}{2\Delta t}\right) \tag{3.35}$$

$$\begin{aligned} T_2^{n+1/2} + V^{n+1/2} - T_0^{n+1/2} + \bar{C} + \\ \left(\alpha - \frac{1}{4}\right)\left[\left(q^{n+1} - q^n\right)^T (K - S)\left(q^{n+1} - q^n\right)\right] \\ = T_2^{n-1/2} + V^{n-1/2} - T_0^{n-1/2} \\ + \left(\alpha - \frac{1}{4}\right)\left[\left(q^n - q^{n-1}\right)^T (K - S)\left(q^n - q^{n-1}\right)\right] \end{aligned} \tag{3.36}$$

Introducing the definition of the energy function

$$\begin{aligned} \mathscr{H}^{*n+1/2} + \bar{C} + \left(\alpha - \frac{1}{4}\right)\left[\left(q^{n+1} - q^n\right)^T (K - S)\left(q^{n+1} - q^n\right)\right] = \\ \mathscr{H}^{*n-1/2} + \left(\alpha - \frac{1}{4}\right)\left[\left(q^n - q^{n-1}\right)^T (K - S)\left(q^n - q^{n-1}\right)\right] \end{aligned} \tag{3.37}$$

For a choice of $\alpha = 1/4$, the following relation exists

$$\mathscr{H}^{*n+1/2} + \bar{C} = \mathscr{H}^{*n-1/2} \tag{3.38}$$

At this stage in the development, it should be noted that a positive valued $\mathscr{H}^*$ may be ensured by selection of coordinate system. It is clear that for a choice of $\alpha = 1/4$ that $\mathscr{H}^{*n+1/2} < \mathscr{H}^{*n-1/2}$ for a damped system. Thus, the integration scheme results in bounded energy, and unconditional stability regardless of time step size. Even more note worthy is that in the absence of damping, the energy function

is constant regardless of time step size. This suggests large time step sizes may be utilized to give a reasonable approximation of motion.

For the case that $\alpha \neq 1/4$, an assessment of the integrator stability may still be made. First, note that in general, $K - S$ is not necessarily positive definite. Nevertheless, the case of a negative semi-definite $K - S$ would suggest that spin softening effects have softened a structure such that it has no effective stiffness, eliminating load bearing capability. Therefore, it is assumed that the quantity $K - S$ remains positive definite for practical systems of interest. Thus, the right hand side of Eq. 3.37 may be treated as a positive valued constant for $\alpha \geq 1/4$. It can be noted for $(1/4 \leq \alpha \leq 1/2)$ the value $\mathscr{H}^{*n+1/2}$ will be bounded for any time step size Δt, implying a stable integration scheme.

III.C.2. Considerations for Gyric systems with circulatory effects and non-conservative forces

Gyric systems may be subjected to external forces that introduce non-conservative effects into the system. Furthermore, for a Gyric system, time-varying, prescribed angular velocity $\Omega(t)$ gives rise to Circulatory terms. The Circulatory matrix introduces sign indefiniteness in energy relations, and is not of use in constructing stable integration schemes. Therefore, Circulatory effects will be included via forcing terms as non-conservative forces. This decouples the Circulatory effect from an otherwise conservative or bounded energy system. Thus, the overall non-conservative forces $(\bar{Q}_{nc})$ may be expressed as a combination of circulatory and non-conservative exter-

nal forces.

$$\bar{Q}_{nc}(t) = Q_{nc} + Q(t)_{circulatory} \tag{3.39}$$

$$Q(t)_{circulatory} = Q_H(t) - H(t)q \tag{3.40}$$

The presence of non-conservative forces gives rise to work being performed on the system. Work at the $n + 1/2$ mid-step is defined as

$$W^{n+1/2} = \frac{(q^{n+1} + q^n)}{2}\bar{Q}_{nc}^{n+1/2} \tag{3.41}$$

A similar relation exists for $W^{n-1/2}$. Thus, the previous energy function balance equation (Eq. 3.37) across time steps for a Gyric system may be modified to account for external forces.

$$\begin{aligned} &\mathscr{H}^{*n+1/2} + \bar{C} + \left(\alpha - \frac{1}{4}\right)\left[\left(q^{n+1} - q^n\right)^T (K - S)\left(q^{n+1} - q^n\right)\right] + W^{n+1/2} \\ &= \mathscr{H}^{*n-1/2} + \left(\alpha - \frac{1}{4}\right)\left[\left(q^n - q^{n-1}\right)^T (K - S)\left(q^n - q^{n-1}\right)\right] + W^{n-1/2} \end{aligned} \tag{3.42}$$

Since work from external forces is being performed on the system, the energy function will not be constant. However, since the developed integration method ensures stability for a conservative system, the predicted motion of the system will be bounded for simulations with bounded non-conservative forces. For choice of $\alpha = 1/4$ in the absence of damping, the change in energy function across a time step will simply be the change in work across that time step. The accuracy of the value of work, and thus $\mathscr{H}^*$ will be related to the accuracy of the solution. This may introduce more stringent requirements on time step size to provide sufficient resolution of transient external forces and displacements. Furthermore, the dependency of Circulatory forcing on generalized displacements may enforce time step size requirements related to

the maximum natural frequency [74] of the generalized displacements to result in a stable integration procedure.

III.C.3. Implementation of time integration method

This section details the actual implementation of the integration method into a numerical framework. The finite difference discretization described in early section may be employed to arrive at a set of linear equations that calculate displacements at a current time step utilizing system matrices and displacements at the previous two time steps. Thus, the method is not "self-starting" and will require displacements to be specified a $t = -\Delta t$ and $t = -2\Delta t$.

An effective stiffness matrix and force vector may be calculated as follows

$$\bar{K}_{n+1} q^{n+1} = \bar{F}_{n+1} \tag{3.43}$$

$$\bar{K}_{n+1} = (K_{n+1} - S_{n+1}) a_1 + (C_{n+1} + G_{n+1}) a_2 + M_{n+1} \tag{3.44}$$

$$\begin{aligned} \bar{F}_{n+1} &= \left(F_{c_{n+1}} + F_{nc_{n+1}}\right) a_3 + M_{n+1}\{A\} + (K_{n+1} - S_{n+1})\{B\} \\ &+ (C_{n+1} + G_{n+1})\{D\} \end{aligned} \tag{3.45}$$

$$\{A\} = 2q^n - q^{n-1}, \qquad \{B\} = -a_1 q^{n-1} - a_4 q^n, \qquad \{D\} = a_2 q^{n-1} \tag{3.46}$$

$$\begin{aligned} a_1 &= \alpha (\Delta t)^2, \qquad a_2 = \frac{\Delta t}{2}, \\ a_3 &= \frac{a_1}{\alpha}, \qquad a_4 = a_3 - 2a_1, \qquad \frac{1}{4} \leq \alpha \leq \frac{1}{2} \end{aligned} \tag{3.47}$$

Therefore, a time integration procedure which updates $\bar{K}_{n+1}$ and $\bar{F}_{n+1}$ at each time step, and solves for displacements q^{n+1} may implemented.

III.D. An illustrative Gyric problem

A simple, illustrative problem was considered to examine the applicability of the Dean integration method to Gyric systems. A simplified problem allows the dominant aspects of a particular class of problem to be studied while considering a problem that is tractable both computationally and theoretically. A simple two degree of freedom (DOF) problem was considered for the illustrative Gyric problem.

Consider a point mass m located in the $x_1 - x_2$ plane. The point mass is attached to a rigid, massless bar via two springs applying a restoring force in the x_1 and x_2 directions with spring constants k_1 and k_2 respectively. The rigid, massless bar lies in the x_1-x_2 plane. One end of the bar occupies the origin O' and the other occupies the coordinate $(\bar{x}, 0)$. This is the initial location of the point mass in the x_1-x_2 plane, and the springs are assumed unstretched when the point mass occupies this position. The mass is free to displace in the x_1 direction (u) and in the x_2 direction (v). Thus, this simple configuration illustrating a Gyric system with a "Circulatory" effect is a 2 DOF system. The plane rotates about an axis normal to the plane (x_3 direction), passing through the origin O'. A time varying angular velocity $\Omega(t)$ may be specified. No damping is considered. An illustration of this system is shown in Figure III.1.

III.D.1. Formulation of equations of motion

The position vector for the point mass at any time "coordinatized" in a rotating hub frame (x_i) is

$$\vec{r} = [\bar{x} + u]\,\hat{x}_1 + v\hat{x}_2 \tag{3.48}$$

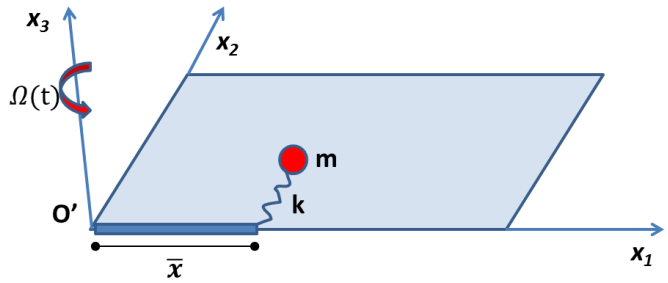

Figure III.1. Illustration of simplified Gyric system

The velocity vector for the point mass at any time coordinatized in a rotating hub frame (x_i) is

$$\vec{v} = [\dot{u} - v\Omega(t)]\,\hat{x}_1 + [\dot{v} + (\bar{x} + u)\,\Omega(t)]\,\hat{x}_2 \tag{3.49}$$

The kinetic energy of the system is

$$T = \frac{1}{2}m\vec{v}\cdot\vec{v} = \frac{1}{2}m\left[\dot{u}^2 + \dot{v}^2 + 2(\bar{x}\dot{v} + \dot{v}u - v\dot{u})\Omega(t) + \left(\bar{x}^2 + 2\bar{x}u + u^2 + v^2\right)\Omega(t)^2\right] \tag{3.50}$$

The potential energy of the system is

$$V = \frac{1}{2}\left(k_1u^2 + k_2v^2\right) \tag{3.51}$$

Forming the Lagrangian, $\mathscr{L}$ and utilizing Lagrange's equation allows for the equations of motion for the system to be formulated.

$$m\ddot{u} - 2m\Omega(t)\dot{v} + \left(k_1 - m\Omega(t)^2\right)u - m\dot{\Omega}(t)v = m\bar{x}\Omega(t)^2 \tag{3.52}$$

$$m\ddot{v} + 2m\Omega(t)\dot{u} + \left(k_2 - m\Omega(t)^2\right)v + m\dot{\Omega}(t)u = -m\bar{x}\dot{\Omega}(t) \tag{3.53}$$

Normalizing by m and introducing the following matrix definitions:

$$M\ddot{q} + G\dot{q} + (K - S + H)q = F_c + F_{nc} \tag{3.54}$$

$$
\begin{aligned}
M &= \begin{bmatrix} 1 & 0 \\ 0 & 1 \end{bmatrix}, \qquad K = \begin{bmatrix} \omega_1^2 & 0 \\ 0 & \omega_2^2 \end{bmatrix}, \qquad G = 2\Omega(t) \begin{bmatrix} 0 & -1 \\ 1 & 0 \end{bmatrix} \\
S &= \Omega(t)^2 \begin{bmatrix} 1 & 0 \\ 0 & 1 \end{bmatrix}, \qquad H = \dot{\Omega}(t) \begin{bmatrix} 0 & -1 \\ 1 & 0 \end{bmatrix}, \\
F_c &= \begin{Bmatrix} \bar{x}\Omega(t)^2 \\ 0 \end{Bmatrix}, \qquad F_{nc} = \begin{Bmatrix} 0 \\ -\bar{x}\dot{\Omega(t)} \end{Bmatrix}, \qquad q = \begin{Bmatrix} u(t) \\ v(t) \end{Bmatrix}
\end{aligned} \tag{3.55}
$$

Such that M and K are the mass and stiffness matrices respectively. The rotating system introduces G, S, and H are the Gyric, spin softening, and Circulatory matrices respectively. Finally, F_c, F_{nc}, and q are the conservative force vector, non-conservative force vector, and displacement vector respectively. Here, $\omega_1^2 = \frac{k_1}{m}$ and $\omega_2^2 = \frac{k_2}{m}$ are the natural frequencies for the non-rotating system. Thus, the design parameters for the illustrative Gyric system are $\bar{x}$, ω_1, and ω_2, with the system rotating at some prescribed angular velocity $\Omega(t)$.

For this study, $\omega_1 = \omega_2 = 10$ rad/s and $\bar{x} = 3m$ were considered with initial displacements of $u = v = 0$. Various $\Omega(t)$ profiles were considered.

III.D.2. Establishing a reference solution

For each angular velocity profile considered, an explicit ODE solver (Runge-Kutta 4th order with adaptive time stepping [81]) was used to generate a reference solution for 10 seconds of simulation time. Tolerances on the solver were tightened to minimize energy dissipation due to numerical effects. Furthermore, for relatively short simulation times energy dissipation should be minimal. For $\Omega(t)$ profiles that included circulatory effects, runs were completed with and without the circulatory

matrix terms to ensure the circulatory matrix had a significant effect on the problem at hand.

III.D.3. Time integration studies using a simple conservative Gyric system

First, a conservative Gyric system is considered. The angular velocity profile is constant with respect to time with a value of $2\pi\ rad/s$. The elimination of $\dot{\Omega}(t)$ terms removes the effect of the circulatory matrix. Various time step sizes were considered and using the Dean integrator and an unconditionally stable Newmark-β integrator [68, 82] (constant average acceleration scheme). The results of these two-implicit schemes were compared to the reference solution (Runge-Kutta 4th order) with regards to displacements, velocities, and energy function $\mathscr{H}^*$. Time step sizes of 0.01, 0.1, and 1 seconds were considered.

Figure III.2 shows the results for a time step size of 0.01 seconds. All methods are in very good agreement with regards to displacements and velocities. Inspection of $\mathscr{H}^*$ value shows that both Dean and Newmark-β integration methods conserve this value exactly. Furthermore, the explicit Runge-Kutta time integration method dissipates energy despite using much finer time steps. Such energy dissipation is common for explicit time integration methods.

Figure III.3 shows the results for a time step size of 0.1 seconds. With regards to magnitudes of displacements and velocities, the two implicit methods appear to perform similarly. Similar trends are observed for the conservation of $\mathscr{H}^*$ using the Dean and Newmark-β integration methods.

Figure III.4 shows the results for a time step size of 1 seconds. The quality

of the solution does appear to degrade at this coarser time step. Nevertheless, the magnitudes of displacement and velocity predicted by the Dean and Newmark-β integration methods are comparable to those predicted by the reference explicit integration method. Again, similar trends for conservation of $\mathscr{H}^*$ are seen at this coarser time step. This suggests that certain schemes of the Newmark-β method may be $\mathscr{H}^*$ conserving for conservative Gyric systems. Indeed, this is proved in the next section.

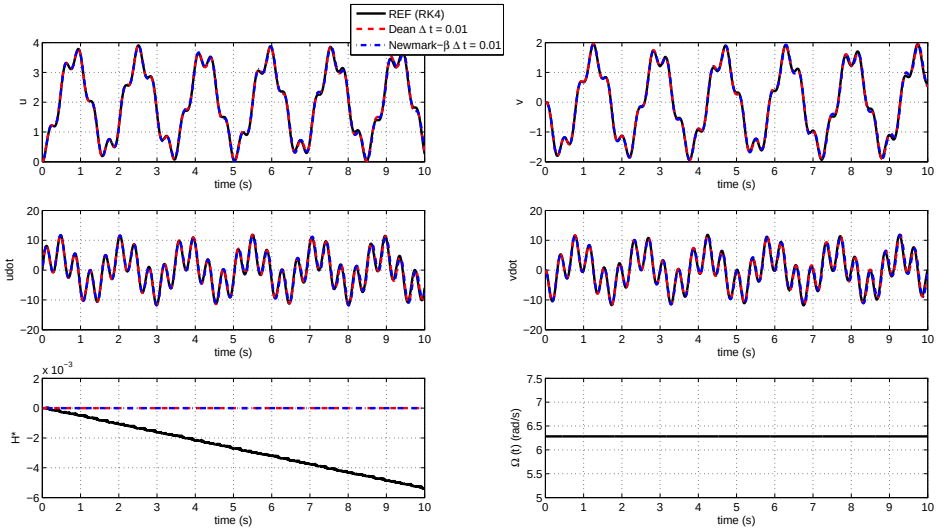

Figure III.2. Time integration comparison for a simple conservative Gyric system ($\Delta t = 0.01\ s$)

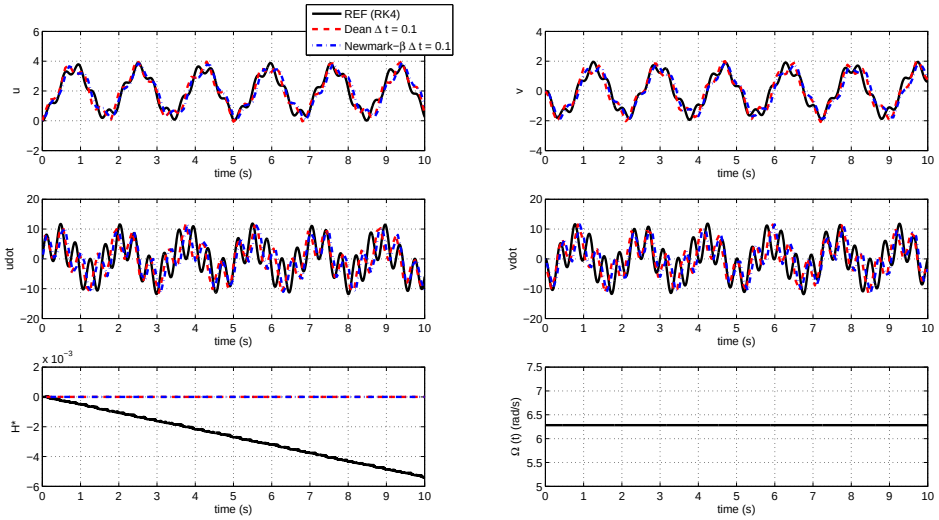

Figure III.3. Time integration comparison for a simple conservative Gyric system ($\Delta t = 0.1\ s$)

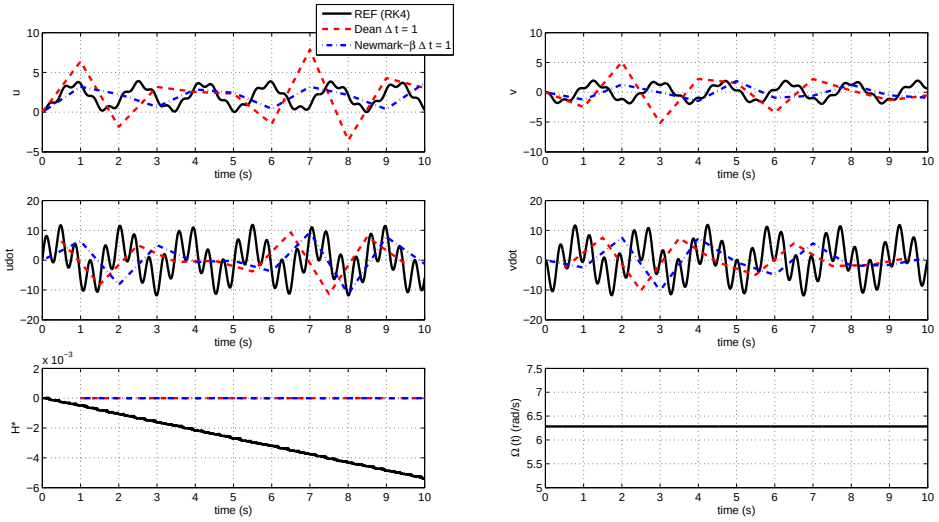

Figure III.4. Time integration comparison for a simple conservative Gyric system ($\Delta t = 1.0\ s$)

III.D.4. Time integration studies using a simple Gyric system with circulatory effects

The non-conservative Gyric system with circulatory effects is a unique system in which the Gyric Dean integration method was not developed for. The skew symmetric nature of the circulatory matrix introduces a sign indefinite term in the energy function. Therefore, it is of no use in constructing stable integration schemes from energy principles. Furthermore, the skew symmetric circulatory matrix and spoil the assumed symmetric positive definite characteristics of an effective stiffness matrix. This may cause problems in other implicit integration methods as well.

For proper treatment of non-conservative terms, the product of the circulatory matrix and displacement vector was removed from the left hand side and placed on the right hand side as a non-conservative force. This essentially models a conservative system under the influence of non-conservative forces. This should result in a stable integration scheme with a better prediction of the energy function, $\mathscr{H}^*$. However, the quality of energy predictions will be affected by treatment of the circulatory effect via non-conservative forces, as this introduces a nonlinearity in the non-conservative forcing.

The aforementioned configuration was considered with a time varying angular velocity profile. A piecewise angular velocity profile of $2\pi t$ from $t = 0$ to 5 seconds and 10π from $t = 5$ to 10 seconds was considered. As shown in Figure III.5 the time step size of 0.01 seconds produces very good agreement with the reference solution. Figure III.6 shows the results for a time step size of 0.1 seconds while introducing the circulatory effects via non-conservative forcing. The energy function predicted

by the Gyric Dean integration method is in very good agreement with the reference solution. At $t = 10$ seconds the energy function $\mathscr{H}^*$ predicted by the Gyric Dean integrator has a discrepancy of only 4% compared to the reference solution while the Newmark-β integration method has a discrepancy of 60%.

It is notable that at time steps larger than 0.1 seconds neither Newmark-β or the Gyric Dean method predict $\mathscr{H}^*$ accurately. This is due to a reasonable prediction of displacements being required to accurately characterize the circulatory forcing. One may note that the natural frequency of the non-rotating system is 10 rad/s, and the resulting period of 0.1 seconds is the same as the coarsest time step considered. At time steps larger than this, an accurate representation of motion is not expected.

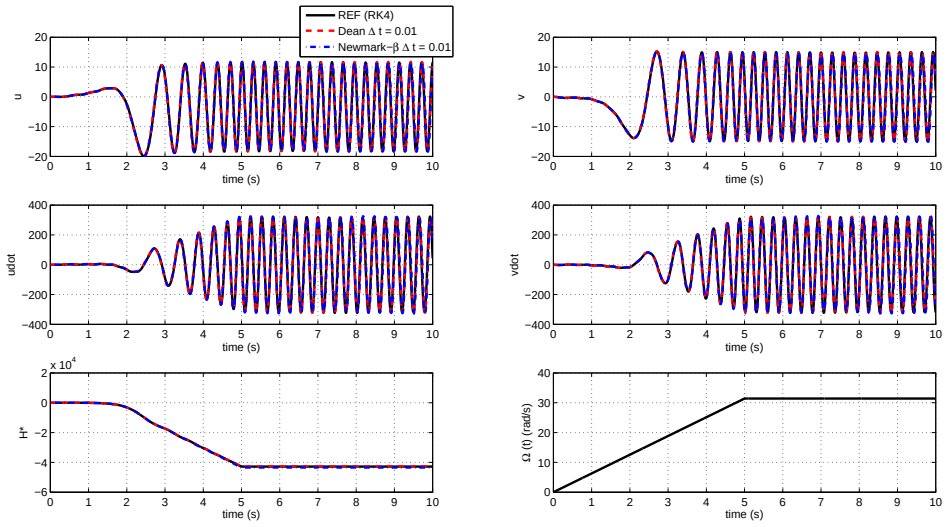

Figure III.5. Time integration comparison for a simple Gyric system with circulatory terms($\Delta t = 0.01\ s$)

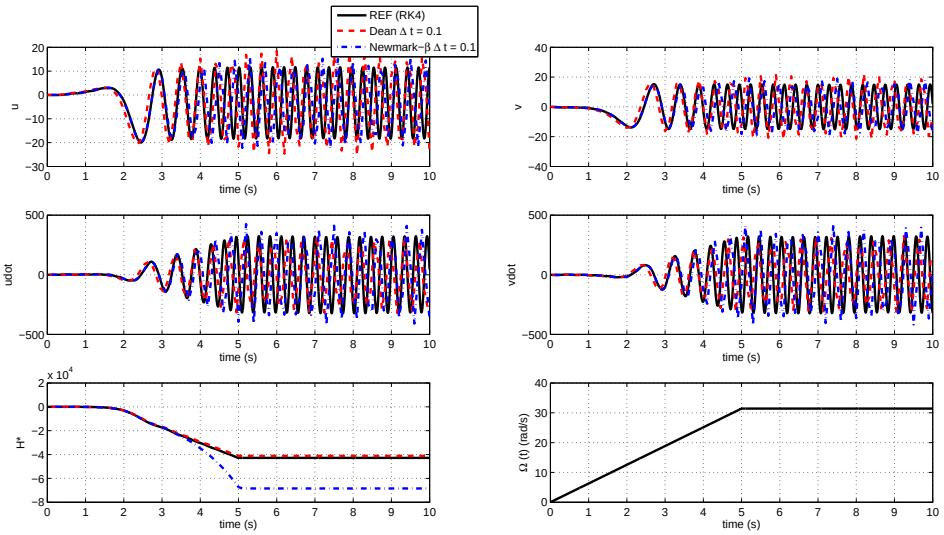

Figure III.6. Time integration comparison for a simple Gyric system with circulatory terms($\Delta t = 0.1\ s$)

III.E. Energy preservation of Newmark-β method with respect to conservative Gyric systems

A previous section examined the application of the Dean integration method for a simple, conservative Gyric system. The common Newmark-β time integration method was also applied to this simple, conservative Gyric system. As expected, the energy preserving Dean method conserved the Hamiltonian of the simple system. Interestingly, the Newmark-β integration method also conserved the Hamiltonian for the constant average acceleration scheme that was considered. This served as a reminder that certain schemes of the Newmark-β integration method are energy conserving for conservative, flexible systems as has been shown by Hughes [83]. It also leads one to consider if the Newmark-β method can also be shown to be Hamiltonian conserving for a general conservative Gyric system.

First, let the forward-difference and mean-value operators considered by Hughes be introduced.

$$[d_n] = d_{n+1} - d_n \tag{3.56}$$

$$\langle d_n \rangle = \frac{1}{2}\left(d_{n+1} + d_n\right) \tag{3.57}$$

Next, consider the flexible, Gyric system shown below.

$$Ma_{n+1} + (C+G)\, v_{n+1} + (K - S + H)\, d_{n+1} = Q_{c\ n+1} + Q_{nc\ n+1} \tag{3.58}$$

Such that d, v, and a are displacement, velocity, and acceleration respectively. The subscript $n+1$ denotes the values at the $n+1$th time step.

Expressions for displacement and velocity for the Newmark-β method are shown below.

$$d_{n+1} = d_n + \Delta t v_n + \frac{\Delta t^2}{2}\left[(1-2\beta)\, a_n + 2\beta a_{n+1}\right] \tag{3.59}$$

$$v_{n+1} = v_n + \Delta t\left[(1-\alpha)\, a_n + \alpha a_{n+1}\right] \tag{3.60}$$

Furthermore, let the velocity and displacement difference across a timestep be expressed as

$$[v_n] = \Delta t a_{n+\alpha} \tag{3.61}$$

$$[d_n] = \Delta t \langle v_n \rangle + \Delta t^2 \left(\beta - \frac{\alpha}{2}\right)[a_n] \tag{3.62}$$

Such that

$$a_{n+\alpha} = (1-\alpha)\, a_n + \alpha a_{n+1} \tag{3.63}$$

For a conservative Gyric system ($C = 0$, $H = 0$, $Q_{nc} = 0$) with constant mass, Gyric, and stiffness matrices and conservative force vectors, the following relations exist.

$$M[a_n] + G[v_n] + (K - S)[d_n] = 0. \tag{3.64}$$

$$M\langle a_n\rangle + G\langle v_n\rangle + (K-S)\langle d_n\rangle = Q_c \tag{3.65}$$

Now, consider the difference in kinetic energy sub-function T_2 from time step n to $n+1$.

$$[T_2(v_n)] = [v_n]^T M\langle v_n\rangle \tag{3.66}$$

As shown by Hughes

$$\begin{aligned}[T_2(v_n)] &= a_{n+\alpha}^T M\left([d_n] - \Delta t^2\left(\beta - \frac{\alpha}{2}\right)[a_n]\right) \\ &= \left(\langle a_n\rangle + \left(\alpha - \frac{1}{2}\right)[a_n]\right)^T M[d_n] - \Delta t^2\left(\beta - \frac{\alpha}{2}\right)[a_n]\end{aligned} \tag{3.67}$$

Employing Eqs. 3.64 and 3.65 in conjunction with the symmetry of the mass matrix allows this energy function to be written as

$$\begin{aligned}[T_2(v_n)] &= \left[Q_c^T + \langle v_n\rangle^T G - \langle d_n\rangle^T (K-S)\right. \\ &+ \left.\left(\alpha - \frac{1}{2}\right)\left([v_n]^T G - [d_n]^T (K-S)\right)\right][d_n] \\ &- \Delta t^2\left(\beta - \frac{\alpha}{2}\right)[a_n]\end{aligned} \tag{3.68}$$

Next, the difference in strain energy across a time step may be introduced as well as the difference in the kinetic energy sub-function T_0.

$$[U(d_n)] = [d_n]^T K\langle d_n\rangle \tag{3.69}$$

$$[T_0(d_n)] = Q_c^T[d_n] + [d_n]^T S\langle d_n\rangle \tag{3.70}$$

$$\begin{aligned}[T_2(v_n)] - [T_0(d_n)] + [U(d_n)] &= \left[\langle v_n\rangle^T G + \left(\alpha - \frac{1}{2}\right)[v_n]^T G\right][d_n] \\ &- \left(\alpha - \frac{1}{2}\right)[d_n]^T (K-S)[d_n] \\ &- \Delta t^2\left(\beta - \frac{\alpha}{2}\right) a_{n+\alpha}^T M[a_n]\end{aligned} \tag{3.71}$$

Next, realizing the definition of the Hamiltonian function in a difference form and introducing the definition $[d_n]$ allows the following expression to be formed.

$$\begin{aligned}[H(v_n, d_n)] &= \Delta t \langle v_n \rangle^T G \langle v_n \rangle + \Delta t^2 \left(\beta - \frac{\alpha}{2}\right) \left[\langle v_n \rangle^T G[a_n] - a_{n+\alpha}^T M[a_n]\right] \\ &+ \left(\alpha - \frac{1}{2}\right) \left[[v_n]^T G[d_n] - [d_n]^T (K - S)[d_n]\right] \end{aligned} \tag{3.72}$$

Exploiting the skew-symmetry of the Gyric matrix allows the difference Hamiltonian across a timestep to be expressed as

$$\begin{aligned}[H(v_n, d_n)] &= \Delta t^2 \left(\beta - \frac{\alpha}{2}\right) \left[\langle v_n \rangle^T G[a_n] - a_{n+\alpha}^T M[a_n]\right] \\ &+ \left(\alpha - \frac{1}{2}\right) \left[[v_n]^T G[d_n] - [d_n]^T (K - S)[d_n]\right] \end{aligned} \tag{3.73}$$

Furthermore, for the constant averaged acceleration method ($\beta = \frac{1}{4}$ and $\alpha = \frac{1}{2}$) the Hamiltonian is indeed conserved for a conservative Gyric system.

$$[H(v_n, d_n)] = 0 \tag{3.74}$$

Thus, the constant average acceleration scheme for the Newmark-β time integration method has been shown to be Hamiltonian conserving for conservative Gyric systems.

III.F. Conclusions

A previously developed energy conserving time integration method has been extended to consider Gyric systems such as wind turbines. While energy in a conservative Gyric system is not constant, a quantity known as the energy function $\mathscr{H}^*$ is. A proof of non-constant energy, but constant $\mathscr{H}^*$ for a conservative Gyric system under conservative loadings has been shown in this chapter. The energy function of a conservative Gyric system was used to construct an unconditionally stable

integration method. This relates the boundedness of the integration method to a physical, energy related quantity. An approach for accounting for non-conservative Gyric systems with dissipative circulatory terms as a non-conservative force has also been presented. The implementation of this integration method into a numerical framework (such as the finite element method) has also been discussed.

The energy preserving Gyric integration method was assessed using a simple, illustrative 2 DOF problem. Such a problem models characteristics of a more complicated system while remaining very tractable conceptually and computationally. The energy preserving Gyric integration method was compared to a conventional Newmark-β implicit integrator. During this study, it was observed that the Newmark-β integration method also conserved $\mathscr{H}^*$ for a conservative Gyric system. This was further investigated, and a proof of $\mathscr{H}^*$ conservation for the constant averaged acceleration scheme of the Newmark-β method was also given.

These energy preserving time integration implicit methods for Gyric systems may serve as an alternative numerical tool for the time integration of Gyric systems. For the problems considered, the tool has exhibited desirable energy characteristics. This is due to the use of a physical, energy related quantity being utilized to construct an unconditionally stable time integration method. Coarser time steps will still result in conservation of $\mathscr{H}^*$ for a conservative Gyric system, indicating large time steps may give a reasonable characterization of motion amplitudes for preliminary design studies.

CHAPTER IV

DIRECT LINEARIZATION VIA A METHOD OF QUADRATIC MODES

Although linearized equations of motion do not fully embody the nature of a nonlinear system, such equations are very useful for gaining insight into system response and for developing feedback controllers. A potentially laborious approach for obtaining linearized representations of a system is to develop full nonlinear equations of motion and then perform linearization by inspection about some equilibrium configuration. Herein, more efficient techniques for arriving at linearized equations of motion are discussed and a new linearization procedure is suggested.

One efficient approach is direct linearization, and considers a Lagrangian treatment of a system. Kinetic and potential energy functions are described in terms generalized displacements and velocities, and other system specific parameters (mass, stiffness, geometry, etc.). Parish et al. [58] investigated direct linearization and generalized the procedure to consider not only discrete, but continuous and hybrid rheonomic systems. Although direct linearization is a relatively efficient procedure, the associated energy functions are system specific, and can take any form with any degree of complexity. Furthermore, for very complex energy functions certain contributions may not even manifest themselves after linearization. Thus, the approach under development seeks to express these energy functions in a more standardized and minimal form.

Segalman and Dohrmann [56, 57] developed a unique approach to construct

linearized equations of motion known as the method of quadratic modes. This work was motivated by the realization that premature linearization of kinematics can exclude important physics from certain problems, in particular rotational motion of flexible bodies. Thus, Segalman and Dohrmann advocated performing a Taylor series expansion of the nonlinear response of a system and retaining terms that were up to quadratic order in generalized displacements. This quadratic description was used in conjunction with Hamilton's principle to construct partially nonlinear equations of motion for a flexible system with rotating and floating frame effects. This approach ensures the bare minimum of nonlinearities are present in the equations of motion, such that the influence of nonlinearities are still present in the linearized equations of motion. The downfall of this approach is that the analyst must linearize the partial nonlinear equations of motion by inspection.

The two aforementioned approaches for linearization of dynamical systems each have advantages and downfalls. While direct linearization is a well defined procedure for developing linearized equations of motion, the analyst must construct energy functions at the front end of the procedure that are unique and system dependent. The method of quadratic modes has a clearly defined form for system kinematics up front, but requires a "manual" linearization by inspection to arrive at linearized equations of motion. The approach suggested herein seeks to take advantage of the strengths of both methods. Direct linearization via a method of quadratic modes exploits the well defined quadratic kinematic form of the method of quadratic modes to form energy functions to be employed in a direction linearization procedure. For a general system, the representations in this approach might appear involved. Nev-

ertheless, this procedure has a well defined form for direct linearization that can be implemented into automated software for use in developing linearized equations of motion for general dynamical systems in an efficient manner.

This chapter first presents a high level overview of the aforementioned methods. The process of direct linearization, a method of quadratic modes, and the proposed combined approach are flow charted and inputs and outputs or each method are discussed, as well as critical steps. A subsequent section gives a more detailed overview of direct linearization procedures for discrete rheonomic systems. Relevant details of a method of quadratic modes are also discussed. Finally, the details of the combined approach are presented.

IV.A. Flow charts of various methods

The aforementioned methods for linearization of dynamical systems have distinct differences. This section highlights the overall process of linearization using each method without being concerned with the specific details of the "internal" processes of a method. Only inputs, outputs, and key steps are discussed.

IV.A.1. Flow chart of direct linearization

As previously mentioned, the direct linearization procedure requires that kinetic energy $T(\dot{q}, q)$ and potential energy $V(q)$ functions for a system are known. Kinetic energy is decomposed into parts that are quadratic $T_2(q, \dot{q})$, linear $T_1(q, \dot{q})$, and constant $T_0(q)$ with respect to generalized velocities $\dot{q}$. These energy expressions may also be a function of generalized displacements q. Linearization must be performed

about a previously determined equilibrium configuration, and such a configuration is determined by solving the nonlinear static equilibrium equations for a system. Thus, the inputs for the direct linearization procedure are the energy functions and equilibrium solution. Next, a well defined linearization procedure produces outputs of linearized coefficient matrices. Figure IV.1 shows the basic flow chart associated with the direct linearization procedure for a discrete rheonomic system.

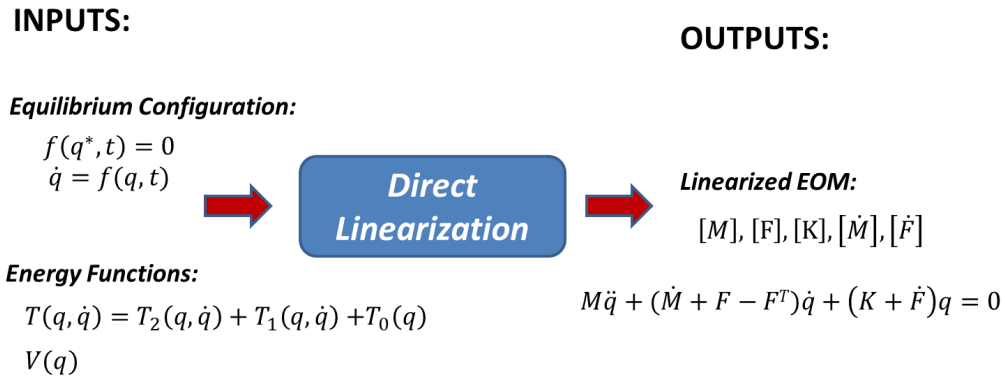

Figure IV.1. Flowchart describing the direct linearization procedure

IV.A.2. Flow chart of a method of quadratic modes

The method of quadratic modes [56] describes displacement and velocities up to quadratic order using temporally varying degrees of freedom $q_i(t)$, and spatially varying linear and quadratic functions $h_m^i(\vec{\chi})$ and $g_m^{ij}(\vec{\chi})$ respectively. Note that $g_m^{ij} = g_m^{ji}$. Thus, displacement of a material point $\vec{\chi}$ at time t may be described by

$$u_m(\vec{\chi}, t) = q_i(t)h_m^i(\vec{\chi}) + q_i(t)q_j(t)g_m^{ij}(\vec{\chi}) \tag{4.1}$$

The method also requires specification of an internal force field for the system that is linear in generalized displacements.

$$f(\vec{\chi}, t) = q_i(t)\tilde{f}^i(\vec{\chi}) \tag{4.2}$$

Here, summation is implied on the indices i and j.

Furthermore, floating and rotating frame effects may be considered by specifying a vector p_m describing the translation of a reference frame with respect to an inertial frame, as well as a spin tensor Ω_{ij} that accounts for a rotating frame. Thus, the inputs to this method are $h^i_m(\vec{\chi})$, $g^{ij}_m(\vec{\chi})$, p_m, and Ω_{ij}. Using a well defined procedure, partial nonlinear equations of motion are developed. Next, an intermediate step requires determining the equilibrium solution and using this solution to perform linearization by inspection. This step is "manual" in nature and is performed by the analyst. The final form of nonlinear equations are the same as those obtained through a direct linearization procedure. This process is illustrated in the flow chart shown in Figure IV.2. The overbar on coefficient matrices in this figure denotes that effective coefficient matrices are obtained through this method. Coefficient matrices are not further decomposed as in the direct linearization procedure.

IV.A.3. Flow chart of proposed method

As mentioned previously, the proposed linearization method seeks to leverage the strengths of direct linearization and a method of quadratic modes in a combined manner. The quadratic modes kinematic description along with an equilibrium configuration is supplied to the procedure as an input. The proposed method constructs energy functions "internally" from the kinematic description and direct linearization

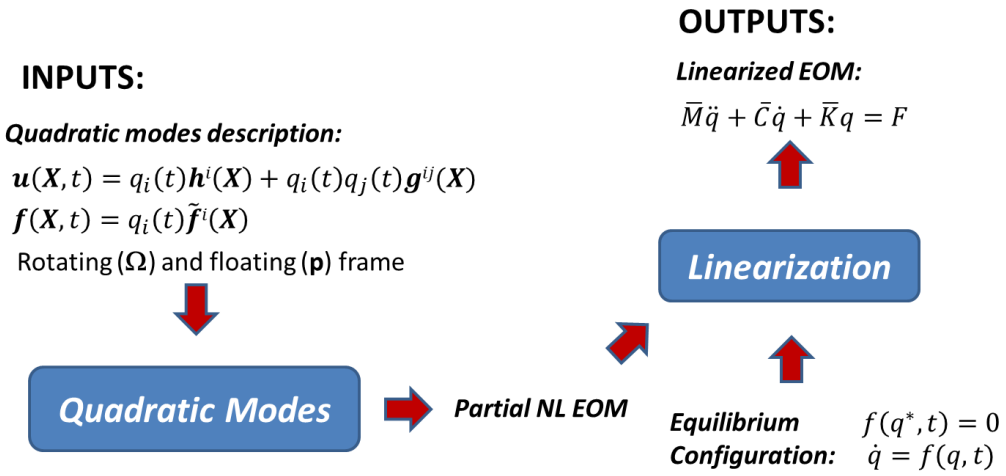

Figure IV.2. Flowchart describing the method of quadratic modes linearization procedure

is used to arrive at linearized coefficient matrices as an output. A flow chart of the proposed framework is shown in Figure IV.3. Details of direct linearization via quadratic modes are discussed in a subsequent section.

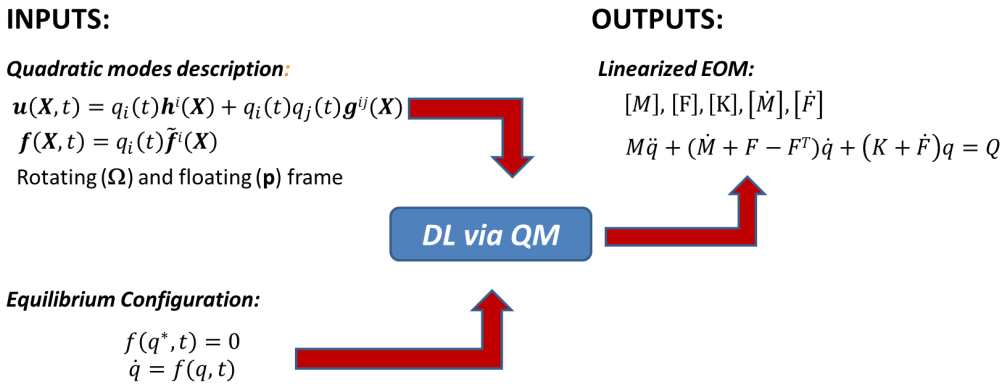

Figure IV.3. Flowchart describing the proposed linearization procedure

IV.B. Overview of direct linearization of rheonomic systems

Parish et al. [58] have shown that direct linearization of a discrete rheonomic system is achieved by computing the following partial derivatives of energy functions and evaluating the expressions at the desired equilibrium point.

$$M_{ij} = \left.\frac{\partial^2 T_2}{\partial \dot{q}_i \partial \dot{q}_j}\right|_{(eq)} \tag{4.3}$$

$$F_{ij} = \left.\frac{\partial^2 T_1}{\partial q_i \partial \dot{q}_j}\right|_{(eq)} \tag{4.4}$$

$$K_{ij} = \left.\frac{\partial^2 U}{\partial q_i \partial q_j}\right|_{(eq)} \tag{4.5}$$

Such that U is the dynamic potential composed of T_0 and the potential energy function V(and possibly a strain energy function, $\mathscr{U}$), $U = V + \mathscr{U} - T_0$. Here, $|_{(eq)}$ denotes the quantity is evaluated at the equilibrium state. The equilibrium state is determined by solving the static equilibrium equation for the system.

$$\frac{\partial^2 T_1}{\partial t \partial \dot{q}_i} + \frac{\partial U}{\partial q_i} = 0 \tag{4.6}$$

The resulting linearized equations of motion are

$$M_{ij}\ddot{q}_j + \left(\dot{M}_{ij} + F_{ji} - F_{ij}\right)\dot{q}_j + \left(\dot{F}_{ji} + K_{ij}\right)q_j = Q_j \tag{4.7}$$

The overdot in these terms represents explicit partial differentiation with respect to time. For discrete reheonomic systems, the kinetic energy sub-functions may be expressed in terms of Lagrangian vectors as shown below. These vectors, however, are system dependent and do not have a general form when using the direct linearization approach alone. Here, the scalar M represents the mass of a particle in the system.

$$T_2 = \frac{1}{2} M \tau_m^i \tau_m^j \dot{q}_i \dot{q}_j \tag{4.8}$$

$$T_1 = M \tau_m^i \tau_m^0 \dot{q}_i \tag{4.9}$$

$$T_0 = \frac{1}{2} M \tau_m^0 \tau_m^0 \tag{4.10}$$

IV.C. Employing a method of quadratic modes representation

The method of quadratic modes [56] describes displacement and velocities up to quadratic order using temporally varying degrees of freedom $q_i(t)$, and spatially varying linear and quadratic functions $h_m^i(\vec{\chi})$ and $g_m^{ij}(\vec{\chi})$ respectively. Note that $g_m^{ij} = g_m^{ji}$. Thus, displacement of a material point $\vec{\chi}$ at time t may be described by

$$u_m(\vec{\chi}, t) = q_i(t) h_m^i(\vec{\chi}) + q_i(t) q_j(t) g_m^{ij}(\vec{\chi}) \tag{4.11}$$

The velocity relative to the body frame is

$$\dot{u}_m(\vec{\chi}, t) = \dot{q}_i(t) h_m^i(\vec{\chi}) + 2\dot{q}_i(t) q_j(t) g_m^{ij}(\vec{\chi}) \tag{4.12}$$

Furthermore, a conservative force vector that is linear in generalized displacements may be expressed as

$$F_{C_m}(\vec{\chi}, t) = q_i(t) f_m^i \tag{4.13}$$

One may account for rigid body translation and rotation by considering velocity of the body frame $\dot{p}_m$, angular velocity spin tensor Ω_{ij}, and a rotation tensor $R_{ij}(t)$ from the reference configuration to configuration at time t.

Therefore, the inertial velocity of a particle located at material point $\vec{\chi}$ is

$$\dot{r}_m = \dot{p}_m + \Omega_{mn} R_{nl} \left(\chi_l + u_l \right) + R_{ml} \dot{u}_l \tag{4.14}$$

$$\dot{r}_m = \dot{p}_m + \Omega_{mn} R_{nl} \left(\chi_l + q_k h_l^k + q_k q_r g_l^{kr} \right) + R_{ml} \left(\dot{q}_k h_l^k + 2 \dot{q}_k q_r g_l^{kr} \right) \tag{4.15}$$

As shown earlier, the kinetic energy function for rheonomic systems may be expressed using Lagrangian vectors (τ_m^0, τ_m^i). Furthermore, it should be noted that considering rheonomic systems is also sufficient for considering scleronomic systems as these are a specific subset of rheonomic systems. Expressing velocity in terms of Lagrangian vectors yields

$$\dot{r}_m = \frac{\partial r_m}{\partial t} + \frac{\partial r_m}{\partial q_i} \dot{q}_i = \tau_m^0 + \tau_m^i \dot{q}_i \tag{4.16}$$

Here, $\frac{\partial}{\partial t}$ denotes explicit partial differentiation with respect to time. From Eq. 4.15 one may express Lagrangian vectors in terms of the quadratic modes representation.

$$\tau_m^0 = \dot{p}_m + \Omega_{mn} R_{nl} \left(\chi_l + q_r h_l^r + q_r q_k g_l^{rk} \right) \tag{4.17}$$

$$\tau_m^i = R_{ml} \left(h_l^i + 2 q_k g_l^{ik} \right) \tag{4.18}$$

The potential energy function V may be constructed from the conservative F_{C_m} vector that was presented earlier

$$V = \frac{1}{2} F_{C_m} R_{ml} u_l \tag{4.19}$$

For some configurations, the potential energy is more readily expressed in terms of strain energy rather than the above expression for work of conservative forces. The strain energy at a particular material point (or strain energy density) is expressed as:

$$\mathscr{U} = \frac{1}{2} E \left(\epsilon_{11}^2 + \epsilon_{22}^2 + \epsilon_{33}^2 \right) + 2G \left(\epsilon_{23}^2 + \epsilon_{13}^2 + \epsilon_{12}^2 \right) \tag{4.20}$$

Using Voigt notation allows this expression to be written more compactly

$$\mathscr{U} = \frac{1}{2} C_{ij} \bar{\epsilon}_i \bar{\epsilon}_j \tag{4.21}$$

Such that

$$\overline{\epsilon} = \left[\epsilon_{11}, \epsilon_{22}, \epsilon_{33}, \epsilon_{23}, \epsilon_{13}, \epsilon_{12}\right]^T \tag{4.22}$$

$$\mathbf{C} = \begin{bmatrix} E & 0 & 0 & 0 & 0 & 0 \\ 0 & E & 0 & 0 & 0 & 0 \\ 0 & 0 & E & 0 & 0 & 0 \\ 0 & 0 & 0 & 4G & 0 & 0 \\ 0 & 0 & 0 & 0 & 4G & 0 \\ 0 & 0 & 0 & 0 & 0 & 4G \end{bmatrix} \tag{4.23}$$

The expression for the strain tensor in terms of displacements is

$$\epsilon_{ij} = \frac{1}{2}\left(\frac{\partial u_i}{\partial x_j} + \frac{\partial u_j}{\partial x_i} + \frac{\partial u_m}{\partial x_i}\frac{\partial u_m}{\partial x_j}\right) \tag{4.24}$$

Utilizing the quadratic modes representation of the displacement field results in the following expression for the strain tensor

$$\begin{aligned} \epsilon_{ij} &= \frac{1}{2}\left[q_k\left(h^k_{i,j} + h^k_{j,i}\right) + q_k q_s\left(h^k_{m,i}h^s_{m,j} + g^{ks}_{i,j} + g^{ks}_{j,i}\right)\right. \\ &+ \left. q_k q_s q_r\left(h^r_{m,j}g^{ks}_{m,i} + h^k_{m,i}g^{sr}_{m,j}\right) + q_k q_r q_s q_v g^{ks}_{m,i}g^{rv}_{m,j}\right] \end{aligned} \tag{4.25}$$

Let the following definitions be introduced to express the strain energy in a form compatible with Voigt notation.

$$\hat{h}^k_\alpha = h^k_{i,j} + h^k_{j,i} \tag{4.26}$$

$$\hat{g}^{ks}_\alpha = h^k_{m,i}h^s_{m,j} + g^{ks}_{i,j} + g^{ks}_{j,i} \tag{4.27}$$

$$\hat{f}^{ksr}_\alpha = h^r_{m,j}g^{ks}_{m,i} + h^k_{m,i}g^{sr}_{m,j} \tag{4.28}$$

$$\hat{l}^{ksrv}_\alpha = g^{ks}_{m,i}g^{rv}_{m,j} \tag{4.29}$$

Mapping between α and i, j in these equations is shown in Eq. 4.22. Thus, the strain components in Voigt notation simplify to

$$\epsilon_\alpha = \frac{1}{2}\left[q_k \hat{h}^k_\alpha + q_k q_s \hat{g}^{ks}_\alpha + q_k q_s q_r \hat{f}^{ksr}_\alpha + q_k q_s q_r q_v \hat{l}^{ksrv}_\alpha\right] \tag{4.30}$$

The above expression for strain is quartic in generalized displacements q_k. Accordingly, the resulting expression for strain energy will be octic in generalized displacements. Retaining these terms is likely unnecessary for arriving at equations of motion that reasonably characterize the behavior of a system. Future use of the above equation will truncate higher order terms as necessary.

Thus, the once system specific energy functions necessary for a direct linearization approach can be characterized using a standard form by employing the method of quadratic modes kinematic description.

IV.D. Direct linearization of discrete rheonomic systems via a method of quadratic modes

The direct linearization procedure presented by Parish et al. [58] generates system matrices for equations of motion from partial derivatives of kinetic and potential energy functions. Herein, the quadratic modes descriptions of position and velocity are utilized to provide a more direct approach. First, the equation governing the equilibrium state solution is presented. The equations of motion are linearized about this state. Next, the linearized equations of motion are presented in terms of the method of quadratic modes kinematic description.

IV.D.1. Equilibrium configuration solution

Definition of T_1 and T_0 in terms of the Lagrangian vectors and the potential energy function V and strain energy function $\mathscr{U}$, can be utilized to develop an equilibrium equation solution

$$\frac{\partial^2 T_1}{\partial t \partial \dot{q}_i} + \frac{\partial U}{\partial q_i} = \frac{\partial^2 T_1}{\partial t \partial \dot{q}_i} + \frac{\partial V}{\partial q_i} + \frac{\partial \mathscr{U}}{\partial q_i} - \frac{\partial T_0}{\partial q_i} = 0 \tag{4.31}$$

$$\begin{aligned} M\left(\frac{\partial \tau_m^i}{\partial t}\tau_m^0 + \tau_m^i \frac{\partial \tau_m^0}{\partial t} - \tau_m^0 \frac{\partial \tau_m^0}{\partial q_i}\right) &+ \frac{1}{2}\left(\frac{\partial F_{C_m}}{\partial q_i} R_{ml} u_l + F_{C_m} R_{ml} \frac{\partial u_l}{\partial q_i}\right) \\ &+ C_{mn}\bar{\epsilon}_n \frac{\partial \epsilon_m}{\partial q_i} = 0 \end{aligned} \tag{4.32}$$

For the quadratic modes representation of the Lagrangian vectors, it can be shown that

$$\frac{\partial \tau_m^i}{\partial t} - \frac{\partial \tau_m^0}{\partial q_i} = 0 \tag{4.33}$$

Thus, the equilibrium configuration solution reduces to

$$M\tau_m^i \frac{\partial \tau_m^0}{\partial t} + \frac{1}{2}\left(R_{ml} f_m^i u_l + R_{ml} f_m^k \frac{\partial u_l}{\partial q_i}\right) + C_{mn}\bar{\epsilon}_n \frac{\partial \bar{\epsilon}_m}{\partial q_i} = 0 \tag{4.34}$$

The quadratic modes representation of the Lagrangian vectors and displacement were shown in a previous section. The explicit time derivative of τ_m^0 is

$$\frac{\partial \tau_m^0}{\partial t} = \ddot{p}_m + \left(\dot{\Omega}_{mn} R_{nl} + \Omega_{mn}\Omega_{nr} R_{rl}\right)\left(\chi_l + q_r h_l^r + q_r q_k g_l^{rk}\right) \tag{4.35}$$

Note that expressing the Lagrangian vectors in terms of the quadratic modes representation effectively allows the expression of the kinetic energy function in terms of the quadratic modes representation.

The partial derivative of potential energy with respect to generalized displacements is

$$\frac{\partial V}{\partial q_i} = \frac{1}{2} q_k R_{ml}\left(f_m^i\left(h_l^k + q_v g_l^{kv}\right) + f_m^k\left(h_l^i + 2q_v g_l^{iv}\right)\right) \tag{4.36}$$

The expression for the entries of the Voigt strain vector ($\bar{\epsilon}_i$) in terms of a quadratic modes representation was presented in an early section. The partial derivative of the strain component with respect to generalized displacements is shown below. Note that higher order terms have been truncated such that the equilibrium solution is cubic with respect to generalized displacements.

$$\begin{aligned} \frac{\partial \epsilon_m}{\partial q_i} &= \frac{1}{2}\left[\hat{h}^i_\alpha + q_k\left(\hat{g}^{ik}_m + \hat{g}^{ki}_m\right) + q_k q_s\left(\hat{f}^{iks}_\alpha + \hat{f}^{kis}_\alpha + \hat{f}^{ksi}_\alpha\right)\right. \\ &+ \left. 2q_k q_s q_r\left(l^{iksr}_\alpha + l^{ksir}_\alpha\right)\right] \end{aligned} \tag{4.37}$$

The contribution of strain energy to the equilibrium may be calculated (up to cubic in generalized displacements).

$$\begin{aligned} C_{mn}\bar{\epsilon}_n\frac{\partial \bar{\epsilon}_m}{\partial q_i} &= \frac{1}{2}C_{mn}\left[q_k\hat{h}^k_n\hat{h}^i_m + q_k q_s\left(\hat{h}^k_n\hat{g}^{is}_m + \hat{h}^k_n\hat{g}^{si}_m + \hat{h}^i_m\hat{g}^{sk}_n + \hat{h}^i_m\hat{g}^{ks}_n\right)\right. \\ &+ q_k q_s q_r\left(\hat{h}^k_n\hat{f}^{isr}_m + \hat{h}^k_n\hat{f}^{sir}_m + \hat{h}^k_n\hat{f}^{rsi}_m + \hat{g}^{ks}_n\hat{g}^{ir}_m + \hat{g}^{ks}_n\hat{g}^{ri}_m\right. \\ &+ \left.\left.\hat{f}^{ksr}_n\hat{h}^i_m\right)\right] \end{aligned} \tag{4.38}$$

These expressions may be combined to construct the equilibrium equation to determine the equilibrium configuration of the system.

$$\begin{aligned} 0 &= MR_{ml}\left[h^i_l\left(\Omega_{mn}\Omega_{nr}R_{rp}\chi_p + \dot{\Omega}_{mn}R_{np}\chi_p + \ddot{p}_m\right)\right. \\ &+ q_k\left\{2g^{ik}_l\ddot{p}_m + \left(R_{rp}\Omega_{nr}\Omega_{mn} + \dot{\Omega}_{mn}\right)\left(h^i_l\left(h^k_p + q_v g^{kv}\right)\right.\right. \\ &+ \left.\left.\left.2g^{ik}_l\left(\chi_p + q_s h^s_p + 2q_s q_v g^{sv}_p\right)\right)\right\}\right] \\ &+ \frac{1}{2}q_k R_{ml}\left(f^i_m\left(h^k_l + q_v g^{kv}_l\right) + f^k_m\left(h^i_l + 2q_v g^{iv}_l\right)\right) \\ &+ \frac{1}{2}C_{mn}\left[q_k\hat{h}^k_n\hat{h}^i_m + q_k q_s\left(\hat{h}^k_n\hat{g}^{is}_m + \hat{h}^k_n\hat{g}^{si}_m + \hat{h}^i_m\hat{g}^{sk}_n + \hat{h}^i_m\hat{g}^{ks}_n\right)\right. \\ &+ \left. q_k q_s q_r\left(\hat{h}^k_n\hat{f}^{isr}_m + \hat{h}^k_n\hat{f}^{sir}_m + \hat{h}^k_n\hat{f}^{rsi}_m + \hat{g}^{ks}_n\hat{g}^{ir}_m + \hat{g}^{ks}_n\hat{g}^{ri}_m + \hat{f}^{ksr}_n\hat{h}^i_m\right)\right] \end{aligned} \tag{4.39}$$

The following transformations may be employed to express the static equilibrium equation in a co-rotating frame.

$$\ddot{\hat{p}}_i = R_{ij}^T \ddot{p}_j, \qquad \hat{\Omega}_{il} = R_{ij}^T \Omega_{jk} R_{kl}, \qquad \dot{\hat{\Omega}}_{il} = R_{ij}^T \dot{\Omega}_{jk} R_{kl} \tag{4.40}$$

In a co-rotating frame, the static equilibrium equation is

$$\begin{aligned} 0 &= M\left[h_m^i\left(\hat{\Omega}_{mn}\hat{\Omega}_{np}\chi_p + \dot{\hat{\Omega}}_{mp}\chi_p + \ddot{\hat{p}}_m\right)\right. \\ &+ q_k\left\{2g_m^{ik}\ddot{\hat{p}}_m + \left(\hat{\Omega}_{mn}\hat{\Omega}_{np} + \dot{\hat{\Omega}}_{mp}\right)\left(h_m^i\left(h_p^k + q_v g^{kv}\right)\right.\right. \\ &+ \left.\left.\left. 2g_m^{ik}\left(\chi_p + q_s h_p^s + 2q_s q_v g_p^{sv}\right)\right)\right\}\Big] \\ &+ \frac{1}{2}q_k\left(f_m^i\left(h_m^k + q_v g_m^{kv}\right) + f_m^k\left(h_m^i + 2q_v g_m^{iv}\right)\right) \\ &+ \frac{1}{2}C_{mn}\left[q_k\hat{h}_n^k\hat{h}_m^i + q_k q_s\left(\hat{h}_n^k\hat{g}_m^{is} + \hat{h}_n^k\hat{g}_m^{si} + \hat{h}_m^i\hat{g}_n^{sk} + \hat{h}_m^i\hat{g}_n^{ks}\right)\right. \\ &+ \left. q_k q_s q_r\left(\hat{h}_n^k\hat{f}_m^{isr} + \hat{h}_n^k\hat{f}_m^{sir} + \hat{h}_n^k\hat{f}_m^{rsi} + \hat{g}_n^{ks}\hat{g}_m^{ir} + \hat{g}_n^{ks}\hat{g}_m^{ri} + \hat{f}_n^{ksr}\hat{h}_m^i\right)\right] \end{aligned} \tag{4.41}$$

The above expression is also useful for determining the load vector associated with the equations of motion (in a co-rotating frame) by simply setting $q_i = 0$.

$$\hat{\mathscr{F}}_i = -M\left[h_m^i\left(\hat{\Omega}_{mn}\hat{\Omega}_{np}\chi_p + \dot{\hat{\Omega}}_{mp}\chi_p + \ddot{\hat{p}}_m\right)\right] \tag{4.42}$$

IV.D.2. Linearized mass matrix

The direct linearization procedure results in the following definition of the mass matrix in terms of Lagrangian vectors

$$M_{ij} = M\tau_m^i\tau_m^j\big|_{(eq)} \tag{4.43}$$

Substitution of the quadratic modes description of the Lagrangian vectors yields

$$M_{ij} = MR_{ml}R_{mp}\left(h_l^i + 2\tilde{q}_k g_l^{ik}\right)\left(h_p^j + 2\tilde{q}_v g_p^{jv}\right) \tag{4.44}$$

Here, $\tilde{q}_k$ represents the solution associated with an equilibrium configuration that the equations of motion are being linearized about. Expansion of this expression results in the following linearized mass matrix:

$$M_{ij} = MR_{ml}R_{mp}\left[h_l^i h_p^j + 2\tilde{q}_k\left(h_l^i g_p^{jk} + h_p^j g_l^{ik} + 2\tilde{q}_v g_l^{ik} g_p^{jv}\right)\right] \tag{4.45}$$

In a co-rotating frame, the linearized mass matrix may be expressed as

$$\hat{M}_{ij} = M\left[h_m^i h_m^j + 2\tilde{q}_k\left(h_m^i g_m^{jk} + h_m^j g_m^{ik} + 2\tilde{q}_v g_m^{ik} g_m^{jv}\right)\right] \tag{4.46}$$

IV.D.3. Linearized Gyric matrix

The direct linearization procedure results in the following definition of the matrix F_{ij} in terms of Lagrangian vectors

$$F_{ij} = M\left(\frac{\partial \tau_m^j}{\partial q_i}\tau_m^0 + \tau_m^j \frac{\partial \tau_m^0}{\partial q_j}\right)\Bigg|_{(eq)} \tag{4.47}$$

The resulting expression for F_{ij} using the quadratic modes description is

$$\begin{aligned} F_{ij} &= MR_{ml}\left[\left(\Omega_{mn}R_{np}h_p^i h_l^j + 2g_l^{ij}\left(\dot{p}_m + \Omega_{ms}R_{sp}\chi_p\right)\right)\right. \\ &+ \left. 2\tilde{q}_k\left\{\Omega_{mn}R_{np}\left(h_p^i g_l^{jk} + h_l^j g_p^{ik} + g_l^{ij}h_p^k + \tilde{q}_r\left(g_p^{kr}g_l^{ij} + 2g_p^{ir}g_l^{jk}\right)\right)\right\}\right] \end{aligned} \tag{4.48}$$

The Gyric matrix G_{ij} is skew-symmetric in nature such that $G_{ij} = F_{ij} - F_{ji}$. Exploiting the symmetric nature of $g_m^{ij} = g_m^{ji}$ allows the Gyric matrix to be expressed as

$$\begin{aligned} G_{ij} &= M\Omega_{mn}R_{np}R_{ml}\left[h_p^i h_l^j - h_p^j h_l^i\right. \\ &+ \left. 2\tilde{q}_k\left\{h_p^i g_l^{jk} - h_p^j g_l^{ik} + h_l^j g_p^{ik} - h_l^i g_p^{jk} + 2\tilde{q}_r\left(g_p^{ir}g_l^{jk} - g_p^{jr}g_l^{ik}\right)\right\}\right] \end{aligned} \tag{4.49}$$

In a co-rotating frame, the linearized Gyric matrix may be expressed as

$$\begin{aligned}\hat{G}_{ij} &= M\hat{\Omega}_{mp}\left[h_p^i h_m^j - h_p^j h_m^i\right. \\ &+ \left. 2\tilde{q}_k\left\{h_p^i g_m^{jk} - h_p^j g_m^{ik} + h_m^j g_p^{ik} - h_m^i g_p^{jk} + 2\tilde{q}_r\left(g_p^{ir} g_m^{jk} - g_p^{jr} g_m^{ik}\right)\right\}\right]\end{aligned} \tag{4.50}$$

IV.D.4. Linearized stiffness matrix

The direct linearization procedure results in the following definition of the stiffness matrix in terms of $T_0(q)$, strain energy function $\mathscr{U}(q)$, and potential energy function $V(q)$.

$$K_{ij} = \frac{\partial^2 U}{\partial q_i \partial q_j} = \frac{\partial^2 V}{\partial q_i \partial q_j} + \frac{\partial^2 \mathscr{U}}{\partial q_i \partial q_j} - \frac{\partial^2 T_0}{\partial q_i \partial q_j} \tag{4.51}$$

Using the quadratic modes description of displacement results in the following second order partial differentiation of potential energy

$$\frac{\partial^2 V}{\partial q_i \partial q_j} = \frac{1}{2} R_{ml}\left[f_m^i h_l^j + f_m^j h_l^i + 2q_k\left(f_m^i g_l^{jk} + f_m^j g_l^{ik} + f_m^k g_l^{ij}\right)\right] \tag{4.52}$$

Second order differentiation of the strain energy function with respect to generalized displacements results in the following expression.

$$\frac{\partial^2 \mathscr{U}}{\partial q_i \partial q_j} = C_{mn}\left(\frac{\partial \epsilon_m}{\partial q_i}\frac{\partial \epsilon_n}{\partial q_j} + \epsilon_n \frac{\partial^2 \epsilon_m}{\partial q_i \partial q_j}\right) \tag{4.53}$$

The terms ϵ_m and $\frac{\partial \epsilon_m}{\partial q_i}$ were defined in a previous section. The second order differentiation of strain is defined below.

$$\begin{aligned}\frac{\partial^2 \epsilon_m}{\partial q_i \partial q_j} &= \frac{1}{2}\left[\hat{g}_m^{ij} + \hat{g}_m^{ji} + q_k\left(\hat{f}_m^{ijk} + \hat{f}_m^{jik} + \hat{f}_m^{jki} + \hat{f}_m^{ikj} + \hat{f}_m^{kij} + \hat{f}_m^{kji}\right)\right. \\ &+ \left. 2q_k q_s\left(2\hat{l}_m^{iksj} + 2\hat{l}_m^{jkis} + \hat{l}_m^{ijks} + \hat{l}_m^{ksij}\right)\right]\end{aligned} \tag{4.54}$$

Retaining terms up to second order in generalized degrees of freedom results in

$$\begin{aligned}
\frac{\partial^2 \mathscr{U}}{\partial q_i \partial q_j} &= \frac{1}{4} C_{mn} \Big[\hat{h}_m^i \hat{h}_n^j \\
&+ q_k \left\{ \left(\hat{g}_m^{ik} + \hat{g}_m^{ki} \right) \hat{h}_n^j + \left(\hat{g}_n^{jk} + \hat{g}_n^{kj} \right) \hat{h}_m^i + \left(\hat{g}_m^{ij} + \hat{g}_m^{ji} \right) \hat{h}_n^k \right\} \\
&+ q_k q_s \left\{ \left(\hat{g}_m^{ik} + \hat{g}_m^{ki} \right) \left(\hat{g}_n^{js} + \hat{g}_n^{sj} \right) + \left(\hat{f}_m^{iks} + \hat{f}_m^{kis} + \hat{f}_m^{ksi} \right) \hat{h}_n^j \right. \\
&+ \left(\hat{f}_n^{jks} + \hat{f}_n^{kjs} + \hat{f}_n^{ksj} \right) \hat{h}_m^i + \left(\hat{g}_m^{ij} + \hat{g}_m^{ji} \right) \hat{g}_n^{ks} \\
&+ \left. \left(\hat{f}_m^{ijs} + \hat{f}_m^{jis} + \hat{f}_m^{jsi} + \hat{f}_m^{isj} + \hat{f}_m^{sij} + \hat{f}_m^{sji} \right) \hat{h}_n^k \right\} \Big] \\
&+ H.O.T.
\end{aligned} \tag{4.55}$$

Second order differentiation of T_0 in terms of the Lagrangian vectors results in the following expression

$$\frac{\partial^2 T_0}{\partial q_i \partial q_j} = M \left(\frac{\partial \tau_m^0}{\partial q_i} \frac{\partial \tau_m^0}{\partial q_j} + \tau_m^0 \frac{\partial^2 \tau_m^0}{\partial q_i \partial q_j} \right) \tag{4.56}$$

Using the quadratic modes description of displacements results in the following second order differentiation of T_0

$$\begin{aligned}
\frac{\partial^2 T_0}{\partial q_i \partial q_j} &= M \Omega_{mn} R_{nl} \left[\left(\Omega_{ms} R_{sp} \left(h_l^i h_p^j + 2 g_l^{ij} \chi_p \right) + 2 g_l^{ij} \dot{p}_m \right) \right. \\
&+ \left. 2 q_k \Omega_{ms} R_{sp} \left\{ h_l^i g_p^{jk} + h_p^j g_l^{ik} + h_p^k g_l^{ij} + q_v \left(g_l^{ij} g_p^{kv} + 2 g_l^{ik} g_p^{jv} \right) \right\} \right]
\end{aligned} \tag{4.57}$$

Therefore, the linearized stiffness matrix expressed in terms of a quadratic modes representation of displacement is

$$
\begin{aligned}
K_{ij} &= \frac{1}{2}R_{ml}\left[f_m^i h_l^j + f_m^j h_l^i + 2\tilde{q}_k\left(f_m^i g_l^{jk} + f_m^j g_l^{ik} + f_m^k g_l^{ij}\right)\right] \\
&- M\Omega_{mn}R_{nl}\left[\left(\Omega_{ms}R_{sp}\left(h_l^i h_p^j + 2g_l^{ij}\chi_p\right) + 2g_l^{ij}\dot{p}_m\right)\right. \\
&+ \left. 2\tilde{q}_k\Omega_{ms}R_{sp}\left\{h_l^i g_p^{jk} + h_p^j g_l^{ik} + h_p^k g_l^{ij} + \tilde{q}_v\left(g_l^{ij}g_p^{kv} + 2g_l^{ik}g_p^{jv}\right)\right\}\right] \\
&+ \frac{1}{4}C_{mn}\left[\hat{h}_m^i\hat{h}_n^j + q_k\left\{\left(\hat{g}_m^{ik} + \hat{g}_m^{ki}\right)\hat{h}_n^j + \left(\hat{g}_n^{jk} + \hat{g}_n^{kj}\right)\hat{h}_m^i + \left(\hat{g}_m^{ij} + \hat{g}_m^{ji}\right)\hat{h}_n^k\right\}\right. \\
&+ q_k q_s\left\{\left(\hat{g}_m^{ik} + \hat{g}_m^{ki}\right)\left(\hat{g}_n^{js} + \hat{g}_n^{sj}\right) + \left(\hat{f}_m^{iks} + \hat{f}_m^{kis} + \hat{f}_m^{ksi}\right)\hat{h}_n^j\right. \\
&+ \left(\hat{f}_n^{jks} + \hat{f}_n^{kjs} + \hat{f}_n^{ksj}\right)\hat{h}_m^i + \left(\hat{g}_m^{ij} + \hat{g}_m^{ji}\right)\hat{g}_n^{ks} \\
&+ \left.\left.\left(\hat{f}_m^{ijs} + \hat{f}_m^{jis} + \hat{f}_m^{jsi} + \hat{f}_m^{isj} + \hat{f}_m^{sij} + \hat{f}_m^{sji}\right)\hat{h}_n^k\right\}\right]
\end{aligned}
\tag{4.58}
$$

In a co-rotating frame, the linearized stiffness matrix may be expressed as

$$
\begin{aligned}
\hat{K}_{ij} &= \frac{1}{2}\left[f_m^i h_l^j + f_m^j h_l^i + 2\tilde{q}_k\left(f_m^i g_l^{jk} + f_m^j g_l^{ik} + f_m^k g_l^{ij}\right)\right] \\
&- M\hat{\Omega}_{ml}\left[\left(\hat{\Omega}_{mp}\left(h_l^i h_p^j + 2g_l^{ij}\chi_p\right) + 2g_l^{ij}\dot{\hat{p}}_m\right)\right. \\
&+ \left. 2\tilde{q}_k\hat{\Omega}_{mp}\left\{h_l^i g_p^{jk} + h_p^j g_l^{ik} + h_p^k g_l^{ij} + \tilde{q}_v\left(g_l^{ij}g_p^{kv} + 2g_l^{ik}g_p^{jv}\right)\right\}\right] \\
&+ \frac{1}{4}C_{mn}\left[\hat{h}_m^i\hat{h}_n^j + q_k\left\{\left(\hat{g}_m^{ik} + \hat{g}_m^{ki}\right)\hat{h}_n^j + \left(\hat{g}_n^{jk} + \hat{g}_n^{kj}\right)\hat{h}_m^i + \left(\hat{g}_m^{ij} + \hat{g}_m^{ji}\right)\hat{h}_n^k\right\}\right. \\
&+ q_k q_s\left\{\left(\hat{g}_m^{ik} + \hat{g}_m^{ki}\right)\left(\hat{g}_n^{js} + \hat{g}_n^{sj}\right) + \left(\hat{f}_m^{iks} + \hat{f}_m^{kis} + \hat{f}_m^{ksi}\right)\hat{h}_n^j\right. \\
&+ \left(\hat{f}_n^{jks} + \hat{f}_n^{kjs} + \hat{f}_n^{ksj}\right)\hat{h}_m^i + \left(\hat{g}_m^{ij} + \hat{g}_m^{ji}\right)\hat{g}_n^{ks} \\
&+ \left.\left.\left(\hat{f}_m^{ijs} + \hat{f}_m^{jis} + \hat{f}_m^{jsi} + \hat{f}_m^{isj} + \hat{f}_m^{sij} + \hat{f}_m^{sji}\right)\hat{h}_n^k\right\}\right]
\end{aligned}
\tag{4.59}
$$

Note that this linearized stiffness matrix is an effective stiffness matrix, containing both structural stiffness terms and so called "spin softening" terms as a results of

rotational effects. The spin softening matrix $\hat{S}$ may be defined as

$$\begin{aligned}\hat{S}_{ij} &= M\hat{\Omega}_{ml}\left[\left(\hat{\Omega}_{mp}\left(h_l^i h_p^j + 2g_l^{ij}\chi_p\right) + 2g_l^{ij}\dot{\hat{p}}_m\right)\right. \\ &+ \left. 2\tilde{q}_k\hat{\Omega}_{mp}\left\{h_l^i g_p^{jk} + h_p^j g_l^{ik} + h_p^k g_l^{ij} + \tilde{q}_v\left(g_l^{ij}g_p^{kv} + 2g_l^{ik}g_p^{jv}\right)\right\}\right]\end{aligned} \tag{4.60}$$

Thus, the previous expression for the linearized stiffness matrix reduces to

$$\begin{aligned}\hat{K}_{ij} &= \frac{1}{2}\left[f_m^i h_l^j + f_m^j h_l^i + 2\tilde{q}_k\left(f_m^i g_l^{jk} + f_m^j g_l^{ik} + f_m^k g_l^{ij}\right)\right] \\ &+ \frac{1}{4}C_{mn}\left[\hat{h}_m^i\hat{h}_n^j + q_k\left\{\left(\hat{g}_m^{ik} + \hat{g}_m^{ki}\right)\hat{h}_n^j + \left(\hat{g}_n^{jk} + \hat{g}_n^{kj}\right)\hat{h}_m^i + \left(\hat{g}_m^{ij} + \hat{g}_m^{ji}\right)\hat{h}_n^k\right\}\right. \\ &+ q_k q_s\left\{\left(\hat{g}_m^{ik} + \hat{g}_m^{ki}\right)\left(\hat{g}_n^{js} + \hat{g}_n^{sj}\right) + \left(\hat{f}_m^{iks} + \hat{f}_m^{kis} + \hat{f}_m^{ksi}\right)\hat{h}_n^j\right. \\ &+ \left(\hat{f}_n^{jks} + \hat{f}_n^{kjs} + \hat{f}_n^{ksj}\right)\hat{h}_m^i + \left(\hat{g}_m^{ij} + \hat{g}_m^{ji}\right)\hat{g}_n^{ks} \\ &+ \left.\left.\left(\hat{f}_m^{ijs} + \hat{f}_m^{jis} + \hat{f}_m^{jsi} + \hat{f}_m^{isj} + \hat{f}_m^{sij} + \hat{f}_m^{sji}\right)\hat{h}_n^k\right\}\right] \\ &- \hat{S}_{ij}\end{aligned} \tag{4.61}$$

IV.D.5. Linearized $\dot{M}_{ij}$ matrix

The linearized $\dot{M}_{ij}$ matrix is calculated by considering the explicit time derivative of the linearized mass matrix. The following expression for the time derivative of the transformation matrix R_{ij} must be employed.

$$\dot{R}_{ij} = \Omega_{ik}R_{kj} \tag{4.62}$$

$$\dot{M}_{ij} = M\left(\Omega_{ms}R_{sl}R_{mp} + \Omega_{ms}R_{sp}R_{ml}\right)\left[h_l^i h_p^j + 2\tilde{q}_k\left(h_p^j g_l^{ik} + 2\tilde{q}_v g_l^{ik}g_p^{jv}\right)\right] \tag{4.63}$$

In a co-rotating frame, the linearized $\dot{M}_{ij}$ is expressed as

$$\begin{aligned}\dot{\hat{M}}_{ij} &= M\hat{\Omega}_{ml}\left[h_l^i h_m^j + 2\tilde{q}_k\left(h_m^j g_l^{ik} + 2\tilde{q}_v g_l^{ik}g_m^{jv}\right)\right] \\ &+ M\hat{\Omega}_{ml}\left[h_m^i h_l^j + 2\tilde{q}_k\left(h_l^j g_m^{ik} + 2\tilde{q}_v g_m^{ik}g_l^{jv}\right)\right]\end{aligned} \tag{4.64}$$

Exploiting the skew-symmetry of the spin tensor reveals that for the quadratic modes description of a deformable body in a floating and rotating reference frame $\dot{\hat{M}}_{ij}$ is zero.

$$\dot{\hat{M}}_{ij} = M\left(\hat{\Omega}_{ml} + \hat{\Omega}_{lm}\right)\left[h^i_m h^j_l + 2\tilde{q}_k\left(h^j_l g^{ik}_m + 2\tilde{q}_v g^{ik}_m g^{jv}_l\right)\right] = 0 \tag{4.65}$$

IV.D.6. Linearized Circulatory matrix

The linearized Circulatory matrix is calculated by considering the explicit time derivative of the linearized F_{ij} matrix.

$$\begin{aligned}
\dot{F}_{ij} &= M\left(\Omega_{ms}R_{sl}\right)\left[\left(\Omega_{mn}R_{np}h^i_p h^j_l + 2g^{ij}_l\left(\dot{p}_m + \Omega_{ms}R_{sp}\chi_p\right)\right)\right. \\
&+ \left. 2\tilde{q}_k\left\{\Omega_{mn}R_{np}\left(h^i_p g^{jk}_l + h^j_l g^{ik}_p + g^{ij}_l h^k_p + \tilde{q}_r\left(g^{kr}_p g^{ij}_l + 2g^{ir}_p g^{jk}_l\right)\right)\right\}\right] \\
&+ MR_{ml}\left[2g^{ij}_l\ddot{p}_m + \left(\dot{\Omega}_{mn}R_{np} + \Omega_{ms}\Omega_{sn}R_{np}\right)\left(h^i_p h^j_l + 2g^{ij}_l\chi_p\right)\right. \\
&+ 2\tilde{q}_k\left\{\left(\dot{\Omega}_{mn}R_{np} + \Omega_{ms}\Omega_{sn}R_{np}\right)\left(h^i_p g^{jk}_l + h^j_l g^{ik}_p + g^{ij}_l h^k_p\right.\right. \\
&+ \left.\left.\left. \tilde{q}_r\left(g^{kr}_p g^{ij}_l + 2g^{ir}_p g^{jk}_l\right)\right)\right\}\right]
\end{aligned} \tag{4.66}$$

In a co-rotating frame the linearized Circulatory matrix may be expressed as

$$\begin{aligned}
\dot{\hat{F}}_{ij} &= M\hat{\Omega}_{ml}\left[\left(\hat{\Omega}_{mp}h^i_p h^j_l + 2g^{ij}_l\left(\dot{\hat{p}}_m + \hat{\Omega}_{mp}\chi_p\right)\right)\right. \\
&+ \left. 2\tilde{q}_k\left\{\hat{\Omega}_{mp}\left(h^i_p g^{jk}_l + h^j_l g^{ik}_p + g^{ij}_l h^k_p + \tilde{q}_r\left(g^{kr}_p g^{ij}_l + 2g^{ir}_p g^{jk}_l\right)\right)\right\}\right] \\
&+ M\left[2g^{ij}_m\ddot{\hat{p}}_m + \left(\dot{\hat{\Omega}}_{mp} + \hat{\Omega}_{ms}\hat{\Omega}_{sp}\right)\left(h^i_p h^j_m + 2g^{ij}_m\chi_p\right)\right. \\
&+ 2\tilde{q}_k\left\{\left(\dot{\hat{\Omega}}_{mp} + \hat{\Omega}_{ms}\hat{\Omega}_{sp}\right)\left(h^i_p g^{jk}_m + h^j_m g^{ik}_p + g^{ij}_m h^k_p\right.\right. \\
&+ \left.\left.\left. \tilde{q}_r\left(g^{kr}_p g^{ij}_m + 2g^{ir}_p g^{jk}_m\right)\right)\right\}\right]
\end{aligned} \tag{4.67}$$

Further simplifications can be made due to the skew-symmetry of the spin tensor.

$$\begin{aligned}\dot{\hat{F}}_{ij} &= M\left[2\hat{\Omega}_{ml}g_l^{ij}\dot{\hat{p}}_m + 2g_m^{ij}\ddot{\hat{p}}_m + \dot{\hat{\Omega}}_{mp}\left(h_p^i h_m^j + 2g_m^{ij}\chi_p\right)\right] \\ &+ 2\tilde{q}_k\left\{\dot{\hat{\Omega}}_{mp}\left(h_p^i g_m^{jk} + h_m^j g_p^{ik} + g_m^{ij}h_p^k + \tilde{q}_r\left(g_p^{kr}g_m^{ij} + 2g_p^{ir}g_m^{jk}\right)\right)\right\}\Big]\end{aligned} \tag{4.68}$$

Thus, all relevant linearized coefficient matrices for direct linearization of a discrete rheonomic system have been described in a standard form using the kinematic representation from a method of quadratic modes.

IV.E. Simple examples of employing linearization procedures

The simple example considered by Segalman and Dohrmann [57] was analyzed using the techniques of a method of quadratic modes, direct linearization, and direct linearization via a method of quadratic modes. This example considers a beam with foreshortening effects and a tip mass. This simple, single degree of freedom problem accounts for the relevant details of a method of quadratic modes, but can also be analyzed using direct linearization and the newly developed direct linearization via a method of quadratic modes.

IV.E.1. Rotating beam

The case of a rotating beam with tip mass and foreshortening effects was considered using the approaches of a method of quadratic modes, direct linearization, and direct linearization via a method of quadratic modes.

IV.E.1.a. Development using a method of quadratic modes

For the aforementioned beam affixed to a rotating hub frame, the relevant terms for a method of quadratic modes are shown below.

$$\chi_L = \begin{bmatrix} L \\ 0 \end{bmatrix} \tag{4.69}$$

$$h_L^1 = \begin{bmatrix} 0 \\ L \end{bmatrix} \tag{4.70}$$

$$g_L^{11} = \begin{bmatrix} -\alpha L \\ 0 \end{bmatrix} \tag{4.71}$$

$$F_s = \begin{bmatrix} 0 \\ s\kappa L \end{bmatrix} \tag{4.72}$$

$$\hat{p} = \begin{bmatrix} 0 \\ 0 \end{bmatrix} \tag{4.73}$$

$$\left[\hat{\Omega}\right] = \begin{bmatrix} 0 & -\dot{\theta} \\ \dot{\theta} & 0 \end{bmatrix} \tag{4.74}$$

Employing Eq. 31 from [56] results in the following partial nonlinear equation of motion being generated.

$$mL^2\ddot{s} + \left[mL^2\dot{\theta}^2\left(2\alpha - 1\right) + \kappa L^2\right]s + 4m\alpha L^2 s\dot{s}\dot{\theta} + 2m\alpha L^2\ddot{\theta}s^2 = -mL^2\ddot{\theta} \tag{4.75}$$

Identification of the equilibrium configuration $s = 0$ allows linearization by inspection.

$$mL^2\ddot{s} + \left[mL^2\dot{\theta}^2\left(2\alpha - 1\right) + \kappa L^2\right]s = -mL^2\ddot{\theta} \tag{4.76}$$

IV.E.1.b. Development using direct linearization

For the aforementioned beam, the Lagrangian vectors to be utilized in a direct linearization procedure for a discrete rheonomic system are shown below.

$$\vec{\tau}_s = \begin{bmatrix} -2\alpha L s \\ L \end{bmatrix} \tag{4.77}$$

$$\vec{\tau}_0 = \begin{bmatrix} -L\dot{\theta}s \\ L\dot{\theta}\left(1 - s^2\alpha\right) \end{bmatrix} \tag{4.78}$$

The direct linearization procedure described by Parish [58] allows kinetic and potential energy functions to be constructed.

$$T_2(s,\dot{s}) = \frac{1}{2}mL^2\left(1 + 4\alpha^2 s^2\right)\dot{s}^2 \tag{4.79}$$

$$T_1(s,\dot{s}) = mL^2\left[2\alpha s^2 + \dot{\theta}\left(1 - \alpha s^2\right)\right]\dot{s} \tag{4.80}$$

$$U(s) = \frac{1}{2}\kappa L^2 s^2 - \frac{1}{2}m\left[L^2\dot{\theta}^2\left(1 - 2\alpha - \alpha^2 s^2\right)\right]s^2 - \frac{1}{2}mL^2\dot{\theta}^2 \tag{4.81}$$

With these energy functions constructed, the linearized coefficient matrices may be calculated about the equilibrium configuration $s = 0$.

$$[M] = mL^2\left[1 + 4\alpha^2 s_{eq}^2\right]|_{s_{eq}=0} = mL^2 \tag{4.82}$$

$$[\dot{M}] = 0 \tag{4.83}$$

$$[F] = mL^2\left[\left(4\alpha - 2\dot{\theta}\alpha\right)s_{eq}\right]|_{s_{eq}=0} = 0 \tag{4.84}$$

$$[\dot{F}] = \left[-2mL^2\dot{\theta}\alpha s_{eq}\right]|_{s_{eq}=0} = 0 \tag{4.85}$$

$$\begin{aligned} [K] &= \left[\kappa L^2 + mL^2\dot{\theta}^2(2\alpha - 1) + 6mL^2\alpha^2\dot{\theta}^2 s_{eq}^2\right]|_{s_{eq}=0} \\ &= \kappa L^2 + mL^2\dot{\theta}^2(2\alpha - 1) \end{aligned} \tag{4.86}$$

Thus, the resulting linearized equation of motion are

$$\begin{aligned} [M]\ddot{s} &+ \left([F]^T - [F] + [\dot{M}]\right)\dot{s} + \left([K] + [\dot{F}]\right)s = \\ mL^2\ddot{s} &+ \left[\kappa L^2 + mL^2\dot{\theta}^2\left(2\alpha - 1\right)\right]s = -mL^2\ddot{\theta} \end{aligned} \tag{4.87}$$

As expected, this is the same linearized equation of motion derived using a method of quadratic modes. Note that the procedures developed by Parish et al. do not directly yield a conservative force term for the system, but this may be recovered from the static equilibrium equation.

IV.E.1.c. Development using direct linearization via a method of quadratic modes

The previous quadratic modes representation along with the direct linearization via quadratic modes equations are used to derive equations of motion in a much more efficient manner. Note that the following force basis is introduced to be consistent with the direct linearization via quadratic modes approach.

$$\tilde{f} = \begin{bmatrix} 0 \\ \\ \kappa L \end{bmatrix} \tag{4.88}$$

Furthermore, the equilibrium solution $s = 0$ is considered. Use of Eq. 4.46 yields the following linearized mass matrix

$$\hat{M} = mL^2 \tag{4.89}$$

Use of Eqs. 4.50 and 4.68 shows $\hat{G} = 0$ and $\dot{\hat{F}} = 0$. Furthermore, use of Eq. 4.59 yields the following stiffness matrix.

$$\hat{K} = \kappa L^2 + mL^2\dot{\theta}^2\left(2\alpha - 1\right) \tag{4.90}$$

Use of Eq. 4.42 results in the following forcing term.

$$\hat{\mathscr{F}} = -mL^2\ddot{\theta} \tag{4.91}$$

As expected the resulting linearized equation of motion is consistent with previous development methods.

$$\hat{M}\ddot{s} + \hat{G}\dot{s} + \left(\hat{K} + \hat{\dot{F}}\right) s = mL^2\ddot{s} + \left[mL^2\dot{\theta}^2\left(2\alpha - 1\right) + \kappa L^2\right] s = -mL^2\ddot{\theta} \tag{4.92}$$

IV.E.2. Linearly accelerating beam

The case of a linearly accelerating beam with tip mass and foreshortening effects was considered using the approaches of a method of quadratic modes, direct linearization, and direct linearization via a method of quadratic modes.

IV.E.2.a. Development using a method of quadratic modes

For the aforementioned beam affixed to a linearly accelerating frame, the relevant terms for a method of quadratic modes are shown below.

$$\chi_L = \begin{bmatrix} L \\ 0 \end{bmatrix} \tag{4.93}$$

$$h_L^1 = \begin{bmatrix} 0 \\ L \end{bmatrix} \tag{4.94}$$

$$g_L^{11} = \begin{bmatrix} -\alpha L \\ 0 \end{bmatrix} \tag{4.95}$$

$$F_s = \begin{bmatrix} 0 \\ s\kappa L \end{bmatrix} \tag{4.96}$$

$$\hat{\ddot{p}} = \begin{bmatrix} a \\ 0 \end{bmatrix} \tag{4.97}$$

$$\left[\hat{\Omega}\right] = \begin{bmatrix} 0 & 0 \\ 0 & 0 \end{bmatrix} \tag{4.98}$$

Employing Eq. 31 from [56] results in the following equation of motion being generated for the equilibrium solution $s = 0$.

$$mL^2\ddot{s} + \left(\kappa L^2 - 2m\alpha aL\right) s = 0 \tag{4.99}$$

IV.E.2.b. Development using direct linearization

For the aforementioned beam, the Lagrangian vectors to be utilized in a direct linearization procedure for a discrete rheonomic system are shown below.

$$\vec{\tau}_s = \begin{bmatrix} -2\alpha Ls \\ L \end{bmatrix} \tag{4.100}$$

$$\vec{\tau}_0 = \begin{bmatrix} at \\ 0 \end{bmatrix} \tag{4.101}$$

The direct linearization procedure described by Parish [58] allows kinetic and potential energy functions to be constructed.

$$T_2(s, \dot{s}) = \frac{1}{2} m \left(4\alpha^2 L^2 s^2 + L^2\right) \dot{s}^2 \tag{4.102}$$

$$T_1(s, \dot{s}) = -2m\alpha aLts\dot{s} \tag{4.103}$$

$$U(s) = \frac{1}{2}\kappa L^2 s^2 - \frac{1}{2} m a^2 t^2 \tag{4.104}$$

With these energy functions constructed, the linearized coefficient matrices may be calculated about the equilibrium configuration $s = 0$.

$$[M] = mL^2 \left[1 + 4\alpha^2 s_{eq}^2\right] |_{s_{eq}=0} = mL^2 \tag{4.105}$$

$$[\dot{M}] = 0 \tag{4.106}$$

$$[F] = -2m\alpha Lat \tag{4.107}$$

$$[\dot{F}] = -2m\alpha La \tag{4.108}$$

$$[K] = \kappa L^2 \tag{4.109}$$

Thus, the resulting linearized equation of motion are

$$\begin{aligned} [M]\ddot{s} &+ \left([F]^T - [F] + [\dot{M}]\right)\dot{s} + \left([K] + [\dot{F}]\right)s = \\ mL^2\ddot{s} &+ \left(\kappa L^2 - 2m\alpha aL\right)s = 0 \end{aligned} \tag{4.110}$$

As expected, this is the same linearized equation of motion derived using a method of quadratic modes.

IV.E.2.c. Development using direct linearization via a method of quadratic modes

The previous quadratic modes representation along with the direct linearization via quadratic modes equations are used to derive equations of motion in a much more efficient manner. Again, the equilibrium solution $s = 0$ is considered. Use of Eq. 4.46 yields the following linearized mass coefficient

$$\hat{M} = mL^2 \tag{4.111}$$

Use of Eq. 4.50 yields $\hat{G} = 0$. Furthermore, use of Eq. 4.59 yields the following stiffness coefficient.

$$\hat{K} = \kappa L^2 \tag{4.112}$$

Use of Eq. 4.68 yields the following $\dot{\hat{F}}$.

$$\dot{\hat{F}} = -2m\alpha aL \tag{4.113}$$

Use of Eq. 4.42 results in the following forcing term.

$$\hat{\mathscr{F}} = 0 \tag{4.114}$$

As expected the resulting linearized equation of motion is consistent with those produced with other linearization procedures.

$$\hat{M}\ddot{s} + \hat{G}\dot{s} + \left(\hat{K} + \dot{\hat{F}}\right) s = mL^2\ddot{s} + \left(\kappa L^2 - 2m\alpha aL\right) s = 0 \tag{4.115}$$

IV.F. Conclusions

This chapter presented a new linearization procedure for discrete rheonomic systems known as direct linearization via a method of quadratic modes. The method adopted the efficiency of direct linearization methods, while overcoming some inherent drawbacks, such as the inability to characterize kinetic and potential energy functions in a standard form. The method of quadratic modes can provide a means to satisfy the desire for a standardized form of these energy functions. Using a well defined kinematic description allowed for energy functions to be developed in a well defined form. Thus, a direct linearization procedure has been developed that only requires a kinematic description of a system without a need for further processing by the analyst. Although the specific details of this approach may seem involved, the true power of the method lies in the well-defined form of system kinematics which may be implemented into software for automating the development of linearized rep-

resentation of dynamical systems. Finally, the various approaches were demonstrated on a simple, single degree of freedom system.

CHAPTER V

FINITE ELEMENT FORMULATION FOR A GYRIC BEAM IN A FLOATING FRAME

The direct linearization via a method of quadratic modes procedure presented in Chapter IV was employed to arrive at a finite element formulation for a Timoshenko beam with Gyric effects. This chapter first presents the quadratic modes representation for the deformation of a Timoshenko beam and employs the method presented in the previous chapter to develop finite element equations of motion for a Gyric beam in a floating frame. Use of modal methods to efficiently obtain a reduced order structural model of finite element assembly of beam elements is also discussed in this chapter.

V.A. Quadratic modes representation of Timoshenko beam displacements

The local deformation of a Timoshenko beam in a rotating frame is shown below

$$\vec{d}(x,t) = \begin{bmatrix} u_0(x,t) + \bar{z}\theta_y(x,t) - \bar{y}\theta_z(x,t) \\ v_0(x,t) - \bar{z}\theta_x(x,t) \\ w_0(x,t) + \bar{y}\theta_x(x,t) \end{bmatrix} \tag{5.1}$$

Now, consider an n-noded finite beam element. For the Timoshenko beam element there will be six degrees of freedom per node, such that

$$\vec{q^i} = [u_{0i}, v_{0i}, w_{0i}, \theta_{xi}, \theta_{yi}, \theta_{zi}]^T \tag{5.2}$$

Let the Galerkin approximation be employed such that the deformation of the beam are represented by shape functions and nodal values of displacements. For axial extension, the expression is

$$u_0(x,t) = \Sigma_{i=1}^{n} u_{0i}(t) N_{1i}(x) \tag{5.3}$$

The shape functions associated with the displacements $v_0(x,t)$, $w_0(x,t)$, $\theta_x(x,t)$, $\theta_y(x,t)$, and $\theta_z(x,t)$ are $N_2(x)$, $N_3(x)$, $N_4(x)$, $N_5(x)$, and $N_6(x)$ respectively. These shape functions may be of any order (ie. linear, quadratic, etc).

Thus, the quadratic modes representation of local beam deformations may be realized as

$$\vec{h}_j^1 = [N_{1j}(x), 0, 0]^T \tag{5.4}$$

$$\vec{h}_j^2 = [0, N_{2j}(x), 0]^T \tag{5.5}$$

$$\vec{h}_j^3 = [0, 0, N_{3j}(x)]^T \tag{5.6}$$

$$\vec{h}_j^4 = [0, -\bar{z}N_{4j}(x), \bar{y}N_{4j}(x)]^T \tag{5.7}$$

$$\vec{h}_j^5 = [\bar{z}N_{5j}(x), 0, 0]^T \tag{5.8}$$

$$\vec{h}_j^6 = [-\bar{y}N_{6j}(x), 0, 0]^T \tag{5.9}$$

The spin tensor Ω is specified as

$$[\Omega] = \begin{bmatrix} 0 & -\omega_z(t) & \omega_y(t) \\ \omega_z(t) & 0 & -\omega_x(t) \\ -\omega_y(t) & \omega_x(t) & 0 \end{bmatrix} \tag{5.10}$$

The translation of the floating frame is specified as

$$\vec{p} = \begin{bmatrix} p_1(t) \\ p_2(t) \\ p_3(t) \end{bmatrix} \tag{5.11}$$

V.B. Finite element mass matrix

Employing Eq. 4.46 allows the mass matrix to be written in a co-rotating frame. Furthemore, let the particle mass "M" in Eq. 4.46 be replaced by material point density ρ. The overall mass matrix will take the form of sub-matrices such that

$$[M] = \begin{bmatrix} M_{11} & M_{12} & M_{13} & M_{14} & M_{15} & M_{16} \\ M_{21} & M_{22} & M_{23} & M_{24} & M_{25} & M_{26} \\ M_{31} & M_{32} & M_{33} & M_{34} & M_{35} & M_{36} \\ M_{41} & M_{42} & M_{43} & M_{44} & M_{45} & M_{46} \\ M_{51} & M_{52} & M_{53} & M_{54} & M_{55} & M_{56} \\ M_{61} & M_{62} & M_{63} & M_{64} & M_{65} & M_{66} \end{bmatrix} \tag{5.12}$$

$$M_{11}^{ij} = \int_V (\rho N_{1i}(x) N_{1j}(x))\, dV \tag{5.13}$$

$$M_{12}^{ij} = M_{13}^{ij} = M_{14}^{ij} = 0 \tag{5.14}$$

$$M_{15}^{ij} = \int_V (\rho \bar{z} N_{1i}(x) N_{5j}(x))\, dV \tag{5.15}$$

$$M_{16}^{ij} = \int_V (-\rho \bar{y} N_{1i}(x) N_{6j}(x))\, dV \tag{5.16}$$

$$M_{22}^{ij} = \int_V (\rho N_{2i}(x) N_{2j}(x))\, dV \tag{5.17}$$

$$M_{23}^{ij} = M_{25}^{ij} = M_{26}^{ij} = 0 \tag{5.18}$$

$$M_{24}^{ij} = \int_V \left(-\rho \bar{z} N_{2i}(x) N_{4j}(x)\right) dV \tag{5.19}$$

$$M_{33}^{ij} = \int_V \left(\rho N_{3i}(x) N_{3j}(x)\right) dV \tag{5.20}$$

$$M_{34}^{ij} = \int_V \left(\rho \bar{y} N_{3i}(x) N_{4j}(x)\right) dV \tag{5.21}$$

$$M_{35}^{ij} = M_{36}^{ij} = 0 \tag{5.22}$$

$$M_{44}^{ij} = \int_V \left(\rho(\bar{y}^2 + \bar{z}^2) N_{4i}(x) N_{4j}(x)\right) dV \tag{5.23}$$

$$M_{45}^{ij} = M_{46}^{ij} = 0 \tag{5.24}$$

$$M_{55}^{ij} = \int_V \left(\rho \bar{z}^2 N_{5i}(x) N_{5j}(x)\right) dV \tag{5.25}$$

$$M_{56}^{ij} = \int_V \left(-\rho \bar{y} \bar{z} N_{5i}(x) N_{6j}(x)\right) dV \tag{5.26}$$

$$M_{66}^{ij} = \int_V \left(\rho \bar{y}^2 N_{6i}(x) N_{6j}(x)\right) dV \tag{5.27}$$

Note that the linearized mass matrix is symmetric ($M_{ij}^{kl} = M_{ji}^{lk}$). Next, let integration about the cross-section mass center be performed. To accomplish this, let $\bar{y}(x) = y(x) + y_{cm}(x)$ and $\bar{z}(x) = z(x) + z_{cm}(x)$. Integration about the cross-section mass center results in the following relations $\int_A \rho(x) y(x) dA = 0$, $\int_A \rho(x) z(x) dA = 0$. The following definitions are introduced with regards to cross-sectional mass properties.

$$\int_A \rho dA = \rho A(x) \tag{5.28}$$

$$\int_A \rho z(x)^2 dA = \rho I_{yy}(x) \tag{5.29}$$

$$\int_A \rho y(x)^2 dA = \rho I_{zz}(x) \tag{5.30}$$

$$\int_A \rho y(x) z(x) dA = \rho I_{yz}(x) \tag{5.31}$$

$$\int_A \rho \left(y(x)^2 + z(x)^2\right) dA = \rho J(x) \tag{5.32}$$

This allows the mass sub-matrices to be specified in terms of effective section properties, with integration along the length of the beam.

$$M_{11}^{ij} = \int_L (\rho A(x) N_{1i}(x) N_{1j}(x))\, dx \tag{5.33}$$

$$M_{12}^{ij} = M_{13}^{ij} = M_{14}^{ij} = 0 \tag{5.34}$$

$$M_{15}^{ij} = \int_L (\rho A(x) z_{cm}(x) N_{1i}(x) N_{5j}(x))\, dx \tag{5.35}$$

$$M_{16}^{ij} = \int_L (-\rho A(x) y_{cm}(x) N_{1i}(x) N_{6j}(x))\, dx \tag{5.36}$$

$$M_{22}^{ij} = \int_L (\rho A(x) N_{2i}(x) N_{2j}(x))\, dx \tag{5.37}$$

$$M_{23}^{ij} = M_{25}^{ij} = M_{26}^{ij} = 0 \tag{5.38}$$

$$M_{24}^{ij} = \int_L (-\rho A(x) z_{cm}(x) N_{2i}(x) N_{4j}(x))\, dx \tag{5.39}$$

$$M_{33}^{ij} = \int_L (\rho A(x) N_{3i}(x) N_{3j}(x))\, dx \tag{5.40}$$

$$M_{34}^{ij} = \int_L (\rho A(x) y_{cm}(x) N_{3i}(x) N_{4j}(x))\, dx \tag{5.41}$$

$$M_{35}^{ij} = M_{36}^{ij} = 0 \tag{5.42}$$

$$M_{44}^{ij} = \int_L \left(\bar{\rho J}(x) N_{4i}(x) N_{4j}(x)\right) dx \tag{5.43}$$

$$M_{45}^{ij} = M_{46}^{ij} = 0 \tag{5.44}$$

$$M_{55}^{ij} = \int_L \left(\rho \bar{I}_{yy}(x) N_{5i}(x) N_{5j}(x)\right) dx \tag{5.45}$$

$$M_{56}^{ij} = \int_L \left(-\bar{\rho I}_{yz}(x) N_{5i}(x) N_{6j}(x)\right) dx \tag{5.46}$$

$$M_{66}^{ij} = \int_L \left(\rho \bar{I}_{zz}(x) N_{6i}(x) N_{6j}(x)\right) dx \tag{5.47}$$

Such that

$$\rho \bar{I}_{yy}(x) = \rho I_{yy}(x) + \rho A(x) z_{cm}(x)^2 \tag{5.48}$$

$$\rho\bar{I}_{zz}(x) = \rho I_{zz}(x) + \rho A(x) y_{cm}(x)^2 \tag{5.49}$$

$$\rho\bar{I}_{yz}(x) = \rho I_{yz}(x) + \rho A(x) y_{cm}(x) z_{cm}(x) \tag{5.50}$$

$$\rho\bar{J}(x) = \rho J(x) + \rho A(x) \left(y_{cm}(x)^2 + z_{cm}(x)^2 \right) \tag{5.51}$$

V.C. Finite element spin softening matrix

Employing Eq. 4.60 allows for the finite element spin softening matrix to be formulated in a co-rotating frame. The procedure is similar to that for developing finite element mass matrix.

$$S_{11}^{ij} = \left(\omega_z^2 + \omega_y^2 \right) \int_L \left(\rho A(x) N_{1i}(x) N_{1j}(x) \right) dx \tag{5.52}$$

$$S_{12}^{ij} = -\omega_x \omega_y \int_L \left(\rho A(x) N_{1i}(x) N_{2j}(x) \right) dx \tag{5.53}$$

$$S_{13}^{ij} = -\omega_x \omega_z \int_L \left(\rho A(x) N_{1i}(x) N_{3j}(x) \right) dx \tag{5.54}$$

$$S_{14}^{ij} = \int_L \left(\rho A(x) \left(-y_{cm}(x) \omega_x \omega_z + z_{cm}(x) \omega_x \omega_y \right) N_{1i}(x) N_{4j}(x) \right) dx \tag{5.55}$$

$$S_{15}^{ij} = \left(\omega_y^2 + \omega_z^2 \right) \int_L \left(\rho A(x) z_{cm}(x) N_{1i}(x) N_{5j}(x) \right) dx \tag{5.56}$$

$$S_{16}^{ij} = -\left(\omega_y^2 + \omega_z^2 \right) \int_L \left(\rho A(x) y_{cm}(x) N_{1i}(x) N_{6j}(x) \right) dx \tag{5.57}$$

$$S_{22}^{ij} = \left(\omega_x^2 + \omega_z^2 \right) \int_L \left(\rho A(x) N_{2i}(x) N_{2j}(x) \right) dx \tag{5.58}$$

$$S_{23}^{ij} = -\omega_y \omega_z \int_L \left(\rho A(x) N_{2i}(x) N_{3j}(x) \right) dx \tag{5.59}$$

$$S_{24}^{ij} = -\int_L \left(\rho A(x) \left(z_{cm}(x) \left(\omega_x^2 + \omega_z^2 \right) + y_{cm}(x) \omega_y \omega_z \right) N_{2i}(x) N_{4j}(x) \right) dx \tag{5.60}$$

$$S_{25}^{ij} = -\omega_x \omega_y \int_L \left(\rho A(x) z_{cm}(x) N_{2i}(x) N_{5j}(x) \right) dx \tag{5.61}$$

$$S_{26}^{ij} = \omega_x \omega_y \int_L \left(\rho A(x) y_{cm}(x) N_{2i}(x) N_{6j}(x) \right) dx \tag{5.62}$$

$$S_{33}^{ij} = \left(\omega_x^2 + \omega_y^2\right) \int_L \left(\rho A(x) N_{3i}(x) N_{3j}(x)\right) dx \tag{5.63}$$

$$S_{34}^{ij} = \int_L \left(\rho A(x) \left(y_{cm}(x) \left(\omega_x^2 + \omega_y^2\right) + z_{cm}(x)\omega_y\omega_z\right) N_{3i}(x) N_{4j}(x)\right) dx \tag{5.64}$$

$$S_{35}^{ij} = -\int_L \left(\rho A(x) z_{cm}(x)\omega_x\omega_z N_{3i}(x) N_{5j}(x)\right) dx \tag{5.65}$$

$$S_{36}^{ij} = \int_L \left(\rho A(x) y_{cm}(x)\omega_x\omega_z N_{3i}(x) N_{6j}(x)\right) dx \tag{5.66}$$

$$\begin{aligned} S_{44}^{ij} &= \int_L \Big(\left(\rho \bar{I}_{yy}(x) \left(\omega_x^2 + \omega_z^2\right) + \rho \bar{I}_{zz}(x) \left(\omega_x^2 + \omega_y^2\right)\right. \\ &+ \left.\left(2\rho \bar{I}_{yz}(x)\omega_y\omega_z\right)\right) N_{4i}(x) N_{4j}(x)\Big) dx \end{aligned} \tag{5.67}$$

$$S_{45}^{ij} = \int_L \left(\left(-\rho \bar{I}_{yz}(x)\omega_x\omega_z + \rho \bar{I}_{yy}(x)\omega_x\omega_y\right) N_{4i}(x) N_{5j}(x)\right) dx \tag{5.68}$$

$$S_{46}^{ij} = \int_L \left(\left(-\rho \bar{I}_{yz}(x)\omega_x\omega_y + \rho \bar{I}_{zz}(x)\omega_x\omega_z\right) N_{4i}(x) N_{6j}(x)\right) dx \tag{5.69}$$

$$S_{55}^{ij} = \left(\omega_y^2 + \omega_z^2\right) \int_L \left(\rho \bar{I}_{yy}(x) N_{5i}(x) N_{5j}(x)\right) dx \tag{5.70}$$

$$S_{56}^{ij} = -\left(\omega_y^2 + \omega_z^2\right) \int_L \left(\rho \bar{I}_{yz}(x) N_{5i}(x) N_{6j}(x)\right) dx \tag{5.71}$$

$$S_{66}^{ij} = \left(\omega_y^2 + \omega_z^2\right) \int_L \left(\rho \bar{I}_{zz}(x) N_{6i}(x) N_{6j}(x)\right) dx \tag{5.72}$$

Note that the spin softening matrix is symmetric ($S_{ij}^{kl} = S_{ji}^{lk}$).

V.D. Finite element Gyric matrix

Employing Eq. 4.50 allows for the finite element Gyric matrix to be formulated in a co-rotating frame. The procedure is similar to that for developing finite element mass matrix.

$$G_{11}^{ij} = G_{22}^{ij} = G_{33}^{ij} = G_{44}^{ij} = G_{55}^{ij} = G_{66}^{ij} = 0 \tag{5.73}$$

$$G_{12}^{ij} = -2\omega_z \int_L \left(\rho A(x) N_{1i}(x) N_{2j}(x)\right) dx \tag{5.74}$$

$$G_{13}^{ij} = 2\omega_y \int_L (\rho A(x) N_{1i}(x) N_{3j}(x))\, dx \tag{5.75}$$

$$G_{14}^{ij} = 2 \int_L (\rho A(x) \left(\omega_y y_{cm}(x) + \omega_z z_{cm}(x)\right) N_{1i}(x) N_{3j}(x))\, dx \tag{5.76}$$

$$G_{15}^{ij} = G_{16}^{ij} = 0 \tag{5.77}$$

$$G_{23}^{ij} = -2\omega_x \int_L (\rho A(x) N_{2i}(x) N_{3j}(x))\, dx \tag{5.78}$$

$$G_{24}^{ij} = -2\omega_x \int_L (\rho A(x) y_{cm}(x) N_{2i}(x) N_{4j}(x))\, dx \tag{5.79}$$

$$G_{25}^{ij} = 2\omega_z \int_L (\rho A(x) z_{cm}(x) N_{2i}(x) N_{5j}(x))\, dx \tag{5.80}$$

$$G_{26}^{ij} = -2\omega_z \int_L (\rho A(x) y_{cm}(x) N_{2i}(x) N_{6j}(x))\, dx \tag{5.81}$$

$$G_{34}^{ij} = -2\omega_x \int_L (\rho A(x) z_{cm}(x) N_{3i}(x) N_{4j}(x))\, dx \tag{5.82}$$

$$G_{35}^{ij} = -2\omega_y \int_L (\rho A(x) z_{cm}(x) N_{3i}(x) N_{5j}(x))\, dx \tag{5.83}$$

$$G_{36}^{ij} = 2\omega_y \int_L (\rho A(x) y_{cm}(x) N_{3i}(x) N_{6j}(x))\, dx \tag{5.84}$$

$$G_{45}^{ij} = -2 \int_L \left(\left(\rho \bar{I}_{yy}(x)\omega_z + \rho \bar{I}_{yz}(x)\omega_y\right) N_{4i}(x) N_{5j}(x)\right) dx \tag{5.85}$$

$$G_{46}^{ij} = 2 \int_L \left(\left(\rho \bar{I}_{zz}(x)\omega_y + \rho \bar{I}_{yz}(x)\omega_z\right) N_{4i}(x) N_{6j}(x)\right) dx \tag{5.86}$$

$$G_{56}^{ij} = 0 \tag{5.87}$$

Note that the Gyric matrix is skew=symmetric ($G_{ij}^{kl} = -G_{ji}^{lk}$).

V.E. Finite element Circulatory matrix

Employing Eq. 4.67 allows for the finite element Circulatory matrix to be formulated in a co-rotating frame. The procedure is similar to that for developing finite element mass matrix.

$$H_{11}^{ij} = H_{22}^{ij} = H_{33}^{ij} = H_{44}^{ij} = H_{55}^{ij} = H_{66}^{ij} = 0 \tag{5.88}$$

$$H_{12}^{ij} = -\dot{\omega}_z \int_L (\rho A(x) N_{1i}(x) N_{2j}(x))\, dx \tag{5.89}$$

$$H_{13}^{ij} = \dot{\omega}_y \int_L (\rho A(x) N_{1i}(x) N_{3j}(x))\, dx \tag{5.90}$$

$$H_{14}^{ij} = \int_L (\rho A(x) \left(\dot{\omega}_y y_{cm}(x) + \dot{\omega}_z z_{cm}(x)\right) N_{1i}(x) N_{3j}(x))\, dx \tag{5.91}$$

$$H_{15}^{ij} = H_{16}^{ij} = 0 \tag{5.92}$$

$$H_{23}^{ij} = -\dot{\omega}_x \int_L (\rho A(x) N_{2i}(x) N_{3j}(x))\, dx \tag{5.93}$$

$$H_{24}^{ij} = -\dot{\omega}_x \int_L (\rho A(x) y_{cm}(x) N_{2i}(x) N_{4j}(x))\, dx \tag{5.94}$$

$$H_{25}^{ij} = \dot{\omega}_z \int_L (\rho A(x) z_{cm}(x) N_{2i}(x) N_{5j}(x))\, dx \tag{5.95}$$

$$H_{26}^{ij} = -\dot{\omega}_z \int_L (\rho A(x) y_{cm}(x) N_{2i}(x) N_{6j}(x))\, dx \tag{5.96}$$

$$H_{34}^{ij} = -\dot{\omega}_x \int_L (\rho A(x) z_{cm}(x) N_{3i}(x) N_{4j}(x))\, dx \tag{5.97}$$

$$H_{35}^{ij} = -\dot{\omega}_y \int_L (\rho A(x) z_{cm}(x) N_{3i}(x) N_{5j}(x))\, dx \tag{5.98}$$

$$H_{36}^{ij} = \dot{\omega}_y \int_L (\rho A(x) y_{cm}(x) N_{3i}(x) N_{6j}(x))\, dx \tag{5.99}$$

$$H_{45}^{ij} = -\int_L \left(\left(\rho \bar{I}_{yy}(x)\dot{\omega}_z + \rho \bar{I}_{yz}(x)\dot{\omega}_y\right) N_{4i}(x) N_{5j}(x)\right) dx \tag{5.100}$$

$$H_{46}^{ij} = \int_L \left(\left(\rho \bar{I}_{zz}(x)\dot{\omega}_y + \rho \bar{I}_{yz}(x)\dot{\omega}_z\right) N_{4i}(x) N_{6j}(x)\right) dx \tag{5.101}$$

$$H_{56}^{ij} = 0 \tag{5.102}$$

Note that the Circulatory matrix is skew-symmetric ($H_{ij}^{kl} = -H_{ji}^{lk}$).

V.F. Finite element stiffness matrix

Employing Eq. 4.59 allows for the finite element stiffness matrix to be formulated. Geometric nonlinearities give rise to "stress stiffening" or "geometric stiffness", which introduce nonlinear terms into the stiffness matrix.

First, consider the linear portion of the stiffness matrix. Note that integration of the cross-sectional area is considered to occur about the flexural axis. Therefore, terms such as $\int_A y dA = \int_A z dA = 0$. Furthermore, let some arbitrary coupling terms be introduced in the constitutive matrix C_{mn}, represented by the terms α_{mn}. This allows for a general stiffness matrix that can be adapted to the couplings that arise due to composite material layups. The following definitions are introduced with regards to cross-sectional mass properties.

$$\int_A E dA = EA(x) \tag{5.103}$$

$$\int_A G dA = GA(x) \tag{5.104}$$

$$\int_A E z(x)^2 dA = EI_{yy}(x) \tag{5.105}$$

$$\int_A E y(x)^2 dA = EI_{zz}(x) \tag{5.106}$$

$$\int_A E y(x) z(x) dA = EI_{yz}(x) \tag{5.107}$$

$$\int_A G\left(y(x)^2 + z(x)^2\right) dA = GJ(x) \tag{5.108}$$

$$[C] = \begin{bmatrix} E & 2\alpha_{12} & 2\alpha_{13} & 2\alpha_{14} & 2\alpha_{15} & 2\alpha_{16} \\ & E & 2\alpha_{23} & 2\alpha_{24} & 2\alpha_{25} & 2\alpha_{26} \\ & & E & 2\alpha_{34} & 2\alpha_{35} & 2\alpha_{36} \\ & & & 4G & 4\alpha_{45} & 4\alpha_{46} \\ & & & & 4G & 4\alpha_{56} \\ SYM & & & & & 4G \end{bmatrix} \tag{5.109}$$

$$K_{11}^{ij} = \int_L \left(EA(x) N_{1i}'(x) N_{1j}'(x) \right) dx \tag{5.110}$$

$$K_{12}^{ij} = \int_L \left(\alpha_{16} A(x) N_{1i}'(x) N_{2j}'(x) \right) dx \tag{5.111}$$

$$K_{13}^{ij} = \int_L \left(\alpha_{15} A(x) N_{1i}'(x) N_{3j}'(x) \right) dx \tag{5.112}$$

$$K_{15}^{ij} = -\int_L \left(\alpha_{15} A(x) N_{1i}'(x) N_{5j}(x) \right) dx \tag{5.113}$$

$$K_{16}^{ij} = \int_L \left(\alpha_{16} A(x) N_{1i}'(x) N_{6j}(x) \right) dx \tag{5.114}$$

$$K_{22}^{ij} = \int_L \left(GA(x) N_{2i}'(x) N_{2j}'(x) \right) dx \tag{5.115}$$

$$K_{23}^{ij} = \int_L \left(\alpha_{56} A(x) N_{2i}'(x) N_{3j}'(x) \right) dx \tag{5.116}$$

$$K_{25}^{ij} = -\int_L \left(\alpha_{56} A(x) N_{2i}'(x) N_{5j}(x) \right) dx \tag{5.117}$$

$$K_{26}^{ij} = -\int_L \left(GA(x) N_{2i}'(x) N_{6j}(x) \right) dx \tag{5.118}$$

$$K_{33}^{ij} = \int_L \left(GA(x) N_{3i}'(x) N_{3j}'(x) \right) dx \tag{5.119}$$

$$K_{35}^{ij} = \int_L \left(GA(x) N_{3i}'(x) N_{5j}(x) \right) dx \tag{5.120}$$

$$K_{36}^{ij} = \int_L \left(\alpha_{56} A(x) N_{3i}'(x) N_{6j}(x) \right) dx \tag{5.121}$$

$$K_{44}^{ij} = \int_L \left(GJ(x) N_{4i}'(x) N_{4j}'(x) \right) dx \tag{5.122}$$

$$K_{45}^{ij} = \int_L \left(\left(-\alpha_{15} I_{yz}(x) + \alpha_{16} I_{yy}(x) \right) N'_{4i}(x) N'_{5j}(x) \right) dx \tag{5.123}$$

$$K_{46}^{ij} = \int_L \left(\left(\alpha_{15} I_{zz}(x) - \alpha_{16} I_{yz}(x) \right) N'_{4i}(x) N'_{6j}(x) \right) dx \tag{5.124}$$

$$K_{55}^{ij} = \int_L \left(E I_{yy}(x) N'_{5i}(x) N'_{5j}(x) + GA(x) N_{5i}(x) N_{5j}(x) \right) dx \tag{5.125}$$

$$K_{56}^{ij} = -\int_L \left(E I_{yz}(x) N'_{5i}(x) N'_{6j}(x) + \alpha_{56} A(x) N_{5i}(x) N_{6j}(x) \right) dx \tag{5.126}$$

$$K_{66}^{ij} = \int_L \left(E I_{zz}(x) N'_{6i}(x) N'_{6j}(x) + GA(x) N_{6i}(x) N_{6j}(x) \right) dx \tag{5.127}$$

Let all other sub-matrices be zero, and the linear portion of the stiffness matrix be symmetric, $K_{ij}^{mn} = K_{ji}^{nm}$.

Geometric nonlinearities in the form of "stress stiffening" effects may also be included in the finite element formulation for the stiffness matrix. Using Eq. 4.59, and including first order nonlinearities in the stiffness matrix allows for the stiffening of the primary bending terms $\tilde{K}_{22}^{ij}$ and $\tilde{K}_{33}^{ij}$ to be formulated. A complete formulation of stress stiffening effects including stress stiffening as a result couplings may also be obtained through direct linearization via a method of quadratic modes.

The expressions for the "stress stiffening" matrices for uncoupled bending are shown below:

$$\tilde{K}_{22}^{ij} = \int_L \left(EAu'(x) N'_{2i}(x) N'_{2j}(x) \right) dx \tag{5.128}$$

$$\tilde{K}_{33}^{ij} = \int_L \left(EAu'(x) N'_{3i}(x) N'_{3j}(x) \right) dx \tag{5.129}$$

It should be noted that when incorporating geometric nonlinearities certain strain terms are often neglected due to their insignificance relative to other terms. This is likely to be formulation dependent and will not be discussed here.

V.G. Finite element load vector

Employing Eq. 4.42 allows for the finite element load vector to be formulated to account for floating frame effects. Other forces may be accounted for by considering virtual work and employing Galerkin approximations.

$$\begin{aligned} F_1^i &= \int_L \left(\rho A(x) \left(\left(\omega_y^2 + \omega_z^2\right) \chi_1(x) - \omega_x \left(\omega_y \chi_2(x) + \omega_z \chi_3(x)\right)\right.\right. \\ &+ \left.\left. \dot{\omega}_z \chi_2(x) - \dot{\omega}_y \chi_3(x) - \ddot{p}_1\right) N_{1i}(x)\right) dx \end{aligned} \tag{5.130}$$

$$\begin{aligned} F_2^i &= \int_L \left(\rho A(x) \left(\left(\omega_x^2 + \omega_z^2\right) \chi_2(x) - \omega_y \left(\omega_z \chi_3(x) + \omega_x \chi_1(x)\right)\right.\right. \\ &- \left.\left. \dot{\omega}_z \chi_1(x) + \dot{\omega}_x \chi_3(x) - \ddot{p}_2\right) N_{2i}(x)\right) dx \end{aligned} \tag{5.131}$$

$$\begin{aligned} F_3^i &= \int_L \left(\rho A(x) \left(\left(\omega_x^2 + \omega_y^2\right) \chi_3(x) - \omega_z \left(\omega_x \chi_1(x) + \omega_y \chi_2(x)\right)\right.\right. \\ &+ \left.\left. \dot{\omega}_y \chi_1(x) - \dot{\omega}_x \chi_2(x) - \ddot{p}_3\right) N_{3i}(x)\right) dx \end{aligned} \tag{5.132}$$

$$\begin{aligned} F_4^i &= \int_L \left(\rho A(x) \left[-z_{cm}(x) \left(\left(\omega_x^2 + \omega_z^2\right) \chi_2(x) - \omega_y \left(\omega_z \chi_3(x) + \omega_x \chi_1(x)\right)\right.\right.\right. \\ &- \left.\left. \dot{\omega}_z \chi_1(x) + \dot{\omega}_x \chi_3(x) - \ddot{p}_2\right) + y_{cm}(x) \left(\left(\omega_x^2 + \omega_y^2\right) \chi_3(x)\right. \\ &- \left.\left.\left. \omega_z \left(\omega_x \chi_1(x) + \omega_y \chi_2(x)\right) + \dot{\omega}_y \chi_1(x) - \dot{\omega}_x \chi_2(x) - \ddot{p}_3\right)\right] N_{4i}(x)\right) dx \end{aligned} \tag{5.133}$$

$$\begin{aligned} F_5^i &= \int_L \left(\rho A(x) z_{cm}(x) \left(\left(\omega_y^2 + \omega_z^2\right) \chi_1(x) - \omega_x \left(\omega_y \chi_2(x) + \omega_z \chi_3(x)\right)\right.\right. \\ &+ \left.\left. \dot{\omega}_z \chi_2(x) - \dot{\omega}_y \chi_3(x) - \ddot{p}_1\right) N_{5i}(x)\right) dx \end{aligned} \tag{5.134}$$

$$\begin{aligned} F_6^i &= -\int_L \left(\rho A(x) y_{cm}(x) \left(\left(\omega_y^2 + \omega_z^2\right) \chi_1(x) - \omega_x \left(\omega_y \chi_2(x) + \omega_z \chi_3(x)\right)\right.\right. \\ &+ \left.\left. \dot{\omega}_z \chi_2(x) - \dot{\omega}_y \chi_3(x) - \ddot{p}_1\right) N_{6i}(x)\right) dx \end{aligned} \tag{5.135}$$

V.H. Reduced order modeling of a finite element assembly

A finite element assembly can be composed of a relatively large number of degrees of freedom. For a finite element model with n degrees of freedom there will be n system modes, and thus for a high degree of freedom model, a number of higher modes are included. These higher modes are typically associated with high frequency and low amplitude motion, and may not be of substantial interest in determining the general response of a system. This can be especially true for preliminary design studies. Furthermore, for transient analysis explicit integration methods will have time steps dictated by higher frequency modes of a system, and it may be desirable to exclude higher frequency modes to relax time step size restrictions. For implicit time integration methods, which allow for unconditional stability regardless of time step size, only certain frequencies will be captured. Therefore, higher frequency system modes may not manifest themselves in the predicted motion history, and these can be excluded for efficiency gains.

The reduced order model will be constructed by employing modal methods [80] that consider modal analysis of the assembled linear structural mass and stiffness matrices as shown below

$$M\ddot{q}(t) + Kq(t) = F(t) \tag{5.136}$$

Assuming a solution form $q(t) = \phi \exp(i\omega t)$ allows the equation of motion to be cast into the form of the standard eigenvalue problem.

$$\left(M^{-1}K_{ij} - \omega^2 I\right)\phi = 0 \tag{5.137}$$

For an n degree of freedom system, n eigenvectors and the associated eigenvalues

represent mode frequencies and shapes respectively. An $n \times n$ modal matrix (Φ) that contains all the system modes may be created such that the columns are the eigenvectors/modes shapes (ϕ) of the system.

$$[\Phi] = [\phi_1 \mid \phi_2 \mid \phi_3 \mid ... \mid \phi_n \,] \tag{5.138}$$

Alternatively, a reduced $n \times m$ modal matrix ($\tilde{\Phi}$) may be constructed that only contains m selected system modes.

$$[\tilde{\Phi}] = [\phi_1 \mid \phi_2 \mid \phi_3 \mid ... \mid \phi_m \,] \tag{5.139}$$

The degrees of freedom may then be represented in a reduced modal space ($\eta(t)$) such that

$$q(t) = \tilde{\Phi}\eta(t) \tag{5.140}$$

This allows the aforementioned mass and stiffness matrices (as well as the force vector) to be transformed to this reduced modal space

$$\tilde{M} = \tilde{\Phi}^T M \tilde{\Phi} \tag{5.141}$$

$$\tilde{K} = \tilde{\Phi}^T K \tilde{\Phi} \tag{5.142}$$

Next, the Gyric, spin softening, and Circulatory assembled system matrices will be transformed to the reduced modal space. First, consider the assembled Gyric matrix which was developed in the previous section and shown to be linear in the angular velocities ω_x, ω_y, and ω_z. For efficiency, the angular velocities will be factored out of the expressions for the Gyric matrix, and only the coefficients (dependent on element geometry and mass properties) will be transformed. This may be conveniently done "on the fly" at run time using the method described below. Consider

the assembled Gyric matrix which is a function of angular velocities.

$$G = G\left(\omega_x, \omega_y, \omega_z\right) \tag{5.143}$$

Selective evaluation of the this expression with certain angular velocity components set to zero and other set to unity can yield the following coefficient matrices expressed in reduced modal space

$$\tilde{G}_x = \tilde{\Phi}^T G\left(1,0,0\right)\tilde{\Phi} \tag{5.144}$$

$$\tilde{G}_y = \tilde{\Phi}^T G\left(0,1,0\right)\tilde{\Phi} \tag{5.145}$$

$$\tilde{G}_z = \tilde{\Phi}^T G\left(0,0,1\right)\tilde{\Phi} \tag{5.146}$$

Thus, the reduced Gyric matrix may be efficiently calculated as

$$\tilde{G} = \omega_x \tilde{G}_x + \omega_y \tilde{G}_y + \omega_z \tilde{G}_z \tag{5.147}$$

The reduced spin-softening matrix may be calculated in a similar manner. As shown in the previous section, the assembled spin softening matrix is quadratic in angular velocities ω_x, ω_y, and ω_z. Consider the assembled spin-softening matrix which is a function of angular velocities.

$$S = S\left(\omega_x, \omega_y, \omega_z\right) \tag{5.148}$$

Again, selective evaluation of this expression with certain angular velocity components set to zero and other set to unity can yield the following coefficient matrices expressed in reduced modal space

$$\tilde{S}_{xx} = \tilde{\Phi}^T S\left(1,0,0\right)\tilde{\Phi} \tag{5.149}$$

$$\tilde{S}_{yy} = \tilde{\Phi}^T S\left(0,1,0\right)\tilde{\Phi} \tag{5.150}$$

$$\tilde{S}_{zz} = \tilde{\Phi}^T S\left(0,0,1\right)\tilde{\Phi} \tag{5.151}$$

$$\tilde{S}_{xy} = \tilde{\Phi}^T S\left(1,1,0\right)\tilde{\Phi} - \tilde{S}_{xx} - \tilde{S}_{yy} \tag{5.152}$$

$$\tilde{S}_{xz} = \tilde{\Phi}^T S\left(1,0,1\right)\tilde{\Phi} - \tilde{S}_{xx} - \tilde{S}_{zz} \tag{5.153}$$

$$\tilde{S}_{yz} = \tilde{\Phi}^T S\left(0,1,1\right)\tilde{\Phi} - \tilde{S}_{yy} - \tilde{S}_{zz} \tag{5.154}$$

Thus, the reduced spin-softening matrix may be efficiently calculated as

$$\tilde{S} = \omega_x^2\tilde{S}_{xx} + \omega_y^2\tilde{S}_{yy} + \omega_z^2\tilde{S}_{zz} + \omega_x\omega_y\tilde{S}_{xy} + \omega_x\omega_z\tilde{S}_{xz} + \omega_y\omega_z\tilde{S}_{yz} \tag{5.155}$$

The assembled Circulatory matrix takes on a similar for to the assembled Gyric matrix, but the expressions are linear in angular accelerations $\dot{\omega}_x$, $\dot{\omega}_y$, and $\dot{\omega}_z$. Consider the assembled Circulatory matrix which is a function of angular accelerations.

$$H = H\left(\dot{\omega}_x, \dot{\omega}_y, \dot{\omega}_z\right) \tag{5.156}$$

Selective evaluation of this expression with certain angular velocity components set to zero and other set to unity can yield the following coefficient matrices expressed in reduced modal space

$$\tilde{H}_x = \tilde{\Phi}^T H\left(1,0,0\right)\tilde{\Phi} \tag{5.157}$$

$$\tilde{H}_y = \tilde{\Phi}^T H\left(0,1,0\right)\tilde{\Phi} \tag{5.158}$$

$$\tilde{H}_z = \tilde{\Phi}^T H\left(0,0,1\right)\tilde{\Phi} \tag{5.159}$$

Thus, the reduced Circulatory matrix may be efficiently calculated as

$$\tilde{H} = \dot{\omega}_x\tilde{H}_x + \dot{\omega}_y\tilde{H}_y + \dot{\omega}_z\tilde{H}_z \tag{5.160}$$

Stress stiffening effects cannot be separated into linear coefficient matrices as was performed with the Gyric, spin softening, and Circulatory matrices. Therefore,

the assembled stress stiffening matrix is calculated in a conventional manner and transformed with the reduced modal matrix as shown below.

$$\tilde{K}_{ss} = \tilde{\Phi}^T K_{ss} \tilde{\Phi} \tag{5.161}$$

Finally, the reduced force vector may be calculated. The force vector may be decomposed into two parts: external forces and body forces. Body forces are due to the translational and angular acceleration and angular velocity of the floating frame the beam formulation has been derived in. The body forces are linear in translational accelerations $\ddot{p}_1$, $\ddot{p}_2$, and $\ddot{p}_3$ and angular accelerations $\dot{\omega}_x$, $\dot{\omega}_y$, and $\dot{\omega}_z$. As with the spin-softening matrix, the body forces are quadratic in angular velocities ω_x, ω_y, and ω_z. Consider the assembled body force vector which is a function of these velocities and accelerations.

$$F^{body} = F^{body}\left(\ddot{p}_1, \ddot{p}_2, \ddot{p}_3, \omega_x, \omega_y, \omega_z, \dot{\omega}_x, \dot{\omega}_y, \dot{\omega}_z\right) \tag{5.162}$$

Selective evaluation of the following expression with certain angular velocity components set to zero and others set to unity can yield the following coefficient vectors expressed in reduced modal space

$$\tilde{F}_{p1}^{body} = \tilde{\Phi}^T F\left(1,0,0,0,0,0,0,0,0\right) \tag{5.163}$$

$$\tilde{F}_{p2}^{body} = \tilde{\Phi}^T F\left(0,1,0,0,0,0,0,0,0\right) \tag{5.164}$$

$$\tilde{F}_{p3}^{body} = \tilde{\Phi}^T F\left(0,0,1,0,0,0,0,0,0\right) \tag{5.165}$$

$$\tilde{F}_{xx}^{body} = \tilde{\Phi}^T F\left(0,0,0,1,0,0,0,0,0\right) \tag{5.166}$$

$$\tilde{F}_{yy}^{body} = \tilde{\Phi}^T F\left(0,0,0,0,1,0,0,0,0\right) \tag{5.167}$$

$$\tilde{F}_{zz}^{body} = \tilde{\Phi}^T F\left(0,0,0,0,0,1,0,0,0\right) \tag{5.168}$$

$$\tilde{F}_{xy}^{body} = \tilde{\Phi}^T F\left(0,0,0,1,1,0,0,0,0\right) - \tilde{F}_{xx}^{body} - \tilde{F}_{yy}^{body} \tag{5.169}$$

$$\tilde{F}_{xz}^{body} = \tilde{\Phi}^T F\left(0,0,0,1,0,1,0,0,0\right) - \tilde{F}_{xx}^{body} - \tilde{F}_{zz}^{body} \tag{5.170}$$

$$\tilde{F}_{yz}^{body} = \tilde{\Phi}^T F\left(0,0,0,0,1,1,0,0,0\right) - \tilde{F}_{yy}^{body} - \tilde{F}_{zz}^{body} \tag{5.171}$$

$$\tilde{F}_{x}^{body} = \tilde{\Phi}^T F\left(0,0,0,0,0,0,1,0,0\right) \tag{5.172}$$

$$\tilde{F}_{y}^{body} = \tilde{\Phi}^T F\left(0,0,0,0,0,0,0,1,0\right) \tag{5.173}$$

$$\tilde{F}_{z}^{body} = \tilde{\Phi}^T F\left(0,0,0,0,0,0,0,0,1\right) \tag{5.174}$$

Thus, the reduced body force vector may be efficiently calculated as

$$\begin{aligned} \tilde{F}^{body} &= \ddot{p}_1 \tilde{F}_{p1}^{body} + \ddot{p}_2 \tilde{F}_{p2}^{body} + \ddot{p}_3 \tilde{F}_{p3}^{body} + \omega_x^2 \tilde{F}_{xx}^{body} + \omega_y^2 \tilde{F}_{yy}^{body} + \omega_z^2 \tilde{F}_{zz}^{body} \\ &+ \omega_x \omega_y \tilde{F}_{xy}^{body} + \omega_x \omega_z \tilde{F}_{xz}^{body} + \omega_y \omega_z \tilde{F}_{yz}^{body} + \dot{\omega}_x \tilde{F}_{x}^{body} + \dot{\omega}_y \tilde{F}_{y}^{body} \\ &+ \dot{\omega}_z \tilde{F}_{z}^{body} \end{aligned} \tag{5.175}$$

The external force vector $F(t)^{ext}$ may simply be transformed using the reduced modal matrix and the external and body force vectors may be added to arrive at the total reduced force vector for the system

$$\tilde{F}(t)^{ext} = \tilde{\Phi}^T F(t)^{ext} \tag{5.176}$$

$$\tilde{F}(t) = \tilde{F}(t)^{ext} + \tilde{F}^{body} \tag{5.177}$$

Finally, the total reduced order system may be expressed as

$$\tilde{M}\ddot{\eta}(t) + \tilde{G}\dot{\eta}(t) + \left[\tilde{K} + \tilde{K}_{ss} - \tilde{S} + \tilde{H}\right]\eta(t) = \tilde{F}(t) \tag{5.178}$$

This reduced order model formulation has been implemented into the Offshore Wind Energy Simulation Toolkit, and may serve as a means for analyst to create

efficient, configuration specific reduced order models for use in preliminary design studies.

V.I. Conclusions

This chapter employed the direct linearization via a method of quadratic modes procedure presented in Chapter IV to arrive at a finite element formulation for a Timoshenko beam with Gyric effects. First, the quadratic modes representation for the deformation of a Timoshenko beam was presented and the developed procedure was employed to formulate finite element equations of motion for a Gyric beam in a floating frame. Furthermore, this chapter also discussed the use of modal methods to obtain a reduced order model of a finite element assembly. Reduced order methods allow the dominant modes of a system to be captured while neglecting less dominant, higher order modes for efficiency gains.

CHAPTER VI

CONSIDERATIONS OF AEROELASTIC STABILITY IN WIND ENERGY SYSTEMS

This chapter presents considerations for aeroelastic stability in wind energy systems. The previous literature review in Chapter I discussed previous research in aeroelastic stability of both HAWT and VAWT configurations. Indeed, flutter was observed for a small-scale VAWT design [22] and may be an issue for very large HAWT blade designs [60]. This chapter begins with a brief discussion of an aeroelastic formulation that employs Theodorsen unsteady aerodynamic theory to consider classical flutter. The modification of a core structural dynamics modal analysis capability for aeroelastic effects is discussed, and a finite element formulation of two aeroelastic representations is presented.

The core structural dynamics capability in OWENS was leveraged to produce an aeroelastic design tool for HAWT blades and this tool is demonstrated on two HAWT configurations. Differences in analysis predictions amongst the various aeroelastic representations are also discussed, with different trends seen for utility scale and very large blade designs. These predictions are also contrasted with previous flutter estimates using a legacy design tool [59]. Furthermore, a transient analysis capability using a time-domain unsteady aerodynamics model is considered to serve as another means for aeroelastic stability predictions. Transient aeroelastic results are compared to modal analysis results using two different aeroelastic representations and similarities and differences are noted. Finally, it is noted that transient

aeroelastic capability may provide a more robust analysis approach for time varying aeroelastic systems.

VI.A. Aeroelastic formulation

The underlying structural structural dynamics formulation present in the OWENS toolkit, as discussed in Chapter II, was employed to consider aeroelastic analysis of wind energy systems. The fundamental formulation of a Gyric beam element formulated in Chapter V was employed with slight modification to include aeroelastic effects. Aerodynamic mass, damping, and stiffness matrices may be constructed using Theodorsen unsteady aerodynamic theory [23] and appended to a conventional structural dynamics formulation with Gyric effects. This modified formulation may then be employed to assess aerodynamic stability through modal analysis.

To summarize, the resulting system of equations for a rotating structure characterized by an assembly of Gyric beam elements is

$$M\ddot{q} + (C + G(\Omega))\,\dot{q} + (K(q) - S(\Omega))\,q = F_{cent}(\Omega) + F_{np} \tag{6.1}$$

Here, M, C, and $K(q)$ are mass, damping, and stiffness matrices typically associated with conventional structural dynamics analysis and q is a generalized degree of freedom vector. Overdots represent explicit time derivatives. Note that the stiffness matrix may contain nonlinearities such as the aforementioned "stress stiffening" phenomenon. $G(\Omega)$ is the skew-symmetric Gyric matrix that is linear in rotor speed (Ω) and $S(\Omega)$ is the spin-softening matrix that is quadratic in rotor speed. $F_{cent}(\Omega)$ is the centrifugal force vector that is also quadratic in rotor speed and F_{np} is a force vector due to non-potential forces such as aerodynamic loads.

Considering Theodorsen's unsteady airfoil theory [23] allows aerodynamic effects into a conventional structural dynamics analysis. The expressions for aerodynamic lift and moments are in terms of the flapping and twisting motion of a cross-section as shown below.

$$\begin{aligned} L &= \pi\rho_\infty b^2\left[\ddot{w} + V\dot{\theta} - ba\ddot{\theta}\right] \\ &+ 2\pi\rho_\infty VbC(k)\left[\dot{w} + V\theta + b\left(\frac{1}{2} - a\right)\dot{\theta}\right] \end{aligned} \tag{6.2}$$

$$\begin{aligned} M &= \pi\rho_\infty b^2\left[ba\ddot{w} - Vb\left(\frac{1}{2} - a\right)\dot{\theta} - b^2\left(\frac{1}{8} + a^2\right)\ddot{\theta}\right] \\ &+ 2\pi\rho_\infty Vb^2\left(a + \frac{1}{2}\right)C(k)\left[\dot{w} + V\theta + b\left(\frac{1}{2} - a\right)\dot{\theta}\right] \end{aligned} \tag{6.3}$$

Here, b is the semi-chord of an airfoil section, a is the location of the elastic axis in semi chord fractions aft of the half chord, V is the freestream velocity over the blade section, ρ_∞ is air density, and $C(k)$ is the complex valued Theodorsen function. The flapwise motion of the blade section is represented by $w(t)$ and the torsional motion of the section is represented by $\theta(t)$. These parameters are illustrated in Figure VI.1.

Here, $k = \frac{\omega b}{V}$ is a "reduced frequency" dependent on the oscillatory motion of the cross-section. The Theodorsen function $C(k)$ is complex in nature and models the amplitude reduction and phase lag in aerodynamic forcing as a result of unsteady effects due to shed vortices at the trailing edge of a blade section. While expressions for lift are traditionally expressed in terms of freestream velocity V, for a rotating turbine blade $V = r\Omega$ such that r is the spanwise distance along the blade from the hub axis. Thus, in addition to geometric and environmental parameters, the aerody-

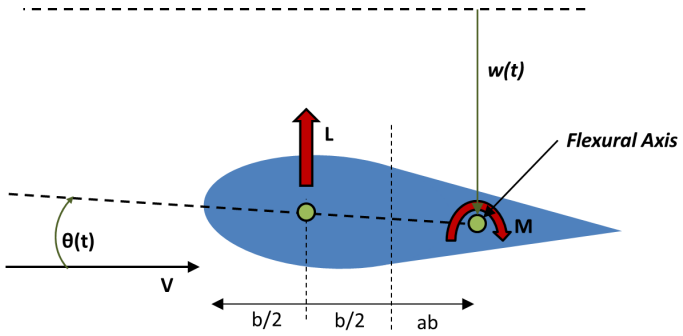

Figure VI.1. Schematic of two-dimensional airfoil section

namic loads are a function of generalized displacements, velocities, and accelerations as well as reduced frequency k. Aerodynamic mass, damping, and stiffness matrices can be formulated in a finite element formulation, and the aeroelastic second order system with rotational effects is shown below

$$[M + M_A]\,\ddot{q} + [C + G(\Omega) + C_A\,(\Omega, k)]\,\dot{q} + \tag{6.4}$$

$$[K(q) - S(\Omega) + K_A\,(\Omega, k)]\,q = F_{cent}(\Omega) + F_A(\Omega)$$

Here, $M_A(\Omega)$, $C_A(\Omega, k)$, $K_A(\Omega, k)$ are aerodynamic mass, damping, and stiffness matrices respectively. The vector $F_A(\Omega)$ represents aerodynamic forces due to nonelastic effects (ie. rigid angle of attack, manufactured blade twist, etc). This concludes the formulation overview for a finite beam element with rotational effects under aerodynamic loading consistent with Theodorsen's unsteady aerodynamic theory. Theodoresen's unsteady theory is formulated in the frequency domain making the above system ideal for modal analysis to assess the aeroelastic stability of the system. For modal analysis, only the left hand side of Eq. 6.4 needs to be considered.

The aforementioned expressions for unsteady lift and moment may be employed as non-potential forces in a finite element formulation through the use of Hamilton's

principle. As suggested in the previous section these terms may then be cast as effective aerodynamic mass, damping and stiffness matrices. Herein, two aerodynamic representations will be considered: a complex representation employed by Lobitz [59] and a real valued representation developed by Wright and Cooper [62] that may be adapted for finite element analysis.

VI.A.1. Finite element formulation for a complex valued aeroelastic representation

The approach employed by Lobitz [59] results in a relatively straight forward formulation in that the Theodorsen function $C(k)$ is simply treated as a complex valued parameter in the expressions for aerodynamic mass, damping and stiffness.

Employing the convention for labeling of finite element sub-matrices presented in Chapter V allows the following aerodynamic mass sub-matrices to be formulated. Note that in these expressions, a sign correction has been employed to account for the fact that Theodorsen aerodynamics considers downward flap positive and the structural dynamics formulation considers upward flap positive.

$$M_{A33}^{ij} = \pi\rho_\infty \int_V \left(b^2(x) N_{3i}(x) N_{3j}(x)\right) dV \tag{6.5}$$

$$M_{A34}^{ij} = M_{A43}^{ij} = -\pi\rho_\infty \int_V \left(b^3(x) a(x) N_{3i}(x) N_{4j}(x)\right) dV \tag{6.6}$$

$$M_{A44}^{ij} = -\pi\rho_\infty \int_V \left[b^4(x) \left(\frac{1}{8} + a^2(x)\right) N_{4i}(x) N_{4j}(x)\right] dV \tag{6.7}$$

Note that here, a variation in semichord $b(x)$ and elastic axis location $a(x)$ along the length of the element is considered. Similarly, the aerodynamic damping sub-matrices may be formulated as

$$C_{A33}^{ij} = 2\pi\rho_\infty \int_V \left[b(x) V(x) C(k) N_{3i}(x) N_{3j}(x)\right] dV \tag{6.8}$$

$$C_{A34}^{ij} = -\pi\rho_\infty \int_V \left[b^2(x)V(x) \left(1 + C(k) \left\{1 - 2a(x)\right\}\right) N_{3i}(x)N_{4j}(x) \right] dV \tag{6.9}$$

$$C_{A43}^{ij} = 2\pi\rho_\infty \int_V \left[b^2(x)V(x)C(k) \left(a(x) + \frac{1}{2}\right) \left(1 - 2a(x)\right) N_{4i}(x)N_{3j}(x) \right] dV \tag{6.10}$$

$$\begin{aligned} C_{A44}^{ij} &= -\pi\rho_\infty \int_V \left[b^3(x)V(x) \left(\left\{ a(x) + \frac{1}{2} \right\} C(k) \left\{1 - 2a(x)\right\} \right. \right. \\ &+ \left. \left. \left(a(x) - \frac{1}{2}\right) \right) N_{4i}(x)N_{4j}(x) \right] dV \end{aligned} \tag{6.11}$$

The free stream velocity $V(x)$ is also allowed to vary along the element length since velocity is related to rotor speed and the position of a point in the rotating hub frame. Finally, the aerodynamic stiffness sub-matrices may be formulated as

$$K_{A34}^{ij} = -2\pi\rho_\infty \int_V \left[b(x)V^2(x)C(k)N_{3i}(x)N_{4j}(x) \right] dV \tag{6.12}$$

$$K_{A44}^{ij} = -2\pi\rho_\infty \int_V \left[b^2(x)V^2(x) \left(a(x) + \frac{1}{2}\right) C(k)N_{4i}(x)N_{4j}(x) \right] dV \tag{6.13}$$

These aerodynamic matrices are conveniently implemented alongside a conventional structural dynamics finite element implementation. The representation, however, is complex in nature due to the complex Theodorsen function. A complex eigenvalue solver may be employed, but as will be shown there is still some ambiguity in the physical meaning of these eigenvalues and their relation to the aeroelastic stability properties of a system. Indeed, for conventional, real-valued structural dynamics systems frequency and damping is readily extracted from the eigenvalues of the state space representation of the system. The eigenvalues of conventional, real valued structural dynamic systems occur in complex conjugate pairs. As shown in Appendix B, however, complex systems in general do not result in complex conjugate eigenvalue pairs and the physical meaning of these eigenvalues is unclear. Thus, although a complex aeroelastic representation has a fairly straightforward formulation

the resulting system does not lend itself well to conventional structural dynamics analysis techniques and associated insights/experience with these systems.

VI.A.2. Finite element formulation for a real valued aeroelastic representation

An alternative aeroelastic representation may be considered as shown by Wright and Cooper [62]. The previous complex valued aeroelastic representation did not consider the form of the complex valued Theodorsen function $C(k)$. This complex function was simply calculated and employed in a finite element formulation as a complex valued parameter. One may, however, realize this function in terms of real valued functions $F(k)$ and $G(k)$ such that

$$C(k) = F(k) + iG(k) \tag{6.14}$$

Thus, this form can be employed in the expression of non-potential work in Hamilton's principle and imaginary values can be "absorbed" in the quasi-velocity terms that result from assumed oscillatory motion. That is

$$\theta(t) = \theta_0 e^{i\omega t} \tag{6.15}$$

$$\dot{\theta}(t) = i\omega\theta_0 e^{i\omega t} \tag{6.16}$$

$$\ddot{\theta}(t) = -\omega^2\theta_0 e^{i\omega t} \tag{6.17}$$

As demonstrated by Wright and Cooper [62], the unsteady lift function shown in Eq. 6.2 may be re-cast by introducing the assumed oscillatory motion of plunging and pitching along with the definition of the reduced frequency (k).

$$L = \rho V^2 \left(L_w w + L_{\dot{w}} \frac{b\dot{w}}{V} + L_\theta b\theta + L_{\dot{\theta}} \frac{b^2\dot{\theta}}{V} \right) \tag{6.18}$$

Such that

$$L_w = 2\pi\left(-\frac{k^2}{2} - G(k)k\right) \tag{6.19}$$

$$L_{\dot{w}} = 2\pi F(k) \tag{6.20}$$

$$L_\theta = 2\pi\left[\frac{k^2 a}{2} + F(k) - G(k)k\left(\frac{1}{2} - a\right)\right] \tag{6.21}$$

$$L_{\dot{\theta}} = 2\pi\left[\frac{1}{2} + F(k)\left(\frac{1}{2} - a\right) + \frac{G(k)}{k}\right] \tag{6.22}$$

Similarly, the unsteady pitching moment shown in Eq. 6.3 can be expressed as

$$M = \rho V^2\left(M_w b w + M_{\dot{w}}\frac{b^2\dot{w}}{V} + M_\theta b^2\theta + M_{\dot{\theta}}\frac{b^3\dot{\theta}}{V}\right) \tag{6.23}$$

Such that

$$M_w = 2\pi\left[-\frac{k^2 a}{2} - G(k)\left(a + \frac{1}{2}\right)k\right] \tag{6.24}$$

$$M_{\dot{w}} = 2\pi\left(a + \frac{1}{2}\right)F(k) \tag{6.25}$$

$$M_\theta = 2\pi\left[\frac{k^2}{2}\left(\frac{1}{8} + a^2\right) + F(k)\left(a + \frac{1}{2}\right) - G(k)k\left(a + \frac{1}{2}\right)\left(\frac{1}{2} - a\right)\right] \tag{6.26}$$

$$M_{\dot{\theta}} = 2\pi\left[-\frac{k}{2}\left(\frac{1}{2} - a\right) + F(k)k\left(a + \frac{1}{2}\right)\left(\frac{1}{2} - a\right) + \frac{G(k)}{k}\left(a + \frac{1}{2}\right)\right] \tag{6.27}$$

A more thorough development of this approach is detailed by Wright and Cooper [62] and can be employed in a finite element representation. The resulting system is a completely real valued representation, that is more amenable to conventional structural dynamics analysis. That is, the system retains complex conjugate eigenvalue pairs and conventional frequency and damping extraction routines can be employed to extract physically meaningful frequency and damping values for the aeroelastic system.

The associated finite element matrices for aerodynamic damping and stiffness can be obtained using the same approach as in the last section. One can note

that the introduction of assumed oscillatory motion manifests acceleration effects as terms in the aerodynamic stiffness matrix. Thus, for this representation, there is no aerodynamic mass matrix.

$$M_A = 0 \tag{6.28}$$

Real valued aerodynamic damping sub-matrices may be formulated as

$$C_{A33}^{ij} = \rho_\infty \int_V \left(L_{\dot{w}}(x) b(x) V(x) N_{3i}(x) N_{3j}(x)\right) dV \tag{6.29}$$

$$C_{A34}^{ij} = -\rho_\infty \int_V \left(L_{\dot{\theta}}(x) b^2(x) V(x) N_{3i}(x) N_{4j}(x)\right) dV \tag{6.30}$$

$$C_{A43}^{ij} = \rho_\infty \int_V \left(M_{\dot{w}}(x) b^2(x) V(x) N_{4i}(x) N_{3j}(x)\right) dV \tag{6.31}$$

$$C_{A44}^{ij} = -\rho_\infty \int_V \left(M_{\dot{\theta}}(x) b^3(x) V(x) N_{4i}(x) N_{4j}(x)\right) dV \tag{6.32}$$

Similarly, the real valued aerodynamic stiffness sub-matrices may formulated as

$$K_{A33}^{ij} = \rho_\infty \int_V \left(L_w(x) V^2(x) N_{3i}(x) N_{3j}(x)\right) dV \tag{6.33}$$

$$K_{A34}^{ij} = -\rho_\infty \int_V \left(L_\theta(x) b(x) V^2(x) N_{3i}(x) N_{4j}(x)\right) dV \tag{6.34}$$

$$K_{A43}^{ij} = \rho_\infty \int_V \left(M_w(x) b(x) V^2(x) N_{4i}(x) N_{3j}(x)\right) dV \tag{6.35}$$

$$K_{A44}^{ij} = -\rho_\infty \int_V \left(M_{\dot{\theta}}(x) b^2(x) V^2(x) N_{4i}(x) N_{4j}(x)\right) dV \tag{6.36}$$

In contrast to the complex valued representation, this aeroelastic representation is analogous to a conventional, real valued structural dynamics representation. As such, existing techniques for extracting physical information such as frequency, damping, and mode shape information from system eigenvalues may be employed.

VI.B. BLade Aeroelastic Stability Tool (BLAST)

The BLade Aeroelastic Stability Tool (BLAST) is an offspring of the OWENS modular framework. BLAST is a finite element design tool capable of predicting aeroelastic stability characteristics of HAWT blades with arbitrary geometry and material composition. The modular design of the OWENS toolkit allowed the core structural dynamics analysis capability to be extracted, enhanced with the aforementioned aeroelastic formulations, and employed as a design tool for HAWT blades. BLAST may be viewed as a more robust extension of previous aeroelastic design tools for HAWT blades such as the Sandia legacy flutter tool developed by Lobitz [59]. BLAST is programmed in MATLAB, which allows the software to be extremely portable and integrated with the SNL blade design tool NuMAD [79].

The bulk of the modeling and implementation of BLAST was supported by the OWENS toolkit, and a relatively simple mesh generator was created for discretizing HAWT blade configurations from the popular NREL FAST [70] file format was created. This requires the calculation of effective properties of a blade design be calculated using pre-processors such as effective section properties of a blade design (BPE [54], PreComp [55], VABS [53], etc.). Lastly, BLAST was enhanced with automated iterative analysis procedures for performing aeroelastic stability analysis as well as features for visualizing frequency and damping trends across a range of rotor speeds and associated mode shapes. The following subsections present analysis procedures and a demonstration of BLAST using both complex and real valued representations. The differences between predictions obtained using the two representations are also discussed.

VI.B.1. Analysis procedures

Inspection of Eq. 6.4 shows the coefficient matrices of the second order system are dependent on rotor speed Ω, modal reduced frequency k, and generalized displacements q. Rotor speed may be specified as an operating condition similar to velocity in a traditional flutter analysis for an aircraft. Furthermore, the equations of motion may be linearized about the equilibrium configuration corresponding to the specified rotor speed. This equilibrium configuration is determined by solving the nonlinear static elasticity equation of motion shown below.

$$[K(q) - S(\Omega)]\, q = F_{cent}(\Omega) \tag{6.37}$$

With the equilibrium configuration q_{eq} determined, a linearized system may be analyzed through pre-stressed modal analysis.

$$[M + M_A]\, \ddot{q} + [C + G(\Omega) + C_A\,(\Omega, k)]\, \dot{q} + \tag{6.38}$$

$$[K(q_{eq}) - S(\Omega) + K_A\,(\Omega, k)]\, q = 0$$

Unfortunately, the linearized equations of motion are still a function of ω which will be unknown until modal analysis is performed. Thus, an iterative procedure termed "p-k iteration" in the literature [61] is employed to converge between a "guess" frequency, and a "predicted" frequency for the system under aeroelastic effects.

The following steps outline the procedure for a flutter analysis as implemented into BLAST:

1. Select a rotor speed (Ω) of interest.

2. Perform a static nonlinear analysis under centrifugal loads at rotor speed Ω to obtain an equilibrium solution.

3. Provide a guess modal frequency and predict the modal response of the system.

4. Select a mode of interest and update the guess modal frequency used in the previous step.

5. Repeat steps 3 and 4 until the guess and predicted frequencies for the mode of interest are converged.

6. Select the next mode of interest and repeat steps 3 and 4 until all modes of interest have been explored for the rotor speed specified in step 2.

7. Repeat steps 1 through 6 for all rotor speeds of interest.

8. Examine frequency and damping trends for the system across rotor speeds for potential aeroelastic instabilities.

VI.B.2. Demonstration of BLAST

BLAST was used to investigate two different blade configurations. The first blade considered was a 33 meter "utility scale" blade designed for used on a 1.5MW turbine. The second was a very large 100 meter turbine design. These blades allow one to consider a conventional blade and the current trend of increasing length and flexibility in modern turbine blade designs. The flutter speed of each blade is predicted using BLAST while employing both complex and real valued representations.

VI.B.2.a. Flutter analysis of the WindPACT 1.5MW blade

The 33 meter NREL WindPACT 1.5MW blade [84] was analyzed using BLAST as well as by Lobitz [59]. This blade has a designed maximum rotor speed of 20.5

RPM. Lobitz predicted a flutter speed of 43.4 RPM using the legacy flutter tool. In a comparative effort, BLAST was employed to conduct on a flutter analysis of the WindPACT 1.5MW blade.

The automated nature of BLAST allowed a larger number of lower system modes to be considered over a range of rotor speeds. Figure VI.2 shows the frequency and damping ratios of a number of modes from 0 to 45 RPM rotor speed using the complex aeroelastic representation in BLAST, and interesting behavior is observed for a number of modes. The analysis revealed potential instabilities (negative effective damping) on-setting at rotor speeds of 26.6, 36.1, and 42.3 RPM. The 26.6 and 36.1 RPM potential flutter speeds have a "soft" flutter trend or relatively shallow cross over to negative damping at the predicted flutter speed indicating structural damping will likely delay the onset of flutter for these modes. Furthermore, these "softer" modes are typically higher modes of the system. Nevertheless, "hard" flutter or a steep crossover to negative damping is observed for the 42.3 RPM flutter modes. The 42.3 RPM rotor speed is within 2.5% of that predicted by Lobitz. Thus, good agreement is seen considering differences in modeling approaches between the two analysis tools, which both employ the complex aeroelastic representation.

Figure VI.3 shows the mode shape associated with the predicted flutter mode at 42.3 RPM. Analysis of the aeroelastic system using a state space representation yields complex valued mode shapes. Mode shapes are visualized by examining the real component (0 degree phase mode shape) and the imaginary component (90 degree phase mode shape). The mode shape consists of a first torsional component, 2nd flapwise component, and 2nd edgewise component. The torsional and flapwise

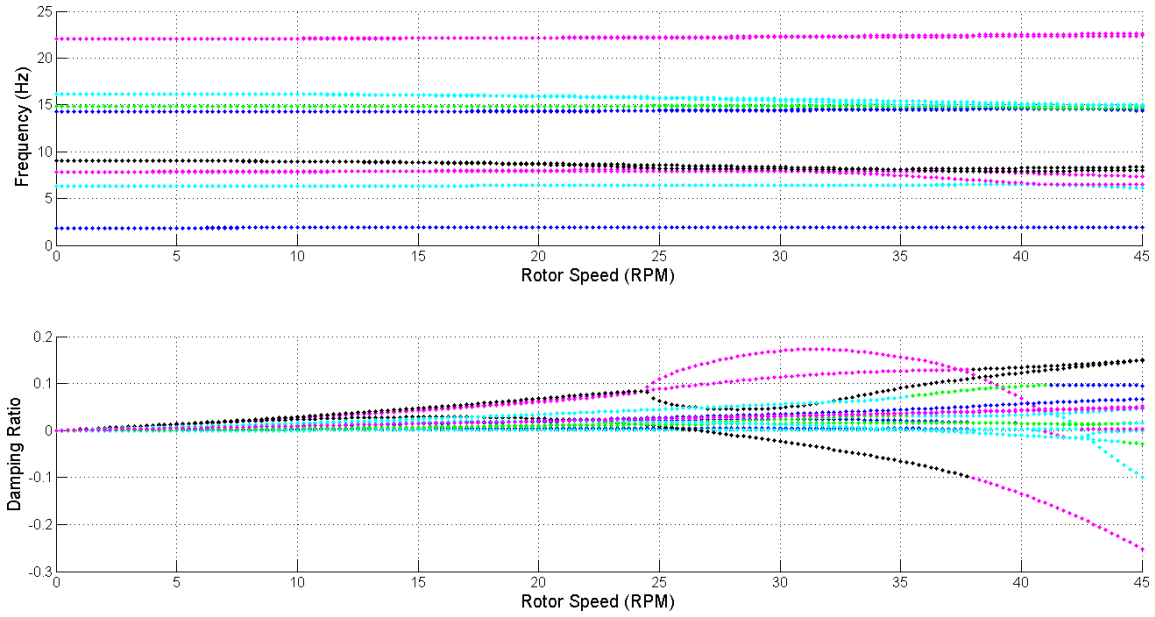

Figure VI.2. Frequency and damping ratio vs. rotor speed complex valued BLAST predictions for WindPACT 1.5MW blade

modes are characteristic of flutter. The second edgewise component results from the coupling of the flutter mode with an edgewise mode, but can also be attributed to structural twist and couplings arising from the Coriolis rotational effects.

The Wind PACT 1.5MW blade was also analyzed using a real valued aeroelastic representation in BLAST, and the frequency and damping versus rotor speed trends are shown in Figure VI.4. As expected, the eigenvalues of this system occur in complex conjugate pairs. Furthermore, "hard" flutter onset is observed at a rotor speed of 40.6 RPM (a 4% difference relative to the 42.3 RPM "hard" flutter mode observed for the BLAST analysis with a complex valued representation). The mode shape associated with this flutter mode is shown in Figure VI.5. The shape is a bit different than that predicted from the complex valued aeroelastic representation(Figure VI.3), but is indicative of a flutter mode with a 2nd flapwise component, and a first torsional

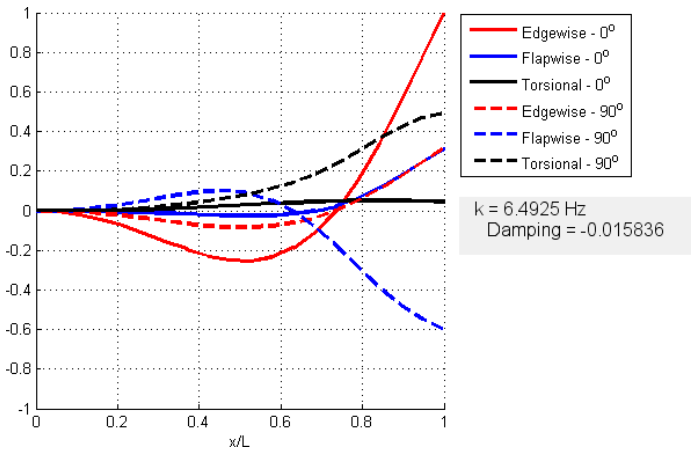

Figure VI.3. Flutter mode shape for the WindPACT 1.5MW blade predicted using complex valued BLAST

component. It is notable that the "softer" flutter modes apparent in predictions from the complex aeroelastic representation do not manifest themselves in the real valued predictions. Furthermore, the complex valued representation predicts a flutter mode shape with primarily edgewise motion which is not typically characteristic of flutter. The real value representation, however, does have a more conventional flutter mode shape with some edgewise component due to structural/gyroscopic couplings.

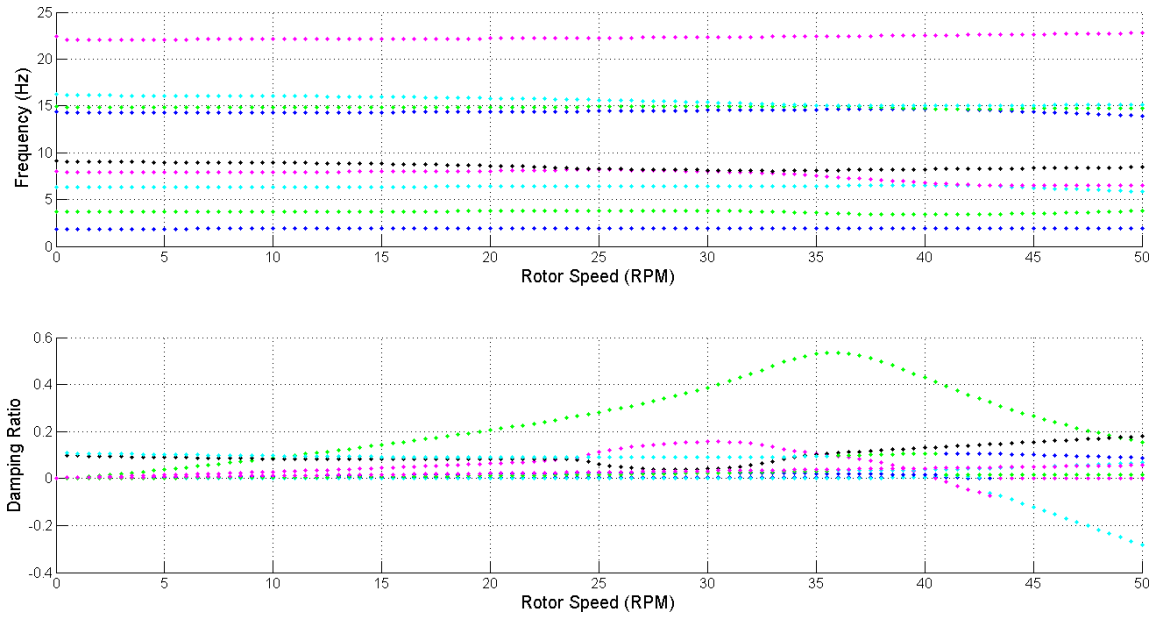

Figure VI.4. Frequency and damping ratio vs. rotor speed real valued BLAST predictions for WindPACT 1.5MW blade

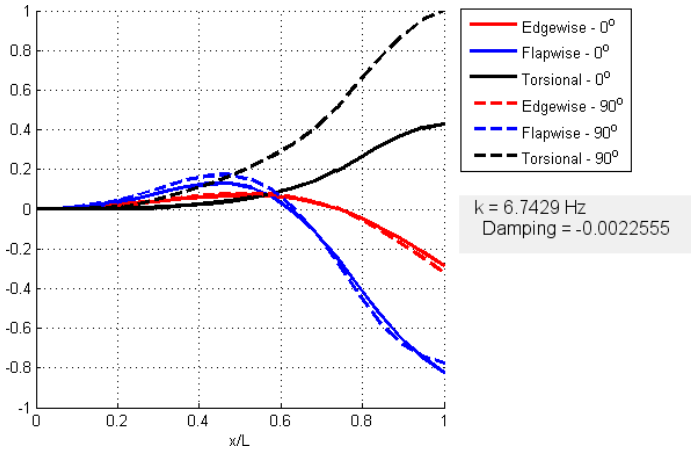

Figure VI.5. WindPACT 1.5MW flutter mode shape predicted using real valued BLAST

VI.B.2.b. Flutter analysis of the Sandia SNL100-00 blade

The Sandia 100 meter all glass turbine blade [85] was also analyzed for flutter instabilities using BLAST. Initial predictions using the legacy flutter tool predicted a relatively low flutter margin on this very large blade [60]. This blade has been designed with an operational rotor speed of 7.44 RPM.

The BLAST predictions for frequency and damping vs. rotor speed for the SNL100-00 blade are shown in Figure VI.6. Two potential flutter modes are identified, one at 9.68 RPM (flutter margin of 1.30) and the other 14.40 RPM (flutter margin of 1.94). Neither of these are consistent with previous predictions using the legacy flutter tool for the SNL100-00 [60] which predicted a flutter margin around unity for the SNL100-00. This may be due to the differences in geometric representation becoming more significant for the larger SNL100-00 blade than the smaller WindPACT 1.5MW blade analyzed earlier. The lower 9.68 RPM margin of flutter condition exhibits a softer flutter trend and is a higher mode than that of the 14.40 RPM flutter speed mode. Inspection of the mode shapes associated with each of these potential flutter modes shows a 2nd flapwise component coupled with a 1st torsional component which is representative of a classical flutter mode.

The SNL100-00 blade was also analyzed using the real valued implementation in BLAST. The frequency and damping vs. rotor speed trends for this analysis are shown in Figure VI.7. Hard flutter onset is observed at 13.05 RPM, and the mode shape associated with this flutter mode is shown in Figure VI.8. The mode shape is indicative of a flutter mode with 2nd flapwise components and 1st torsional components. This flutter rotor speed is between the softer 9.68 RPM and harder 14.40

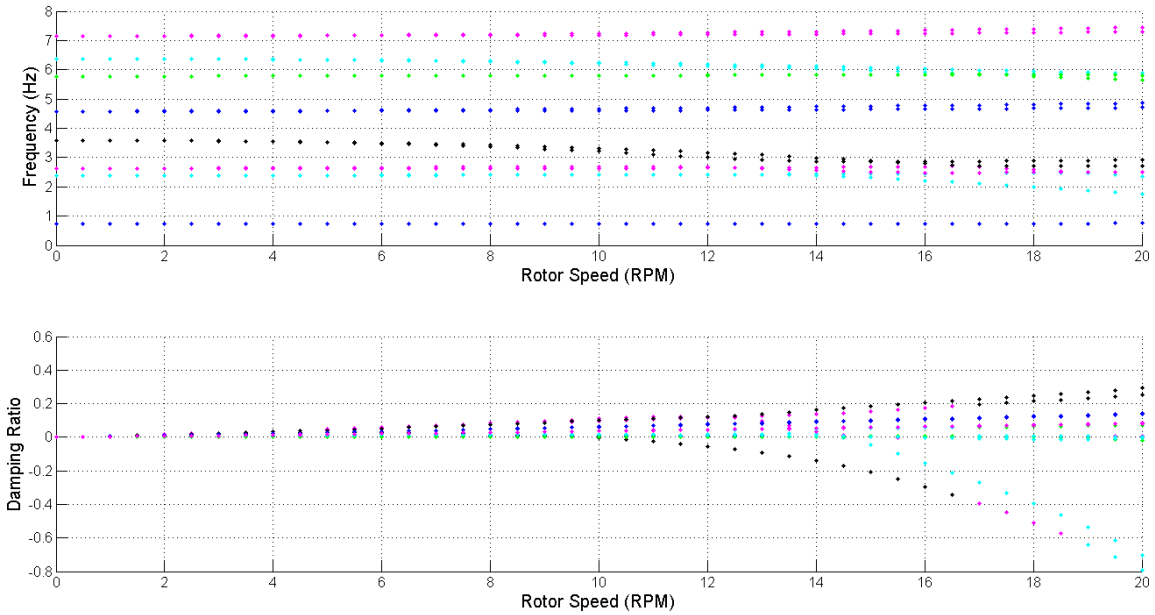

Figure VI.6. Frequency and damping ratio vs. rotor speed BLAST predictions for SNL100-00 blade

RPM flutter speeds predicted by the complex valued aeroelastic representation in BLAST. These potential flutter speeds have a 26% and 10% difference respectively to the 13.05 RPM prediction from the real valued representation. Thus, for the larger blade, the differences between the two representations become more significant. Perhaps more noteworthy is that the real aeroelastic representation predicts a flutter margin (1.75) that is much higher than initial estimates for this blade.

As this section has shown, revised BLAST predictions for the SNL100 indicate flutter may not be as significant a concern for larger blades as the legacy flutter tool suggested. Thus, future work should seek to assess the accuracy of aeroelastic predictions of current design tools to predict flutter in very large turbine blade designs. This may include considering of more robust aeroelastic stability analysis than considered in the current version of BLAST.

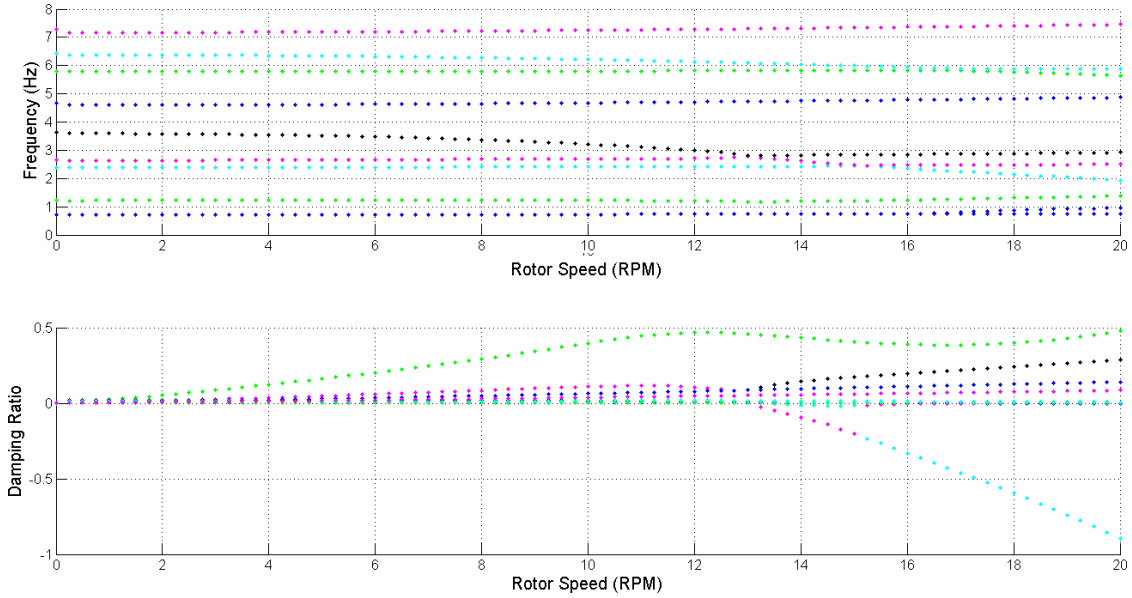

Figure VI.7. Frequency and damping ratio vs. rotor speed real valued BLAST predictions for SNL100 blade

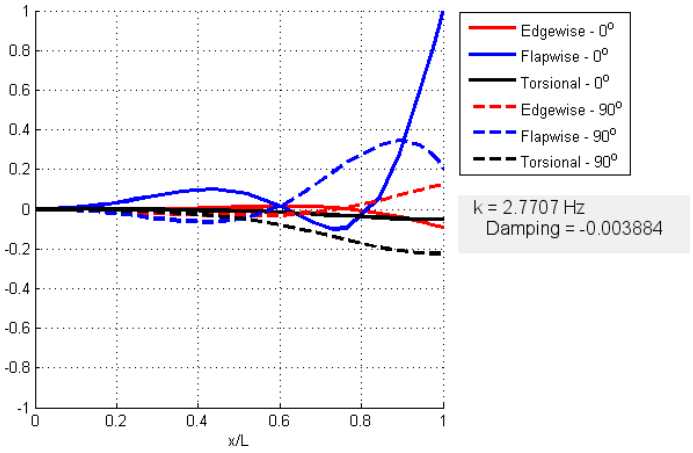

Figure VI.8. SNL100-00 flutter mode shape predicted using real valued BLAST

VI.C. Time-domain modeling of unsteady aerodynamics and aeroelastic stability

The previous modeling approaches employed modal analysis and a frequency domain representation of unsteady aerodynamic effects. Such an approach is suit-

able for non time-varying systems such as a wind turbine blade rotating at constant rotor speed in still air without considering inflow effects. Nevertheless, effects such as time-varying inflow velocity and gravitational effects may be important to include for very large and heavy blade designs, and inclusion of these effects in aeroelastic stability analysis will require modeling approaches capable of considering periodic time varying systems. Floquet-Lyapunov analysis [86] is one approach for investigating periodic time-varying aeroelastic systems. Another alternative is to employ transient analysis in conjunction with a time-domain model of unsteady aerodynamic effects. The motions of the system may be analyzed and signal processing tools may be employed to extract frequency and damping information that would typically be obtained through a frequency domain analysis. This approach has the advantage of being able to consider effects such as a time-varying gravity vector, inflow velocity, sharp gusts, and startup/shutdown in a straightforward manner.

A time-domain model also allows for yet another flutter prediction to compare with the results of modal analysis using complex and real valued aeroelastic representations. Accordingly, the transient unsteady aerodynamics model developed by Leishman [65, 66] was considered and implemented into an a transient structural dynamics analysis tool capable of modeling a wind turbine blade as a collection of beam elements. Herein, an overview of the transient unsteady aerodynamics model is given, and the two frequency-domain modeling approaches and the time-domain approach are applied to a simple, demonstrative example. The time-domain modeling of unsteady aerodynamics essentially eliminates complex values associated with the Theodorsen function and allows a comparison of the transient behavior with the

predicted modal results of the aforementioned aeroelastic representations.

VI.C.1. Overview of Leishman unsteady aerodynamics model

Theodorsen unsteady aerodynamics considers the lift force and pitching moment on an airfoil section due to the pitching and plunging motion of the airfoil. Some terms are inertial in nature and are simply due to the acceleration of the airfoil section through a fluid medium. These often manifest themselves as "added mass" terms and require no special treatment for inclusion in transient analysis. These terms are commonly referred to as "non-circulatory" and are present in Eqs. 6.2 and 6.3 as the terms without the Theodorsen function $C(k)$. Other contributions to the lift force and pitching moment are termed "circulatory" and these are the terms in Eqs. 6.2 and 6.3 that contain the Theodorsen function. Circulatory effects are due to the shed wake as a result of the pitching and plunging motion of an airfoil section. The Theodorsen function is complex in nature, dependent on the frequency of airfoil motion, and well adapted for frequency domain analysis. Including these effects in a transient analysis, however, requires an alternative approach.

Leishman [65] has developed a formulation that includes the unsteady effects associated with Theodorsen unsteady aerodynamics, but represents the unsteady aspects of circulatory effects in a convenient state-space representation. This allows unsteady aerodynamic loads to be easily computed along side a structural dynamics formulation in state-space form. First, consider the quasi-steady angle of attack of a pitching and plunging airfoil section

$$\alpha_{qs}(t) = \frac{\dot{w}(t)}{V} + \theta_x(t) + b\left(\frac{1}{2} - a\right)\frac{\dot{\theta}_x(t)}{V} \tag{6.39}$$

Such that $w(t)$, $\theta_x(t)$, b, and a are defined as before in the previous formulation section.

Next, the lift coefficient due to unsteady circulatory effects can be expressed in the time-domain via the Duhmamel's superposition integral and a Wagner indicial (or step) response

$$C_l^{circ}(t) = 2\pi \left[\alpha_{qs}(0)\phi_W(S) + \int_0^S \frac{d\alpha_{qs}}{d\sigma}\phi_W(S-\sigma)d\sigma \right] \tag{6.40}$$

Such that S is aerodynamic time ($S = Vt/b$). Like the Theodorsen function, the Wagner function (ϕ_W) serves to model the effect of shed wake. Both the Theodorsen function and Wagner functions are known in terms of Bessel functions, and as Leishman has emphasized [66] both are related through Fourier transforms. For convenience in evaluation of the Duhamel integral, the Wagner function is approximated in an exponential form.

$$\phi_W(S) = 1 - A_1 \exp(-b_1 S) - A_2 \exp(-b_2 S) \tag{6.41}$$

In this work, the approximation developed by Leishman ($A_1 = 0.2048$, $A_2 = 0.2952$, $b_1 = 0.0557$, and $b_2 = 0.333$) has been employed. Finally, the state-space form of the Duhamel integral may be introduced

$$\begin{bmatrix} \dot{z}_1(t) \\ \dot{z}_2(t) \end{bmatrix} = \begin{bmatrix} 0 & 1 \\ -b_1 b_2 \left(\frac{V}{b}\right)^2 & -(b_1+b_2)\frac{V}{b} \end{bmatrix} \begin{bmatrix} z_1(t) \\ z_2(t) \end{bmatrix} + \begin{bmatrix} 0 \\ \alpha_{qs}(t) \end{bmatrix} \tag{6.42}$$

The aerodynamic states (z_i) contain the information regarding the history of unsteady effects, and allow the influence of shed vortices to be accounted for in a time domain analysis. The instantaneous circulatory sectional lift coefficient is simply

calculated from the current aerodynamic states (z_i) as

$$C_l^{circ}(t) = 2\pi \begin{bmatrix} \frac{b_1 b_2}{2}\left(\frac{V}{b}\right)^2 & (A_1 b_1 + A_2 b_2)\frac{V}{b} \end{bmatrix} \begin{bmatrix} z_1(t) \\ z_2(t) \end{bmatrix} + \pi\alpha_{qs}(t) \tag{6.43}$$

Leishman presents a more thorough development of this model and extends the model to account for flapped airfoils, sharp gusts, and time-varying velocities in [65].

VI.C.2. Application of modeling approaches to a simplified example

A simple, uniform blade with length of 50 meters was considered, using a uniform discretization of 2 beam elements. The blade properties were specified to be the same as that of the root section on the WindPACT 1.5MW blade. A uniform chord of 2 meters was considered, the aerodynamic center was specified at the quarter chord, and the lift curve slope was specified as 2π. Furthermore, the flexural axis was specified to coincide with the aerodynamic center. To reduce the flutter speed, a significant edgewise mass center offset of 1 meter aft of the flexural axis was specified.

First, the original complex aeroelastic representation and modified real valued aeroelastic representation in BLAST were employed to predict the flutter behavior of this simple configuration using both complex and real valued representations. Structural nonlinearities (stress stiffening effects) were deactivated for simplicity. Frequency and damping trends versus rotor speed are shown in Figures VI.9 and VI.10. As expected, the complex valued representation does not contain complex conjugate pairs. One mode of the complex representation aeroelastic system appears to always have an effective negative damping, and another appears to have a flutter onset at approximately 56-57 RPM. A different trend is predicted by the real valued

representation with a flutter onset at 47-48 RPM.

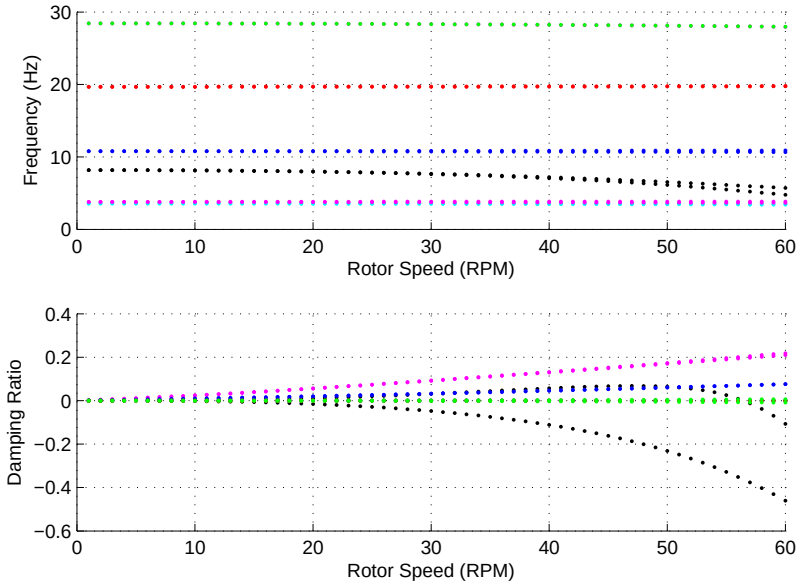

Figure VI.9. Frequency and damping ratio vs. rotor speed complex valued BLAST predictions for 2 element uniform blade

The time-domain unsteady aerodynamics model was employed in conjunction with structural dynamics analysis to obtain a time-domain prediction of aeroelastic stability in the simplified configuration. The unsteady aerodynamic load prediction and structural dynamics analysis were coupled in a "tight" manner, using an explicit ordinary differential equation (ODE) solver to perform time integration. In other words, the states of the structural dynamics system were time integrated concurrently with the states of the unsteady aerodynamics load calculations using an overall system of the first order ODE form $\dot{x} = f(t, x)$ which may be solved using "canned" explicit time integration schemes.

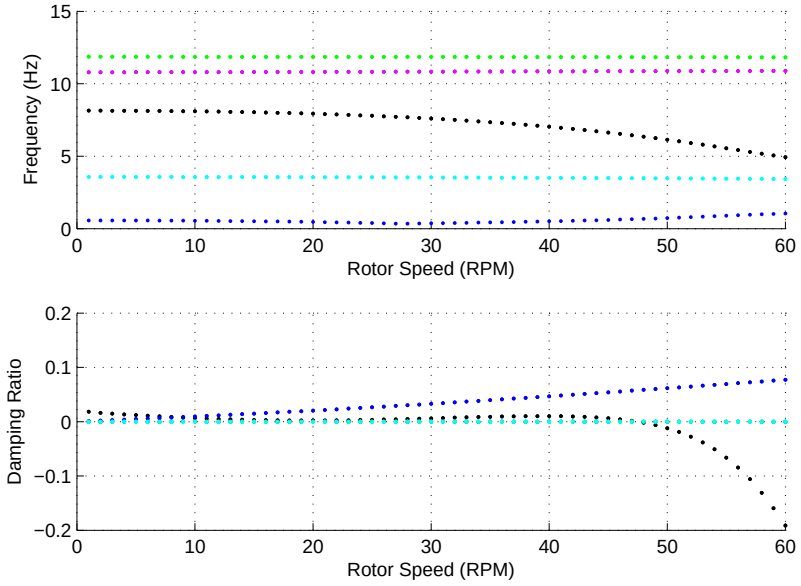

Figure VI.10. Frequency and damping ratio vs. rotor speed real valued BLAST predictions for 2 element uniform blade

Time-domain flutter predictions were performed by specifying a constant rotor speed, and prescribing some initial excitation of a constant force/moment of $1.0 \times 10^5 N$ and $1.0 \times 10^5 N \cdot m$ at the blade tip along the flapping and pitching axis respectively for the first 0.1 seconds of simulation. After this time, the excitation force was removed and the aeroelastic system was allowed to respond naturally. This initial forcing excited the modes associated with flutter (flapping and pitching), and allowed the stability of the system to be assessed during the transient analysis. Rotor speeds were examined in an increasing manner until an instability was observed in the system.

Figure VI.11 shows the blade tip flapping and pitching versus time using the time-domain unsteady aerodynamics model. Damping is observed in the system, indicating aerodynamic damping is present as no structural damping is considered.

An instability was observed at 49 RPM and further analysis revealed the onset of the instability around 48.8 RPM as shown in Figure VI.12. This agrees remarkably well with the real valued representation employed in the modified BLAST software, and further supports the use of this aeroelastic representation in place of the complex valued representation.

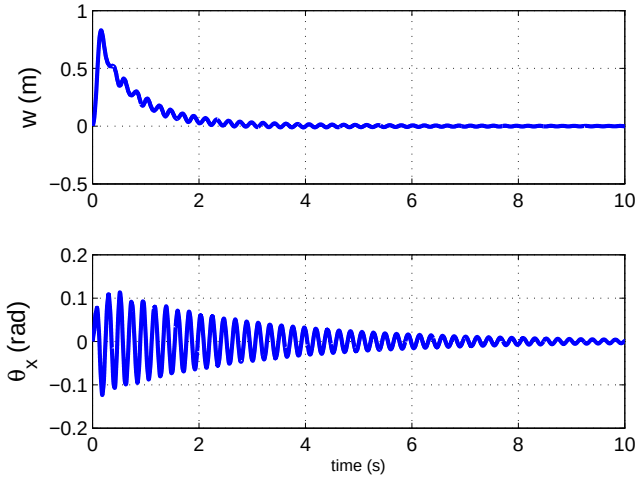

Figure VI.11. Blade tip plunging and pitching vs. time at 48 RPM with Leishman unsteady aerodynamics model loads

One discrepancy between the modal and transient analysis being compared in this section is the structural theory employed between the two analysis types. The modal analysis performed in both original and modified BLAST makes use of Euler-Bernoulli beam theory while the transient unsteady aerodynamics model has been implemented into a structural dynamics framework that makes use of Timoshenko beam theory. Accordingly, a limited frequency-domain aeroelastic analysis capability was employed with the Timoshenko beam element implementation. This allowed

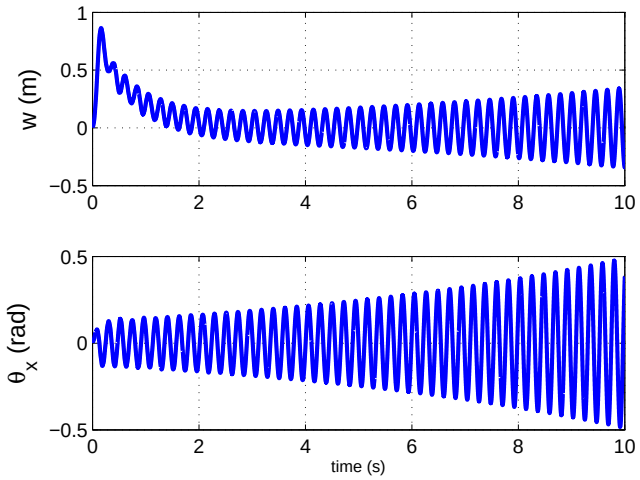

Figure VI.12. Blade tip plunging and pitching vs. time at 48.8 RPM with Leishman unsteady aerodynamics model loads

a better comparison of the transient analysis predictions with those from modal analysis. Note that only the real valued aeroelastic representation was considered in this limited flutter implementation. Figure VI.13 shows the frequency and damping trends of the modal aeroelastic analysis employing Timoshenko beam theory from 43 to 50 RPM. Note that beyond 47 RPM, it was difficult to reach a converged solution using the simple iterative procedures implemented with the limited flutter capability. Nevertheless, the damping and frequency trends were extrapolated using curve fitting tools to predict the flutter speed and the corresponding flutter mode frequency. Future work could implement more robust iteration algorithms to be used in conjunction with the aeroelastic Timoshenko beam implementation.

The extrapolated trends reveal a predicted flutter speed of 48.1 RPM from modal analysis. The flutter speed of 48.8 predicted via transient analysis is within 1.5% agreement with this modal prediction. The frequency content of the flutter mode

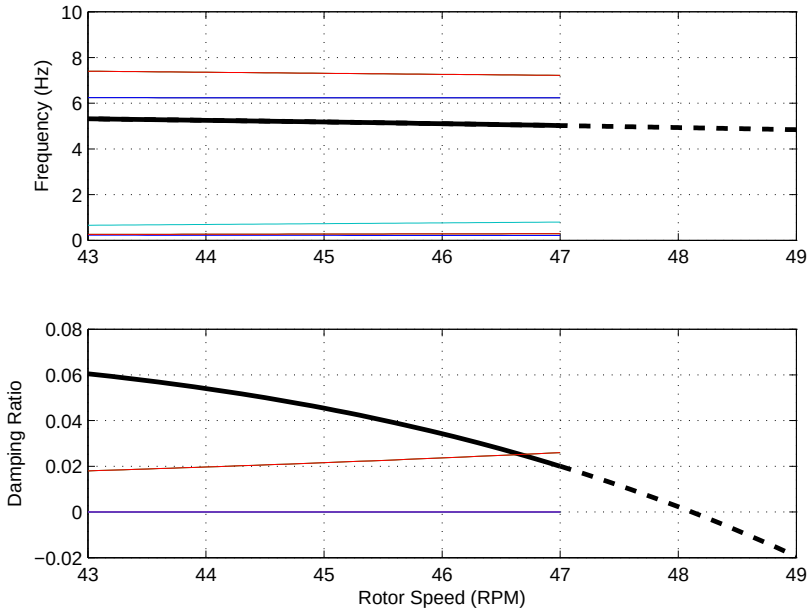

Figure VI.13. Frequency and damping trends for aeroelastic Timoshenko beam implementation (dashed lines extrapolating)

from transient analysis was found to be 4.6 Hz which is in decent agreement (6.5%) with the flutter mode frequency of 4.9 Hz extrapolated from the modal analysis results. This level of agreement between the modal analysis of the real valued aeroelastic system and the transient aeroelastic analysis provide a good deal of confidence in the consistency between these frequency and time-domain modeling approaches. This further advocates the use of the real valued aeroelastic representation over the complex valued representation.

VI.D. Conclusions

This chapter has presented aeroelastic formulations for employment in a conventional structural dynamics finite element framework. The core structural dynamics

capability in the OWENS toolkit was employed to develop the BLAST aeroelastic design tool for HAWT blades. BLAST design tool for examining aeroelastic stability of wind turbine blade designs. BLAST was applied to a utility scale 1.5MW blade as well as the SNL100-00 100 meter all glass blade design. The use of a real valued aeroelastic representation appears to be more consistent with conventional structural dynamics analysis, and the physical meaning of eigenvalues of this system are well understood. Revised flutter predictions show an increased flutter margin compared to initial studies, indicating flutter may not be as significant a concern for very large blade designs as originally expected. Furthermore, aeroelastic stability of a simple configuration was examined using a transient aeroelastic analysis and predictions were compared to those from frequency domain analysis. These predictions agreed very well with the real valued aeroelastic representation presented by Wright and Cooper. Thus, it is suggested that future modal analysis of aeroelastic systems make use of this real valued representation.

It should also be noted that employing transient aeroelastic stability analysis can encompass a wider variety of configurations and scenarios. Assumptions of constant rotor speed, zero inflow velocity, and neglecting a time varying gravity vector result in a non time varying system that may be analyzed using conventional modal analysis. In reality, however, these systems are often periodic in nature and this periodicity may have a greater impact on larger blade designs. For example, as blade designs become larger and heavier, neglecting gravity may no longer be justified and the periodic nature of the system will need to be accounted for. Future work may evaluate the need for periodic analysis of large wind energy systems under various

conditions and the transient aeroelastic stability analysis presented in this chapter may be well suited to provide a foundation for future design tools.

CHAPTER VII

DEMONSTRATION OF FEATURES AND COUPLING TO EXTERNAL MODULES IN THE OFFSHORE WIND ENERGY SIMULATION TOOLKIT

Features and coupling to external modules of the OWENS toolkit are demonstrated in this chapter. This includes the implementation of a reduced order model of a VAWT structure. In this verification effort, a VAWT is analyzed using a full order model with the conventional finite element implementation. The full order model predictions serve as a reference and reduced order models containing a subset of system modes are compared to the full order model predictions. In these simulations the accelerations and angular velocities of a floating frame are fully exercised. Both, linear and nonlinear reduced order models are verified in this exercise.

A demonstration of various rotor operation modes is also presented in this chapter. These include a prescribed rotor speed profile, a generator start up mode in which the generator acts as a motor to spin up the turbine, and a self starting turbine which is acted upon by external forces with the generator activated at a later time. In each scenario the structural response of a representative turbine is examined and a successful coupling between the core structural dynamics analysis capability and a generator module is demonstrated. Coupling to a simple model considering drive-shaft effects is also demonstrated.

Demonstration and baseline verification procedures of a two-way coupling between the core structural dynamics analysis capability and a floating platform dy-

namics module are also presented in this chapter. Two-way coupling is demonstrated between various rigid body motions of a system and the deformation of an attached flexible structure. A stable coupling procedure is also demonstrated for unconstrained rigid body motion and the resulting deformation of the attached flexible structure. This verification exercise concludes with verification of buoyancy effects and a demonstration of wave excitation of the platform structure. A demonstration of one-way coupling to VAWT aerodynamics software is also presented.

VII.A. Demonstration and verification of reduced order model for VAWT configurations

The reduced order modeling capability implemented in OWENS was verified by comparing reduced order models to predictions obtained using a full order transient analysis. The configuration used in this verification exercise is an idealized version of the Sandia 34-meter VAWT as shown in Figure VII.1. The blade shape is approximated by a parabolic profile and uniform cross-sectional properties are assumed throughout the blade. Furthermore, no struts are included in the configuration, and the turbine base is fully fixed with the top of the turbine unconstrained. Each blade and tower are composed of 20 elements each. This results in a mesh consisting of 60 elements and 59 nodes (354 total degrees of freedom). Transient analysis is performed using the Newmark-β integration method with a time step size of 0.001 seconds. Ten seconds of simulation time are considered. The deformation of the mid-point of a blade on this VAWT configuration is considered for comparison between reduced and full order models. In particular, reduced order models containing the first 10, 20,

and 30 lowest system modes are included in this verification exercise of the linear reduced model. More modes are included in the verification of a nonlinear reduced order model.

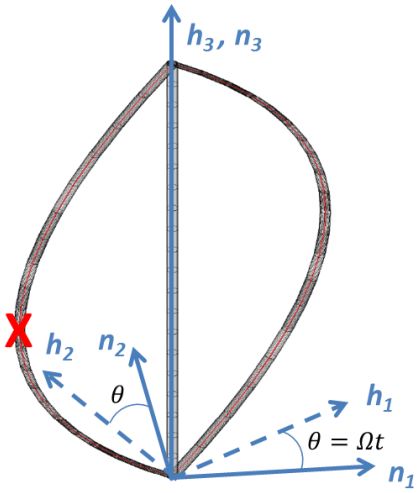

Figure VII.1. Schematic of idealized 34-meter VAWT with inertial (n_i) and hub-fixed (h_i) coordinate systems

VII.A.1. Linear reduced order model verification

This section presents verification procedures of the aforementioned configuration for a linear reduced order model of VAWT structure. First, the structure is subjected to only translational accelerations, followed by angular velocities and accelerations. Linear verification procedures conclude with the structure being subjected to combined translational acceleration and angular velocity and acceleration. Herein, all quantities are expressed in the rotor fixed hub (h_i) frame shown in Figure VII.1.

VII.A.1.a. Reduced order model of VAWT subject to rigid body translation

The VAWT configuration was subjected to translational accelerations of $a_1 = 1.3\frac{m}{s^2}$, $a_2 = 2.5\frac{m}{s^2}$, $a_3 = 9.8\frac{m}{s^2}$. Figures VII.2 through VII.7 show the various displacement components of the midpoint on the VAWT blade (the point denoted by the "X" in Figure VII.1). Overall, very good agreement between the full order model and reduced order models are seen with some discrepancies becoming apparent with the lowest order model containing 10 modes.

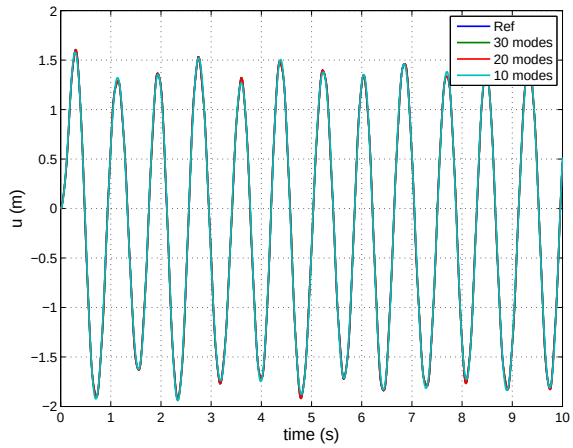

Figure VII.2. VAWT blade midpoint u displacement history for various reduced order models (rigid body translation, linear analysis)

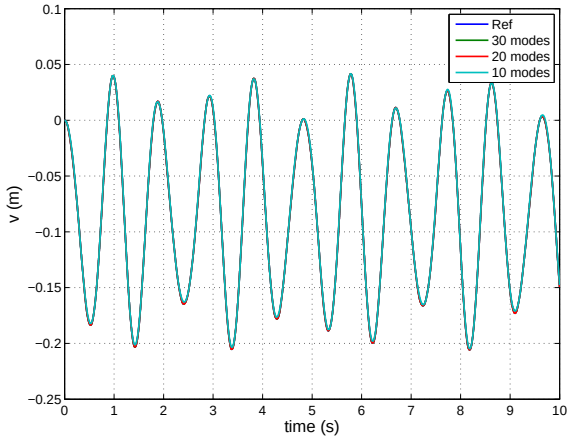

Figure VII.3. VAWT blade midpoint v displacement history for various reduced order models (rigid body translation, linear analysis)

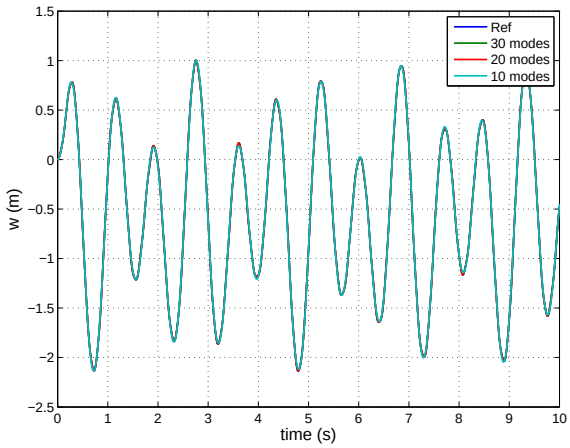

Figure VII.4. VAWT blade midpoint w displacement history for various reduced order models (rigid body translation, linear analysis)

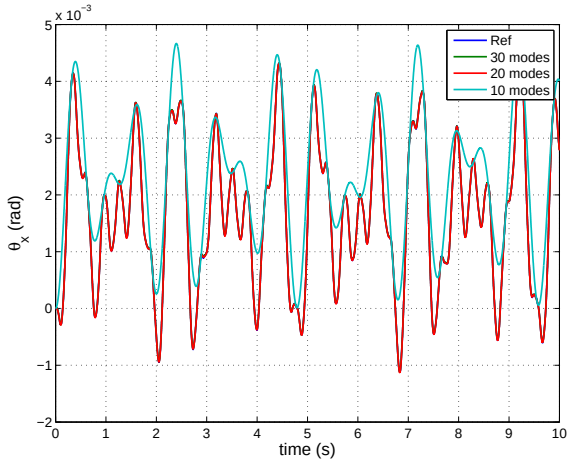

Figure VII.5. VAWT blade midpoint θ_x displacement history for various reduced order models (rigid body translation, linear analysis)

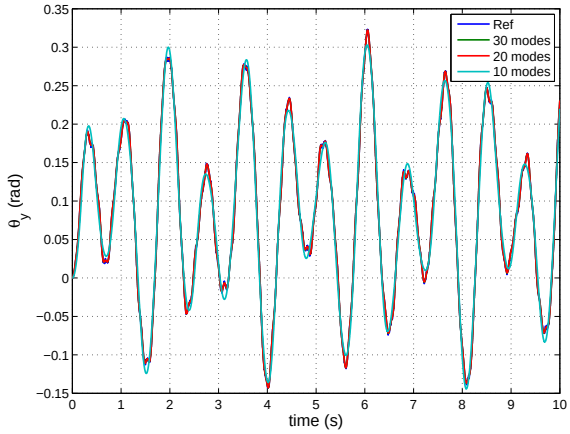

Figure VII.6. VAWT blade midpoint θ_y displacement history for various reduced order models (rigid body translation, linear analysis)

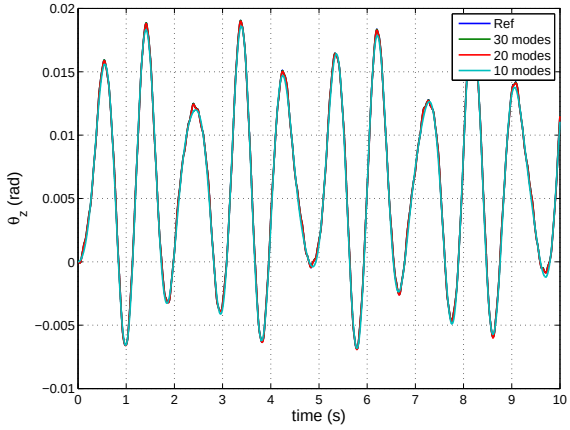

Figure VII.7. VAWT blade midpoint θ_z displacement history for various reduced order models (rigid body translation, linear analysis)

VII.A.1.b. Reduced order model of VAWT subject to rigid body rotation

The VAWT configuration was subjected to the angular velocity profiles (and corresponding angular acceleration profiles) shown in Figure VII.8. Figures VII.9 through VII.14 show the various displacement components of the midpoint on the VAWT blade. Overall, very good agreement between the full order model and reduced order models are seen with some discrepancies becoming apparent with the lowest order model containing 10 modes.

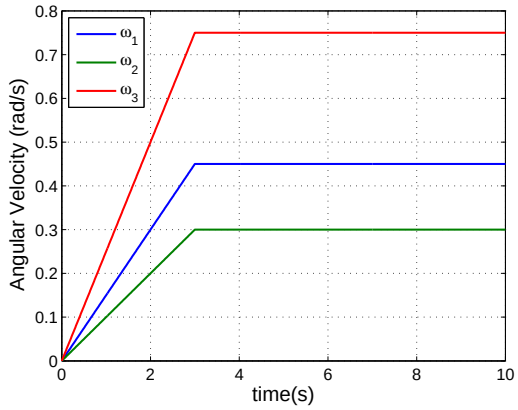

Figure VII.8. Prescribed angular velocity profiles employed in reduced order model verification procedures.

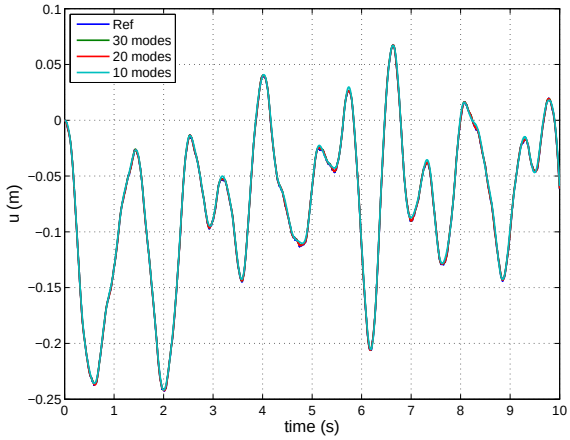

Figure VII.9. VAWT blade midpoint u displacement history for various reduced order models (rigid body rotation, linear analysis)

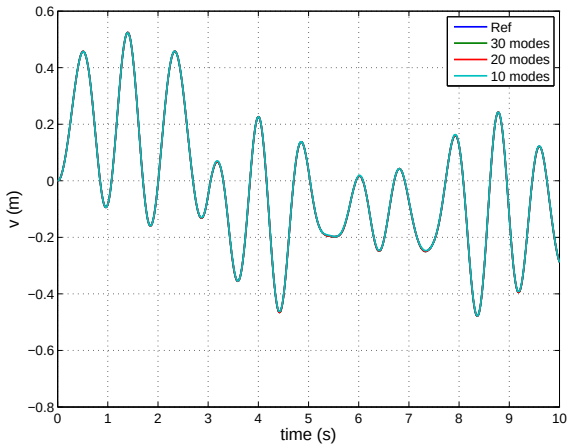

Figure VII.10. VAWT blade midpoint v displacement history for various reduced order models (rigid body rotation, linear analysis)

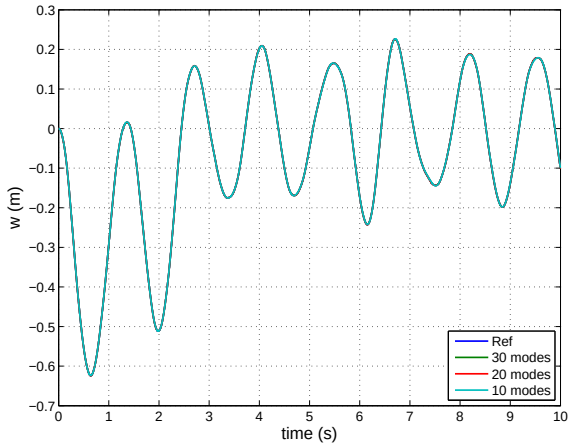

Figure VII.11. VAWT blade midpoint w displacement history for various reduced order models (rigid body rotation, linear analysis)

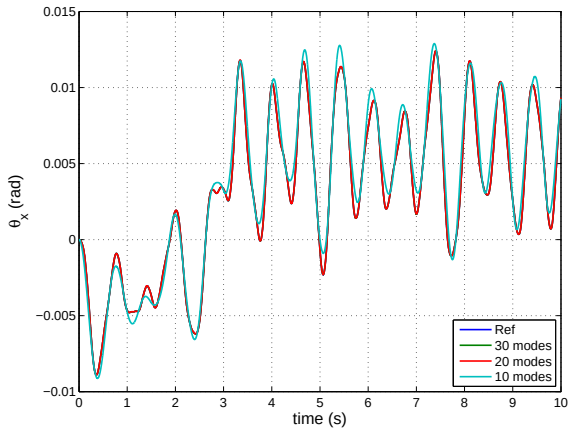

Figure VII.12. VAWT blade midpoint θ_x displacement history for various reduced order models (rigid body rotation, linear analysis)

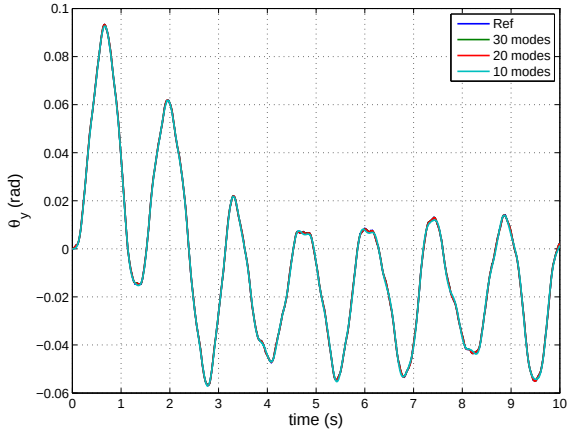

Figure VII.13. VAWT blade midpoint θ_y displacement history for various reduced order models (rigid body rotation, linear analysis)

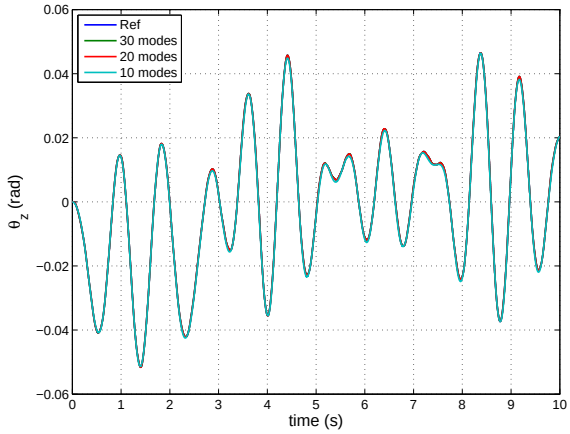

Figure VII.14. VAWT blade midpoint θ_z displacement history for various reduced order models (rigid body rotation, linear analysis)

VII.A.1.c. Reduced order model of VAWT subject to full rigid body motion

The VAWT configuration was subjected to the combined rigid body motions specified in the previous two sub-sections. Figures VII.15 through VII.20 show the various displacement components of the midpoint on the VAWT blade. Overall, very good agreement between the full order model and reduced order models are seen with some discrepancies becoming apparent with the lowest order model containing 10 modes.

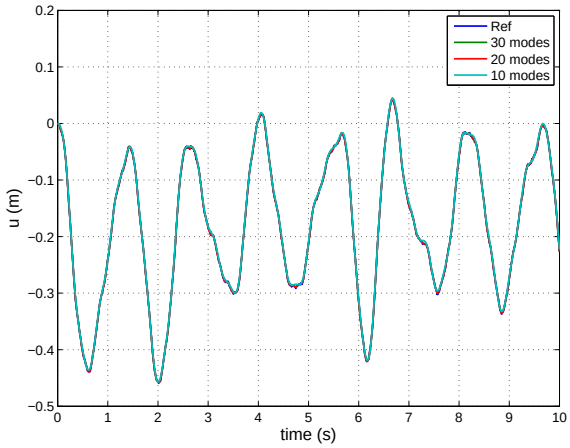

Figure VII.15. VAWT blade midpoint u displacement history for various reduced order models (full rigid body motion, linear analysis)

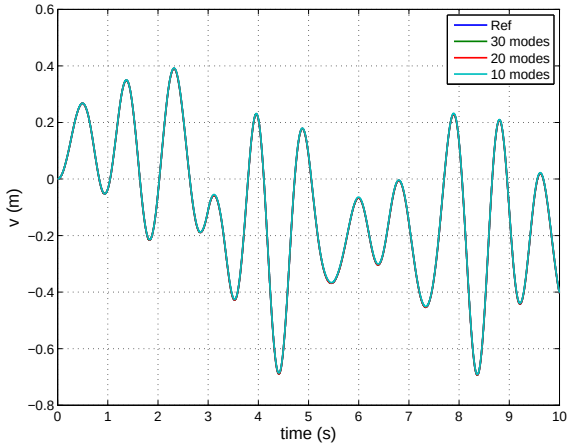

Figure VII.16. VAWT blade midpoint v displacement history for various reduced order models (full rigid body motion, linear analysis)

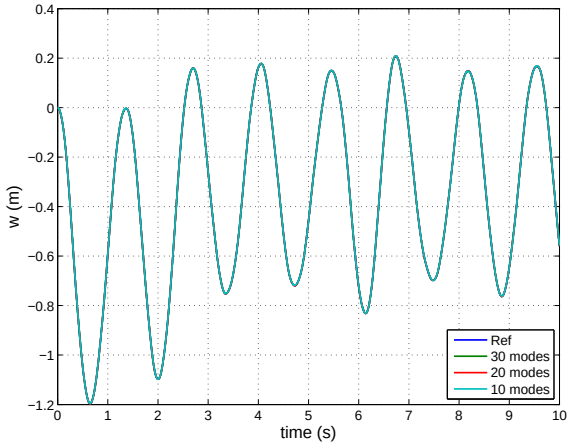

Figure VII.17. VAWT blade midpoint w displacement history for various reduced order models (full rigid body motion, linear analysis)

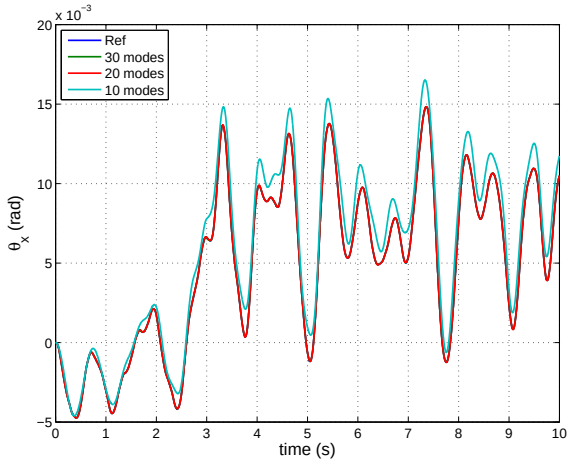

Figure VII.18. VAWT blade midpoint θ_x displacement history for various reduced order models (full rigid body motion, linear analysis)

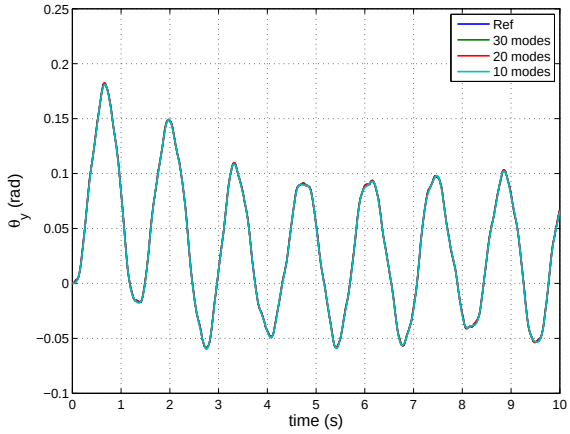

Figure VII.19. VAWT blade midpoint θ_y displacement history for various reduced order models (full rigid body motion, linear analysis)

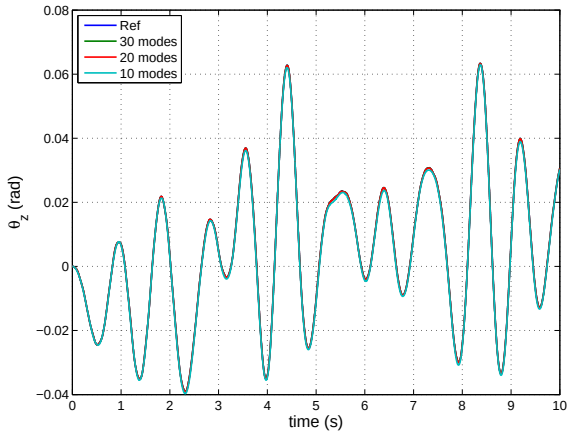

Figure VII.20. VAWT blade midpoint θ_z displacement history for various reduced order models (full rigid body motion, linear analysis)

VII.A.2. Nonlinear reduced order model verification

The aforementioned configuration was subjected to full rigid body motion with the combined translational accelerations and angular accelerations and velocities listed in the previous sub section. Structural nonlinearities in the form of stress-stiffening effects were included in this exercise. Figures VII.21 through VII.26 show the various displacement components of the midpoint on the VAWT blade. Overall, very good agreement is seen between the full order model and reduced order model constructed from the lower 60 modes of the system. Lower order reduced order models (composed of the lower 10, 20, and 30 modes) do not show as good agreement with the full order model. This is likely due to the inability of these low order models to characterize stress stiffening effects appropriately. Stress stiffening of bending modes is directly related to axial deformation in the configuration. Axial stiffness tends to be much stiffer than other flexible modes and would be associated with higher system modes. Thus, reduced order models selected solely as the lower subset of system modes may not accurately account for modes associated with axial deformation and thus would give a poor prediction of stress stiffening effects.

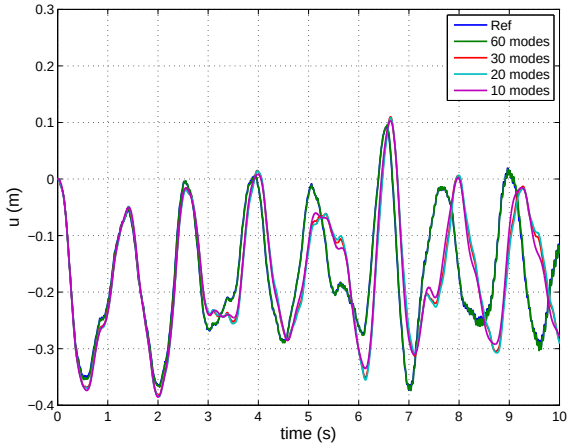

Figure VII.21. VAWT blade midpoint u displacement history for various reduced order models (full rigid body motion, nonlinear analysis)

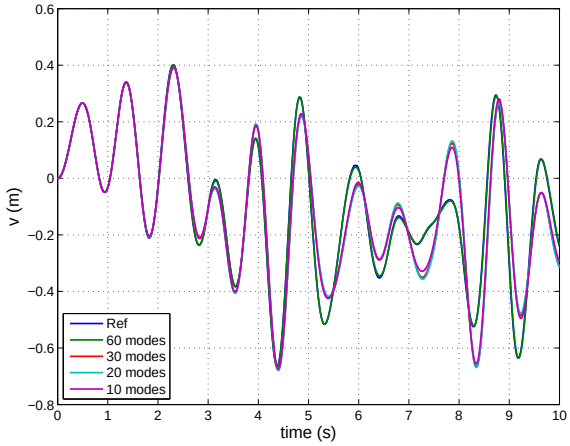

Figure VII.22. VAWT blade midpoint v displacement history for various reduced order models (full rigid body motion, nonlinear analysis)

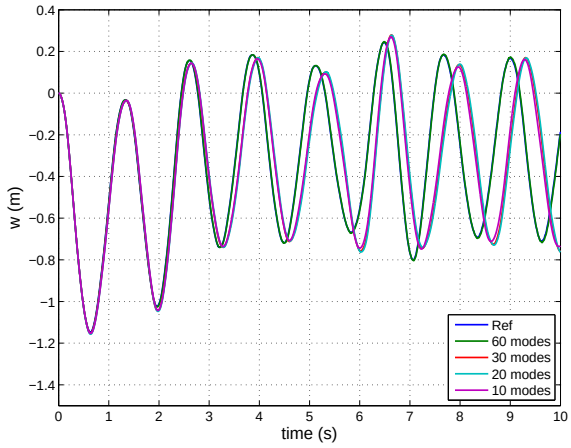

Figure VII.23. VAWT blade midpoint w displacement history for various reduced order models (full rigid body motion, nonlinear analysis)

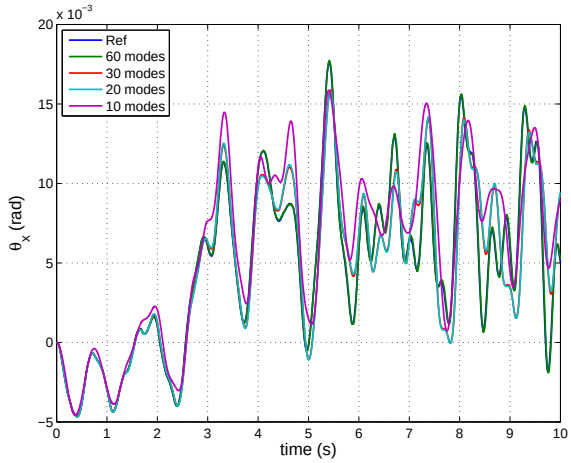

Figure VII.24. VAWT blade midpoint θ_x displacement history for various reduced order models (full rigid body motion, nonlinear analysis)

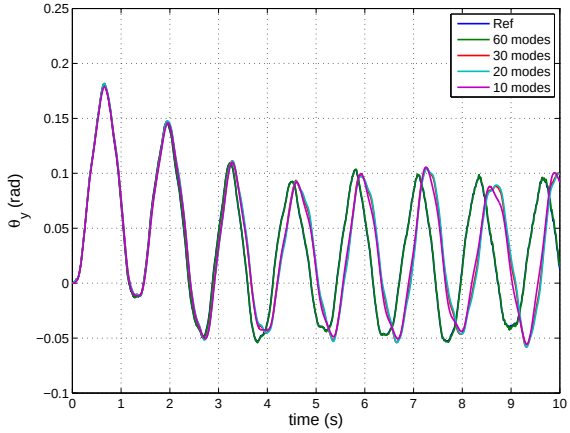

Figure VII.25. VAWT blade midpoint θ_y displacement history for various reduced order models (full rigid body motion, nonlinear analysis)

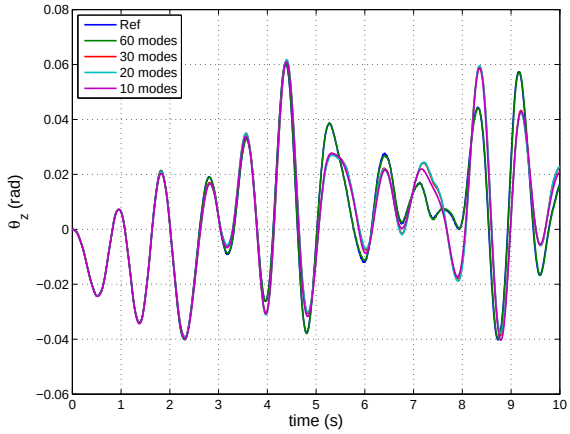

Figure VII.26. VAWT blade midpoint θ_z displacement history for various reduced order models (full rigid body motion, nonlinear analysis)

VII.B. Demonstration of rotor operation modes

This section presents a demonstration and verification of rotor operation modes implemented within OWENS. Available rotor operation modes include:

- Specified rotor speed profile
- Generator start up
- Self-starting rotor

The specified rotor speed profile does not consider any generator or drive train dynamics. The turbine structure is subjected to some specified rotor speed profile that may be prescribed by the analyst in a general manner. Such a capability is useful for examining structural response under general rotor speed profiles without the need to consider generator or drive train effects.

The generator start up mode considers a turbine initially at some constant (likely zero) rotor speed. The generator is initially activated and serves as a motor to provide a starting torque to the rotor. At at some time the turbine will reach a rotor speed that corresponds to zero generator torque. Under the absence of external forces, a rigid rotor or a rotor in static equilibrium would continue to operate at a constant rotor speed. For a flexible rotor, inertial effects of the deformable components may cause some variations in rotor speed around this zero torque speed. Application of external loads on the system (i.e. aerodynamic forces) can cause an effective torque on the rotor that can be resisted (and potentially equilibrated) by an opposing generator torque. This can result in a constant (or approximately constant) rotor speed that is higher than the zero torque generator speed. Under this condition the

generator enters into power generation mode.

The self-starting rotor mode considers an initially deactivated generator, and rotor motion is dependent on external forcing. At some specified time or rotor speed the generator may be activated (ideally at a rotor speed above the zero torque rotor speed of the generator). The generator torque then serves to provide a resistance torque to external loads on the rotor, and power is generated.

In these demonstration and verification exercises, the idealized version of the Sandia 34-meter VAWT depicted in Figure VII.1 is considered. To prevent oscillations due to undamped structural vibrations, a small amount of proportional damping was considered. Such that the system damping matrix is $C = \alpha K + \beta M$, with $\alpha = 0.01$, and $\beta = 0$. Here, M and K are the assembled system mass and stiffness matrices respectively. The Newmark-β time integration method is employed with a time step size of 0.01 seconds for a simulation time of 30 seconds. Structural nonlinearities are deactivated for simplicity. Iteration between the core structural dynamics solver and generator modules is performed until the solution of each module is converged to a tolerance of 1×10^{-8}.

VII.B.1. Demonstration of specified rotor speed mode

The specified turbine configuration was first considered under a prescribed rotor speed profile. The prescribed rotor speed profile is independent of generator or driveshaft effects and no external loading is considered. The specified rotor speed profile is similar to the one resulting from the turbine operating in a generator start up mode that is shown in the next section. Figures VII.27 and VII.28 show the prescribed

rotor speed and rotor acceleration profiles respectively. A linearly increasing rotor speed from 0 Hz at $t = 0$ to 0.5 Hz at $t = 11$ seconds is specified, after which rotor speed is prescribed to be a constant 0.5 Hz.

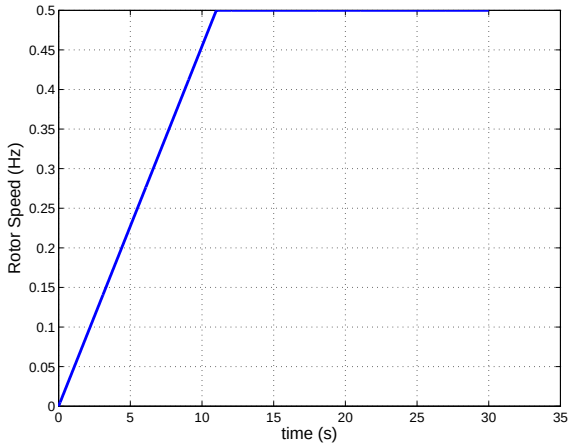

Figure VII.27. Prescribed rotor speed profile

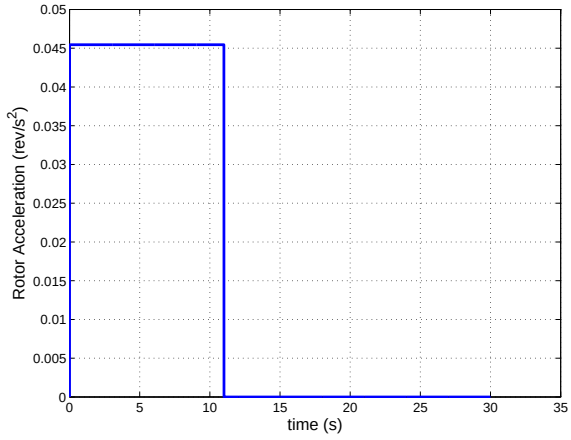

Figure VII.28. Prescribed rotor acceleration profile

Figure VII.29 shows the resulting u displacement of the blade midspan. Note that for this blade a negative u displacement is a radial displacement away from the tower. As shown in Figure VII.29, centrifugal loads on the blades, which are proportional to the square of rotor speed, result in radial displacement of the blade away from the tower. At 11 seconds, the rotor speed is specified to be constant and the u displacement begins to damp to a constant value of -0.104 meters at $t = 30$ seconds. This is consistent with results of a linear static analysis at 0.5 Hz rotor speed which predicts a u displacement of -.105 meters at the blade midspan. Figure VII.30 shows the resulting edgewise (v) displacement of the blade midspan. Circulatory forces (which are proportional to rotor acceleration) excite this motion and this is clearly visible in the edgewise displacement history of the blade midspan. At $t = 11$ seconds and beyond, rotor acceleration is zero and the edgewise motion of the blade midspan begins to damp and is approaching a displacement of zero at 30 seconds. This exercise has served as a demonstration and baseline verification of the prescribed rotor speed operation mode as implemented in the OWENS toolkit.

VII.B.2. Demonstration of generator start up mode

The aforementioned turbine in generator start up mode is considered with generator properties shown in Table VII.1 which result in the generator torque versus speed curve shown in Figure VII.31. This generator has a zero torque speed of 0.5 Hz. Furthermore, for a stationary rotor and active generator, the generator will serve as a motor applying a constant 4.18×10^5 N-m torque to the rotor until a rotor speed of 0.45 Hz is reached. In this initial study, a direct connection between the low

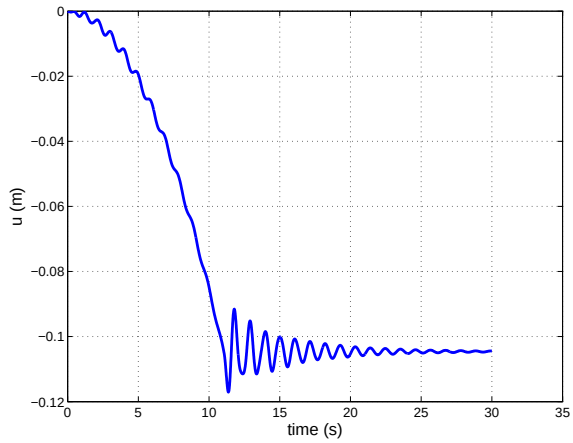

Figure VII.29. Blade midspan u displacement for prescribed rotor speed profile

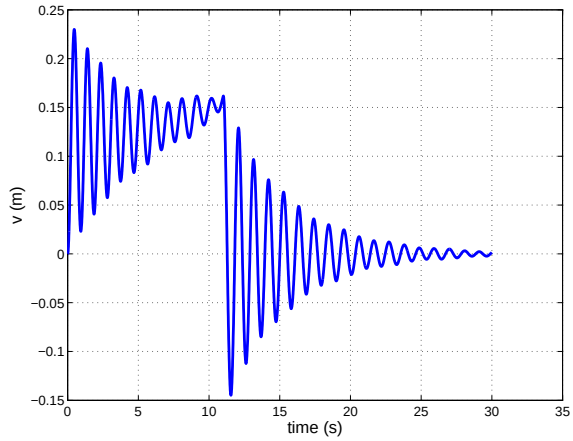

Figure VII.30. Blade midspan v displacement for prescribed rotor speed profile

speed shaft (rotor side) and the generator are considered. That is, no drive train is modeled and a gear ratio of unity is specified.

This demonstration exercise considers a turbine initially at rest, undergoing generator start up procedures. At time $t > 9$ seconds an external torque of 1×10^5 N-m along the axis of rotor rotation is applied to the top of the turbine. This serves as a simple analog to external loads such as aerodynamic loads that would provide

Table VII.1. Generator properties for idealized 34-meter VAWT

Property	Value
Generator rated torque	2.09×10^5 N-m
Zero torque generator speed	0.5 Hz
Pull out ratio	2.0
Generator rated slip percentage	5.0

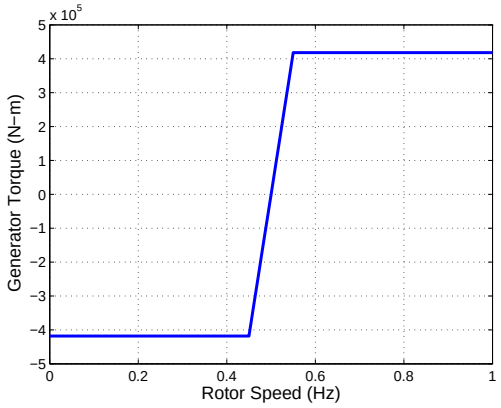

Figure VII.31. Generator torque vs. speed curve used in demonstration and verification procedures

an effective torque on the rotor. Inspection of the generator torque versus speed curve in Figure VII.31 reveals this torque corresponds to a rotor speed of 0.512 Hz, and a generator power value of 322 kW.

Figure VII.32 shows the rotor speed profile for this configuration in generator start up mode. Initially, the rotor speed is linearly increasing, consistent with the constant torque being applied by the generator. Around 0.45 Hz rotor speed (at approximately 9 seconds), the rotor speed begins to level off consistent with the decrease in generator torque magnitude shown in Figure VII.31. Beyond this time, external loading is applied which is equilibrated by the generator torque, resulting in a constant rotor speed of 0.512 Hz as expected. Furthermore, inspection of the

generator power history shown in Figure VII.33 shows power oscillating between 320 and 324 kW near 30 seconds of simulation time. Further damping of the structural motion in the system will likely result in a steady state generator power of 322 kW as expected.

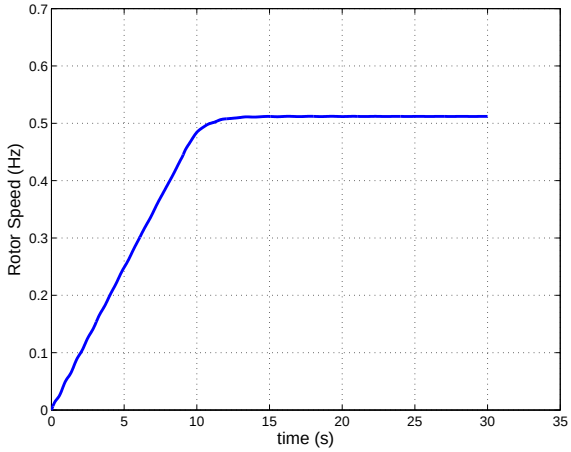

Figure VII.32. Rotor speed vs. time for generator start up mode

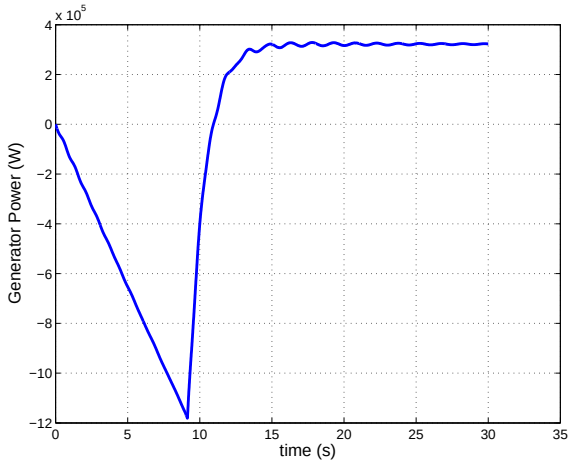

Figure VII.33. Generator power vs. time for generator start up mode

Closer inspection of the generator power history shows the generator is acting as a motor, forcing the rotation of the turbine until approximately 11 seconds, at which point the generator begins operating in power generation mode. Finally, Figure VII.34 shows the rotor acceleration versus time. The sharpest changes in rotor acceleration occur at $t = 0$ and $t = 9$, and these are consistent with the initial application of the generator motoring torque and the application of the external torque respectively. The influence of structural vibration is also clearly visible in the oscillations of the rotor acceleration history. As expected, this value is approaching zero as the rotor approaches a constant speed.

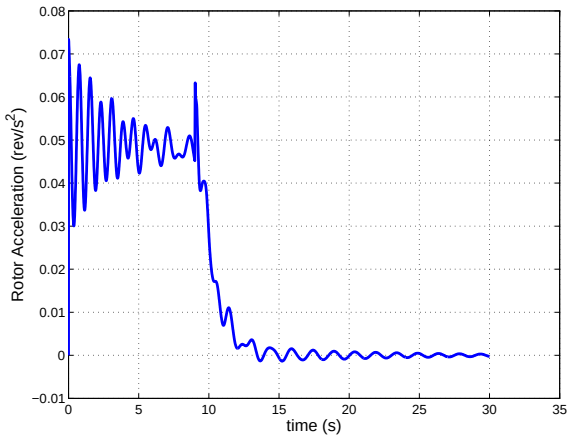

Figure VII.34. Rotor acceleration vs. time for generator start up mode

Figure VII.35 shows the blade midspan u displacement versus time. Note that for the blade considered, u is opposite the radial direction, such that a negative u displacement corresponds to motion away from the tower. One can note that the u displacement is primarily due to centrifugal loadings that are proportional to the

square of the rotor speed. This is apparent in the similarities between the u displacement history and the rotor speed history shown in Figure VII.32. Figure VII.36 shows the edgewise (v) displacement of the blade midspan versus time, with striking similarities to the rotor acceleration history shown in Figure VII.34. This is due to the edgewise loads being composed of Circulatory forcing which is proportional to the rotor acceleration. Furthermore, one can note the similarities of these displacement histories to those in Figures VII.29 and VII.30 which were generated under a prescribed rotor speed profile without considering generator effects. This suggests that prescribed rotor speed profiles may be an adequate means for examining structural response in initial design studies. This exercise has provided a baseline verification of the coupling between the core structural dynamics module and generator module for a VAWT configuration in generator start up mode.

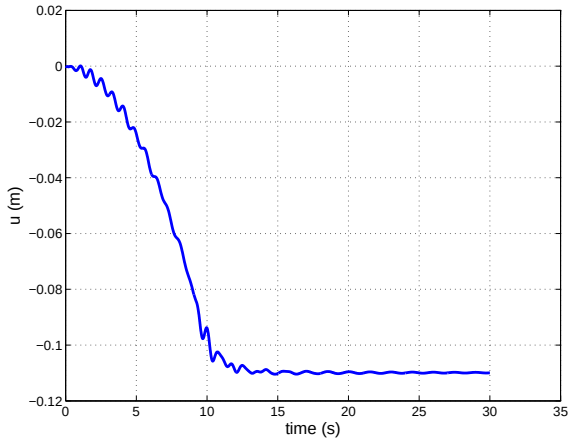

Figure VII.35. Blade midspan u displacement vs. time for generator start up mode

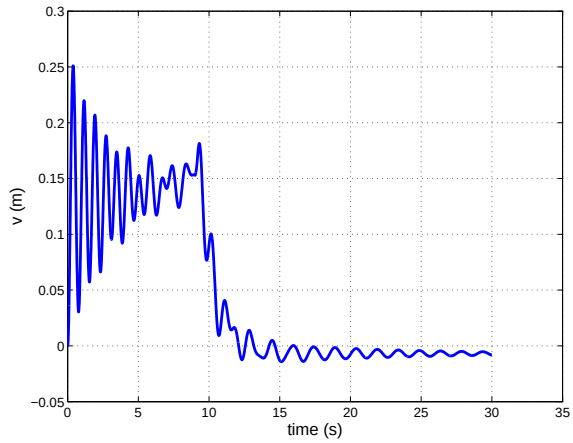

Figure VII.36. Blade midspan v displacement vs. time for generator start up mode

VII.B.2.a. Inclusion of drive-shaft modeling in generator start up mode

The previous demonstration exercise was performed with drive-shaft modeling activated, and the drive-shaft/gearbox was specified to have the properties listed in Table VII.2. The drive-shaft has very high stiffness and relatively low mass associated with it. This results in a very high frequency component in the overall flexible system of the VAWT rotor. Thus, to ensure stability a relatively low time step is required. Thus, a time step of $\Delta t = 1.0 \times 10^{-5}$ seconds has been specified for this demonstration exercise. Overall, the resulting rotor motions and structural displacements are very similar to those of the demonstration without drive-shaft effects.

Table VII.2. Drive-shaft properties for idealized 34-meter VAWT

Property	Value
Drive-shaft stiffness	5.9×10^9 N/rad
Drive-shaft damping	1.0×10^7N-m^2
Gearbox ratio	1.0
Gearbox efficiency	100%

As one would expect, aside from the initial start up, the rotor and drive shaft angular velocity are essentially the same. Key differences are seen at the initial start up as shown in Figure VII.37. The initial torque of the generator on the drive shaft provide a larger angular motion in the drive-shaft before this load is transferred to the rotor. After this initial start up procedure the angular velocity profiles for the rotor and drive-shaft are essentially identical. Furthermore, inspection of the azimuth for the rotor and drive-shaft as shown in Figure VII.38 reveals that the rotor tends to lag behind the drive-shaft by an approximately constant angle. This angle is in fact the steady state compliance in the drive-shaft. Although not shown here, a reversed trend is seen after the rotor begins to operate in power generation mode. The rotor leads with drive-shaft lagging by some small angle of drive-shaft compliance. These results have served as a demonstration of drive-shaft modeling capability and have provided qualitative verification of the drive-shaft implementation in the OWENS toolkit.

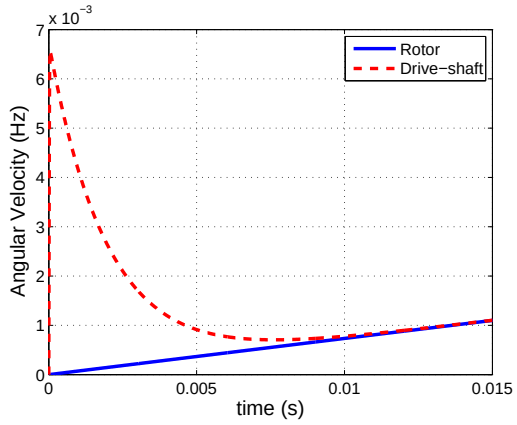

Figure VII.37. Angular velocity vs. time of rotor and drive-shaft for generator start up mode

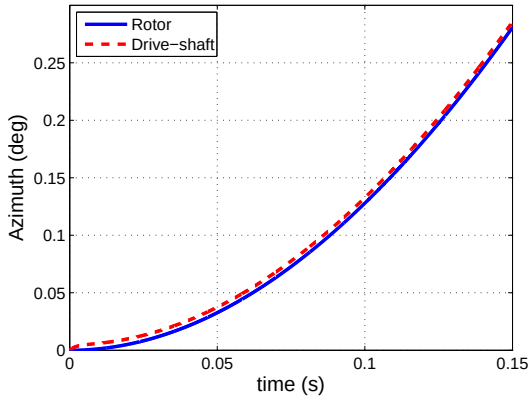

Figure VII.38. Azimuth vs. time of rotor and drive-shaft for generator start up mode

VII.B.3. Demonstration of self starting turbine mode

The aforementioned VAWT configuration was considered in a self starting turbine mode. An external torque of 3×10^5 N-m (representative of any external forcing such as aerodynamic loads) was applied to the top of the turbine along the axis of rotor rotation. This constant external torque is applied throughout the simulation, and the generator is activated at a rotor speed of 0.5 Hz. At this point in the simulation, the generator provides a resisting torque to the externally applied loads and the rotor is expected to reach a constant rotor speed. Inspection of the generator torque vs. speed curve in Figure VII.31 shows that this torque corresponds to a rotor speed of 0.536 Hz and a generator power of 1.01 MW.

Figure VII.39 shows rotor speed versus time for the self starting turbine. The linear increase in rotor speed is consistent with constant external torque applied to the structure, and the smooth leveling off to a constant rotor speed is consistent with

the linearly increasing resistance torque provided by the generator at rotor speeds greater than 0.5 Hz. As expected, this constant rotor speed is 0.536 Hz. Figure VII.40 shows the generator power history for the self starting turbine. The generator is deactivated until a rotor speed of 0.5 Hz is reached (at approximately 14 seconds), at which point power generation sharply increases before leveling off to a value of 1.01 MW at $t = 30$ seconds. The rotor acceleration history for the self starting turbine mode is similar in nature to that for the generator start up mode shown in Figure VII.34, and is not shown here.

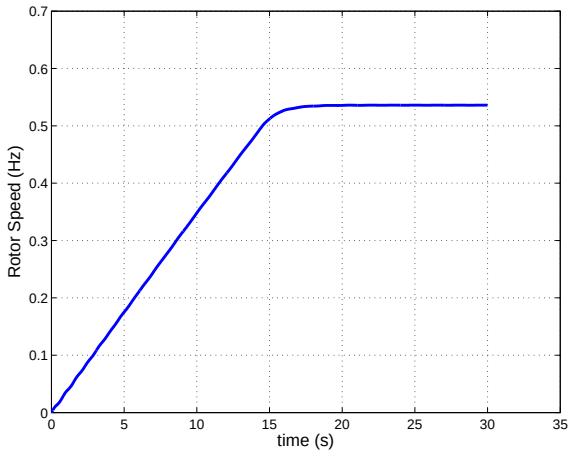

Figure VII.39. Rotor speed vs. time for self starting turbine mode

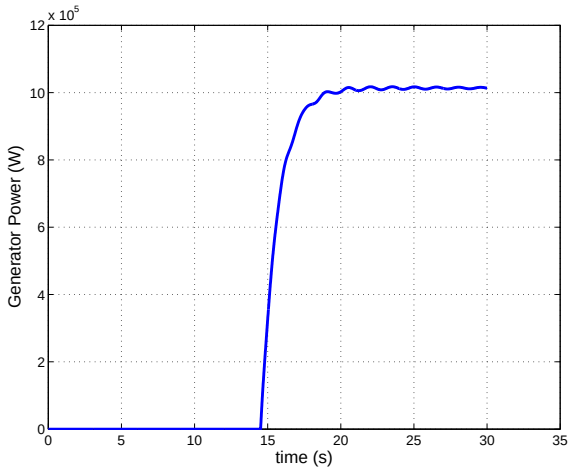

Figure VII.40. Generator power vs. time for self starting turbine mode

VII.C. Demonstration of two-way coupling to platform dynamics software

The coupling methodology described in Chapter II was employed to couple a modified version of the WavEC [44] platform dynamics/hydrodynamics code to the core structural dynamics analysis capability in the OWENS analysis framework. First the configuration considered in the verification procedures is discussed, including the platform and mooring description as well as the representative flexible turbine structure attached to the platform. Baseline verification procedures are then discussed, followed by results demonstrating a successful two-way coupling between the two independent analyses.

VII.C.1. Configuration

This section discusses the configuration used to demonstrate the coupling between the structural dynamics capability in the OWENS toolkit and the WavEC

platform dynamics analysis software. Figure VII.41 presents a schematic of the configuration employed in verification procedures. A flexible structure is attached to a platform being modeled as a rigid body. Surge, sway, and heave are along the h_1, h_2, and h_3 coordinate axes respectively. Roll, pitch, and yaw are about the h_1, h_2, and h_3 coordinate axes respectively.

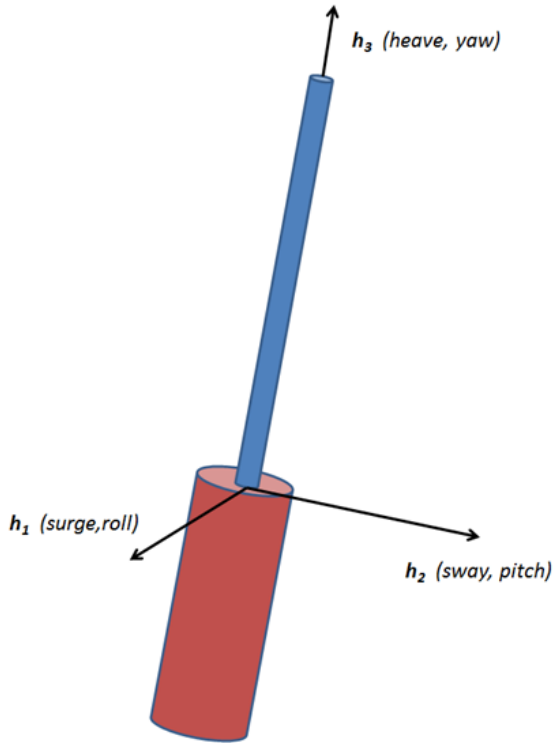

Figure VII.41. Schematic of configuration employed for demonstration of coupling to platform dynamics module

VII.C.1.a. Description of platform

The platform configuration employed in this demonstration is a spar buoy design that was sized from the initial design of a 5MW Darrieus VAWT. The mass of this VAWT design is 973.0 metric tons, and the center of gravity (CG) of the VAWT design is 54.9 meters above the still water line (SWL). The roll and pitch moments of inertia of this design about the structure's center of gravity are 1.35×10^9 kg-m^2. The operating load on the turbine was calculated to be 550.0 kN at a center of pressure 67.0 meters above the still water line. These VAWT system properties were used to perform platform sizing under the following constraints

- Mean pitch angle must be less than 5 degrees.
- Roll/pitch natural periods must be between 25 and 40 seconds.

This resulted in the spar-buoy design with the specifications listed in Table VII.3. This version of WavEC contained a simplified mooring model that considered a system of linear springs attached to the platform to provide restoring force. The stiffness matrix associated with the mooring system (K^{moor}) in WavEC is shown below. The degree of freedom ordering for this stiffness matrix is surge, sway, heave, roll, pitch, and yaw.

Table VII.3. Spar buoy platform properties

Mass	9050 metric tons
Draft	80.0 m
Minor diameter (near SWL)	8.0 m
Major diameter (most of hull)	13.0 m
CG below SWL	63.5 m
Roll inertia about CG	3.4×10^9 kg-m^2
Pitch inertia about CG	3.4×10^9 kg-m^2
Yaw inertia about CG	2.0×10^8 kg-m^2

$$K^{moor} = \begin{bmatrix} 41 & 0 & 0 & 0 & -280 & 0 \\ & 41 & 0 & 280 & 0 & 0 \\ & & 1.2 & 0 & 0 & 0 \\ & & & 31000 & 0 & 0 \\ & & & & 31000 & 0 \\ SYM & & & & & 11000 \end{bmatrix} \times 10^4 \tag{7.1}$$

VII.C.1.b. Description of flexible structure

A representative flexible tower structure was considered with rigid body properties specified to be the same as the rigid turbine properties the aforementioned platform was sized to. The resulting tower was a sizable, flexible structure with a length of 215 meters. The tower was represented by 10 uniform linear Timoshenko beam elements. Mass and stiffness properties of the tower structure are listed in Table VII.4. Note that the torsional moment of inertia of the tower was fictitiously increased to mimic that of the properties for the rigid turbine. For simplicity, the tower is assumed to be mounted at the center of mass of the platform via a clamped connection.

Table VII.4. Flexible structure properties

ρA	4.525×10^3 kg/m
$\rho I_{yy} = \rho I_{zz}$	6.75×10^4 kg-m
ρJ	6.3×10^5 kg-m
ρI_{yz}	0 kg-m
EA	1.9×10^{11} N/m
$EI_{yy} = EI_{zz}$	2.3×10^{12} N-m
GJ	3.0×10^{11} N-m
EI_{yz}	0 N-m

VII.C.2. Demonstration and baseline verification procedures

Preliminary verification procedures considered the isolated motion of individual platform rigid body degrees of freedom. That is surge, sway, heave, roll, pitch, and yaw were each isolated in verification tests. First, step relaxations of each platform mode were considered and the influence of platform motion on the response of the flexible structure attached to the platform was observed. Next, an excitation force was applied to the flexible structure, and the response of the platform was observed. Fast Fourier Transforms (FFTs) of the platform and structural response were observed in each case and the frequency content of platform and structural displacements were checked for consistency. Furthermore, all damping mechanisms were deactivated from the platform module (radiation damping, drag, etc.) and no structural damping was applied to the flexible structure. This verified energy was not being dissipated by the numerical time integration schemes or the coupling procedure. The Gauss-Seidel iterative method was employed to couple the two simulations together, and a convergence criterion of 1×10^{-8} was enforced at each time step for iterations of the coupled structural dynamics and platform analysis. Gravity was deactivated in these initial verification procedures.

A Newmark-β implicit time integration method was considered in the structural dynamics simulation with a time step size of 0.1 seconds. To expedite the analysis, nonlinear effects were deactivated in the structural dynamics simulation. Furthermore, a reduced order model was employed in the structural dynamics simulation which included only the first 10 flexible modes of the tower structure. Although, the linear nature and reduced order of this structural model introduce certain approximations, the goal of this exercise is to verify coupling between a structural dynamics module and platform hydrodynamics module regardless of the fidelity of the individual modules.

Additional tests were conducted that examined the both sway/roll (surge/pitch) response of the coupled platform and structural dynamics analysis. Procedures were similar to those mentioned previously for the isolated degree of freedom testing. Buoyancy effects were verified by examining a coupled platform/structural dynamics analysis under gravity and buoyant loads to confirm the platform design behaved as intended under self-weight and weight of the attached structure. Finally, a full six-degree of freedom platform analysis was also considered under step relaxation and structural excitations as before. This exercise sought to confirm the stability of a fully coupled analysis with all platform degrees of freedom active. For brevity, only the demonstrations of combined sway/roll motion, and simple wave excitation are shown in this section.

VII.C.2.a. Combined sway and roll motion under platform step relaxation

The platform was displaced in sway a distance of 1 meter with all other rigid body modes of the platform except for roll constrained to zero. The attached flexible tower was initially at rest. At $t = 0$ the platform was released and hydrodynamic restoring/mooring forces resulted in harmonic motion of the platform sway and roll motions as well as the attached tower structure. The response of the simulation was simulated for two minutes. Figures VII.42 and VII.43 show the history of platform sway motion and the FFT of this motion respectively. Figures VII.44 and VII.45 show the history of platform roll motion and the FFT of this motion respectively. Figures VII.46 and VII.47 show the history of tower tip displacement in the h_2 direction as well as the FFT of this motion respectively.

Periodicity is difficult to confirm given the interplays of various system modes. Frequencies of 0.025, 0.05, 0.68, and 1.79 Hz are observed in the tower motion, the lowest two being representative of the low frequency platform sway and roll motion and the higher two being representative of the tower structural vibration. A primary frequency of 0.025 Hz is observed in the platform sway motion, and frequencies of 0.025, 0.05, and 0.68 Hz are apparent in the platform roll motion. Closer inspection of the FFTs of platform motion reveals small irregularities in the smooth FFT distribution around 0.05, 0.68, and 1.79 Hz for sway and 1.79 Hz for roll. This suggests there is some impact of the structural vibration on the frequency content of the tower although the forcing as a result of structural vibration is minimal compared to restoring forces acting on the platform. These results are tabulated in Table VII.5, and confirm consistency between the predictions in the platform motions

and structural motions.

Table VII.5. Platform sway/roll and tower frequency content (Hz) as a result of sway step relaxation

Platform Sway	Platform Roll	Tower Motion
0.025	0.025	0.025
0.05 (slight)	0.05	0.05
0.68 (slight)	0.68	0.68
1.79 (slight)	1.79 (slight)	1.79(slight)

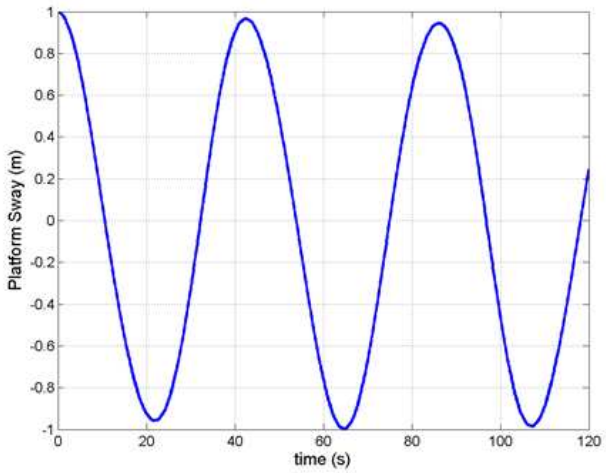

Figure VII.42. Platform sway motion as a result of platform sway step relaxation

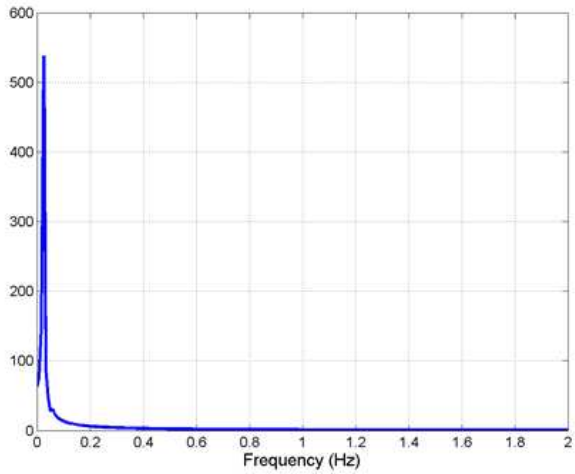

Figure VII.43. FFT of platform sway motion as a result of platform sway step relaxation

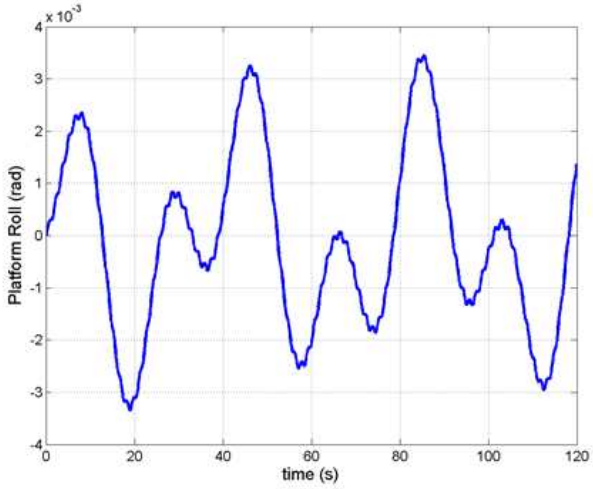

Figure VII.44. Platform roll motion as a result of platform sway step relaxation

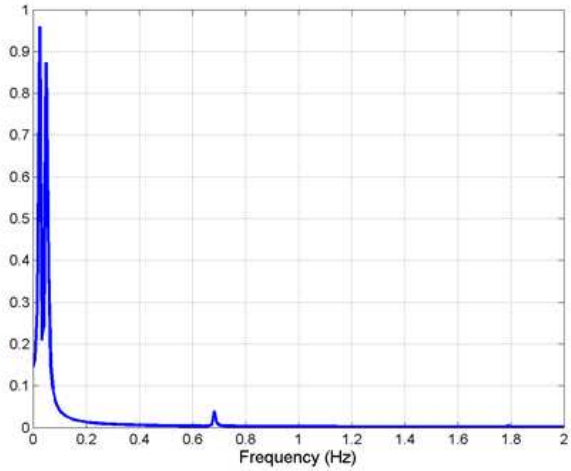

Figure VII.45. FFT of platform roll motion as a result of platform sway step relaxation

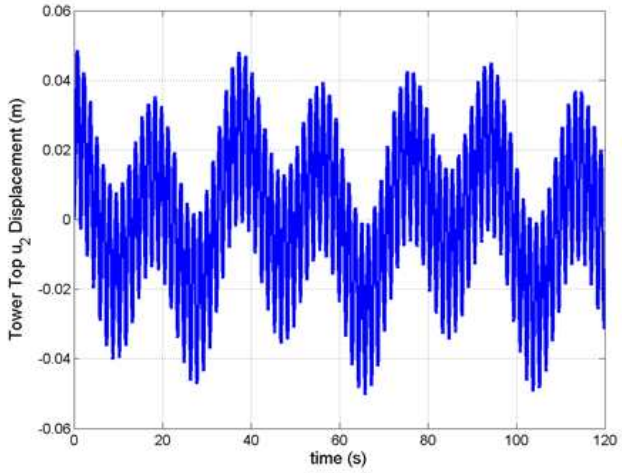

Figure VII.46. Tower top motion as a result of platform sway step relaxation

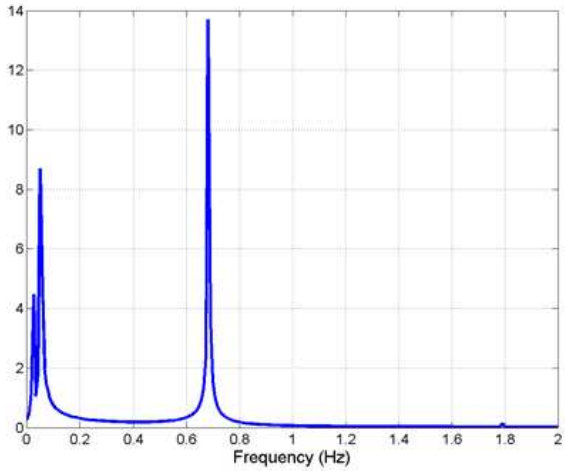

Figure VII.47. FFT of tower top motion as a result of platform sway step relaxation

VII.C.2.b. Combined sway and roll motion under external forcing on flexible structure

The tower structure was excited by applying a force of 1×10^6 N for 1 second to the tower top in the sway direction. This would bring about sway and a roll rotation of the platform. The platform was initially stationary in this verification exercise. After 1 second, the excitation force was removed and the natural response of the system was observed. Figures VII.48 and VII.49 show the history of platform sway motion and the FFT of this motion respectively. Figures VII.50 an VII.51 show the history of platform roll motion and the FFT of this motion respectively. Figures VII.52 and VII.53 show the history of tower tip displacement in the h_2 direction as well as the FFT of this motion respectively.

Again, periodicity is difficult to confirm given the interplays of various system modes. Frequencies of 0.050, 0.68, and 1.79 Hz are observed in the tower motion, the lower being representative of the low frequency platform roll motion and the higher being representative of the tower structural motion. Furthermore, a frequency of the 0.025, 0.05, and 0.68 Hz is observed in the platform sway motion, and frequencies of 0.05, 0.68, and 1.79 Hz are apparent in platform roll motion. Closer inspection of the FFT of platform sway motion reveals a small irregularity in the smooth FFT distribution around 1.79 Hz. This suggests there is some impact of the higher frequency structural motion on the frequency content of the tower although the forcing as a result of higher modes of structural vibration is minimal compared to restoring forces acting on the platform and the lower frequency platform motion. The frequency of 0.025 Hz apparent in the platform sway motion is not visible in the platform roll

or tower motion frequency. However, this frequency was observed in all rigid and flexible structural modes in the platform step relaxation exercise. Thus, it is possible that the coupling of this mode into the platform roll and tower motion is relatively minimal compared to other system motions during the step relaxation test. These results are tabulated in Table VII.6, and confirm consistency between the predictions in the platform motions and structural motions.

Table VII.6. Platform sway/roll and tower frequency content (Hz) as a result of tower forcing

Platform Sway	Platform Roll	Tower Motion
0.025	-	-
0.05	0.05	0.05
0.68	0.68	0.68
1.79 (slight)	1.79	1.79

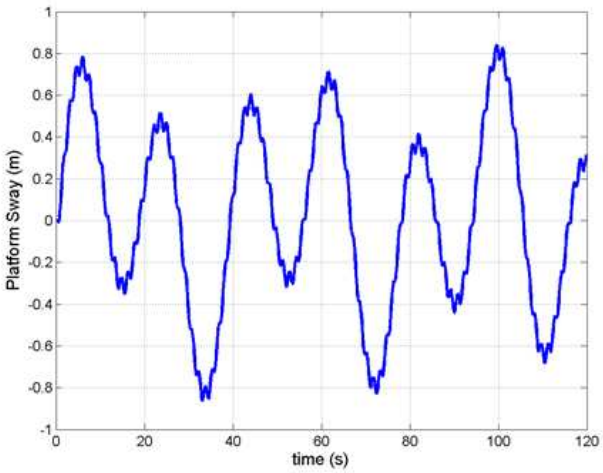

Figure VII.48. Platform sway motion as a result of tower forcing

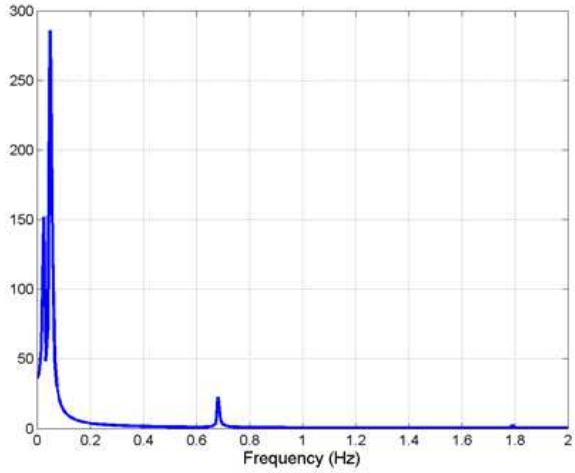

Figure VII.49. FFT of platform sway motion as a result of tower forcing

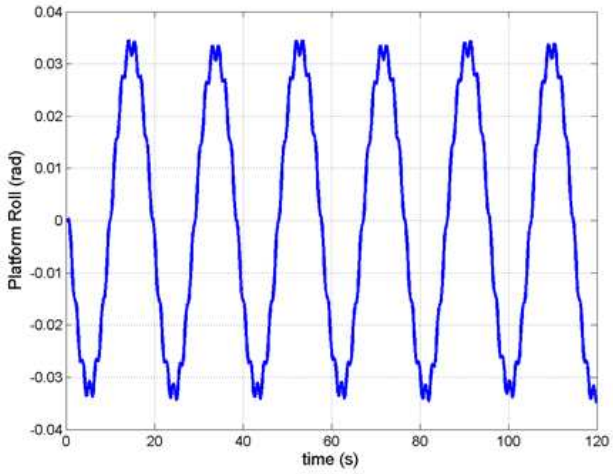

Figure VII.50. Platform roll motion as a result of tower forcing

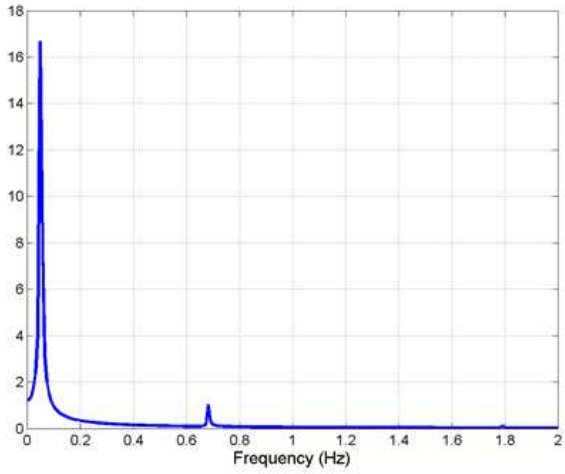

Figure VII.51. FFT of platform roll motion as a result of tower forcing

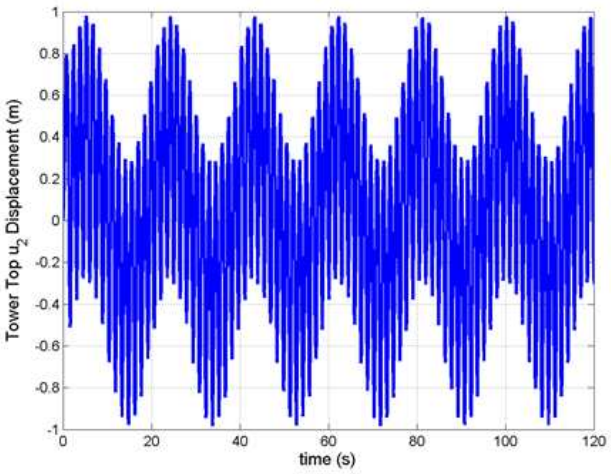

Figure VII.52. Tower top motion as a result of tower forcing

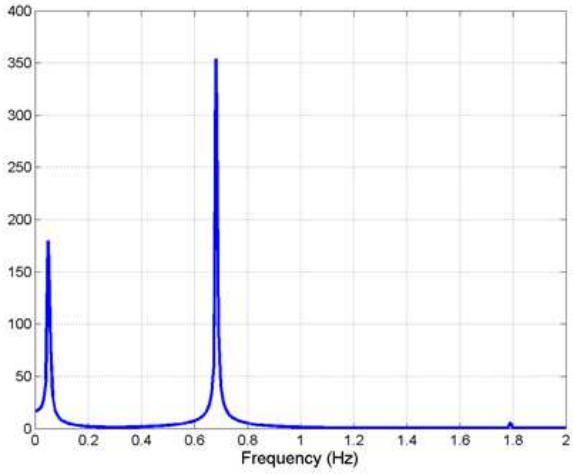

Figure VII.53. FFT of tower top motion as a result of tower forcing

VII.C.2.c. Sensing wave excitation frequency via structural motion

The representative platform/turbine structure configuration was subjected to regular wave excitation with a period of 7 seconds and wave height of 2 meters using the wave excitation functionality in WavEC. All six platform degrees of freedom were active in the simulation, as well as gravity, buoyancy, and damping effects. One minute of simulation time was considered. A regular wave excitation period of 7 seconds corresponds to a wave excitation frequency of 0.14 Hz. This excitation should be evident in the platform motion, and this is confirmed in the surge motion history (and FFT) shown in Figures VII.54 and VII.55 respectively. A peak in the FFT of approximately 0.14 Hz is clear in both platform surge and heave (not shown here), representative of the regular wave excitation frequency. Furthermore, Figures VII.56 and VII.57 show the tower top motion and FFT respectively. An obvious peak around 0.14 Hz is also evident in the FFT of tower motion. This indicates that the regular wave excitation of the platform is manifesting itself in the structural motion of the attached flexible structure.

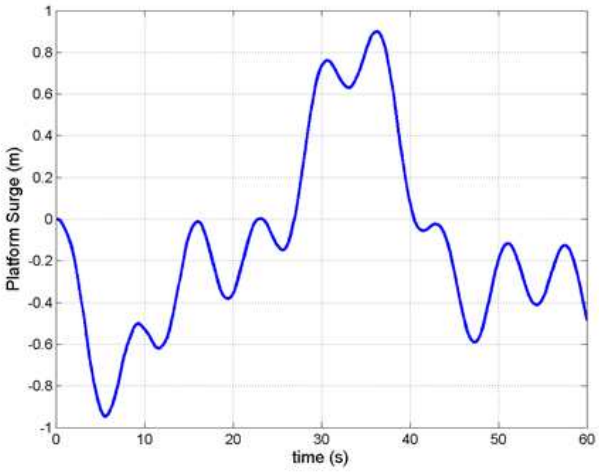

Figure VII.54. Platform surge motion as a result of wave excitation

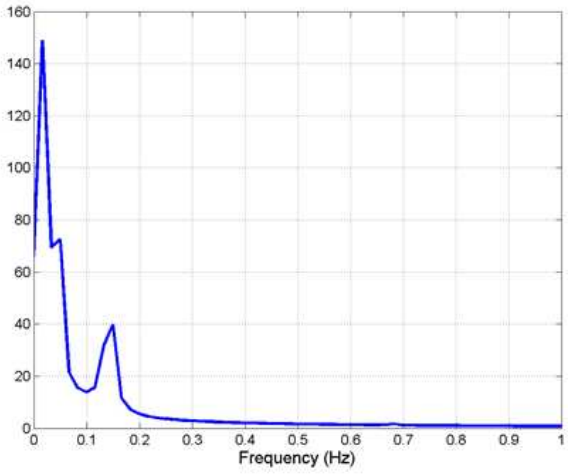

Figure VII.55. FFT of platform surge motion as a result of wave excitation

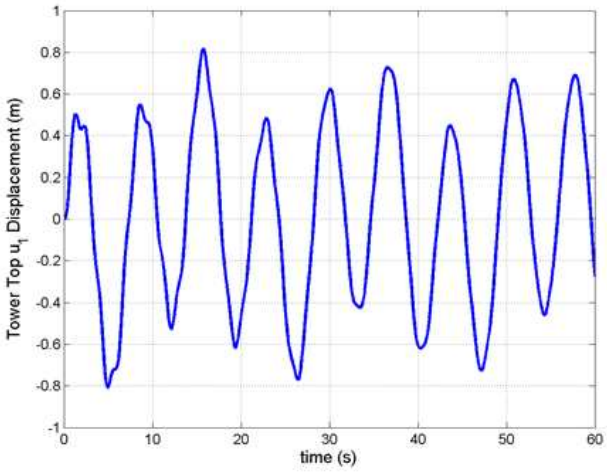

Figure VII.56. Tower top motion as a result of wave excitation

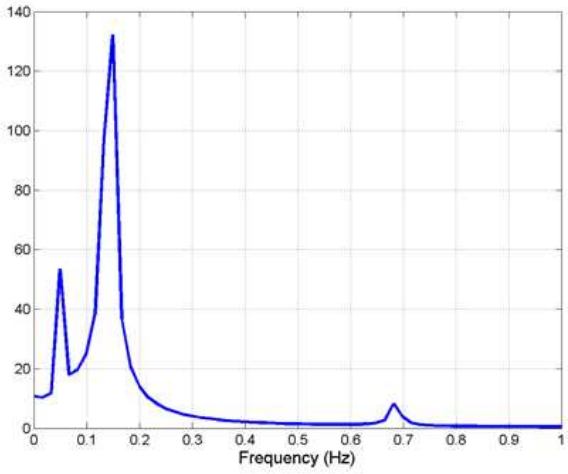

Figure VII.57. FFT of tower top motion as a result of wave excitation

VII.D. Demonstration of coupling to aerodynamics software

The core structural dynamics analysis capability in the OWENS toolkit was interfaced to the Sandia National Laboratories CACTUS VAWT aerodynamics software [38]. The standard version of CACTUS considers a rigid rotor in aerodynamic load calculations, and a one-way coupling was implemented between OWENS and CACTUS. That is, aerodynamic loads calculated using CACTUS are applied in the OWENS structural dynamics analysis, but structural deformations do not influence the load calculations. A modified version of CACTUS will consider structural deformation in load calculations, and future work will interface this modified aerodynamics code into OWENS with two-way coupling.

The one-way coupling of aerodynamics loads allows CACTUS analysis to be performed "offline" and loads to simply be mapped and applied to the structure. Mapping is performed through simple interpolation from the aerodynamic domain or "grid" used to spatially discretize blade geometry in an aerodynamic analysis. If necessary, loads at a specific time in the structural dynamics simulation can be calculated by interpolation of the load history calculated using CACTUS.

The configuration employed in this demonstration was the same idealized 34-meter VAWT from previous demonstrations (shown in Figure VII.1). The rotor was prescribed to rotate at a constant rotor speed of 30 RPM, and a constant, uniform wind speed of 8.9 m/s was considered. The normal and tangential aerodynamic loads obtained at the mid-span location of a blade are shown in Figure VII.58. The loads at the various blade sections of the CACTUS grid were mapped and applied to the nodes of the OWENS finite element mesh and the resulting radial and edgewise

motions of a blade mid-span location are shown in Figure VII.59. In these plots, time has been normalized by the rotor period of revolution T.

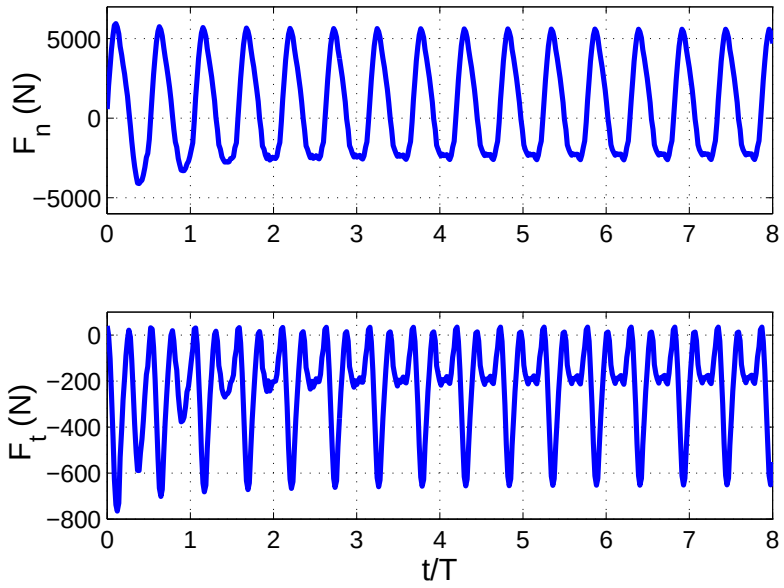

Figure VII.58. Normal and tangential force history at blade midspan generated with CACTUS

Aside from some start up conditions, the loads settle into a periodic state within the first few rotor revolutions. The resulting displacements are bounded and have a similar periodic behavior. This has demonstrated the one-way coupling capability of OWENS to the CACTUS VAWT aerodynamics software. As mentioned, future analysis will make use of two-way aeroelastic coupling as modified aerodynamics software becomes available.

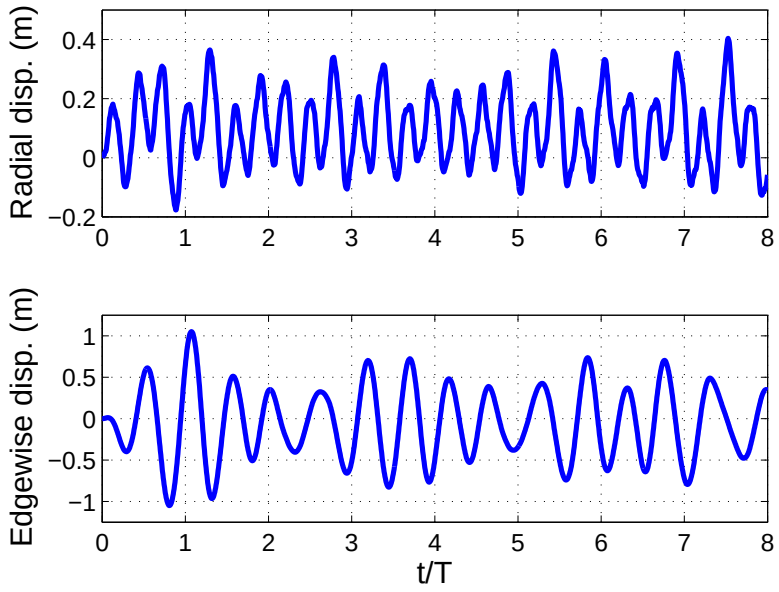

Figure VII.59. Radial and edgewise displacement history of blade midspan under CACTUS loads

VII.E. Conclusions

This chapter presented a demonstration and baseline verification of features and coupling to external modules implemented in the Offshore Wind Energy Simulation toolkit. A reduced order structural model implemented in the OWENS toolkit was also demonstrated and verified in this chapter. This verification effort considered a VAWT configuration analyzed using a full order model via the conventional finite element implementation, which served as a reference solution for the comparison of reduced order models. Both linear and nonlinear reduced order models were verified for a VAWT configuration under full rigid body motion, including translational accelerations and angular velocities and accelerations. Verification exercises revealed that linear reduced order models could capture dominant motion with a relatively

minimal subset of lower system modes. It was also shown that nonlinear reduced order models require more careful selection of the modes the reduced order model is constructed from to ensure reasonable agreement with full order model predictions.

Various rotor operation modes implemented in the OWENS toolkit were demonstrated in this chapter. These included specified rotor speed profiles without generator effects, while others demonstrated a two-way coupling between the structural dynamics analysis capability and a generator module. The ability to simulate a turbine in a generator start up mode and well as a self starting turbine were demonstrated with baseline verification procedures. For the various scenarios considered, the structural response of a representative turbine was examined and a successful coupling between the core structural dynamics analysis capability and a generator module was demonstrated.

This chapter also demonstrated the coupling of the WavEC platform dynamics/hydrodynamics analysis software to the core structural dynamics capability in the OWENS analysis framework through baseline verification procedures. Results were presented which demonstrated the two-way coupling for combined sway/roll motion of a platform along with vibration of the flexible structure. It was shown that platform motion could excite motion in the flexible structure and vice versa. Furthermore, frequency content in rigid body modes and structural vibration were shown to be consistent, indicating a successful coupling between the two analysis codes. The platform was also subjected to regular wave excitation, and it was shown that the wave excitation frequency could be extracted from the vibrational motion of the attached flexible structure. Finally, a simple demonstration of one-way cou-

pling to the CACTUS VAWT aerodynamics software was presented. Future work will focus on a two-way coupling as aerodynamics modules are enhanced to enable this capability.

CHAPTER VIII

STRUCTURAL DYNAMICS OF VERTICAL-AXIS WIND TURBINES

This chapter presents an initial design impact study for assessing the dynamic stability of large multi-megawatt deepwater offshore VAWTs. Understanding the modal dynamics of a system is useful for gaining insight into the fundamental behavior of a system before a large number of loading scenarios are considered. Furthermore, identification of potential instabilities at the initial design stage is critical for proactively mediating undesirable response of a system. The analysis and understanding of very large, highly flexible VAWT structures is further complicated by the rigid body modes of a floating support structure.

In this chapter, two particular types of instabilities in VAWTs are considered, viz., structural dynamic resonance and aeroelastic flutter. First, resonance is considered, followed by aeroelastic stability in a later section. Resonance is a common concern in rotating structures and a known issue in previous VAWT designs [2,87,88]. Dynamic aeroelastic instability or flutter can be a concern for lift-generating structures under aerodynamic loads. Coupling of aerodynamic forcing with a structure's natural modes can lead to large amplitude diverging motion. Recent studies have shown that flutter is a potential issue in very large HAWT blades [59, 60, 64, 89] and may be a concern for very flexible multi-megawatt VAWT structures under large aerodynamic loads as well. Flutter has been observed in smaller-scale VAWT designs [22]. Indeed, for an equivalent power rating, a VAWT design must have much larger (and likely more flexible) blades than a HAWT design. This detail accentuates

the concerns for flutter instabilities.

Previous research investigated smaller scale land-based VAWTs and resonance and flutter concerns were identified. The support conditions or boundary conditions, however, are known to dramatically influence the modal behavior (natural frequencies and mode shapes) of the structural dynamic system [88,90,91]. Thus, it is imperative to understand the behavior of a deepwater offshore turbine affixed to a platform (floating condition) relative to a land-based turbine (fixed condition). In addition, the presence and stability of additional rigid body modes for the floating case should be assessed along with elastic modes. Previous investigations have studied the effects of support condition on the tower modes of offshore HAWTs [92] as well as aeroelastic stability of HAWT configurations [93]. Nevertheless, the fundamental difference between VAWT and HAWT configurations require unique design considerations and design analysis techniques.

This effort will employ the Offshore Wind Energy Simulation toolkit for VAWTs to investigate the stability of floating VAWT configurations. Validation procedures of the OWENS toolkit for VAWTs in Chapter A have demonstrated the ability of the tool to predict the modal response of a rotating land-based VAWT configuration. Herein, the influence of a floating platform configuration on the structural modes of a VAWT is investigated. The goal of such an investigation is to obtain a fundamental understanding of the interplay of platform support conditions and the structural modes of a rotating VAWT structure. Furthermore, the effect of the large rotating structure on the rigid body modes of the turbine/platform system should be analyzed. Resonance concerns for rotating structures are commonly identified by inspecting the

natural frequencies of a system for coincidence with per-rev excitations. For a VAWT, the sensitivity of tower mode resonance to a particular per-rev excitation is closely tied to the number of blades employed in a configuration. Therefore, a fundamental understanding of per-rev resonance sensitivities as a function of number of blades is also sought in this work.

VIII.A. Understanding critical per-rev excitations for tower resonance

Historically, tower resonance has been a concern for vertical-axis wind turbines [2]. Tower mode frequencies vary with respect to rotor speed and "per-rev" crossings may exist on a Campbell diagram within the operating range of a VAWT. Nevertheless, the sensitivity of a VAWT structure to certain per-rev excitations is strongly dependent on the number of blades employed in a VAWT configuration because tower excitation is primarily due to forcing on the attached blades. Previous work developed "rules of thumb" [94] based off of experimental observations [2] of a limited number of VAWT configurations. Herein, a more fundamental understanding of tower forcing frequency content for a VAWT with an arbitrary number of blades is considered.

An analytical expression for frequency content is developed for tower forcing represented in both a rotor-fixed, rotating frame as well as an inertially fixed frame. An important realization is that a harmonic force represented in an inertially fixed frame will have different frequency content than that represented in a rotating frame. Thus, care must be taken to ensure the per-rev excitation is expressed in a frame that is consistent with that used in modal analysis of a rotating structure. The

analytical expressions for per-rev excitations are "numerically validated" using the CACTUS [38] aerodynamics software by examining the effective (collective) tower forcing for VAWT configurations with various numbers of blades.

VIII.A.1. Development of an analytical expression for tower forcing frequency content for a VAWT with an arbitrary number of blades

The effective harmonic forcing on a single blade may be expressed as

$$F_i^{(m)}(\Theta) = \sum_{n=0}^{N_p} \bar{F}_i^{(n)} \cos(n\Theta)\, \hat{b}_i \tag{8.1}$$

$$\Theta = \Omega t + \bar{\phi}^{(m)} \tag{8.2}$$

Such that $F_i^{(m)}$ is the i_{th} component of forcing on the m_{th} blade. $\bar{F}_i^{(n)}$ is the amplitude of forcing associated with an n per-rev excitation, N_p is the number of per-rev excitations considered in constructing the harmonic forcing on a single blade, Θ is the azimuth of blade m, and $\hat{b}_i$ represents a blade fixed frame. Furthermore, Ω is the rotor speed, t is time, and $\bar{\phi}^{(m)}$ is the azimuth of blade m at $t = 0$. This n per-rev harmonics present in this forcing term are due to changes in blade angle of attack as rotor spins at some angular velocity. Indeed, nonlinear system (such as the aerodynamic system representing the flow around a rotating VAWT) are known to have a response with frequencies as multiples of input frequency (such as rotor speed in this case).

Figure VIII.1 illustrates the various frames considered in this development including a blade fixed frame (b_i), a co-rotating/hub fixed frame (h_i), and an inertially fixed frame (n_i). The excitation frequency on a single blade may be monitored by a

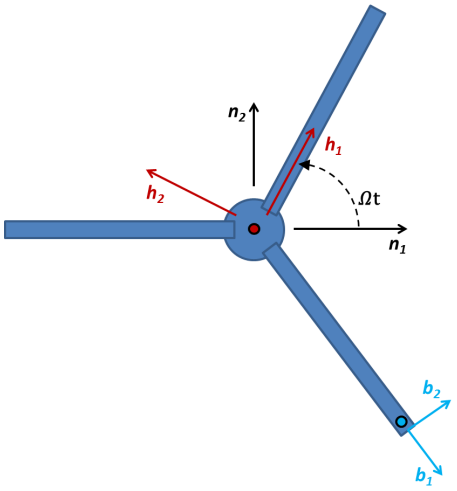

Figure VIII.1. Illustration of various coordinate systems considered in blade/tower forcing

sensor placed on the blade (the blue dot in Figure VIII.1) and measured in a local blade frame (b_i) as shown in the expressions above.

For convenience, let the time be normalized by the period of rotor revolution $\left(\tilde{t} = \frac{t}{T}\right)$. Such that $T = \frac{2\pi}{\Omega}$.

$$F_i^{(m)}\left(\tilde{t}\right) = \sum_{n=0}^{N_p} \bar{F}_i^{(n)} \cos\left(n\left[2\pi\tilde{t} + \bar{\phi}^{(m)}\right]\right) \hat{b}_i \tag{8.3}$$

The contribution of forcing on blade m to the forcing on the tower may be accounted for by transforming the effective force on the blade to account for the azimuth of the blade in the co-rotating/hub frame. The transformation from the co-rotating frame to the blade frame is described by a single-axis rotation matrix about the rotor angular velocity axis (h_3/n_3 axis). This frame is illustrated in Figure VIII.1

as the h_i frame.

$$\left[C_H^B\left(\bar{\phi}^{(m)}\right)\right] = \begin{bmatrix} \cos\bar{\phi}^{(m)} & \sin\bar{\phi}^{(m)} & 0 \\ -\sin\bar{\phi}^{(m)} & \cos\bar{\phi}^{(m)} & 0 \\ 0 & 0 & 1 \end{bmatrix} \tag{8.4}$$

$$F_{Hi}^{(m)}\left(\tilde{t}\right) = C_H^{B^T} F_i^{(m)}\left(\tilde{t}\right) \tag{8.5}$$

The contribution of forcing on a blade may also be coordinatized in a fixed frame by transforming the effective force to account for the instantaneous position of the blade in the rotor azimuth. This frame is illustrated in Figure VIII.1 as the $\hat{n}_i$ frame.

$$\left[C_N^B\left(2\pi\tilde{t} + \bar{\phi}^{(m)}\right)\right] = \begin{bmatrix} \cos\left(2\pi\tilde{t} + \bar{\phi}^{(m)}\right) & \sin\left(2\pi\tilde{t} + \bar{\phi}^{(m)}\right) & 0 \\ -\sin\left(2\pi\tilde{t} + \bar{\phi}^{(m)}\right) & \cos\left(2\pi\tilde{t} + \bar{\phi}^{(m)}\right) & 0 \\ 0 & 0 & 1 \end{bmatrix} \tag{8.6}$$

$$F_{Ni}^{(m)}\left(\tilde{t}\right) = C_N^{B^T}\left(\tilde{t}\right) F_i^{(m)}\left(\tilde{t}\right) \tag{8.7}$$

The effect of all blade loadings on the overall tower forcing is simply a summation of the previous equations over the total number of blades. The effective tower loading measured by a sensor on the rotating VAWT tower (such as that shown in the red dot on Figure VIII.1) can be expressed as:

$$F_{Hi}\left(\tilde{t}\right) = \sum_{m=1}^{N_{blades}} F_{Hi}^{(m)}\left(\tilde{t}\right) \tag{8.8}$$

Furthermore, the effective tower loading in a fixed frame can be expressed as:

$$F_{Ni}\left(\tilde{t}\right) = \sum_{m=1}^{N_{blades}} F_{Ni}^{(m)}\left(\tilde{t}\right) \tag{8.9}$$

A Fourier transform of these expressions is employed to examine the frequency content of tower forcing as a result of aerodynamic forces on blades.

For the tower forcing components coordinatized in the co-rotating frame the Fourier transform(only considering positive frequencies) is:

$$\begin{aligned} F_{H1}(n_t) &= \mathscr{F}\left[F_{H1}\left(\tilde{t}\right)\right] \\ &= \sum_{m=1}^{N_{blades}} \sum_{n=0}^{N_p} \frac{1}{2}\left(\bar{F}_1 \cos\bar{\phi}^{(m)} - \bar{F}_2 \sin\bar{\phi}^{(m)}\right) e^{in\bar{\phi}^{(m)}} \delta\left(n_t - n\right) \end{aligned} \tag{8.10}$$

$$\begin{aligned} F_{H2}(n_t) &= \mathscr{F}\left[F_{H2}\left(\tilde{t}\right)\right] \\ &= \sum_{m=1}^{N_{blades}} \sum_{n=0}^{N_p} \frac{1}{2}\left(\bar{F}_1 \sin\bar{\phi}^{(m)} + \bar{F}_2 \cos\bar{\phi}^{(m)}\right) e^{in\bar{\phi}^{(m)}} \delta\left(n_t - n\right) \end{aligned} \tag{8.11}$$

$$F_{H3}(n_t) = \mathscr{F}\left[F_{H3}\left(\tilde{t}\right)\right] = \sum_{m=1}^{N_{blades}} \sum_{n=0}^{N_p} \frac{1}{2} \bar{F}_3 e^{in\bar{\phi}^{(m)}} \delta\left(n_t - n\right) \tag{8.12}$$

Such that n_t is the per-rev frequency of tower excitation as viewed in the rotating hub frame, and n is a per-rev excitation experienced by a blade.

For the tower forcing coordinatized in a fixed frame the Fourier transform(only considering positive frequencies) is:

$$\begin{aligned} F_{N1}(\bar{n}_t) &= \mathscr{F}\left[F_{N1}\left(\tilde{t}\right)\right] \\ &= \sum_{m=1}^{N_{blades}} \sum_{n=0}^{N_p} \frac{1}{4}\Big[\left(\bar{F}_1 - i\bar{F}_2\right) e^{i(n-1)\bar{\phi}^{(m)}} \delta\left(\bar{n}_t - (n-1)\right) \\ &+ \left(\bar{F}_1 + i\bar{F}_2\right) e^{i(n+1)\bar{\phi}^{(m)}} \delta\left(\bar{n}_t - (n+1)\right)\Big] \end{aligned} \tag{8.13}$$

$$\begin{aligned} F_{N2}(\bar{n}_t) &= \mathscr{F}\left[F_{N2}\left(\tilde{t}\right)\right] \\ &= \sum_{m=1}^{N_{blades}} \sum_{n=0}^{N_p} \frac{1}{4}\Big[\left(\bar{F}_2 + i\bar{F}_1\right) e^{i(n-1)\bar{\phi}^{(m)}} \delta\left(\bar{n}_t - (n-1)\right) \\ &+ \left(\bar{F}_2 - i\bar{F}_1\right) e^{i(n+1)\bar{\phi}^{(m)}} \delta\left(\bar{n}_t - (n+1)\right)\Big] \end{aligned} \tag{8.14}$$

$$F_{N3}(\bar{n}_t) = \mathscr{F}\left[F_{N3}\left(\tilde{t}\right)\right] = \sum_{m=1}^{N_{blades}} \sum_{n=0}^{N_p} \frac{1}{2} \bar{F}_3 e^{in\bar{\phi}^{(m)}} \delta\left(\bar{n}_t - n\right) \tag{8.15}$$

Such that $\bar{n}_t$ is the per-rev frequency of tower excitation as viewed in a fixed frame.

VIII.A.2. Validation of analytical per-rev tower excitation expressing using CACTUS aerodynamics software

The analytical expressions for per-rev tower excitations as a function of number of blades were employed to predict per-rev excitations in both a fixed and rotating frame for VAWTs with 1 to 7 blades. To numerically validate these predictions, the CACTUS [38] aerodynamics software was employed to calculate blade loads that were processed to calculate effective tower loads. These loads were expressed in both rotating and fixed frames and a fast Fourier transform was employed to extract frequency content for comparison of numerically predicted per-revs to those predicted by the analytical expression. Note that only the transverse tower excitations (both fore-aft and side-to-side) were considered in this study as these are of most significant concern in tower resonance.

The VAWT configurations modeled in CACTUS were of the Darrieus type. A constant wind speed and rotor speed were specified. A single blade geometry was chosen and n-bladed VAWTs were modeled using uniform azimuth spacing of blades. No attempt was made to maintain constant rotor solidity across the various configurations. Thus, the magnitude of forcing and power output of the turbines varied with respect to number of blades. Nevertheless, the frequency content of forcing (which is being validated in this study) is independent of rotor solidity and directly related to the number of blades employed in a turbine configuration.

First, the assumed per-rev blade forcing frequency is verified through comparison to forcing on a single blade as predicted via a CACTUS simulation. Figure VIII.2 shows the effective radial blade load vs. azimuth for a single blade. Figure VIII.3

presents a Fast-Fourier Transform (FFT) of the blade effective radial load, with peaks at the per-rev frequencies of 0,1,2,3,4,5,...,N. The same trends are seen in Figures VIII.4 and VIII.5 for the effective edgewise loading on a single blade.

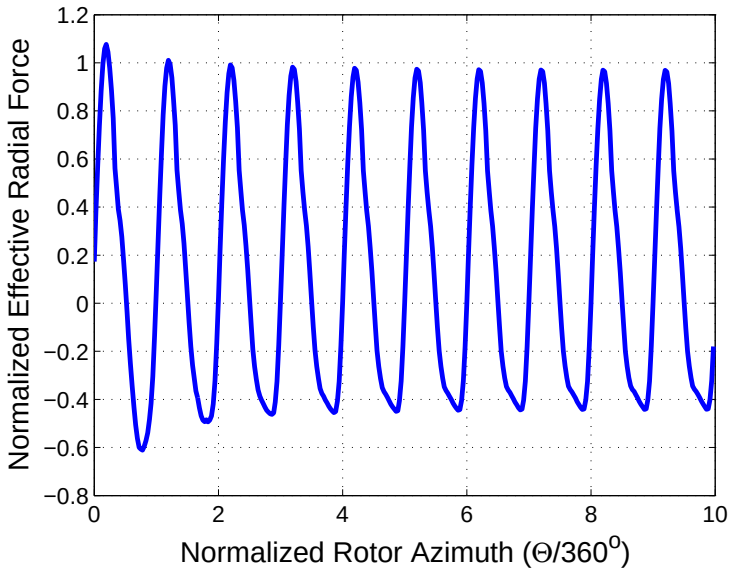

Figure VIII.2. Effective radial force on a single blade vs. normalized azimuth

Table VIII.1 shows the analytical and numerical predictions for per-rev tower excitation for both fixed and rotating frames for VAWT configurations with various numbers of blades. The results of the numerical predictions validate the results of the analytical model. Furthermore, it is noteworthy that for certain configurations a 1 per-rev excitation measured in the hub frame is manifested as a 0 per-rev or constant excitation in the hub-frame. In this case, the 1 per-rev excitation viewed in the rotating frame is an artifact of the coordinate transformation and is not a

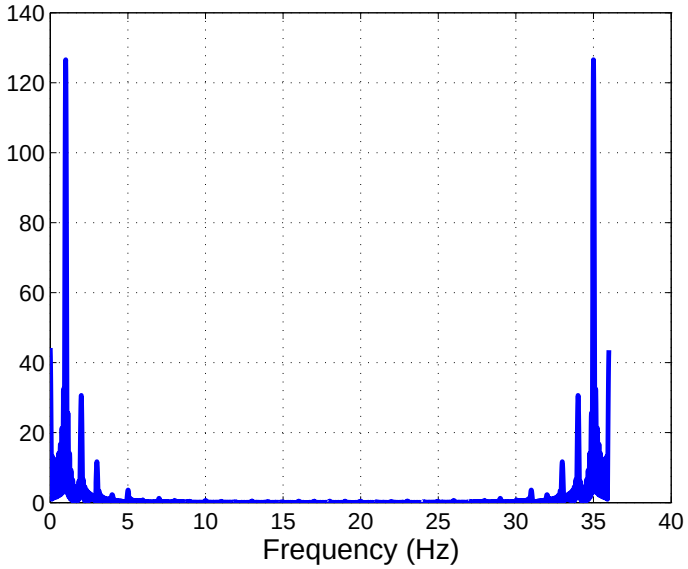

Figure VIII.3. FFT of effective axial force on a single blade vs. normalized azimuth

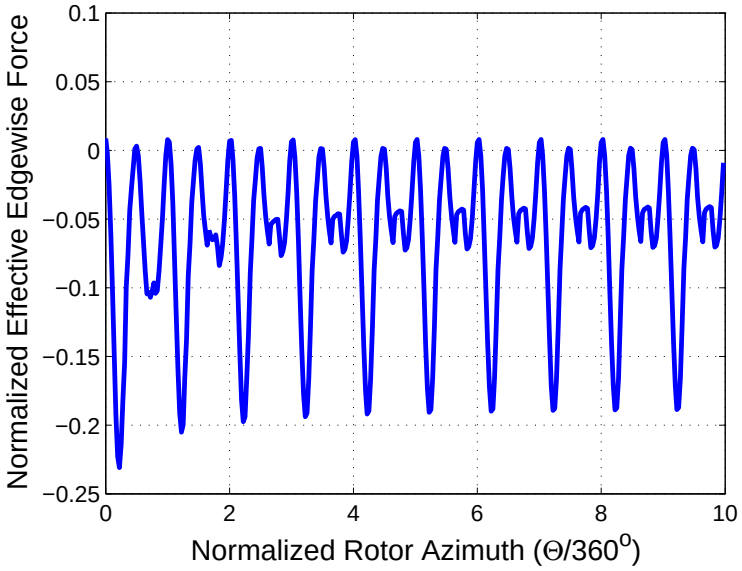

Figure VIII.4. Effective edgewise force on a single blade vs. normalized azimuth

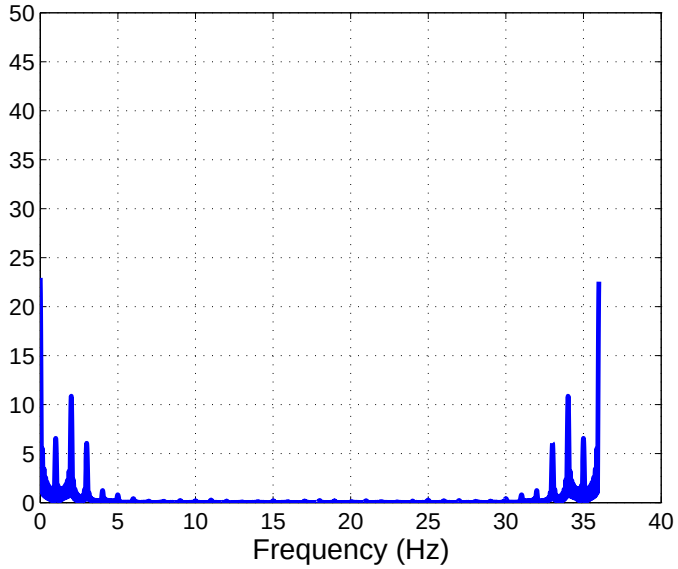

Figure VIII.5. FFT of effective edgewise force on a single blade vs. normalized azimuth

true harmonic excitation from which resonance could result. For example, for one and two-bladed VAWTs a 1 per-rev excitation in the rotating frame manifests as a constant and 2 per-rev excitation in the fixed frame. Thus, for these configurations a 1 per-rev excitation in the rotating hub-frame could drive tower resonance. The analytical expressions also reveal that for VAWTs with 3 or more blades, a 1 per-rev excitation in the hub-frame will only manifest as a constant force in the fixed-frame. Thus, the 1 per-rev excitation in the hub-frame for these configurations will not drive resonance.

Inspection of Table VIII.1 shows certain patterns in the fixed and hub frame per-rev excitations with respect to number of blades. A recursive formula for the i-th critical per-rev excitation as a function of number of blades may be developed

Table VIII.1. Numerical validation of per-rev tower forcing

# of Blades	Fixed-frame (analytical)	Fixed-frame (CACTUS)	Hub-frame (analytical)	Hub-frame (CACTUS)
1	0,1,2,3,4,5	0,1,2,3,4,5	1,2,3,4,5	1,2,3,4,5
2	0,2,4,6,8,10	0,2,4,6,8,10	1,3,5,7,9	1,3,5,7,9
3	0,3,6,9,10,12	0,3,6,9,10,12	1,2,4,5,7	1,2,4,5,7
4	0,4,8,12,16,20	0,4,8,12,16,20	1,3,5,7,9	1,3,5,7,9
5	0,5,10,15,20,25	0,5,10,15	1,4,6,9,11	1,4,6,9,11
6	0,6,12,18,24,30	0,6,12	1,5,7,11,13	1,5,7,11,13
7	0,7,14,21,28,35	0,7,14	1,6,8,13,15	1,6,8,13,15

as shown below. For $N_{blades} \leq 2$, hub frame per-rev excitations are:

$$n_t(i) = \begin{cases} 1 & i = 1 \\ n_t(i-1) + 2 - mod(N_{blades}, 2) & i > 1 \end{cases} \tag{8.16}$$

For $N_{blades} > 2$, hub frame per-rev excitations are:

$$n_t(i) = \begin{cases} 1 & i = 1 \\ n_t(i-1) + 2 + (N_{blades} - 4)|mod(i, 2) - 1| & i > 1 \end{cases} \tag{8.17}$$

Fixed frame per-rev excitations are:

$$\bar{n}_t(i) = (i-1)\, N_{blades} \quad i = 1, 2, ..., N \tag{8.18}$$

VIII.A.3. Interpretation of critical per-rev excitations

These analytical expressions for per-rev tower excitations due to blade loads are useful for understanding the sensitivity of certain VAWT configurations to tower resonance. Modal analysis of a VAWT structure is typically conducted within a co-rotating frame. Thus, the excitation frequencies should also be considered in this frame for consistency to ensure meaningful resonance predictions. Typically, one

constructs a Campbell diagram and inspects the various system modes for per-rev crossings. As shown in this section, the effective tower excitation is sensitive to the number of blades and not all per-rev tower mode crossings can drive resonance. Furthermore, certain configurations show 1 per-rev tower forcing in the co-rotating frame which is not true harmonic forcing, and is merely an artifact of transformations between a co-rotating and fixed frame. With these considerations in mind, Table VIII.2 shows the critical hub-frame per-rev excitations for VAWTs with various numbers of blades. Typically, lower per-rev excitations pose a more significant resonance concern than higher per-revs. Nevertheless, the first 4 per-rev excitations for each VAWT configuration (1-10 blades) are shown. Note that this work has sought to characterize the effects of blade forcing on tower excitation. Other forces acting on the system may give rise to other resonance concerns.

Table VIII.2. Critical per-rev tower resonance design sensitivities (hub-frame)

# of Blades	Per-Rev Sensitivity	Example Configuration
1	1,2,3,4	
2	1,3,5,7	SNL 17-m [2], SNL 34-m [2], DeepWind [87]
3	2,4,5,7	VAWTPower VP60 [88]
4	3,5,7,9	
5	4,6,9,11	
6	5,7,11,13	Lux [95]
7	6,8,13,15	
8	7,9,15,17	
9	8,10,17,19	
10	9,11,19,21	

VIII.B. Initial system design studies on support structure influence of the Sandia 34-meter VAWT

This section presents representative dynamics analysis of a VAWT turbine for various offshore support conditions. The Sandia 34-meter VAWT (without guy wires) is considered as the baseline VAWT configuration in this initial study. Guy wires were removed to to make the baseline configuration more comparable to those deployed offshore which are not likely to make use of guy wire systems. First a ground fixed scenario is considered, followed by a 20- and 30-meter monopile support condition, and a floating platform configuration. The Campbell diagrams of each configuration are generated and the effect of the support type on the modal response of a rotating turbine is considered. In each case, the impact of support structure on resonance concerns is assessed.

VIII.B.1. Monopile support structure

A monopile support foundation was considered by extending the tower properties of the Sandia 34-meter 500 kW VAWT from the turbine base as shown in Figure VIII.6. The boundary condition at the monopile base was a simple cantilevered condition. This is believed to be adequate for examining trends in initial design studies, and more detailed future analysis should make use of more accurate modeling of foundation and hydrodynamic effects as required. Modal analysis of the ground fixed (land-based) and monopile configurations was conducted for rotor speeds of 0 to 50 RPM (the maximum operating speed was 38 RPM for the land-based design). Figures VIII.7, VIII.8, and VIII.9 show the Campbell diagrams for tower, flatwise,

and edgewise modes respectively.

Figure VIII.6. Illustration of 34-meter VAWT on monopile

Historically, resonance in tower modes has been a concern for VAWT structures and Figure VIII.7 suggests the monopile support configuration exacerbates this concern. The monopile support lowers the parked frequencies of tower modes and results in lower crossing of per-rev excitations. Employing the analytical expression for critical per-rev tower mode excitation of a two-bladed VAWT design suggests that 1, 3, and 5 per-rev crossings of tower modes on a Campbell diagram are of concern, with lower per-rev crossings of lower tower modes being more likely to drive resonance. It is notable that while the land-based machine has a potential 1 per-rev resonance at 35 RPM, the 20- and 30-meter monopile configurations have 1 per-rev resonances at 17 and 13 RPM respectively. Similar trends are observed for 3 per-rev tower mode resonances. The land-based configuration has an upper tower mode crossing of the 3 per-rev excitation at about 35 RPM, while the 20- and 30-meter monopile configurations cross this per-rev excitation at 17 and 12 RPM respectively. The lower

tower modes of the land-based, 20-, and 30-meter monopile cross the 3 per-rev excitation at around 17, 8, and 7 RPM respectively. A 5 per-rev crossing of the upper tower mode for the land-based configuration also occurs at 17 RPM, although higher per-rev crossing do not typically pose significant resonance concerns.

Inspecting higher tower modes reveals some interesting behavior for the monopile configurations. The monopile support lowers modal frequencies of the 2nd tower modes closer to frequencies of other system modes. As a result, 2nd tower modes do not exhibit the continuous linearly increasing/decreasing behavior with respect to rotor speed seen for the 1st tower modes. Indeed, the tower mode is seen to shift from one continuous mode to another on the Campbell diagram. Figure VIII.7 illustrates this phenomenon using solid and dashed lines in the 2nd tower modes. For example, the lower 2nd tower mode of the 30-meter monopile configuration begins at one mode, but shifts to another mode around a rotor speed of 15 RPM. This other mode was originally a flatwise mode with a slight tower mode component due to the free tower top boundary condition. As a rotor speed of 15 RPM was approached, the two modes began to interplay and a "hybrid" mode develops that is a combination of tower and flatwise modes. Beyond 15 RPM the mode shapes "swap" and once again become more distinct mode shapes. This phenomenon has been termed "frequency veering" and "mode localization" [96,97] and typically occurs when two modes have similar frequencies, common mode shape attributes, and are varying with some parameter (such as rotor speed in the current study). A similar trend is seen with the 20-meter monopile configuration, but around 40 RPM. This time the tower mode interplays with a edgewise mode with a slight tower component.

The 20-meter monopile configuration shows a 2nd tower mode 5 per-rev crossing at around 38 RPM, while the 30-meter monopile configuration has a 40 RPM 3-per rev crossing and a 26 RPM 5 per-rev crossing. Resonance in higher tower modes was not found to be a concern for the land-based configuration.

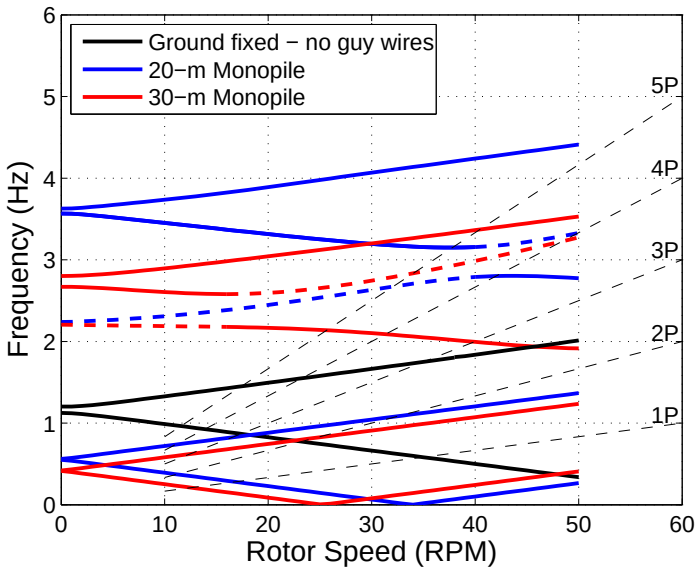

Figure VIII.7. Tower mode Campbell diagrams: 34-meter VAWT on monopile

Figure VIII.8 shows the effect of the monopile support on flatwise modes of the turbine appear to be minimal, with a slight reduction in flatwise mode frequencies compared to the ground fixed VAWT. Herein, mode labeling for the 34-meter VAWT adopts the convention presented in Appendix A and that from previous investigations of this turbine [2]. Overall, the Campbell diagram trends are very similar. One distinct difference is seen for the 2nd antisymmetric flatwise mode of the 30-

meter monopile configuration, which has a distinct decrease in modal frequency for increased rotor speed. The free boundary condition at the turbine top allows for some tower motion in this mode which begins to interplay with the lower 2nd tower mode due to the veering phenomenon discussed earlier.

Figure VIII.9 shows the monopile support has a more noticeable effect on edgewise modes. The lowest edgewise mode (the first "propeller" mode) is slightly influenced by the monopile support conditions, and for longer monopiles, the frequency of this mode is reduced. A noticeably different trend is observed for the 2nd edgewise mode (the first "butterfly" mode). For the 20-meter monopile an increase in modal frequency is apparent, while a decrease occurs for the 30-meter monopile. Again, this is believed to be due to the interplay of this mode with the 2nd tower modes of the system due to the veering phenomenon. For the 20-meter monopile, this coupling occurs with a tower mode that is increasing in frequency due to rotor speed, while the opposite is true for the 30-meter monopile. Higher edgewise modes are difficult to distinguish between other system modes for the monopile configuration due to the shifting of mode frequencies and the resulting coupling. Thus, they will not be discussed here.

Overall, this initial study shows the monopile support significantly reduces the tower mode frequencies of an offshore VAWT configuration and results in resonance concerns at lower rotor speeds. For very large, multi-megawatt VAWT configurations a monopile configuration is expected to further reduce very low frequency modes. The significance of this frequency reduction, however, will be related to the relative length of the monopile support to the scale of the very large VAWT design.

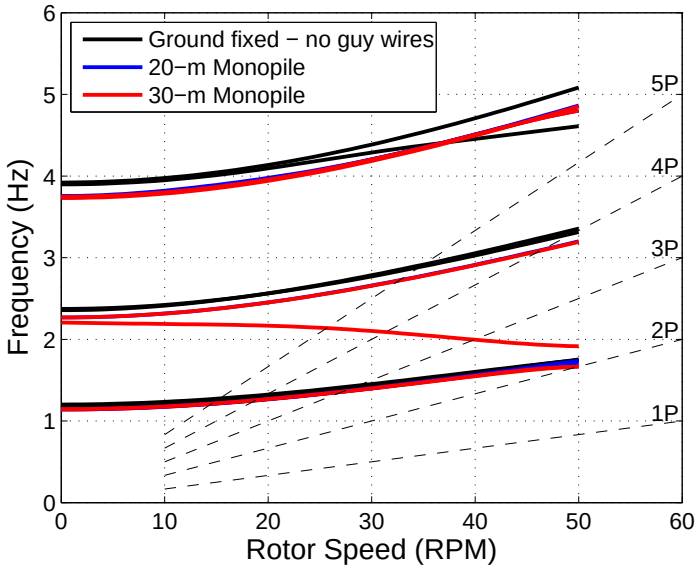

Figure VIII.8. Flatwise mode Campbell diagrams: 34-meter VAWT on monopile

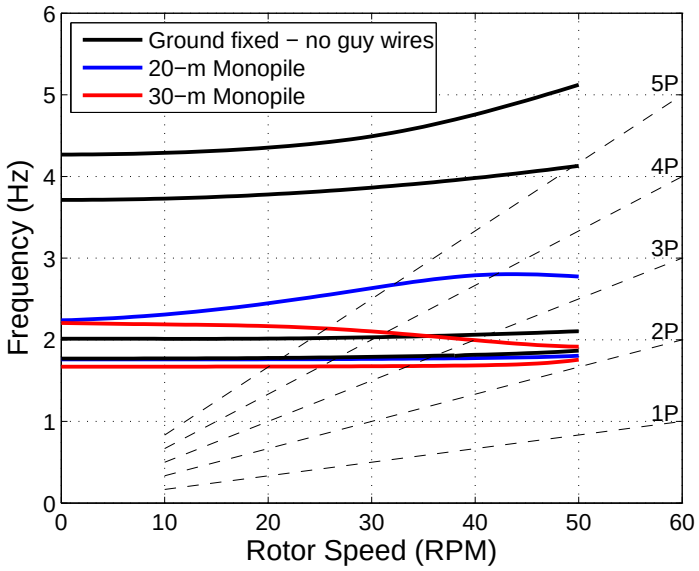

Figure VIII.9. Edgewise mode Campbell diagrams: 34-meter VAWT on monopile

VIII.B.2. Barge/floating support structure

Deployment of VAWTs in deepwater offshore environments will likely make use of floating platform configurations, as monopile configurations are undesirable in a deepwater environment due to installation costs. Furthermore, as identified in the previous section, monopile support structure has potentially detrimental effects on resonance concerns in a VAWT structure. A scaled version of the ITI Energy Barge [92] was considered for an initial design study of an existing VAWT design on a floating support structure. This barge was designed for use with the NREL offshore 5-MW turbine [98], and power laws were used to scale platform mass and inertia properties for use with the Sandia 34-meter 500 kW turbine. This scaling provides a starting point for initial platform dynamics studies on an existing utility scale VAWT. Linear translational and rotational springs were attached to the platform, and the parked rigid body frequencies of the platform/turbine configuration were tuned to those from the ITI Energy Barge/5-MW turbine configuration [92] as shown in Table VIII.3. An approach for employing a Gyric finite element framework for initial design studies of rigid body modes of a floating platform is presented in Appendix D. As before, a Campbell diagram was generated for rotor speeds of 0 to 50 RPM, and the modal response of the system was observed for potential resonance concerns. The flatwise and edgewise modes of the turbine were not significantly affected by the floating support condition, and only tower modes will be discussed herein.

Figure VIII.10 shows the floating platform support system increases the first tower modes of the system from about 1.2 Hz to about 1.53 Hz (a 27.5% increase) for the parked configuration. This increase in natural frequency is due to the floating

Table VIII.3. Rigid body mode frequencies of platform/scaled barge system

Mode	Frequency (Hz)
Surge	0.0076
Sway	0.0076
Heave	0.1283
Roll	0.0980
Pitch	0.0980
Yaw	0.0198

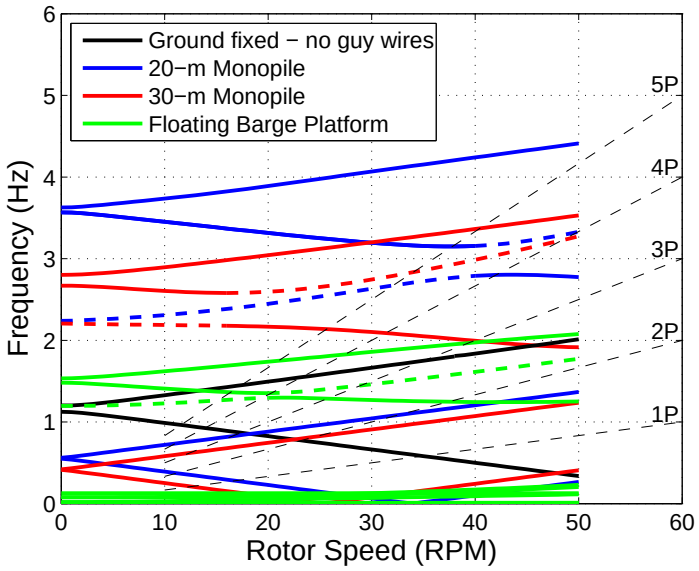

Figure VIII.10. 1st Tower mode and rigid body mode Campbell diagrams for 34-meter VAWT with various support conditions

platform providing a boundary condition to the turbine base that is more like a free boundary condition. Indeed, this may be qualitatively verified by comparing the increased modal frequencies of a "free-free" beam compared to a "fixed-free" beam [99]. Inspection of the Campbell diagram for the floating configuration shows a larger "resonance-free" range of rotor speeds for tower modes. It is notable that

for the rotor speeds considered, a 1 per-rev tower resonance does not exist for the floating configuration. 3 per-rev resonances of the upper and lower tower mode occur at approximately 39 RPM and 26 RPM respectively. Similar per-rev crossings occurred at 35 and 17 RPM on the land-based configuration and 17 and 8 RPM on the 20-meter monopile configuration. Thus, potential resonance issues are delayed until higher rotor speed, especially when compared to monopile configurations. The effect of support conditions on the parked tower modes of the 34-meter VAWT is summarized in Figure VIII.11.

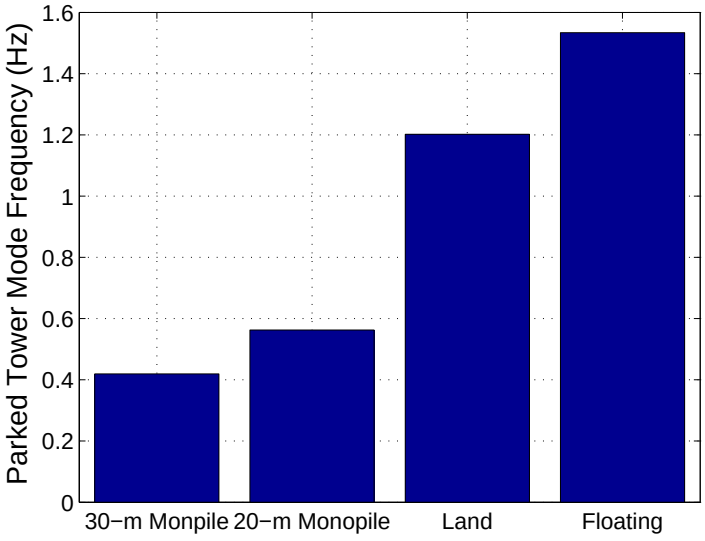

Figure VIII.11. Parked 34-meter VAWT tower mode frequencies for various support conditions

One distinct difference between floating and ground fixed/monopile configurations is the addition of low-frequency rigid body modes for due to the floating

support structure (pitch, roll, yaw, sway, surge, and heave). These rigid body modes are shown in the Campbell diagram of Figure VIII.12. Note that similar to a tower mode, the pitch/roll modes of the turbine are coupled for non-parked conditions. This preliminary design study indicates that a 1 per-rev resonance concern may exist for the rigid body pitch/roll mode of the platform at rotor speeds around 5 RPM. Thus, while the floating platform has the ability to significantly raise tower mode frequencies of a VAWT, alleviating lower per-rev resonance concerns, this comes at the expense of introducing rigid body modes that may be prone to resonance at lower rotor speeds. Appendix C presents a means for assessing the likelihood of rigid body mode resonance for a floating VAWT configuration.

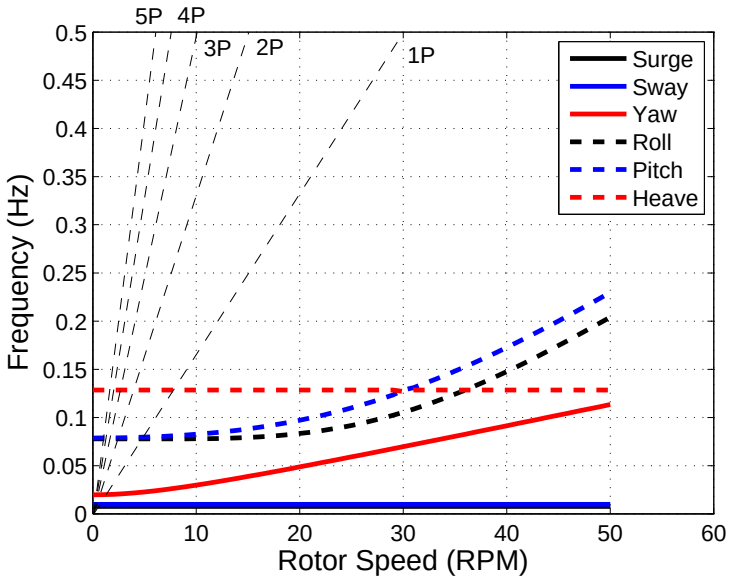

Figure VIII.12. Rigid body mode Campbell diagrams for 34-meter VAWT on floating barge platform

VIII.C. Initial system design studies on support structure influence of a 5MW VAWT configuration

This section presents initial design studies for a multi-megawatt VAWT configuration deployed with a variety of support conditions in an offshore environment. First a land-based scenario is considered to serve as a baseline case. A monopile supported configuration as well as floating barge platform configuration are also considered. Rotational modal analysis of these configurations examines system response at a variety of rotor speeds, seeking to identify potential resonance concerns.

VIII.C.1. Configuration

An initial design of a 5MW Darrieus type VAWT is considered in this analysis. The design features three fiberglass composite blades, affixed at each end to a central, rotating tower. Two horizontal struts provide reinforcing connections between the blade and tower at 5 and 95% of the tower height. The overall height of the VAWT design is 132 meters, and the maximum diameter is 108 meters (height to diameter ratio of 1.22). The maximum chord at the blade roots is 2.57 meters, and minimum chord at the blade equator is 1.92 meters. Operational rotor speed of this initial design is expected to be between 10 and 15 RPM. An illustration of this turbine is presented in Figure VIII.13.

VIII.C.2. Land-based configuration

The three-bladed 5MW VAWT was first considered in the context of a land-based configuration. This would allow for a baseline characterization of the response

Figure VIII.13. Illustration of 5MW VAWT configuration

of a very large VAWT design. A fixed (clamped) boundary condition is prescribed at the tower base and a free condition is prescribed at the tower top. All blade, tower, and strut junctions are modeled as fixed constraints. A Campbell diagram for this configuration is generated by considering pre-stressed modal analysis of the VAWT at various rotor speed equilibrium conditions. That is, an equilibrium condition due to centrifugal and gravity body forces (and the associated "stress stiffening") is obtained at each rotor speed before performing a modal analysis which considers Gyric effects such as spin-softening and Coriolis phenomena.

Figure VIII.14 shows the Campbell diagram for the first 20 modes of the three-bladed 5MW VAWT configuration. Due to the scale of the machine, very low frequency modes are present. Mode labeling is based off of the parked mode shapes, and is classified as either flatwise/radial, edgewise, or a tower mode by the abbreviations "F", "E", or "T" respectively. The preceding number denotes the order of the mode

shape (i.e. 1F is a 1st flatwise mode). As shown on the Campbell diagram in Figure VIII.14, the parked 1st flatwise and edgewise modes have similar frequencies as do the parked 1st tower and 2nd flatwise modes. The introduction of rotational effects results in a coupling of similar, low frequency modes of very large VAWT designs. As noted with the previous investigation of a moderate sized VAWT design, tower modes do not occur in a continuous, smooth manner with respect to increasing rotor speed. Indeed, the frequency veering phenomenon noted in the previous section is present in the lower modes of multi-megawatt VAWT designs. To ensure correct interpretation of the Campbell diagram, care should be taken to inspect the mode shape at critical per-rev crossings.

A number of modes are present on the Campbell diagram in Figure VIII.14. As mentioned before, historically tower modes have been a concern for VAWTs and will be the focus of this discussion. The previous investigation of tower forcing as a result of blade loads indicates a three-bladed VAWT design will have tower mode resonance sensitivity to 2, 4, and 5 per-rev excitations. Inspection of tower mode crossings with the per-rev excitation lines (denoted by the "X" markers) on Figure VIII.14 highlight potential resonance concerns for the land-based 5MW VAWT configuration.

With regards to a two per-rev excitation, the upper and lower 1st tower modes have crossings at 15 and 6.8 RPM respectively. 4 per-rev excitation crossings for the upper and lower tower modes occur at 5.1 and 3.4 RPM respectively, and the corresponding 5 per-rev excitation crossings occur at 3.8 and 2.7 RPM. The 4 and 5 per-rev tower resonances are at lower RPM, below the operating range (10-15 RPM) of the turbine design. It is possible that there is a weaker excitation force

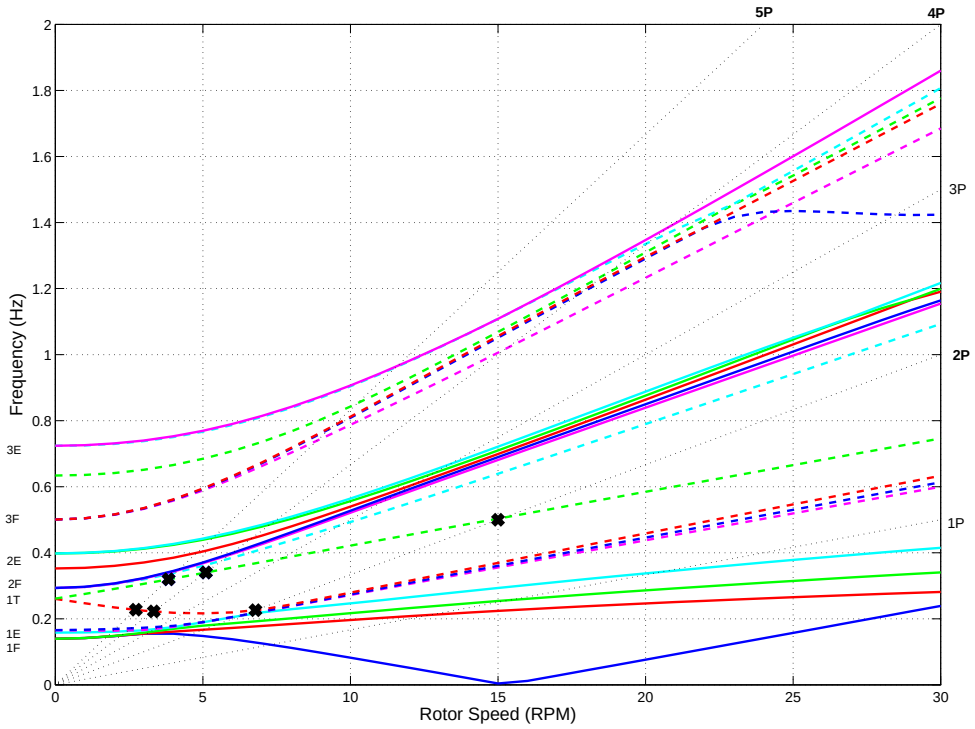

Figure VIII.14. Campbell diagram for 5MW land-based VAWT

associated with these per-rev excitations and the turbine could be operated through this condition without significant concern. The 2 per-rev excitation force, however, is expected to have a more significant magnitude. Interestingly, the frequency veering causes a shallower crossing of a lower tower mode at the 2 per-rev than typically seen on previous VAWT structures [2]. This could be cause for concern as the rotor is operated through this condition. The higher 2 per-rev crossing at 15 RPM is at the upper limit of operating range from initial design specifications. Veering of a 3rd flatwise mode is seen around 23 RPM, and this is due to the interaction of this mode with a higher tower mode, not depicted at earlier RPM (and higher frequency) on the Campbell diagram.

Blade modes are potentially sensitive to all per-rev excitations. A number of 1st blade mode per-rev crossings occur within the operating range of the turbine. Furthermore, a number of 2nd blade modes have higher per-rev crossings between 5 and 13 RPM rotor speed. The degree of resonance concern for these modes will be dependent on the energy associated with higher per-rev excitations and the damping of the associated blade modes. Aeroelastic effects may also provide additional aerodynamic damping to certain system modes, however, these modes are also potentially prone to aeroelastic stability (flutter) concerns. These considerations will be discussed in a subsequent section.

VIII.C.3. Monopile configuration

Next, the 5MW VAWT was considered in the context of an offshore configuration affixed to a 30-meter monopile support. The monopile was modeled as a 30-meter extension of the tower. The connection to the sea-floor foundation was modeled as a simple fixed condition in this initial design study. Figure VIII.15 shows the Campbell diagram for the 30-meter monopile configuration for blade modes up to the 2nd blade edgewise/propeller modes.

As with the 34-meter VAWT the effective increased length of the tower due to the monopile support decreases the natural frequency of tower modes. First tower modes for the parked monopile configuration have frequencies of 0.19 Hz, which is a 27% reduction compared to the land-based design. As can be seen by contrasting the Campbell diagrams for the monopile support and land-based VAWT, the tower modes have critical per-rev crossings at lower rotor speeds due to the reduction in

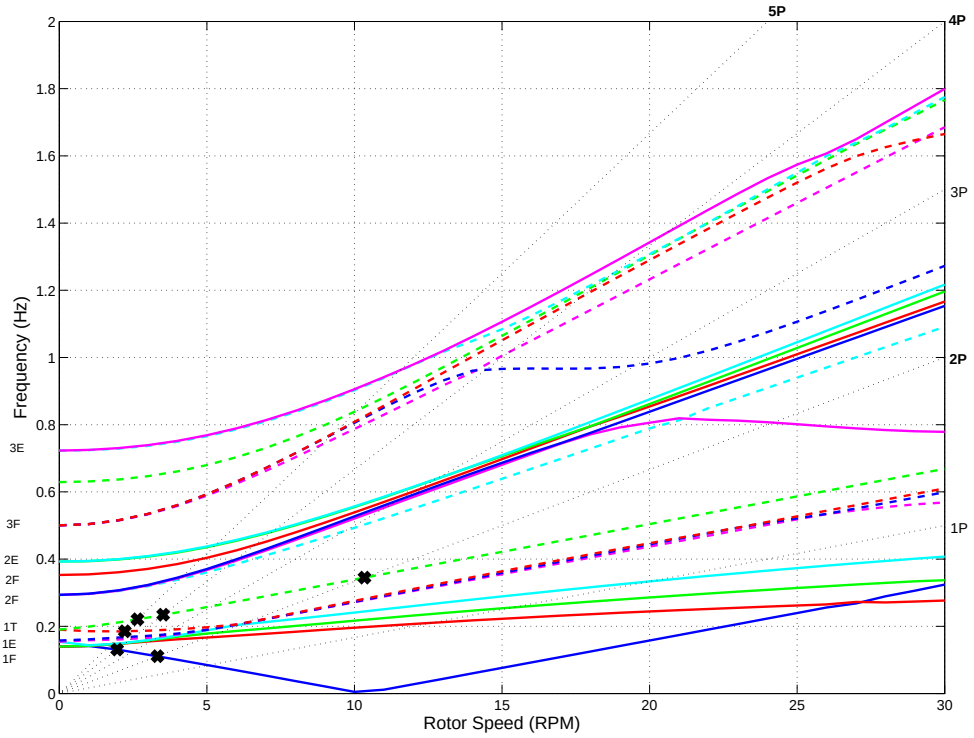

Figure VIII.15. Campbell diagram for 5MW VAWT on 30-meter monopile

tower mode frequencies. Two per-rev tower crossings occur at 3.3 and 10.3 RPM for lower and upper tower modes respectively. This is a significant reduction compared to the land based configuration, especially considering the narrow operating range of the 5MW turbine. 4 and 5 per-rev crossings occur between the rotor speed ranges of 2-3 RPM, again a significant reduction compared to those for the land-based configuration. As seen before, blade modes are relatively unaffected by the change from a ground-based configuration to a 30-meter monopile configuration. Any change in blade modes is primarily due to the veering interaction with higher tower modes that have reduced frequencies as a result of the monopile support.

VIII.C.4. Floating configuration

The aforementioned 5MW VAWT was also considered in the context of an offshore configuration, affixed to a floating platform. The ITI barge platform [92] was considered in this study. For this platform, translational and torsional springs were attached to the based of the turbine and tuned to the rigid body frequencies shown in Table VIII.3. An approach for employing a Gyric finite element framework for initial design studies of rigid body modes of a floating platform is presented in Appendix D. As with other support configurations, blade modes were not significantly affected by support condition, and the tower and rigid body modes of the system were of primary interest. Figure VIII.17 shows the Campbell diagram for the 5MW VAWT with ITI barge platform. Note that the low frequency content and interplay of modes results in the tower mode appearing in various modes in a discontinuous manner due to frequency veering.

The floating support condition significantly increases the frequencies associated with the tower mode. Parked tower modes are increased to 0.67 Hz, a 159% increase compared to the land-based configuration. As a result 2 per-rev crossings of tower modes are delayed until to 18 and 22 RPM, which are outside the operating range of the turbine. The 4 per-rev upper and lower tower mode crossings occur at 10.8 and 9.7 RPM respectively. 5 per-rev upper and lower tower mode crossings occur at 8.5 and 7.7 RPM respectively. These are within the operating range of the turbine and may need to be considered in the refinement of future turbine/platform designs. Nevertheless, the floating support conditions appears to provide a means to alleviate the low tower frequencies apparent in very multi-megawatt offshore VAWT configu-

rations. Figure VIII.16 presents a summary of the parked tower mode frequencies of the 5MW VAWT for various support conditions.

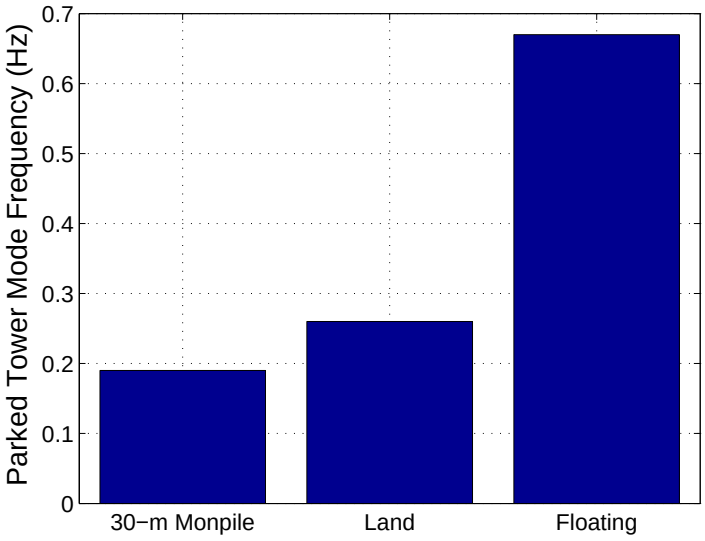

Figure VIII.16. Parked 5MW VAWT tower mode frequencies for various support conditions

This increase in tower mode frequencies comes at the expense of introducing six rigid body modes into the floating system. Overall, only the yaw rigid body mode is appears to be significantly affected by rotor speed, although there is some slight increase in the pitch and roll rigid body modes. Since the tower provides the connection between the turbine and the platform support, platform forcing from the turbine/aerodynamic loads is expected to have the same frequency content as the tower forcing. Thus, the expressions for critical per-rev tower excitations as a function of number of blades are applicable to critical per-rev platform excitations.

Inspection of Figure VIII.17 shows pitch and roll rigid body modes having critical per-rev crossings at approximately 3 RPM and below. Appendix C presents a general means for assessing the likelihood of rigid body mode resonance for a floating VAWT configuration.

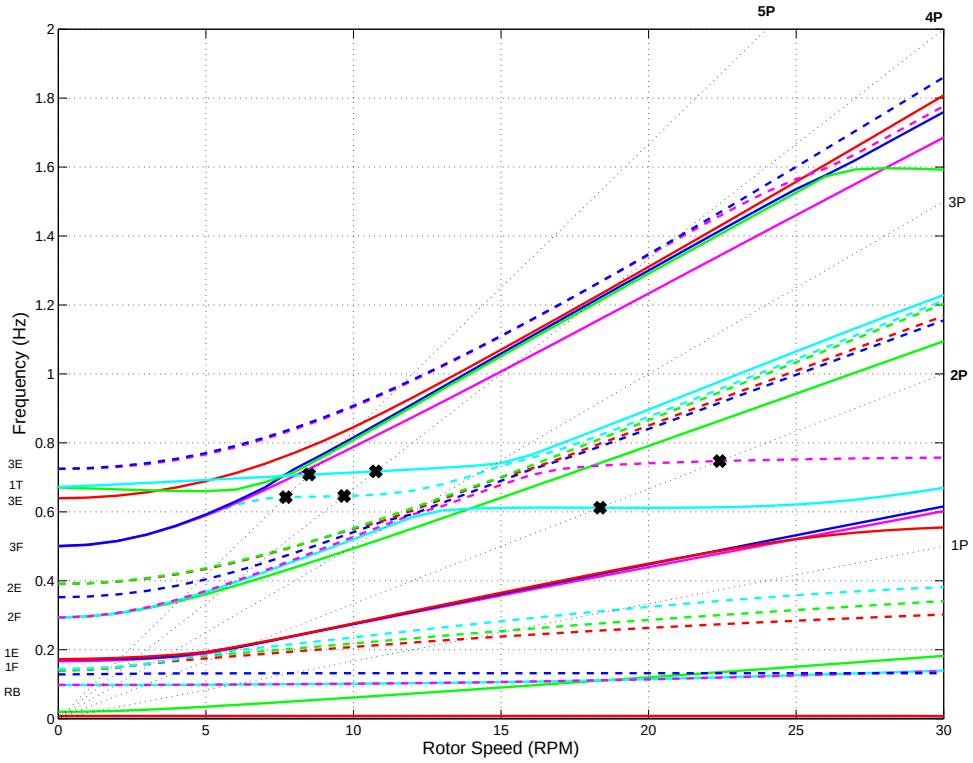

Figure VIII.17. Campbell diagram for 5MW VAWT on barge platform

VIII.D. Initial aeroelastic stability analysis of 5MW VAWT configuration

The low frequency modes associated with a very large VAWT structure, along with high tip-speed ratios make the configuration prone to aeroelastic instability. Accordingly, the aeroelastic capability discussed in Chapter VI was implemented in the OWENS toolkit. This "self-contained" analysis capability is independent of external modules and may be used in fundamental design studies for investigating system response. Initially aeroelastic stability analysis was first conducted on an isolated 5MW VAWT blade to assess the aeroelastic characteristics of the blade design alone. Next, the aeroelastic response of the land-based 5MW VAWT system was considered.

VIII.D.1. Aeroelastic analysis of an isolated blade

Initial design studies regarding aeroelastic stability of an isolated VAWT blade considered a pre-stressed modal analysis at rotor speeds of 0 to 30 RPM. These rotor speeds are well beyond the estimated operational speed of the turbine (10-15 RPM). This analysis considered a VAWT blade with a fully-constrained (clamped) boundary condition prescribed at each blade root. The first 10 modes of the blade were considered in this preliminary analysis. These are believed to be the lower modes that could be prone to flutter. More detailed analysis could consider the possibility of flutter in other modes of the system.

Figure VIII.18 shows the frequency and damping trends vs. rotor speed for the aeroelastic system. The labeling of these modes is based off of the mode shape

associated with a parked analysis. Modes denoted with an "F" are flatwise modes while those with an "E" are edgewise. Gyroscopic effects will result in couplings between the various modes and mode shapes are more difficult to label. A number of interesting damping trends occur at the rotor speeds considered. Some modes are lightly aeroelastically damped (be it positive or negative), and structural damping (not considered in this analysis) will increase the damping of these modes further. Other modes show stronger damping trends, and predictions show flutter onset for the first and second flatwise modes at 9.2 and 11.9 RPM respectively. A lighter flutter onset of the first edgewise mode is also seen at lower rotor speed. Figure VIII.19 shows the mode shape associated with the flutter onset around 9.2 RPM. The mode is coupled between an flatwise and edgewise mode shape. This aeroelastic stability analysis of the isolated VAWT blade reveals potential instabilities in or around the operating range of the the turbine and a re-design of the blade may be necessary to alleviate aeroelastic stability concerns. Next, the aeroelastic response of the turbine system will be considered.

VIII.D.2. Aeroelastic analysis of land-based configuration

Initial design studies assessing aeroelastic stability of the 5MW VAWT configuration were performed, considering the entire VAWT structure by employing pre-stressed modal analysis at rotor speeds of 0 to 30 RPM. This land-based configuration has a cantilevered base and free top. The blade roots are fully-constrained to the tower ends. This results in a very different boundary condition on the blade than that considered in the previous section. Furthermore, including three-blades

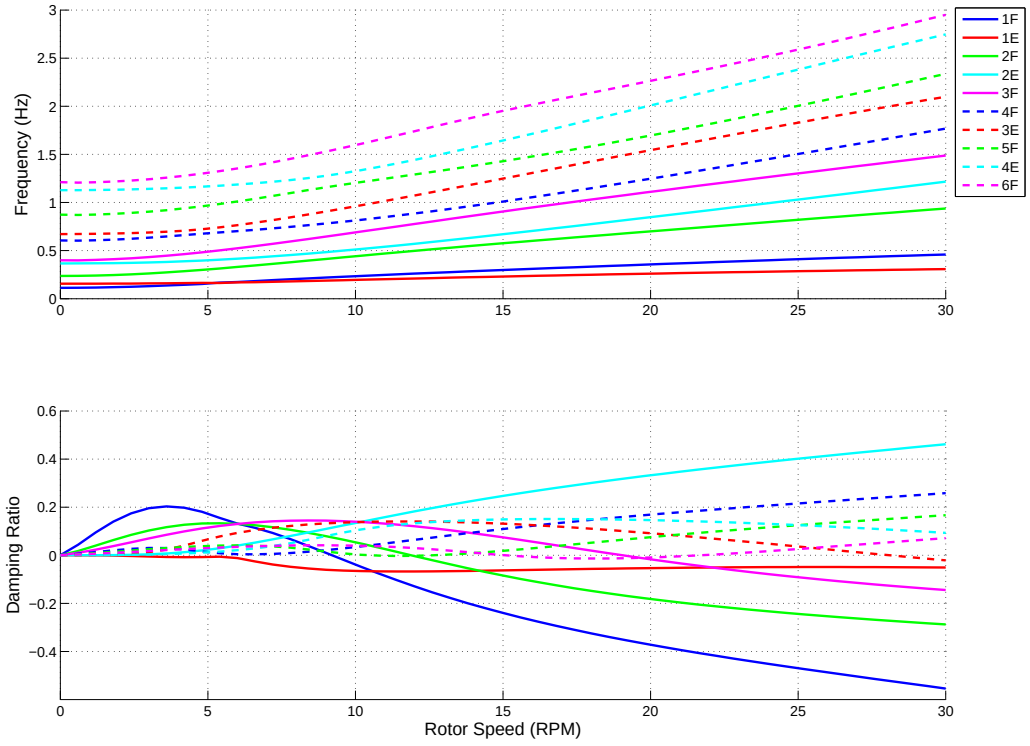

Figure VIII.18. Frequency and damping vs. rotor speed for isolated 5MW blade aeroelastic stability analysis

in the analysis as well as the tower introduces a greater number of modes into the system. The lower 11 modes of the system (up to the second flatwise modes) were considered in this aeroelastic analysis.

Figure VIII.20 shows the frequency and damping vs. rotor speed trends for the land-based 5MW VAWT configuration. As before, mode labeling is based off of the mode shape for the parked configuration. Mode labels are the same as before, but multiple flatwise and edgewise modes exist due to the three-bladed configuration. The number in parentheses serves to provide a unique label to these modes. Some trends are similar to that of the isolated blade analysis, but the three blades of the

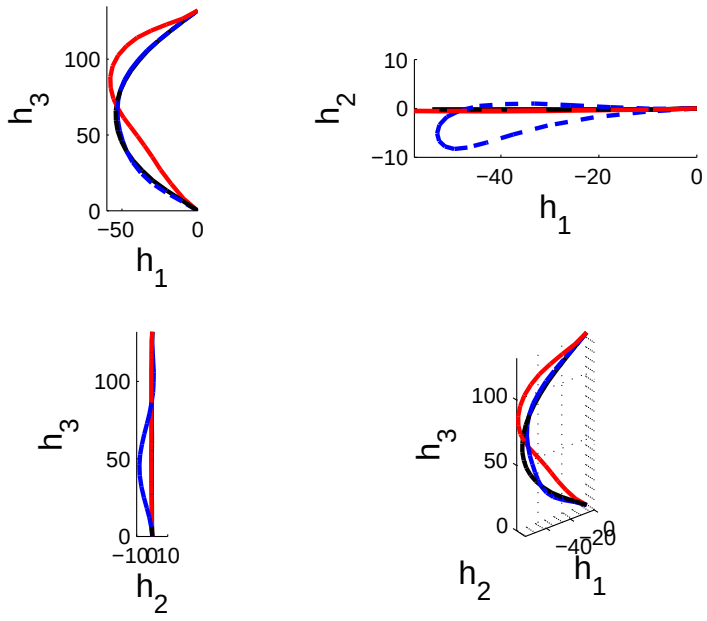

Figure VIII.19. Mode shape of isolated blade 9.2 RPM flutter mode (red: in-phase shape, blue: out-of-phase shape)

VAWT system add additional modes. The first flatwise modes of the system show flutter onset between 8.1 and 9.3 RPM. Additionally, second flatwise modes have flutter onset between 12 and 14 RPM. Inspection of the damping trends also reveals that first edgewise modes have a flutter onset around 4 RPM. These flutter onsets happen in a similar trend as the isolated blade, but at noticeably lower rotor speeds. This is due to the fundamentally different behavior of blade modes as installed on a turbine compared to an isolated blade analysis. Thus, while isolated blade analysis can yield insight into the aeroelastic response of a blade, the response of the blade should also be examined within the context of the entire turbine system.

Figure VIII.21 shows the mode shape for the first flatwise flutter mode at 8.1 RPM. The mode shape consists of coupled first flatwise and first edgewise blade

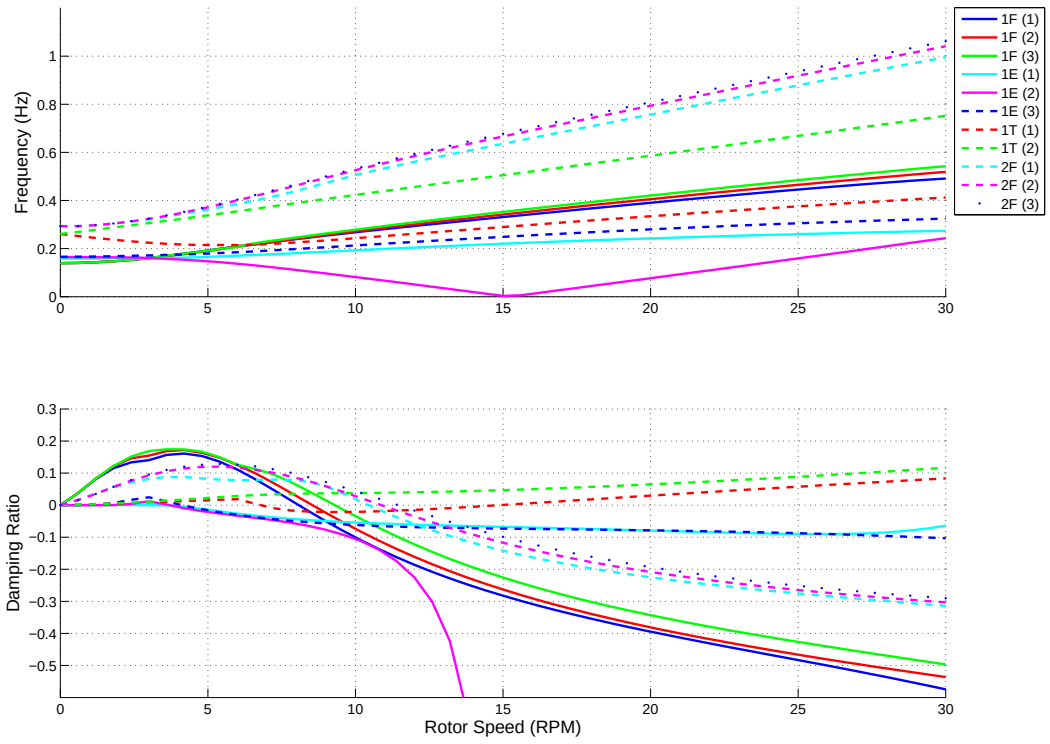

Figure VIII.20. Frequency and damping vs. rotor speed for land-based 5MW VAWT configuration

modes. This is analogous to the "flapping" and "pitching" mode shape of a conventional aircraft wing or HAWT blade under classical flutter. Figure VIII.22 shows the mode shape associated withe the "1st edgewise" mode shown in Figure VIII.20. The mode labeling is based off of the parked mode shape, and inspection of the mode shape at flutter onset reveals that at higher rotor speed this mode has evolved into one that consists primarily of coupled tower modes. Tower modes can result in an effective "flapping" of a VAWT blade, giving rise to this instability. As with the isolated blade analysis, full system aeroelastic analysis suggests blade re-design may be required to mediate aeroelastic instabilities.

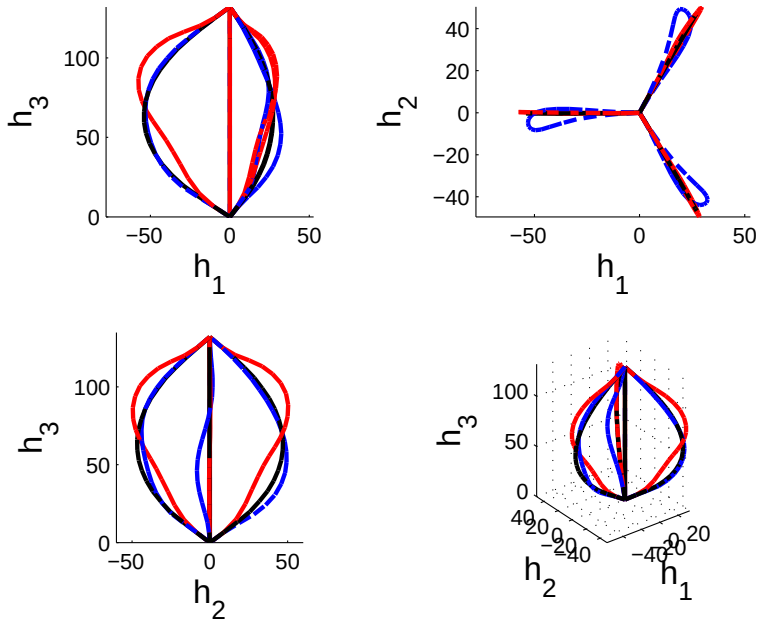

Figure VIII.21. Mode shape of 8.1 RPM VAWT 1st flatwise flutter mode (red: in-phase shape, blue: out-of-phase shape)

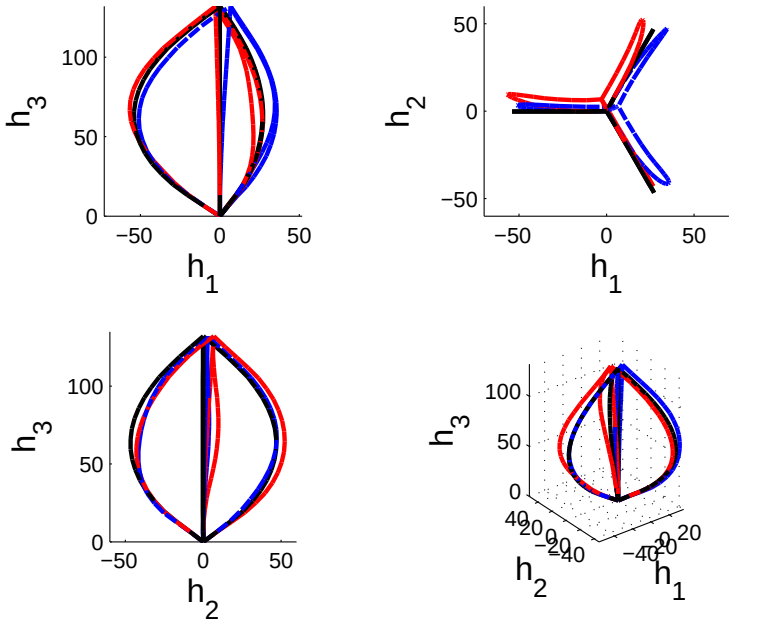

Figure VIII.22. Mode shape of 4 RPM VAWT "1st edgewise" flutter mode (red: in-phase shape, blue: out-of-phase shape)

VIII.E. Conclusions

This chapter has presented an initial design study for assessing the dynamic stability of large multi-megawatt deepwater offshore VAWTs. Historically, tower modes or rotating VAWTs have been prone to resonance due to tower excitations caused by blade loadings. The sensitivity of tower modes to certain per-rev excitation is, however, dependent on the number of blades employed in a VAWT configuration. A greater understanding of this issue was obtained by developing an analytical expression for critical per-rev tower excitation as a function of number of blades. This analytical expression was "numerically validated" by examining the effective tower forcing for various VAWT configurations using the CACTUS VAWT aerodynamics software. This greater understanding of VAWT tower resonance will be invaluable to future VAWT design studies.

An investigation of support structure influence on the modal response of a VAWT was also conducted for a moderate sized 34-meter VAWT configuration and a very large 5MW configuration. Ground-based, monopile, and floating support conditions were considered in these studies. Analysis predictions revealed the monopile configuration served to decrease tower mode frequencies while a floating configuration, which is more like a free support condition, served to increase the frequency of tower modes. This increase in tower frequency for a floating configuration delays critical per-rev crossing until higher rotor speeds and may provide a means to increase the operational rotor speeds of multi-megawatt VAWT configurations compared to land-based and monopile configurations. It was also observed that blade modes were not significantly affected by the support condition.

Aeroelastic stability analysis of an isolated 5MW VAWT blade as well as a land-based 5MW VAWT was considered. Analysis predictions from the isolated blade analysis showed the highly flexible blades, with low frequency modes may be prone to flutter. Considering the land-based VAWT also revealed potential flutter instabilities that may require a re-design to alleviate aeroelastic stability concerns. Future work could consider the aeroelastic stability of VAWT configurations deployed on monopile and floating supports. While some modes of the system are clearly affected by support structure, blade modes (which participate in flutter) appeared to be less sensitive to support condition. Thus, the overall flutter predictions may not be significantly affected by support condition, but this may be confirmed by additional analysis using the OWENS toolkit.

This investigation has also revealed the low frequency nature of modes in multi-megawatt VAWT configurations. Typically, a "hand full" of lower system modes are of interest in examining stability and resonance concerns of a system. The primary justification is that higher modes of a system often occur at higher frequencies and have a greater amount of damping associated with them. Thus, these modes will typically take more energy to excite and are not of immediate concern with regards to resonance. Indeed, previous analysis of moderate sized VAWTs [2] examined a small subset of lower system modes with very good success in predicting system response and identifying primary resonance concerns. The large scale of multi-megawatt VAWT configurations results in a number of system modes with very low frequency. Thus, even "higher" system modes may have frequencies much lower than those that would be seen as the "cut-off" for modes considered in moder-

ately sized, conventional structures. This raises the issue of how many modes should be considered to adequately characterize the response of very large, flexible structure such as the VAWT configuration considered in this section. This concern is only exacerbated by the inclusion of rotational effects, as modal frequencies begin to change with respect to rotor speed. Continued investigation of large VAWT structures with the OWENS toolkit as a design tool that is openly available to the wind energy community is likely to aid in obtaining a better understanding of structural dynamics of very large, rotating structures.

CHAPTER IX

CONCLUSION

This dissertation has presented theoretical developments and practical aspects of dynamic systems with applications to wind energy systems. The primary motivation of this work was the development of a robust design tool for offshore vertical-axis wind turbines (VAWTs). Chapter I discussed the motivation for considering VAWTs for offshore applications, and also presented a literature review on previous VAWT technology and wind energy design tools. It was identified that VAWTs can potentially benefit the needs to reduce cost of energy associated with offshore wind. New design tools, however, would be required to facilitate future development of VAWT technology. Thus, the Offshore Wind ENergy Simulation (OWENS) toolkit has been developed to provide a new, robust VAWT design tool to the wind energy research community. The OWENS toolkit provides a modular analysis framework for considering coupled structural dynamics, aerodynamics, and hydrodynamics analysis of arbitrary VAWT configurations. This chapter will present a chapter summary of the dissertation as well as potential areas for future work.

IX.A. Chapter summary

Chapter II presented an overview of the modular analysis framework considered in the development of the OWENS toolkit. This framework supported the interface of a core structural dynamics solver for flexible, rotating systems to aerodynamics, hydrodynamics, and generator/drive-train modules. A general strategy for coupling

the external modules to a core structural dynamics analysis framework via network sockets was also discussed and a demonstration of coupling strategies on a simple configuration was presented. This chapter also presented the VAWTGen mesh generator, which is capable of generating finite element beam meshes of arbitrary VAWT configurations. This facilitates a high degree of flexibility in developing innovative VAWT designs.

Chapter III presented an energy preserving time integration method for Gyric systems, such as wind turbines. An existing energy conserving time integration methods for flexible systems were proven to be applicable to and energy preserving for Gyric systems. In the process, a thorough development of Gyric systems and energy in Gyric systems was presented. The energy preserving time integration methods were demonstrated on a simple Gyric system, and practical details of implementation into a structural dynamics framework were discussed.

Chapter IV presented a new approach for efficiently developing linear representations of dynamic systems. This process sought to combine existing strategies for developing linearized representations of systems, while eliminating the inherent drawbacks of each. The strengths of each approach were employed to arrive at a powerful and efficient approach for developing linear representations of dynamic systems. This approach was employed in Chapter V to derive a finite element formulation for a "three-dimensional" Timoshenko beam element, with "stress stiffening" effects in a floating frame undergoing general rotational motion. This finite element formulation was implemented into the structural dynamics analysis capability of the OWENS toolkit. This chapter also presented an efficient means for developing a reduced

order model of a VAWT structure represented as an assembly of finite elements.

Chapter VI presented aeroelastic considerations in wind energy systems. Various aeroelastic representations were discussed and modal as well as transient aeroelastic analysis was considered. Aeroelastic stability predictions from modal analysis were contrasted to time-domain approaches, and potential advantages of time-domain approaches in future developments were discussed. The structural dynamics analysis capability in OWENS was also leveraged to develop a new aeroelastic design tool for horizontal-axis wind turbines, and an aeroelastic analysis capability was implemented into the OWENS toolkit for exploring the aeroelastic stability of VAWT configurations.

Chapter VII presented a demonstration of various features in the OWENS toolkit. This included the reduced order modeling capability and various rotor operation modes. A two-way coupling to the WavEC platform dynamics code and a one-way coupling to the CACTUS VAWT aerodynamics code were also demonstrated. Chapter VIII employed the OWENS toolkit to conduct initial design studies of VAWT configurations deployed with offshore support conditions. In particular, the susceptibility of these configurations to tower resonance was investigated. A general analytical expression for identifying critical per-rev excitations for tower resonance of an n-bladed VAWT was also developed. The investigation showed that a floating platform support condition has the potential to raise tower frequencies of VAWT configurations and delay resonance concerns until higher rotor speeds. This could be of significant advantage in multi-megawatt VAWT structures with low frequency tower modes. Initial aeroelastic stability analysis of multi-megawatt VAWT configurations

suggests flutter may be a concern for these large, highly flexible structures.

IX.B. Future work

Future work in the area of direct linearization via quadratic modes may provide a general and robust software implementation of the method. For all but the simplest systems, direct linearization can still be an involved procedure. The method of direct linearization via quadratic modes has provided a well defined form of input for describing a dynamical system and a very well defined procedure for developing linearized equations of motion. While this procedure may appear involved, the well defined form (regardless of the dynamical system) lends itself well to an automated software algorithm. Such a software capability would provide analysts with an efficient means for developing linearized representations of arbitrary dynamical systems.

Furthermore, future work in the area of aeroelastic stability of wind energy systems could seek to consider the periodic nature of wind energy systems. The current modeling approaches for initial aeroelastic design of HAWT blades and VAWT systems discussed in this dissertation neglect periodicity such as time varying inflow, gusts, and gravitational effects. Indeed, neglecting a time-varying gravitational vector on very large and heavy HAWT blade designs may no longer be an adequate assumption when compared to smaller utility scale blades. Future work may seek to investigate methods for aeroelastic stability of periodic systems within the general aeroelastic finite element framework described in this dissertation. This could include investigating efficient techniques for Floquet analysis of aeroelastic systems

or employing transient approaches for unsteady aerodynamics.

The OWENS toolkit is also poised to impact the still developing field of Operational Modal Analysis (OMA). Indeed, OMA has been applied to conventional structures, but very large multi-megawatt VAWT configurations are a special class of flexible, rotating structures. The addition of a floating platform support to these structures is another unique aspect of this configuration. The use of OMA on this unique class of structures will undoubtedly require a robust hardware component, but will also require a modeling component to verify the applicability and identify limitations of OMA with regards to this class of structures. Thus, the OWENS toolkit may serve in modeling efforts associated with OMA of multi-megawatt floating vertical-axis wind turbines.

The OWENS toolkit will continue to be enhanced, including the implementation of a two-way coupling with aerodynamics software. Additionally, other external modules will be implemented as they become available. Indeed, the modular and extensible analysis framework of the OWENS toolkit provides a high degree of flexibility in the future development of the OWENS toolkit. The underlying structural dynamics formulation in the OWENS toolkit may also be further enhanced. This could include higher fidelity structural approaches such as geometrically exact beam theory (GEBT), shell, or even three-dimensional finite element formulations. Furthermore, the general framework of the OWENS toolkit is adaptable to analysis of alternative renewable energy systems such as Marine Hydro-Kinetic (MHK) devices. Thus, the OWENS toolkit is poised to provide a robust and modular analysis capability for renewable energy systems for the foreseeable future.

REFERENCES

[1] Beaudry-Losique, J., Boling, T., Brown-Saracino, J., Gilman, P., Hahn, M., Hart, C., J., J., McCluer, M., Morton, L., Naughton, B., Norton, G., Ram, B., Redding, T., and Wallace, W., "A National Offshore Wind Strategy: Creating an Offshore Wind Energy Industry in the United States," Tech. Rep. DOE/EE-0798, U.S. Department of Energy, Washington, District of Columbia, February 2011.

[2] Sutherland, H. J., Berg, D. E., and Ashwill, T. D., "A Retrospective of VAWT Technology," Tech. Rep. SAND2012-0304, Sandia National Laboratories, Albuquerque, New Mexico, 2012.

[3] Darrieus, G. J. M., "Turbine Having Its Rotating Shaft Transverse to the Flow of Current," U.S Patent # 1834018, December 1931.

[4] Ashwill, T. D., "Initial Structural Response Measurements and Model Validation for the Sandia 34-Meter Test Bed," Tech. Rep. SAND88-0633, Sandia National Laboratories, Albuquerque, New Mexico, 1988.

[5] Ashwill, T. D., "Measured Data for the Sandia 34-Meter Vertical Axis Wind Turbine," Tech. Rep. SAND91-2228, Sandia National Laboratories, Albuquerque, New Mexico, 1989.

[6] Ashwill, T. D. and Veers, P. S., "Structural Response Measurements and Predictions for the Sandia 34-Meter Test Bed," *Proceedings of the 9th ASME Wind Energy Symposium*, 1990, pp. 137–144.

[7] Sutherland, H. J., "On the Fatigue Analysis of Wind Turbines," Tech. Rep. SAND99-0089, Sandia National Laboratories, Albuquerque, New Mexico, 1999.

[8] Sutherland, H., Veers, P. S., and Ashwill, T. D., "Fatigue Life Prediction for Wind Turbines: A Case Study on Loading Spectra and Parameter Sensitivity," *Case Studies for Fatigue Education, ASTM STP 1250*, edited by R. I. Stephens, ASTM, 1994, pp. 174–207.

[9] Ashwill, T. D., J., S. H., and Veers, P. S., "Fatigue analysis of the Sandia 34-Meter Vertical Axis Wind Turbine," *Proceedings of the 9th ASME Wind Energy Symposium*, edited by D. E. Berg, 1990, pp. 145–151.

[10] Van Den Avyle, J. A. and J., S. H., "Fatigue Characterization of a VAWT Blade Material," *Proceedings of the 8th ASME Wind Energy Symposium*, edited by P. Kilmas, 1989, pp. 125–129.

[11] Kilmas, P. C., Gregorek, G., and Sladky, J., "Vertical Axis Wind Turbine Airfoil Treatments: An Update," *Proceedings of the 7th ASME Wind Energy Symposium*, 1988, p. 113.

[12] Schienbein, L. A., "VAWT Aerodynamic Activities at FloWind," *7th Annual VAWT Seminar*, Sandia National Laboratories, Bushland, Texas, April 1987.

[13] Ashwill, T. D., Berg, D. E., Dodd, H. M., Rumsey, M. A., and Sutherland, H. J., "A 34-Meter VAWT Point Design," *Proceedings of the 1991 International Solar Energy Conference*, 1991, pp. 137–144.

[14] Morgan, C. A., Gardner, P., Mays, I. D., and Anderson, M. B., "The Demonstration of a Stall Regulated 100 kW Vertical Axis Wind Turbine," *Proceedings of the European Wind Energy Conference*, European Wind Energy Association, 1989, pp. 645–649.

[15] Price, T. J., "UK Large-scale Wind Power Programme from 1970 to 1990: The Carmathen Bay Experiments and Musgrove Vertical-Axis Turbines," *Wind Engineering*, Vol. 30, No. 3, 2006.

[16] Machielse, L. A. H., Peeters, P. M., and Rieffe, H. C., "Test Result and Design Evaluation of a 15-m Diameter, Cantilever VAWT," *Proceedings of the European Wind Energy Conference*, European Wind Energy Association, October 1986.

[17] Lobitz, D. and Sullivan, W., "VAWTDYN - A Numerical Package for the Dynamic Analysis of Vertical Axis Wind Turbines," Tech. Rep. SAND80-0085, Sandia National Laboratories, Albuquerque, New Mexico, 1980.

[18] Lobitz, D., "Dynamic Analysis of Darrieus Vertical Turbine Rotor," Tech. Rep. SAND80-2820, Sandia National Laboratories, Albuquerque, New Mexico, 1980.

[19] NASA, *The NASTRAN User's Manual*, June 1986.

[20] Douglas, F., *The NASTRAN Programmer's Manual*, NASA, January 1980.

[21] Carne, T., Lobitz, D., Nord, A., and Watson, R., "Finite Element Analysis and Modal Testing of a Rotating Wind Turbine," Tech. Rep. SAND82-0345, Sandia National Laboratories, Albuquerque, New Mexico, 1982.

[22] Popelka, D., "Aeroelastic Stability Analysis of a Darrieus Wind Turbine," Tech. Rep. SAND82-0672, Sandia National Laboratories, Albuquerque, New Mexico, February 1982.

[23] Bisplinghoff, R., Holt, A., and Halfman, R., *Aeroelasticity*, Dover Publications, Inc., Mineola, New York, 1996.

[24] Lobitz, D. W. and Sullivan, W. N., "A Comparison of Finite Element - Predictions and Experimental Data for the Forced Response of the DOE 100 kW Vertical Axis Wind Turbine," Tech. Rep. SAND82-2534, Sandia National Laboratories, Albuquerque, New Mexico, 1982.

[25] Dohrmann, C. R. and Veers, P. S., "Time Domain Structural Calculations for Vertical Axis Wind Turbines," *Proceedings of the 8th ASME Wind Energy Symposium*, 1989, pp. 1–23.

[26] Allet, A., Paraschivoiu, I., and Others, "Aerodynamic Analysis Models for Vertical-Axis Wind Turbines," *International Journal of Rotating Machinery*, Vol. 2, No. 1, 1900, pp. 15–21.

[27] Malcolm, D., "Dynamic Response of a Darrieus Rotor Wind Turbine Subject to Turbulent Flow," *Engineering Structures*, Vol. 10, No. 2, April 1988, pp. 125–134.

[28] Veers, P. S., "Modeling Stochastic Wind Loads on Vertical Axis Wind Turbines," Tech. Rep. September, Sandia National Laboratories, SAND83-1909, 1984.

[29] Sullivan, N. and Leonard, T. M., "A Computer Subroutine for Estimating Aerodynamic Blade Loads on Darrieus Vertical Axis Wind Turbines," Tech. Rep. SAND80-2407, Sandia National Laboratories, Albuquerque, New Mexico, November 1980.

[30] Templin, R. J., "Aerodynamic Performance Theory for the NRC Vertical Axis Wind Turbine," Tech. Rep. LTR-LA-160, NRC of Canada TR, 1974.

[31] Strickland, J. H. and Webster, B. T., "A Vortex Model of the Darrieus Turbine: An Analytical and Experimental Study," Tech. Rep. SAND79-7058, Sandia National Laboratories, Albuquerque, New Mexico, 1980.

[32] Strickland, J., Webster, B., and Nguyen, T., "A Vortex Model of the Darrieus Turbine : An Analytical and Experimental Study," *Journal of Fluids Engineering*, Vol. 101, No. 4, 1979, pp. 500–505.

[33] Strickland, J. H., "The Darrieus Turbine: A Performance Prediction Model Using Multiple Stream Tubes," Tech. Rep. SAND75-041, Sandia National Laboratories, Albuquerque, New Mexico, 1975.

[34] Paraschivoiu, I., "Aerodynamic Loads and Performance of the Darrieus Rotor," *Journal of Energy*, Vol. 6, No. 6, 1981, pp. 406–412.

[35] Paraschivoiu, I., Beguler, C., Delclaux, F., and Fraunie, P., "Aerodynamic Analysis of the Darrieus Rotor Including Secondary Effects," *Journal of Energy*, Vol. 7, No. 5, 1983, pp. 416–422.

[36] Ferreira, C., *The Near Wake of the VAWT, 2D and 3D Views of the VAWT Aerodynamics*, Ph.D. thesis, Delft University of Technology, Delft, the Netherlands, 2009.

[37] Dixon, K., Ferreira, C., Hofemann, C., van Bussel, G., and van Kuik, G., "A 3D Unsteady Panel Method for Vertical Axis Wind Turbines," *The proceedings of the European Wind Energy Conference & Exhibit on EWEC Brussels*, 2008, pp. 1–10.

[38] Murray, J. C. and Barone, M., "The development of CACTUS, a Wind and Marine Turbine Performance Simulation Code," *49th AIAA Aerospace Science Meeting*, American Institute of Aeronautics and Astronautics, Orlando, Florida, 2011, pp. 1–21.

[39] Gormont, R., "A Mathematical Model of Unsteady Aerodynamics and Radial Flow for Application to Helicopter Rotors," Tech. Rep. DAAJ02-71-C-0045, U.S. Army Air Mobility R&D Laboratory, 1973.

[40] Leishman, J. and Beddoes, T., "A Semi-Empirical Method for Dynamic Stall," *Journal of the American Helicopter Society*, Vol. 34, 1989, pp. 3–17.

[41] Jonkman, J. M., "Dynamics Modeling and Loads Analysis of an Offshore Floating Wind Turbine," Tech. Rep. NREL/TP-500-41958, National Renewable Energy Laboratory, Golden, Colorado, 2007.

[42] Jonkman, J. M., "Dynamics of Offshore Floating Wind-turbines - Model Development and Verification," *Wind Energy*, Vol. 12, 2009, pp. 459–492.

[43] Lee, C. H. and N., N. J., *WAMIT User Manual, Versions 6.3, 6.3PC, 6.3S, 6.3S-PC*, WAMIT, Inc., Chestnut Hill, Massachusetts, 2006.

[44] Alves, M., *Numerical Simulation of the Dynamics of Poit Absorber Wave Energy Converters Using Frequency and Time Domain Approaches*, Ph.D. thesis, Technical University of Lisbon, Libson, 2012.

[45] Orcina Ltd., Daltongate, United Kingdom, *OrcaFlex Manual: Version 9.6a*, 2012.

[46] Crespo Da Silva, M., "Non-Linear Flexural-Flexural-Torsional-Extensional Dynamics of Beams - I. Formulation," *International Journal of Solids and Structures*, Vol. 24, No. 12, 1988, pp. 1225–1234.

[47] Crespo Da Silva, M. and Glynn, C., "Non-Linear Flexural-Flexural-Torsional-Extensional Dynamics of Inextensional Beams - I. Equations of Motion," *Journal of Structural Mechanics*, Vol. 6, 1978, pp. 437–448.

[48] Hodges, D. H., "A Mixed Variational Formulation Based on Exact Intrinsic Equations for Dynamics of Moving Beams," *International Journal of Solids and Structures*, Vol. 26, No. Il, 1990, pp. 1253–1273.

[49] Freno, B. and Cizmas, P., "A Computationally Efficient Non-linear Beam Model," *International Journal of Non-Linear Mechanics*, Vol. 46, No. 6, July 2011, pp. 854–869.

[50] Pai, P., *Highly flexible structures: Modeling, Computation, and Experimentation*, American Institute of Aeronautics and Astronautics, Reston, Virginia, 2007.

[51] Reddy, J., *An Introduction to the Finite Element Method*, McGraw-Hill, Boston, 3rd ed., 2005.

[52] Hodges, D., *Nonlinear Composite Beam Theory*, American Institute of Aeronautics and Astronautics, Reston, Virginia, 2006.

[53] Cesnik, C. E. S. and Hodges, D. H., "VABS: A New Concept for Composite Rotor Blade Cross-Sectional Modeling," *Journal of the American Helicopter Society*, Vol. 42, 1997, pp. 27–38.

[54] Malcolm, D. and Laird, D., "Extraction of Equivalent Beam Properties from Blade Models," *Wind Energy*, Vol. 10, 2007, pp. 135–157.

[55] Bir, G. S., *User's Guide to PreComp*, National Renewable Energy Laboratory, 2005.

[56] Segalman, D. J. and Dohrmann, C. R., "A Method for Calculating the Dynamics of Rotating Flexible Structures, Part 1: Derivation," *Journal of Vibration and Acoustics*, Vol. 118, No. 3, 1996, pp. 313.

[57] Segalman, D. J., Dohrmann, C. R., and Slavin, a. M., "A Method for Calculating the Dynamics of Rotating Flexible Structures, Part 2: Example Calculations," *Journal of Vibration and Acoustics*, Vol. 118, No. 3, 1996, pp. 318.

[58] Parish, J. J., Hurtado, J. E., and Sinclair, A. J., "Direct Linearization of Continuous and Hybrid Dynamical Systems," *Journal of Computational and Nonlinear Dynamics*, Vol. 4, No. 3, 2009, pp. 031002.

[59] Lobitz, D., "Aeroelastic Stability Predictions for a MW-sized Blade," *Wind Energy*, Vol. 7, 2004, pp. 211–224.

[60] Resor, B., Owens, B., and Griffith, D., "Aeroelastic Instability of Very Large Wind Turbine Blades," *Proceedings of the European Wind Energy Conference Annual Event*, European Wind Energy Association, Copenhagen, Denmark, April 2012, pp. 1–6.

[61] Hodges, D. and Pierce, G., *Introduction to Structural Dynamics and Aeroelasticity*, Cambridge, New York, 2nd ed., 2011.

[62] Wright, J. and Cooper, J., *Introduction to Aircraft Aeroelasticity and Loads*, Wiley, Hoboken, New Jersey, 1st ed., 2008.

[63] Meirovitch, L., *Computational Methods in Structural Dynamics*, Stijhoff & Noordhoff International Publishers, Rockville, Maryland, 1980.

[64] Hansen, M., "Aeroelastic Instability Problems for Wind Turbines," *Wind Energy*, Vol. 10, 2007, pp. 551–577.

[65] Leishman, J., *Principles of Helicopter Aerodynamics*, Cambridge Aerospace Series, Cambridge University Press, New York, 2000.

[66] Leishman, J., "Unsteady Lift of a Flapped Airfoil by Indicial Concepts," *Journal of Aircraft*, Vol. 31, No. 2, March-April 1994, pp. 288–297.

[67] Schaub, H. and Junkins, J., *Analytical Mechanics of Space Systems*, AIAA Education Series, American Institute of Aeronautics and Astronautics, Reston, Virginia, 2003.

[68] Newmark, N. M., "A Method of Computation for Structural Dynamics," *ASCE Journal of the Engineering Mechanics Division*, Vol. 85, No. EM3, 1959, pp. 67–94.

[69] Dean, E., Glowinski, R., Kuo, Y., and Nasser, M., "On the Discretization of Some Second Order in Time Differential Equations Applications to Nonlinear Wave Problems," *The Proceedings of the NASA-UCLA Workshop on Computational Techniques in Identification and Control of Flexible Flight Structures*, Optimization Software, Inc., Lake Arrowhead, California, 1989, pp. 199–246.

[70] Jonkman, J. and Buhl, M., "FAST User's Guide," Tech. Rep. NREL/EL-500-38230, National Renewable Energy Laboratory, Golden, Colorado, 2005.

[71] Moriarty, P., "AeroDyn Theory Manual," Tech. Rep. NREL/EL-500-36881, National Renewable Energy Laboratory, Golden, Colorado, 2002.

[72] Laino, D. and Hansen, A., *User's Guide to the Wind Turbine Aerodynamics Computer Software AeroDyn*, Windward Engineering, Spanish Fork, Utah, 2002.

[73] Jonkman, J., "The New Modularization Framework for the FAST Wind Turbine CAE Tool," *Proceedings of the 51st AIAA Aerosciences Meeting*, AIAA, Grapevine, Texas, 2013, pp. 1–26.

[74] Belytschko, T., Yen, H. J., and Mullen, R., "Mixed Methods for Time Integration," *Computer Methods in Applied Mechanics and Engineering*, Vol. 17, 1979, pp. 259–275.

[75] Matthies, H., Nekamp, R., and Steindorf, J., "Algorithms for Strong Coupling Procedures," *Computer Methods in Applied Mechanics and Engineering*, Vol. 195, 2006, pp. 2028–2049.

[76] "About Dynamic-Link Libraries," Online: http://msdn.microsoft.com/en-us/library/windows/desktop/ms681914, September 2013.

[77] "Managing Memory-Mapped Files," Online: http://msdn.microsoft.com/en-us/library/ms810613.aspx, September 2013.

[78] "Windows Sockets: Background," Online: http://msdn.microsoft.com/en-us/library/aa271860, September 2013.

[79] Berg, J. and Resor, B., "Numerical Manufacturing and Design Tool (NuMAD v2.0) for Wind Turbine Blades: User's Guide," Tech. Rep. SAND2012-7028, Sandia National Laboratories, Albuquerque, New Mexico, 2012.

[80] Craig, R., *Structural Dynamics: An Introduction to Computer Methods*, Wiley, New York, 1981.

[81] Press, W. H., Teukolsky, S. A., Vetterling, W. T., and Flannery, B. P., *Numerical Recipes 3rd Edition: The Art of Scientific Computing*, Cambridge University Press, 3rd ed., 2007.

[82] Reddy, J. N., *An Introduction to Nonlinear Finite Element Analysis*, Oxford University Press, New York, 2004.

[83] Hughes, J., *The Finite Element Method: Linear static and dynamic finite element analysis*, Prentice-Hall, New Jersey, 1987.

[84] Griffin, D., "WindPACT Turbine Rotor Design Scaling Studies Technical Area 1 - Composite Blades for 80-120 Meter Rotor," Tech. Rep. NREL/SR-500-29492, National Renewable Energy Laboratory, Golden, Colorado, 2001, March.

[85] Griffith, D. and Ashwill, T., "The Sandia 100-meter All-glass Baseline Wind Turbine Blade: SNL100-00," Tech. Rep. SAND2011-3779, Sandia National Laboratories, Albuquerque, New Mexico, 2001.

[86] Friedmann, P. and Hammond, C., "Efficient Numerical Treatment of Periodic Systems with Application to Stability Problems," *International Journal for Numerical Methods in Engineering*, Vol. 11, 1977, pp. 1117–1136.

[87] "DeepWind," Online: http://www.risoecampus.dtu.dk/Research/sustainable_energy/wind_energy/projects/VEA_DeepWind.aspx, July 2013.

[88] Griffith, D., Mayes, R., and Hunter, P., "Excitation Methods for a 60 kW Vertical Axis Wind Turbine," *Proceedings of the IMAC-XXXVIII*, International Modal Assurance Conference, Society for Experimental Mechanics, Jacksonville, Florida, February 2010, pp. 329–338.

[89] Owens, B., Resor, B., and Griffith, D., "Impact of Modeling Approach on Flutter Predictions for Very Large Wind Turbine Blade Designs," *Proceedings of the American Helicopter Society 69th Annual Forum*, American Helicopter Society, Phoenix, Arizona, May 2013, pp. 1–11.

[90] Griffith, D., "Structural Dynamics Analysis and Model Validation of Wind Turbine Structures," *Proceedings of the 50th AIAA/ASME/ASCE/AHS/ASC Structures, Structural Dynamics, and Materials Conference*, American Institute for Aeronautics and Astronautics, Palm Springs, California, May 2009, pp. 1–12, AIAA-2009-2408.

[91] Carne, T., Griffith, D., and Casias, M., "Support Conditions for Experimental Modal Analysis," *Journal of Sound and Vibration*, June 2007, pp. 10–15.

[92] Bir, G. and Jonkman, J., "Modal Dynamics of Large Wind Turbines with Different Support Structures," *Proceedings of the ASME 27th International Conference on Offshore Mechanics and Arctic Engineering (OMAE2008)*, Estoril, Portugal, June 2008, pp. 1–11.

[93] Bir, G. and Jonkman, J., "Aeroelastic Instabilities of Large Offshore and Onshore Wind Turbines," *Journal of Physics: Conference Series, The Science of Making Torque from Wind*, Copenhagen, Denmark, 2007, pp. 125–129.

[94] Lobitz, D., Personal communication, June 2013.

[95] "Lux Turbine Specs," Online: http://72.29.79.135/ luxw, July 2013.

[96] Perkins, N. and Mote, C., "Comments on Curve Veering in Eigenvalue Problems," *Journal of Sound and Vibration*, Vol. 106, No. 3, 1986, pp. 451–463.

[97] Natsiavas, S., "Mode Localization and Frequency Veering in a Non-conservative Mechanical System with Dissimilar Components," *Journal of Sound and Vibration*, Vol. 165, No. 1, 1993, pp. 137–147.

[98] Jonkman, J., Butterfield, S. Musial, W., and Scott, G., "Definition of a 5-MW Reference Wind Turbine Model for Offshore System Development," Tech. Rep. NREL/TP-500-38060, National Renewable Energy Laboratory, Golden, Colorado, February 2007.

[99] Blevins, R., *Formulas for Natural Frequency and Mode Shape*, Krieger Publishing Co., Malabar, Florida, 2001.

[100] ANSYS, Inc., *ANSYS 13.0 Structural Analysis Guide*, 2010.

[101] ANSYS, Inc., *ANSYS 13.0 Verification Manual*, 2010.

[102] Petyt, M., *Introduction to Finite Element Vibration Analysis*, Cambridge University Press, New York, 1990.

APPENDIX A

VERIFICATION AND VALIDATION OF STRUCTURAL DYNAMICS ANALYSIS CAPABILITY IN THE OFFSHORE WIND ENERGY SIMULATION TOOLKIT

Verification and validation procedures were conducted on the finite element implementation of a beam element with Gyric effects and the overall finite element framework of the OWENS toolkit. As part of the core structural dynamics solver, both an Euler-Bernoulli and Timoshenko beam were developed and verified, although validation exercises showed the Timoshenko beam element proved to be more suited for the class of structures (vertical-axis wind turbines) the OWENS toolkit was being developed for. A breadth of verification exercises was considered.

Analytical solutions for simple vibration (without Gyric effects) were considered as well as an analytical solution for a "whirling shaft" which introduced Gyric effects into verification exercises. Analytical solutions are difficult to obtain for all but the simplest configurations. ANSYS® finite element software [100] was also used in a code-to-code comparison with the OWENS finite element framework. ANSYS is a verified commercial code [101], and thus a successful code-to-code comparison serves as a verification exercise for the OWENS tool. This code-to-code comparison allows for realistic structures to be modeled with each code and numerous features to be verified. Finally, an assumed modes approach was employed to consider other features of the Gyric beam element formulation such as mass center offsets, general element orientations in the rotating frame, and coupling factors. The assumed modes

approach provided a second numerical treatment of structural dynamics of a beam. This method is independent of the finite element method, and may serve as another verification procedure to ensure the finite element implementation is correct. The implementation of transient analysis capability using an implicit time integration method was also verified in this appendix. The results of a rotating structure under a general excitation force were checked for consistency with the expected system response from modal analysis predictions.

Validation procedures include comparison of model predictions to experimental data of a rotating vertical-axis wind turbine (VAWT). This validation exercise draws from the well documented Sandia National Laboratories 34-meter VAWT test bed. Parked modal analysis allows natural frequencies and mode shapes of the system to be compared to predictions made using the OWENS toolkit. Furthermore, the rotating effects inherent in the beam element formulation were validated against experimental data for system frequencies across a variety of rotor speeds. Experimental data and predictions are compared in the form of Campbell diagrams for the experimentally documented VAWT configuration.

A.1. Modal analysis analytical verification procedures

This section presents analytical verification procedures for the beam finite element implemented in the OWENS toolkit. The exercise begins with verification using analytical solutions of simple uncoupled vibration modes. After confirming uncoupled vibrations are modeled correctly, Gyric or rotational effects are verified using an analytical solution for a "whirling shaft". The dependency of system fre-

quencies and the resulting phase offsets in mode shapes are verified with respect to the angular velocity of the shaft.

A.1.a. Verification of uncoupled vibration

The fundamental uncoupled motions of the three-dimensional Euler-Bernoulli beam element were examined for agreement with analytical solutions. For these verification procedures the angular velocity associated with rotor speed was set to zero, and the beam was cantilevered at one end. Axes offsets were set to zero to eliminate coupling. Furthermore, the beam axis was aligned with the h_1 axis of the hub-frame. Thus, no transformations were performed to alter the beam orientation in the hub-frame.

A.1.a.i. Axial motion

The published analytical solution and finite element solution for one and two element uniaxial rods published by Petyt [102] were used to verify this motion of the beam element. To simplify comparisons, the rod length, mass per unit length, and axial stiffness were set to unity. Frequencies for the first five modes of the rod are shown in Table A.1.

The analytical solution for frequencies of a uniaxial rod (units of Hz) and mode shape are shown below:

$$\omega_n = \frac{(2n-1)}{4}\sqrt{\frac{E}{\rho L^2}} \tag{A.1}$$

$$\Psi_n = \sin\left((2n-1)\,\frac{\pi x}{2L}\right) \tag{A.2}$$

Table A.1. Frequencies (Hz) for uniaxial rod as predicted by Petyt, OWENS, and analytical solution

	1 el		2 el		10 el	20 el	100 el	Exact
	Petyt	OWENS	Petyt	OWENS	OWENS	OWENS	OWENS	Petyt
n = 1	0.2757	0.2757	0.2510	0.2565	0.2503	0.2501	0.2500	0.2500
n = 2	-	-	0.9029	0.8959	0.7570	0.7517	0.7501	0.7501
n = 3	-	-	-	-	1.2823	1.2580	1.2503	1.2503
n = 4	-	-	-	-	1.8389	1.7721	1.7509	1.7509
n = 5	-	-	-	-	2.4383	2.2971	2.2519	2.2519

The results agree well with those published by Petyt. It is also clear that as the number of elements is increased, the frequencies predicted via FEM are converging to the analytical predictions. The first five mode shapes for the 100 element FEM simulation are shown in Figures A.1 through A.5. There is excellent agreement with the sinusoidal shapes predicted by the analytical solution. With this step complete, the fundamental, uncoupled axial vibration of the beam is considered verified.

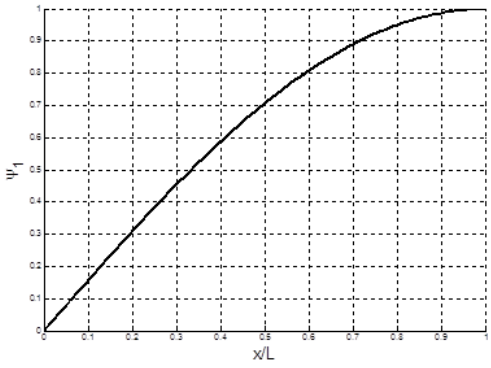

Figure A.1. Uniaxial rod 1st mode shape (100 elements)

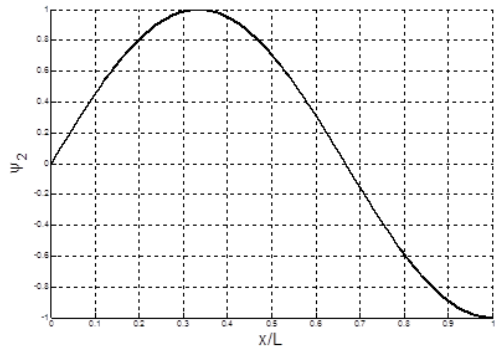

Figure A.2. Uniaxial rod 2nd mode shape (100 elements)

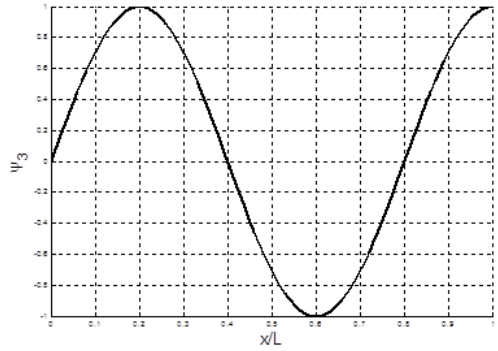

Figure A.3. Uniaxial rod 3rd mode shape (100 elements)

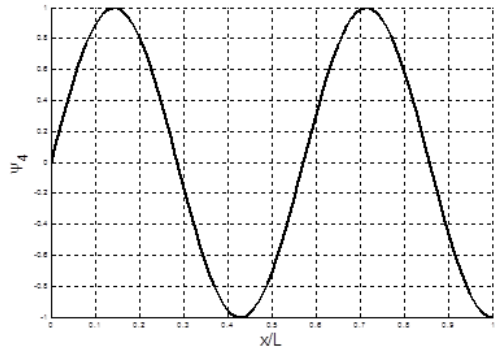

Figure A.4. Uniaxial rod 4th mode shape (100 elements)

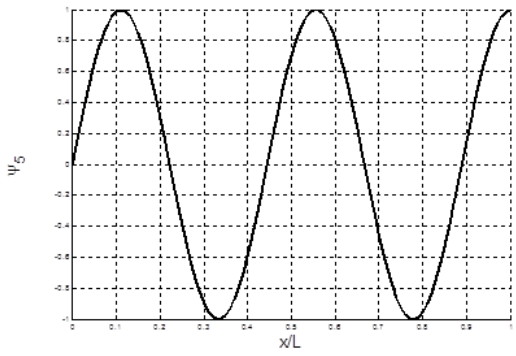

Figure A.5. Uniaxial rod 5th mode shape (100 elements)

A.1.a.ii. Torsional motion

Torsional motion of the beam was verified against published results for analytical and FEM solutions [102]. One can note that the equations of motion for axial and torsional vibration are very similar, only requiring a substitution of material properties between the two. That is, substitution ρ with ρJ and E with GJ. As with the axial vibration ρJ , GJ, and L are set to unity. The frequencies and mode shapes for torsional vibration are shown below. Results for frequencies and mode shapes are identical to those presented in the previous subsection. Verification procedures confirmed these frequencies and mode shapes were predicted for torsional vibration with the OWENS software. Therefore, the results are not duplicated below.

$$\omega_n = \frac{(2n-1)}{4}\sqrt{\frac{GJ}{\rho J L^2}} \tag{A.3}$$

$$\Psi_n = \sin\left((2n-1)\frac{\pi x}{2L}\right) \tag{A.4}$$

A.1.a.iii. Bending motion

Bending motion of the beam was verified against published results for analytical and FEM solutions presented by Petyt [102]. The frequencies and mode shapes for bending vibration are shown below. Results for frequencies (units of Hz) are shown in A.2. Overall, there is very good agreement between the available numerical solution by Petyt and the OWENS software. As the number of elements is increased, the solution appears to be converging to the analytical solution. Figure A.6 and Figure A.7 show the associated mode shapes for these two modes. These results are observed for both uncoupled transverse deflections.

Table A.2. Frequencies (Hz) for beam bending as predicted by Petyt, OWENS, and analytical solution

	1 el		2 el	10 el	20 el	100 el	Exact
	Petyt	OWENS	OWENS	OWENS	OWENS	OWENS	Petyt
n = 1	0.5623	0.5623	0.5599	0.5596	0.5596	0.5596	0.5596
n = 2	5.5397	5.5397	3.5367	3.5070	3.5069	3.5069	3.5069

A.1.b. Whirling shaft verification exercise

The problem of a whirling shaft (see Figure A.8) is considered to perform preliminary verification of the rotational effects present in the dynamic beam formulation. A symmetric, uniform beam is considered with pinned-pinned constraints at each end. The beam is rotated at a constant angular velocity about its flexural axis. An analytical solution for the beam is available, which will serve to verify the rotating effects inherent in the finite element formulation for the beam element. This in-

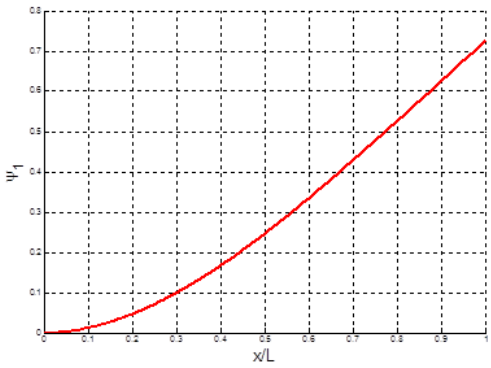

Figure A.6. Beam deflection 1st mode shape (10 elements)

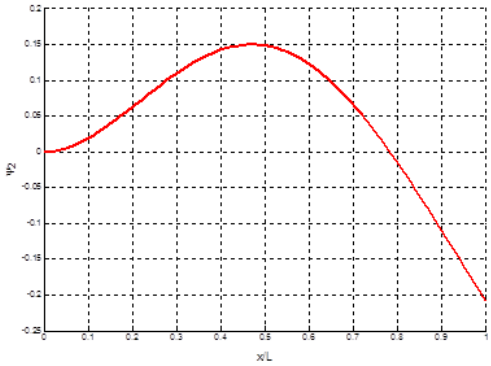

Figure A.7. Beam deflection 2nd mode shape (10 elements)

vestigation will verify the behavior of frequencies with respect to the whirling shaft angular velocity, as well as the associated mode shapes. For this verification process the beam structure was rotated to align the beam axis with the h_3 hub axis of rotation. Furthermore, the torsional and extensional degrees of freedom of the beam were deactivated through constraints. With these constraints specified, OWENS could be employed to perform this verification exercise.

Table A.3 shows the relevant beam properties for the verification procedure.

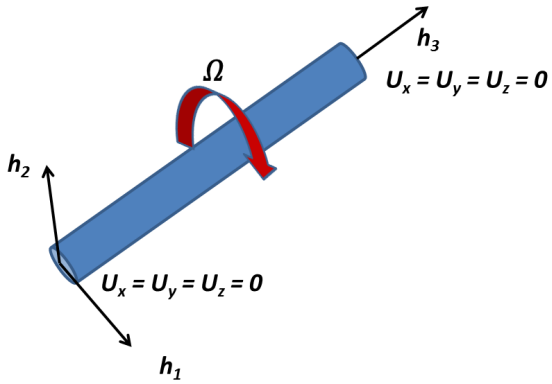

Figure A.8. Illustration of whirling shaft

Table A.3. Whirling shaft beam properties

Property	Value
ρA	1000 kg/m
EI	5×10^{10} N-m^2
L	35 m

A.1.b.i. Analytical solution

An analytical solution for the whirling shaft is referenced by Carne et al. [21]. For a stationary shaft ($\Omega = 0$) the natural frequency and mode shapes are:

$$\nu_n = \left(\frac{n\pi}{L}\right)^2 \sqrt{\frac{EI}{\rho A}} \tag{A.5}$$

$$\left\{ \begin{array}{c} U_x \\ U_y \end{array} \right\}_1 = \sin \frac{n\pi}{L} z \left\{ \begin{array}{c} \cos \nu_n t \\ 0 \end{array} \right\} \tag{A.6}$$

$$\left\{ \begin{array}{c} U_x \\ U_y \end{array} \right\}_2 = \sin \frac{n\pi}{L} z \left\{ \begin{array}{c} 0 \\ \cos \nu_n t \end{array} \right\} \tag{A.7}$$

For a beam with a symmetric cross-section, and zero angular velocity, there will be a repeated frequency and the associated modes will be uncoupled.

For the whirling shaft with angular velocity Ω the natural frequency and shape of a particular mode is

$$\omega_n = |\nu_n \pm \Omega| \tag{A.8}$$

$$\left\{ \begin{array}{c} U_x \\ U_y \end{array} \right\}_1 = \sin \frac{n\pi}{L} z \left\{ \begin{array}{c} \cos \omega_n t \\ \cos\left(\omega_n t + \frac{\pi}{2}\right) \end{array} \right\} \tag{A.9}$$

$$\left\{ \begin{array}{c} U_x \\ U_y \end{array} \right\}_2 = \sin \frac{n\pi}{L} z \left\{ \begin{array}{c} \cos \omega_n t \\ \cos\left(\omega_n t + \frac{3\pi}{2}\right) \end{array} \right\} \tag{A.10}$$

Therefore, all frequencies will be distinct, and there will exist coupling in the modes with a phase offset of 90 degrees for one mode, and 270 (-90) degrees for the other.

Table A.4 shows the frequencies for the whirling shaft from the analytical solution at various shaft angular velocities.

Table A.4. Whirling shaft frequencies (Hz) from analytical solution

Ω(Hz)	0.0		0.5		1.0		2.0		5.0		10.0
n=1	9.07	9.07	8.57	9.57	8.07	10.07	7.07	11.07	4.07	14.07	0.93	19.07
n=2	36.27	36.27	35.77	36.77	35.27	37.27	34.27	38.27	31.27	41.27	26.27	46.27
n=3	81.60	81.60	81.10	82.10	80.60	82.60	79.60	83.60	76.60	86.60	71.60	91.60
n=4	145.07	145.07	144.57	145.57	144.07	146.07	143.07	147.07	140.07	150.07	135.07	155.07
n=5	226.68	226.68	226.18	227.18	225.68	227.68	224.68	228.68	221.68	231.68	216.68	236.68

A.1.b.ii. Numerical results

The whirling shaft was modeled using OWENS, with a uniform mesh of 20 beam elements. The first 10 frequencies of the system were compared to the analytical so-

lution. Table A.5 shows the predicted frequencies at various shaft angular velocities. Table A.6 shows the percent error between the numerical and analytical predictions for the natural frequencies. Overall, there is remarkable agreement. The largest discrepancy is 1.8% at 10 Hz shaft speed. However, at this speed there is a relatively low natural frequency which magnifies the error during the normalization process.

Table A.5. Whirling shaft frequencies (Hz) predicted using finite element analysis

Ω(Hz)	0.0		0.5		1.0		2.0		5.0		10.0
n=1	9.07	9.07	8.57	9.57	8.07	10.07	7.07	11.07	4.07	14.07	0.92	19.08
n=2	36.27	36.27	35.77	36.77	35.27	37.27	34.27	38.27	31.27	41.27	26.29	46.29
n=3	81.61	81.61	81.11	82.11	80.61	82.61	79.61	83.61	76.61	86.61	71.62	91.62
n=4	145.09	145.09	144.59	145.59	144.09	146.09	143.09	147.09	140.09	150.09	135.11	155.11
n=5	226.74	226.74	226.24	227.24	225.74	227.74	224.74	228.74	221.74	231.74	216.75	236.75

Table A.6. Whirling shaft frequencies predicted percent error relative to analytical solution

	Ω(Hz)	0.0		0.5		1.0		2.0		5.0		10.0
n=1	0.00	0.00	0.00	0.00	0.00	0.00	0.01	0.01	0.10	0.03	-1.81	0.09
n=2	0.00	0.00	0.00	0.00	0.00	0.00	0.00	0.00	0.01	0.01	0.06	0.04
n=3	0.00	0.00	0.00	0.00	0.00	0.00	0.00	0.00	0.01	0.01	0.03	0.02
n=4	0.01	0.01	0.01	0.01	0.01	0.01	0.01	0.01	0.01	0.01	0.02	0.02
n=5	0.03	0.03	0.03	0.03	0.03	0.03	0.03	0.03	0.03	0.03	0.03	0.03

Mode amplitude and phase were examined for the case of zero and non-zero shaft speed. For the first 10 modes of the system the mode shapes are shown in Figure A.9. Upon first look at the mode shapes it appears that there is coupling

between the U_x and U_y deflection modes. However, for the stationary shaft, there are repeated frequencies [21]. Therefore, mode shapes of these repeated frequencies may be scaled and combined via the principle of superposition. If one examines the modes for a particular value of n or a particular frequency, one can superpose the scaled mode shapes in order to arrive at two distinct uncoupled modes.

Therefore, the mode shapes agree well with the analytical solution of uncoupled modes. It is also clear that as n increases, the numerical predictions model the analytical mode shape value of $\sin \frac{n\pi}{L} z$.

Next, the mode shapes for the whirling shaft with specified Ω are considered. The analytical solution predicts similar mode shapes as the stationary shaft, but with coupling that is $\pm$ 90 degrees out of phase. For this case, mode shapes will be visualized with amplitude and phase plots. The case below was performed at $\Omega = 1.0$ Hz, but the mode shape and phase trends were confirmed at various shaft speeds.

If one considers a phase offset (β) to be introduced in the following form:

$$\left\{ \begin{array}{c} U_x \\ U_y \end{array} \right\} = \sin \frac{n\pi}{L} z \left\{ \begin{array}{c} \cos \omega_n t \\ \cos \left(\omega_n t + \beta \right) \end{array} \right\} \tag{A.11}$$

Therefore, from the analytical solution, one would expect a β value of 90 degrees for the lower frequency, and -90 degrees for the higher frequency for the modes of a particular value of n. Figures A.10 through A.14 show mode amplitudes and phases that replicated the expected mode shapes and phases from the analytical solution. Note that the mode shape amplitudes for U_x and U_y are coincident on these plots.

A similar verification exercise was conducted for the Timoshenko beam element

with satisfactory results. The results are not shown due to their similarity to the Euler-Bernoulli verification exercise.

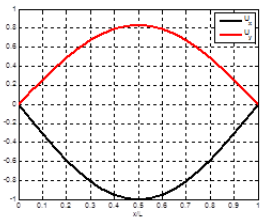

(a) 1st Mode shape for n=1

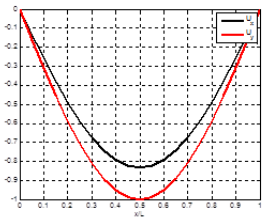

(b) 2nd Mode shape for n=1

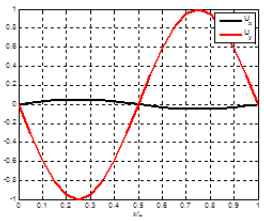

(c) 1st Mode shape for n=2

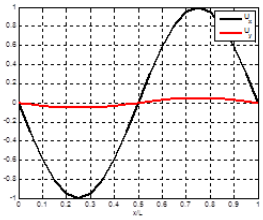

(d) 2nd Mode shape for n=2

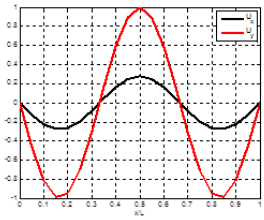

(e) 1st Mode shape for n=3

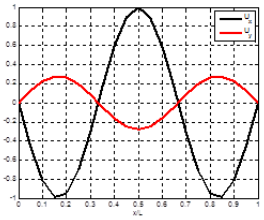

(f) 2nd Mode shape for n=3

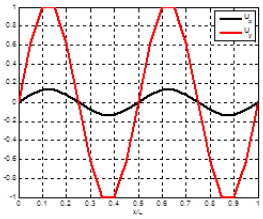

(g) 1st Mode shape for n=4

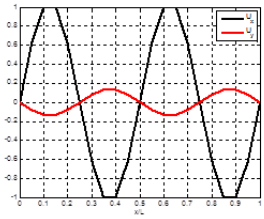

(h) 2nd Mode shape for n=4

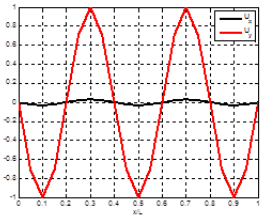

(i) 1st Mode shape for n=5

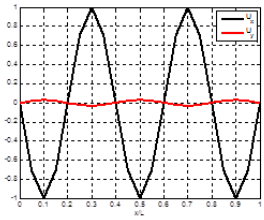

(j) 2nd Mode shape for n=5

Figure A.9. Mode shapes for stationary shaft

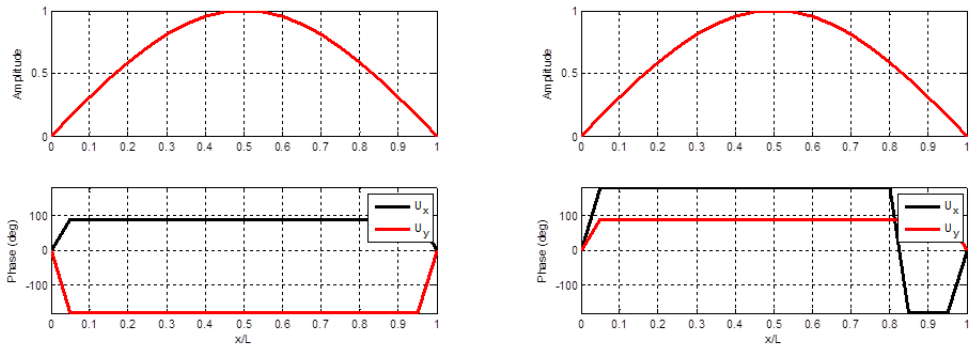

(a) Lower frequency ($\beta = 90^o$) (b) Upper frequency ($\beta = -90^o$)

Figure A.10. Whirling shaft coupled mode shape (n=1)

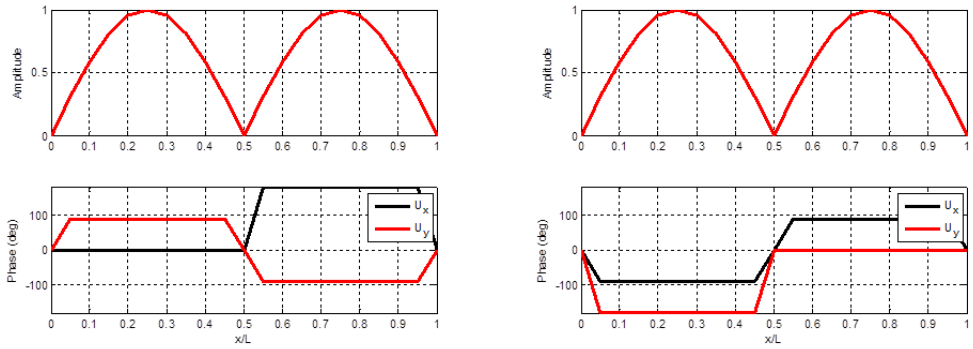

(a) Lower frequency ($\beta = 90^o$) (b) Upper frequency ($\beta = -90^o$)

Figure A.11. Whirling shaft coupled mode shape (n=2)

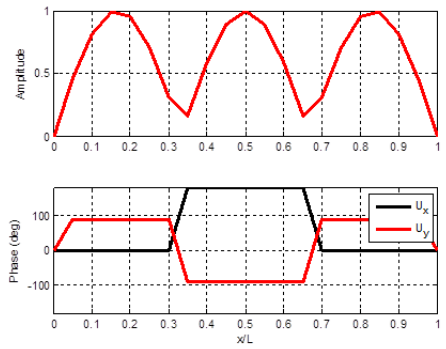

(a) Lower frequency ($\beta = 90^o$)

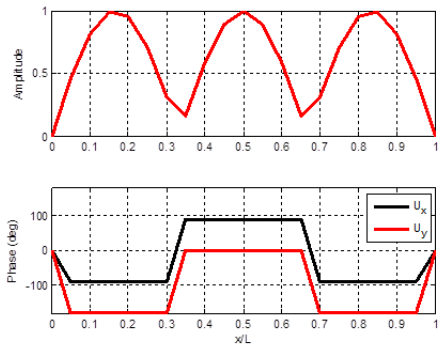

(b) Upper frequency ($\beta = -90^o$)

Figure A.12. Whirling shaft coupled mode shape (n=3)

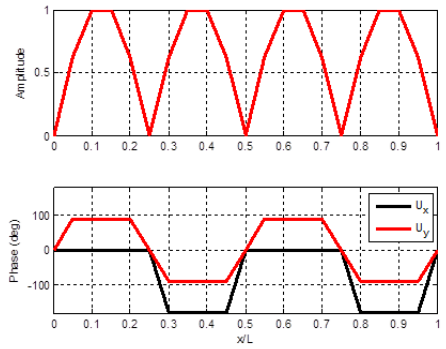

(a) Lower frequency ($\beta = 90^o$)

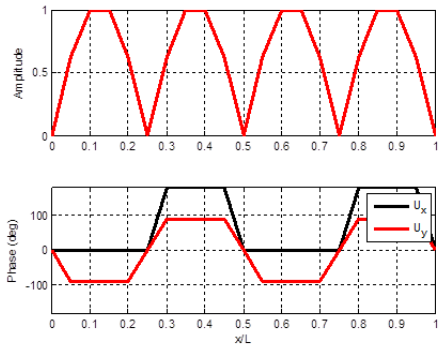

(b) Upper frequency ($\beta = -90^o$)

Figure A.13. Whirling shaft coupled mode shape (n=4)

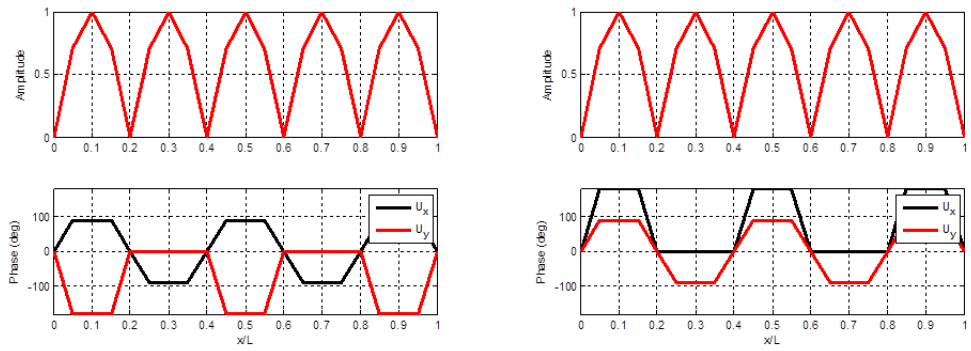

(a) Lower frequency ($\beta = 90^o$)

(b) Upper frequency ($\beta = -90^o$)

Figure A.14. Whirling shaft coupled mode shape (n=5)

A.2. Modal and static analysis numerical verification procedures

This section presents numerical verification procedures including a code-to-code comparison using ANSYS finite element software [100] and use of an assumed modes method. The code-to-code comparison allowed numerous verification exercises to be conducted for the Timoshenko beam element. These included verification of the overall framework by modeling a realistic VAWT structure, including multiple components, non-uniform cross-sectional properties, and concentrated mass. A number of modal and static analysis exercises were conducted, including rotational effects and body forces. The assumed modes method allowed additional features of the finite element implementation to be verified using an independent numerical method. Such features include arbitrarily oriented elements, offset mass center axes, and rotational effects outside of the whirling shaft considerations.

A.2.a. Code-to-code verification exercise

A code-to-code comparison of the OWENS analysis tool to ANSYS finite element software was performed for the case of the Sandia 34-meter VAWT test bed. This report presents a detailed description of the VAWT configuration and finite element model. A code-to-code comparison of modal and static analysis results for a realistic VAWT configuration is performed and excellent agreement is seen for a Timoshenko beam implementation in the OWENS tool. Moderate agreement is seen for the Euler-Bernoulli beam implementation in the OWENS tool for a parked configuration. The remaining verification exercises are performed with a Timoshenko beam element. This element is more robust and gives a more accurate comparison to the ANSYS

implementation.

A.2.a.i. Configuration

The Sandia 34-meter VAWT was considered using comparable models in the OWENS and ANSYS analysis tools. Figure A.15 illustrates the ANSYS model. The markers on the mesh denote concentrated masses of joint hardware. This model was composed of a total of 208 elements and 215 nodes (1290 degrees of freedom). Blade profiles were modeled after original schematics for the 34-meter VAWT. Inspection of component schematics allowed the masses of concentrated joint hardware to be accounted for. Blade section cross-sectional properties were calculated from cross-sectional geometries and aluminum material properties. Strut (tower to blade connection) components were modeled at the tower top and bottom. Although the actual turbine had a guy-wire system, approximate boundary conditions of a pinned tower top and pinned tower base were considered in verification and validation procedures. The tower base torsional degree of freedom aligned with the tower axis (axis of rotor rotation) was also constrained to enforce that the tower base rotate with the hub frame.

A.2.a.ii. Verification of parked modal analysis

A code-to-code comparison between ANSYS and the OWENS toolkit was performed for the parked 34-meter VAWT. The configuration analyzed using each code was is comparable to that described in the configuration section. This section presents comparison of the two software packages as part of the OWENS verification

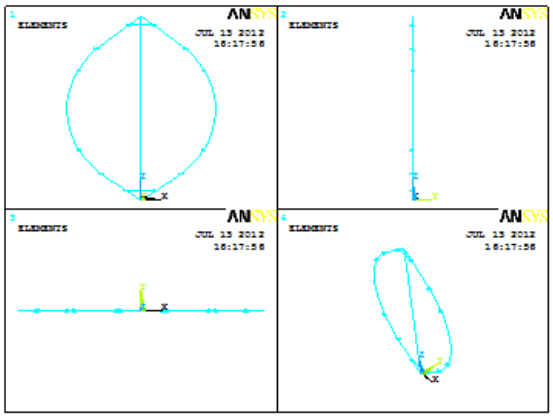

Figure A.15. Sandia 34-meter VAWT ANSYS configuration mesh

procedures. Note that the ANSYS models were prepared with the assumption of constant cross-sectional properties. Therefore, this restriction was temporarily imposed on the OWENS implementation for a more accurate code-to-code comparison. The natural frequencies via the ANSYS and OWENS tools were compared and are shown in Table A.7. It should be noted that ANSYS analysis employs Timoshenko beam theory. Overall, remarkable agreement is seen between the OWENS Timoshenko implementation and ANSYS model with a maximum difference of 0.23% being observed. The Euler-Bernoulli beam has moderate agreement with ANSYS with a maximum difference of 3.6%. Good agreement is also seen in the mode shapes predicted by OWENS and those predicted using ANSYS as shown in Figures A.16 to A.25.

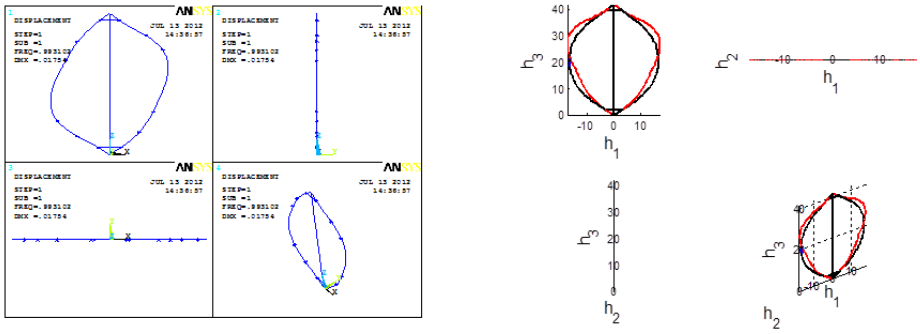

(a) ANSYS 1st anti-symmetric flatwise mode (b) OWENS 1st anti-symmetric flatwise mode

Figure A.16. 1st anti-symmetric flatwise (FA) mode

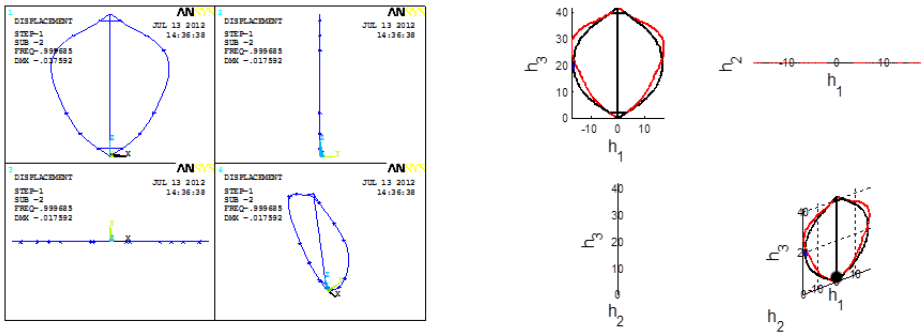

(a) ANSYS 1st symmetric flatwise mode (b) OWENS 1st symmetric flatwise mode

Figure A.17. 1st symmetric flatwise (FS) mode

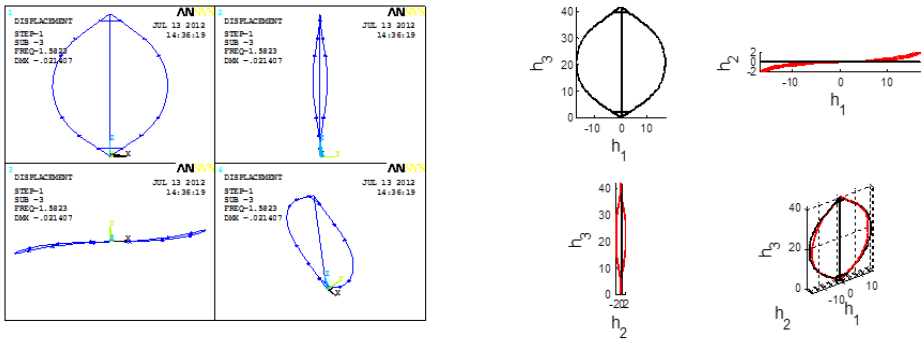

(a) ANSYS 1st propeller mode (b) OWENS 1st propeller mode

Figure A.18. 1st propeller (PR) mode

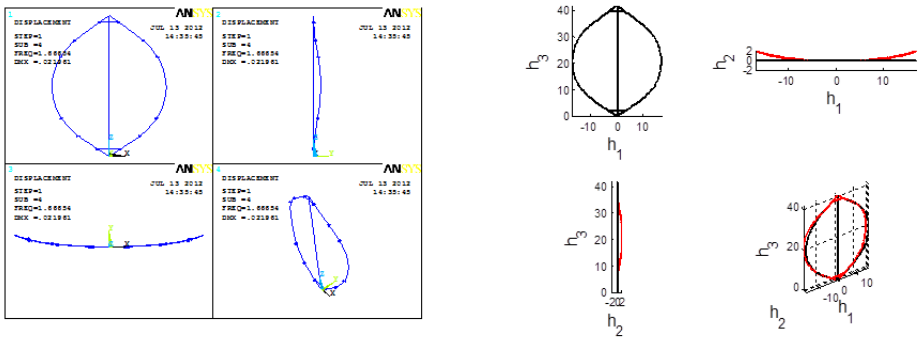

(a) ANSYS 1st butterfly (blade edgewise) mode (b) OWENS 1st butterfly (blade edgewise) mode

Figure A.19. 1st butterfly (blade edgewise - BE) mode

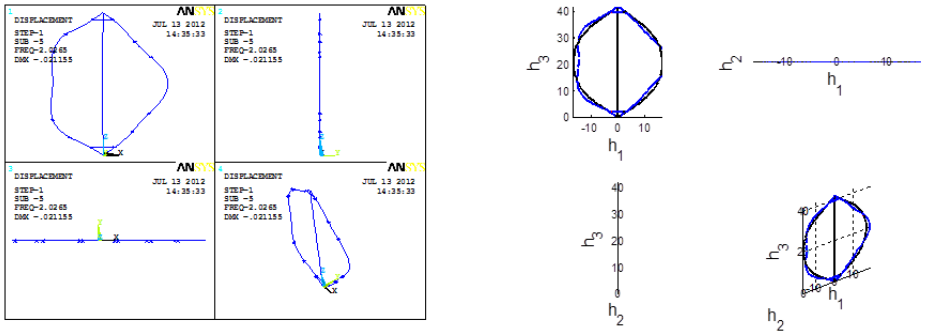

(a) ANSYS 2nd anti-symmetric flatwise mode

(b) OWENS 2nd anti-symmetric flatwise mode

Figure A.20. 2nd anti-symmetric flatwise (FA) mode

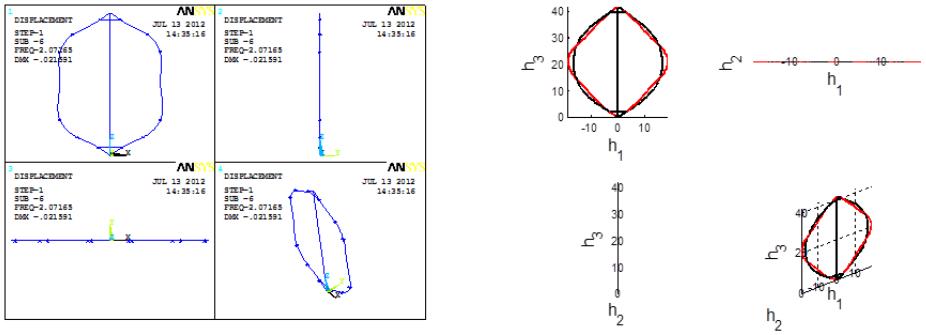

(a) ANSYS 2nd symmetric flatwise mode

(b) OWENS 2nd symmetric flatwise mode

Figure A.21. 2nd symmetric flatwise (FS) mode

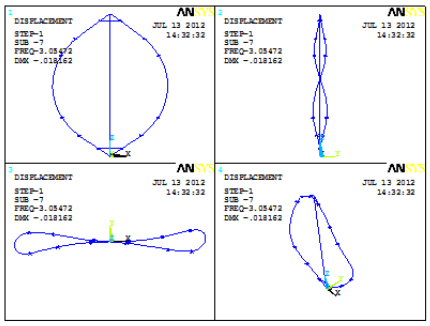

(a) ANSYS 2nd butterfly (blade edgewise) mode

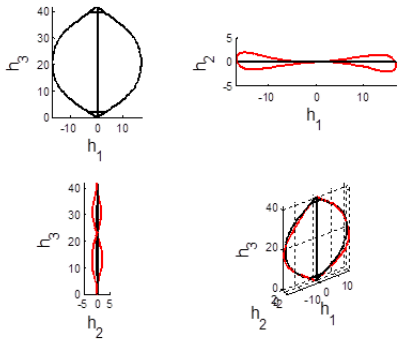

(b) OWENS 2nd butterfly (blade edgewise) mode

Figure A.22. 2nd butterfly (blade edgewise - BE) mode

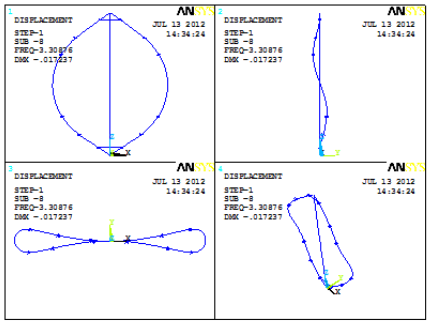

(a) ANSYS 2nd propeller mode

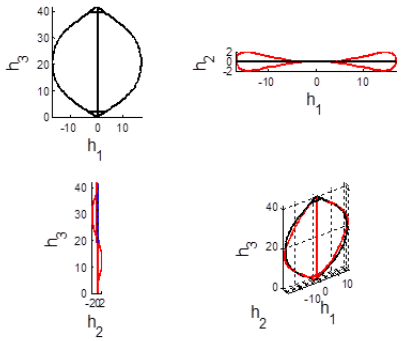

(b) OWENS 2nd propeller mode

Figure A.23. 2nd propeller (PR) mode

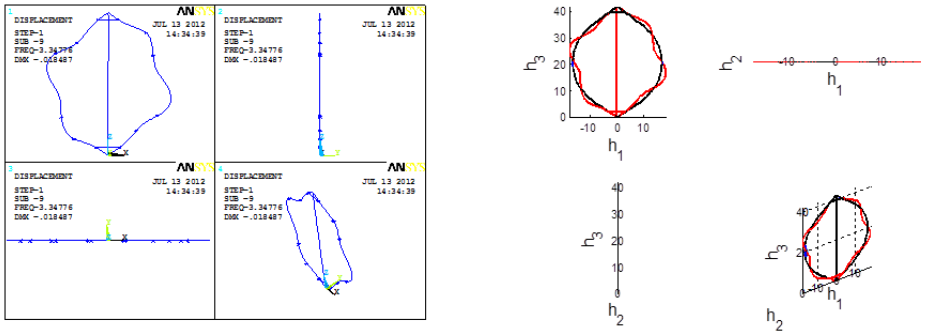

(a) ANSYS 3rd anti-symmetric flatwise mode

(b) OWENS 3rd anti-symmetric flatwise mode

Figure A.24. 3rd anti-symmetric flatwise (FA) mode

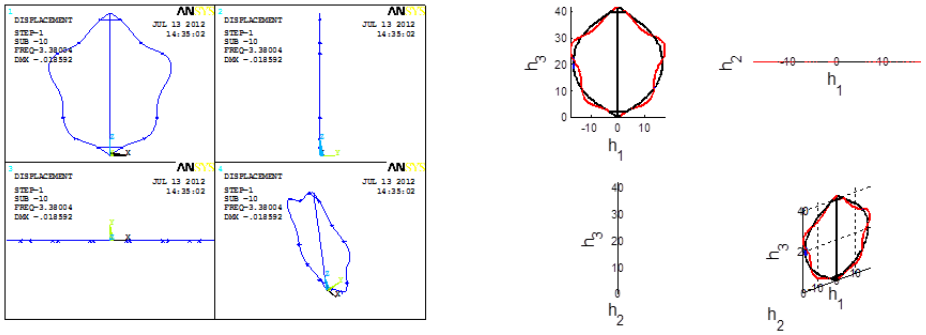

(a) ANSYS 3rd symmetric flatwise mode

(b) OWENS 3rd symmetric flatwise mode

Figure A.25. 3rd symmetric flatwise (FS) mode

Table A.7. Parked natural frequencies (Hz) for 34m VAWT via ANSYS and OWENS tools

ANSYS	OWENS (Timoshenko)	% Difference	OWENS (Euler-Bernoulli)	% Difference
0.9931	0.9938	0.07	0.9642	2.91
0.9997	1.0003	0.06	0.9675	3.22
1.5823	1.5789	0.21	1.5248	3.63
1.6665	1.6660	0.03	1.6645	0.12
2.0265	2.0287	0.11	1.9758	2.50
2.0716	2.0741	0.12	2.0085	3.05
3.0547	3.0489	0.19	2.9981	1.85
3.3088	3.3077	0.03	3.2630	1.38
3.3478	3.3556	0.23	3.2795	2.04
3.3800	3.3877	0.23	3.3021	2.30

A.2.a.iii. Verification of translational acceleration body forces

The aforementioned configuration was considered in verification of body forces due to translational acceleration. Gravitational acceleration (9.81 m/s^2) was applied to the structure along each of the coordinate axes (three separate simulations) and linear static analysis was performed. The deformed meshes between the two analysis tools were compared, along with the relative norms of nodal displacements (U, V, and W) and the maximum displacement vector sums. Table A.8 presents the norms for differences in nodal displacements between the two simulations. Figures A.26 to A.28 present the deformed meshes between the two simulation tools for acceleration in the h_1, h_2, and h_3 directions respectively.

Table A.8. Relative difference norms for displacements between ANSYS and OWENS results for acceleration body forces

	Acceleration in h_1	Acceleration in h_2	Acceleration in h_3
Nodal U	0.0492	0.0000	0.0000
Nodal V	0.0000	0.0119	0.0119
Nodal W	0.0309	0.0000	0.0000
Max Disp Vector Sum	0.0202	0.0095	0.0095

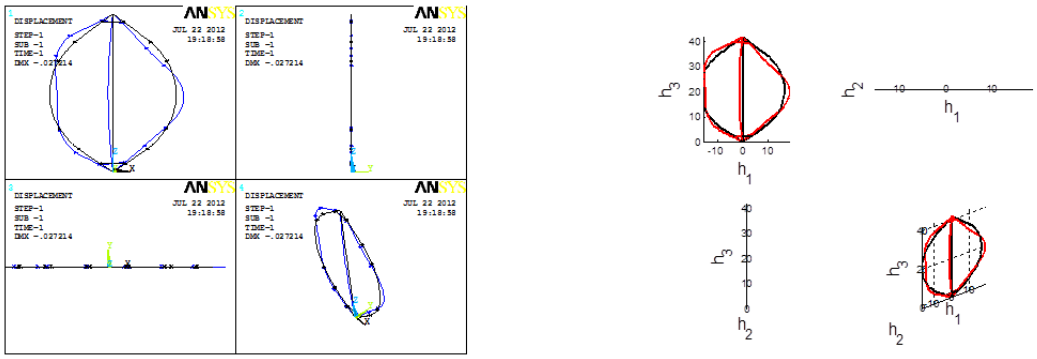

(a) ANSYS result (b) OWENS result

Figure A.26. Deformed mesh for acceleration in h_1 (scale factor = 76.78)

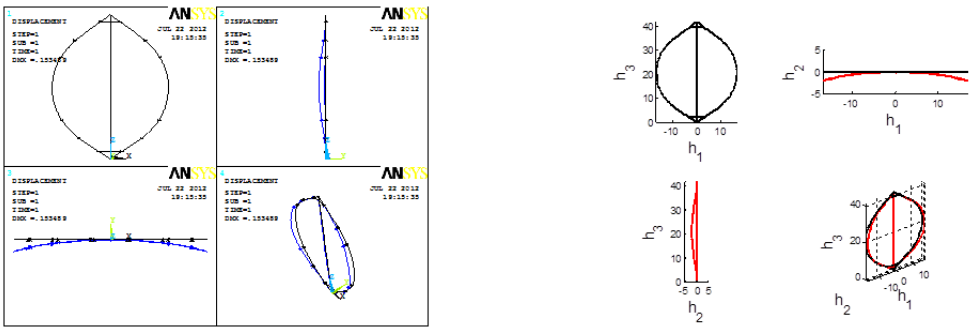

(a) ANSYS result (b) OWENS result

Figure A.27. Deformed mesh for acceleration in h_2 (scale factor = 13.61)

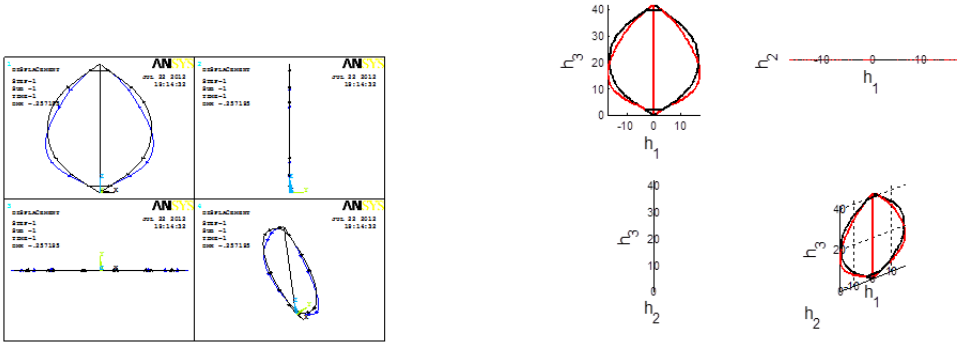

(a) ANSYS result (b) OWENS result

Figure A.28. Deformed mesh for acceleration in h_3 (scale factor = 8.12)

A.2.a.iv. Verification of rotational modal analysis (no stress stiffening)

The aforementioned 34-meter VAWT configuration (including concentrated masses) was considered in a rotational modal analysis. This analysis considered rotation about each coordinate axis independently at an angular velocity of 0.5 Hz. This exercise serves to verify the inclusion of rotational effects on modal analysis including the Coriolis and spin softening phenomenon. Stress stiffening effects due to centrifugal and gravitational loadings were not considered in this verification exercise.

A variety of eigensolver options exist in the ANSYS software. It was observed that the "Damped" eigensolver option agreed best with the results obtained through the OWENS analysis tool. The "Unsymmetric" solver options showed less agreement. Therefore, it is believed that the "Damped" eigensolver option is most similar to the sparse eigenvalue solver used in MATLAB® for unsymmetric matrices. Tables A.9 through A.11 present the differences for frequencies of the first 10 modes between the ANSYS and OWENS analysis tools for rotational modal analysis. Overall, very

good agreement is observed with a maximum difference of 2.2%.

Table A.9. Frequencies (Hz) for 34m VAWT with rotational effects about h_1 via ANSYS and OWENS tools

Mode	$\Omega_x = 0.5$ Hz		
	ANSYS	OWENS	% Diff.
1	0.7866	0.7708	2.00
2	0.8076	0.7929	1.81
3	1.7382	1.7155	1.30
4	1.8104	1.7909	1.08
5	1.9263	1.9273	0.05
6	1.9826	1.9844	0.09
7	3.1294	3.1037	0.82
8	3.3071	3.3143	0.22
9	3.3304	3.3306	0.01
10	3.3813	3.3668	0.43

A.2.a.v. Verification of rotational modal analysis (with stress stiffening)

The aforementioned 34-meter VAWT configuration (including concentrated masses) was considered in a rotational modal analysis. This analysis considered rotation about the tower coordinate axis at an angular velocity of 0.5 Hz. A static analysis was conducted before the modal analysis to account for stress stiffening effects as a result of centrifugal and gravitational loads. This exercise serves to verify the inclusion of rotational effects on modal analysis while accounting for stress-stiffening effects.

As with the last verification exercise, the ANSYS "Damped" eigensolver option was employed. Table A.12 presents system frequencies for the rotating 34-meter

Table A.10. Frequencies (Hz) for 34m VAWT with rotational effects about h_2 via ANSYS and OWENS tools

Mode	$\Omega_y = 0.5$ Hz		
	ANSYS	OWENS	% Diff.
1	0.8459	0.8275	2.18
2	0.8526	0.8343	2.15
3	1.5821	1.5625	1.24
4	1.6664	1.6517	0.88
5	1.9859	1.9835	0.12
6	2.0302	2.0282	0.10
7	3.0542	3.0354	0.62
8	3.3083	3.2947	0.41
9	3.3195	3.3230	0.10
10	3.3489	3.3520	0.09

VAWT with stress stiffening effects included. Overall, very good agreement is observed between OWENS and ANSYS with a maximum difference of 0.53% in the first 10 modes of the system.

Table A.11. Frequencies (Hz) for 34m VAWT with rotational effects about h_3 via ANSYS and OWENS tools

Mode	$\Omega_z = 0.5$ Hz		
	ANSYS	OWENS	% Diff.
1	0.9246	0.9251	0.05
2	0.9260	0.9264	0.04
3	1.4989	1.4956	0.22
4	1.5784	1.5783	0.01
5	1.9925	1.9930	0.02
6	2.0324	2.0340	0.08
7	3.0678	3.0646	0.10
8	3.2508	3.2606	0.30
9	3.3646	3.3692	0.14
10	3.4035	3.4005	0.09

Table A.12. Frequencies (Hz) for 34m VAWT with rotational effects and stress stiffening via ANSYS and OWENS tools

Mode #	$\Omega_z = 0.5$ Hz		
	ANSYS	OWENS	% Difference
1	1.2459	1.2469	0.08
2	1.2465	1.2473	0.06
3	1.6251	1.6200	0.31
4	1.7062	1.7033	0.17
5	2.4256	2.4262	0.02
6	2.4838	2.4857	0.08
7	3.2302	3.2132	0.53
8	3.4679	3.4567	0.32
9	3.8610	3.8665	0.14
10	3.8840	3.8920	0.21

A.2.b. Assumed modes verification exercise

Modal analysis for a simple uniform is performed using a finite element and assumed modes approach. The beam is considered at an arbitrary orientation in a hub fixed frame. Mass center offsets as well as gyroscopic effects are considered. This exercise will be used to further verify the finite element implementation against a separate, unique numerical method.

A.2.b.i. Configuration

The configuration was a fixed-free beam at arbitrary orientation in a hub-fixed frame. The most complicated beam configuration considered has the properties listed in Table A.13. The beam is arbitrarily oriented in the hub frame as shown in Figure A.29.

Table A.13. Uniform beam properties

Property	Value	Property	Value
EA (N)	8.2111e10	ρA (kg/m)	353.43
EI_{yy} (N-m^2)	9.1630e9	ρI_{yy} (kg-m)	616.71
EI_{zz} (N-m^2)	5.6300e9	ρI_{zz} (kg-m)	316.71
GJ (N-m^2)	6.8042e10	ρJ (kg-m)	933.42
EI_{yz} (N-m^2)	2.7490e9	ρI_{yz}(kg-m)	370.00
L (m)	10.00		
y_{cm} (m)	0.40		
z_{cm} (m)	0.15		

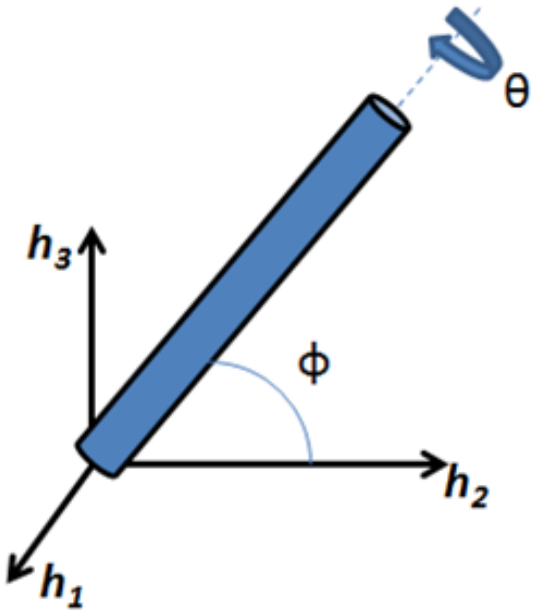

Figure A.29. llustration of beam with arbitrary orientation in the hub frame

A.2.b.ii. Assumed modes methodology

An assumed modes methodology was employed to construct a formulation for a three-dimensional beam with two transverse deflections, extensional, and torsional deformations.

The assumed modes for the beam deflections are assumed to be:

$$\phi_j(x) = \left(\frac{x}{L}\right)^{j+1} \tag{A.12}$$

The assumed modes for the axial and torsional deformations are assumed to be:

$$\psi_j(x) = \left(\frac{x}{L}\right)^{j} \tag{A.13}$$

Such that x is in the local coordinate system along the flexural axis of the beam. The assumed modes approach for modal analysis will consist of using $j = 1, 2, ..., n$ terms

for modal analysis. The associated mass, gyroscopic, and stiffness matrices for the finite element implementation are the same as that of the finite element formulation. However, the assumed modes replace the traditional piecewise finite element shape functions.

For the assumed modes analysis considered in this verification exercise $n = 8$ for bending, axial, and torsional modes.

A.2.b.iii. Verification of finite element implementation

A number of verification cases were considered, each with increasing complexity. For the finite element analysis results shown below 10 linear elements were utilized.

A.2.b.iv. Case 1: Vibration of uniform beam

The uniform beam with properties listed in Table A.13 was considered with angles of $\phi = 40$ degrees and $\theta = 30$ degrees. The beam was further simplified by setting the mass center offsets (y_{cm} and z_{cm}) to zero, and the elastic and inertial coupling terms (EI_{yz} and ρI_{yz}) set to zero. The rotor is stationary for this verification case. Table A.14 shows the frequency and primary mode shapes predictions for assumed modes and finite element analysis along with error (using the assumed modes result as a reference). A "flapwise" mode is considered to have bending deflections primarily in h_3, whereas an "edgewise" mode is considered to have bending deflections primarily in h_2. Overall, very good agreement is seen with more variance between the two methods for the axial and torsion modes.

Table A.14. Comparison of modal analysis for case 1

Mode Number	Mode-shape	FEM Frequency (Hz)	Assumed Modes Frequency(Hz)	Error (%)
1.0000	1st Flapwise	20.9550	20.9550	0.0000
2.0000	1st Edgewise	27.3980	27.3980	0.0000
3.0000	2nd Flapwise	117.9270	117.9280	0.0008
4.0000	2nd Edgewise	142.6010	142.5970	0.0028
5.0000	1st Torsion	213.6670	213.4470	0.1031
6.0000	3rd Flapwise	289.3060	289.1530	0.0529
7.0000	3rd Edgewise	329.4220	329.3760	0.0140
8.0000	1st Axial	381.4460	381.0550	0.1157
9.0000	4th Flapwise	490.7490	490.8890	0.0285
10.0000	4th Edgewise	533.6140	533.6820	0.0127

A.2.b.v. Case 2: Vibration of uniform beam with mass center offsets

The previous case was modified to account for the mass center offsets shown in Table A.13. Table A.15 shows the frequency and primary mode shapes predictions for assumed modes and finite element analysis along with error (using the assumed modes result as a reference). Again, very good agreement is seen with more variance between the two methods for the axial and torsion modes.

A.2.b.vi. Case 3: Vibration of uniform beam with mass center offsets and coupling terms

The previous case was modified to account for the coupling terms (EI_{yz} and ρI_{yz}) offsets shown in Table A.13. Table A.16 shows the frequency and primary mode shapes predictions for assumed modes and finite element analysis along with error (using the assumed modes result as a reference). Inclusion of these terms appears to increase the variance between the two methods, but overall low errors are seen. This

Table A.15. Comparison of modal analysis for case 2

Mode Number	Mode-shape	FEM Frequency (Hz)	Assumed Modes Frequency(Hz)	Error (%)
1.0000	1st Flapwise	20.8800	20.8780	0.0087
2.0000	1st Edgewise	27.3730	27.3730	0.0005
3.0000	2nd Flapwise	115.4740	115.4510	0.0196
4.0000	2nd Edgewise	141.8610	141.8620	0.0008
5.0000	1st Torsional	213.1920	213.6440	0.2113
6.0000	3rd Flapwise	278.7370	278.5630	0.0624
7.0000	3rd Edgewise	327.7240	327.6360	0.0268
8.0000	1st Axial	386.1850	385.7910	0.1022
9.0000	4th Flapwise	470.4440	470.3550	0.0189
10.0000	4th Edgewise	531.1030	531.1550	0.0097

increased discrepancy between the two approaches is likely due to the inadequacy of the assumed mode shape functions to characterize coupling in the deformation modes that result from off-diagonal terms in the mass and stiffness matrices.

Table A.16. Comparison of modal analysis for case 3

Mode Number	Mode-shape	FEM Frequency (Hz)	Assumed Modes Frequency(Hz)	Error (%)
1.0000	1st Flapwise	18.0880	18.1290	0.2262
2.0000	1st Edgewise	28.9880	28.9240	0.2213
3.0000	2nd Flapwise	107.1400	108.5650	1.3126
4.0000	2nd Edgewise	143.8090	142.7790	0.7214
5.0000	1st Torsional	213.2030	213.6130	0.1919
6.0000	3rd Flapwise	274.4840	278.8560	1.5678
7.0000	3rd Edgewise	327.8120	330.1721	0.7148
8.0000	1st Axial	386.8490	385.2848	0.4060
9.0000	4th Flapwise	475.7090	472.7468	0.6266
10.0000	4th Edgewise	547.5430	570.5170	4.0269

A.2.b.vii. Case 4: Vibration of uniform beam with mass center offsets and coupling terms, rotational effects included

The previous case was modified to include a specified rotor speed of 1.2 Hz. Table A.17 shows the frequency and primary mode shapes predictions for assumed modes and finite element analysis along with error (using the assumed modes result as a reference). Inclusion of rotational effects does not appear to affect the error significantly from the previous verification case.

Table A.17. Comparison of modal analysis for case 4

Mode Number	Mode-shape	FEM Frequency (Hz)	Assumed Modes Frequency(Hz)	Error (%)
1.0000	1st Flapwise	18.0040	18.0520	0.2659
2.0000	1st Edgewise	29.0460	28.9730	0.2520
3.0000	2nd Flapwise	107.1260	108.5610	1.3218
4.0000	2nd Edgewise	143.8150	142.7810	0.7242
5.0000	1st Torsional	213.2030	213.6130	0.1919
6.0000	3rd Flapwise	274.4780	278.8380	1.5636
7.0000	3rd Edgewise	327.8140	330.1940	0.7208
8.0000	1st Axial	386.8520	385.2910	0.4051
9.0000	4th Flapwise	475.7080	472.6330	0.6506
10.0000	4th Edgewise	547.5430	570.3870	4.0050

A.2.b.viii. Case 5: Vibration of uniform beam with gyroscopic effects without coupling terms

As another verification case, mass center offsets and rotor speed of 1.2 Hz were included, but coupling terms were excluded. Table A.18 shows the frequency and primary mode shapes predictions for assumed modes and finite element analysis

along with error (using the assumed modes result as a reference). This indicates, that even with rotational effects relatively low error is observed.

Table A.18. Comparison of modal analysis for case 5

Mode Number	Mode-shape	FEM Frequency (Hz)	Assumed Modes Frequency(Hz)	Error (%)
1.0000	1st Flapwise	20.7700	20.7790	0.0433
2.0000	1st Edgewise	27.4630	27.4510	0.0437
3.0000	2nd Flapwise	115.4580	115.4340	0.0208
4.0000	2nd Edgewise	141.8710	141.8710	0.0000
5.0000	1st Torsional	213.1910	213.6430	0.2116
6.0000	3rd Flapwise	278.7310	278.6110	0.0431
7.0000	3rd Edgewise	327.7260	327.6570	0.0211
8.0000	1st Axial	386.1890	385.7870	0.1042
9.0000	4th Flapwise	470.4410	470.2990	0.0302
10.0000	4th Edgewise	531.1040	531.1080	0.0008

A.3. Transient analysis verification

Transient analysis of a rotating VAWT structure was performed using the constant-average acceleration scheme of the Newmark-β implicit time integration method. The configuration considered in this exercise was an idealized version of the Sandia 34-meter VAWT as shown in Figure VII.1. The blade shape is approximated by a parabolic profile and uniform cross-sectional properties are assumed throughout the blade. Furthermore, no struts are included in the configuration, and the turbine base is fully fixed with the top of the turbine unconstrained. Each blade and tower are composed of 20 elements each. This results in a mesh consisting of 60 elements and 59 nodes (354 total degrees of freedom).

The structure was subjected to body forces (gravity and centrifugal loads) throughout the analysis, and the tower top was excited by additional forcing for the first 0.5 seconds of simulation time. During this time, external forces of 1×10^6 N were applied to the tower top in the h_1 an h_2 directions (shown in Figure VII.1). A torque of 1×10^6 N-m was also applied to the tower top along the axis of rotor rotation (h_3). This forcing was expected to excite most of the lower system modes, allowing the modes predicted from a modal analysis to be compared to the frequency content of structural motion from transient analysis. After this time, the system was allowed to respond naturally, being acted upon only by the aforementioned body forces.

Thirty seconds of simulation time were considered, and a time step size of 0.001 seconds was employed. For simplicity, stress-stiffening effects were deactivated in these verification procedures. Flatwise (along h_1) and edgewise (along h_2) displacements of a point on a blade midspan (denoted by the "X" in Figure VII.1) as well as flatwise and edgewise displacements of the tower top were examined, and the frequency content of these displacement histories was investigated by processing the motion history with Fast Fourier Transform (FFT). Figures A.30 and A.31 show the flatwise and edgewise displacement of the blade midspan respectively, and Figures A.32 and A.33 show the FFTs of these motions. Similarly, Figures A.34 and A.35 show the flatwise and edgewise displacement of the tower top respectively, and Figures A.36 and A.37 show the FFTs of these motions.

The frequency content of the selected motions was compared to the system frequencies predicted through modal analysis as shown in Table A.19. Here, the mode

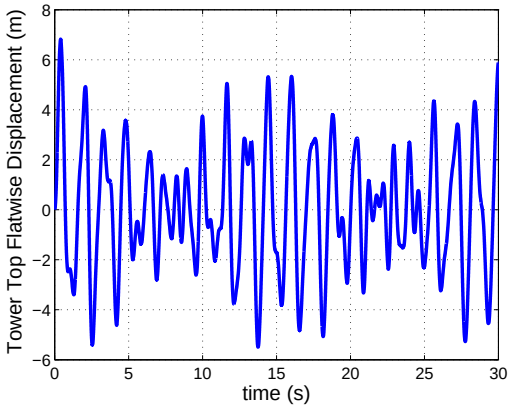

Figure A.30. Tower flatwise displacement history for transient verification exercise

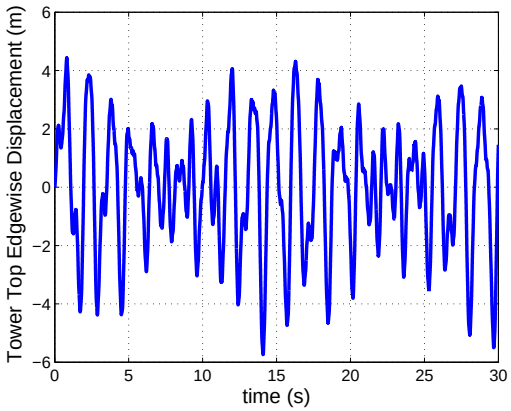

Figure A.31. Tower edgewise displacement history for transient verification exercise

labeling follows the same convention as that employed in the early section. The notation TI denotes a primarily in-plane tower mode, whereas TO denotes a primarily out-of-plane tower mode. Overall, there is very good agreement with the frequencies predicted via modal and transient analysis. Note that the individual degree of freedom motion histories considered do not necessarily contain all frequencies since some modes are associated with flatwise motion, while others are associated with

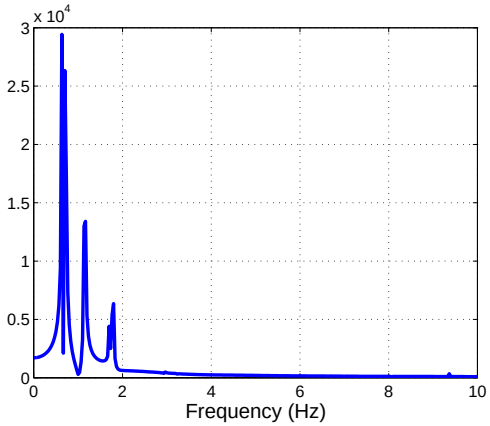

Figure A.32. FFT of tower flatwise displacement history for transient verification exercise

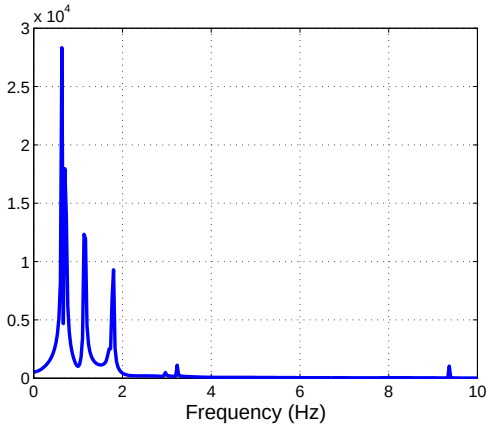

Figure A.33. FFT of tower edgewise displacement history for transient verification exercise

edgewise motion. Furthermore, it should be noted that not all modes excite motion of the tower top. Table A.20 quantifies the percent error of the frequency content of transient simulation using the modal frequency prediction as a reference. Very good agreement is seen, with errors not exceeding 1.6%. Although these tables only present the lowest 10 modes of the system, these trends were confirmed out to the lowest 20 modes of the system. This suggests a successful implementation of the

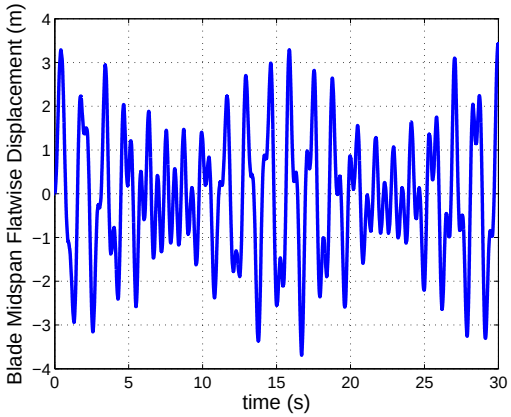

Figure A.34. Blade midspan flatwise displacement history for transient verification exercise

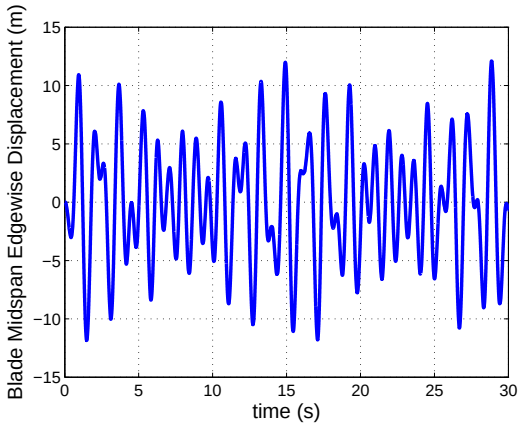

Figure A.35. Blade midspan edgewise displacement history for transient verification exercise

Newmark-β implicit time integration method within the core structural dynamics analysis capability of the OWENS toolkit. Similar verification procedures were also performed for the implicit Dean integrator for Gyric systems with satisfactory results, but the results are not shown here.

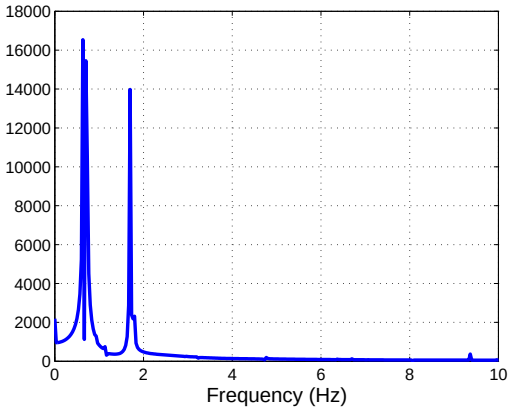

Figure A.36. FFT of blade midspan flatwise displacement history for transient verification exercise

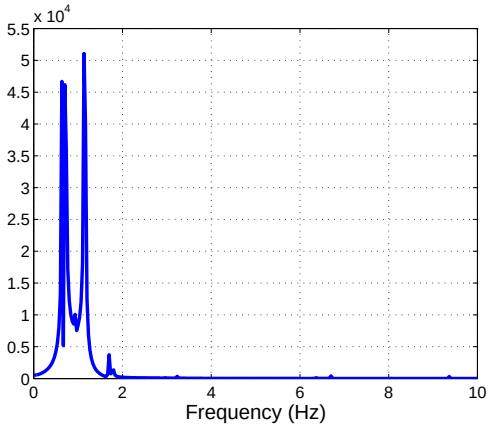

Figure A.37. FFT of blade midspan edgewise displacement history for transient verification exercise

Table A.19. Comparison of frequency content of transient analysis predictions to modal analysis predictions

Mode	Modal Frequency (Hz)	Blade Midspan Flatwise Motion (Hz)	Blade Midspan Edgewise Motion (Hz)	Tower Top In-plane Motion (Hz)	Tower Top Out-of-plane Motion (Hz)
1FA/1TO	0.643	0.633	0.633	0.633	0.633
1FS	0.674	0.675	-	-	-
1TI/1TO	0.711	0.700	0.700	0.700	0.700
1PR	0.940	-	0.933	-	-
1TO/1TI	1.149	1.133	1.133	1.167	1.167
2FA/1TO	1.694	1.700	1.700	1.700	1.700
2FS/2PR	1.694	1.700	1.700	1.700	1.700
2FA/1TO	1.786	1.800	1.800	1.800	1.800
3FS/2PR	2.850	-	2.833	-	-
3FA/2PR	2.953	2.967	2.967	2.967	2.967

Table A.20. Relative error of frequency content of transient analysis predictions to modal analysis predictions

Mode	Modal Frequency (Hz)	Blade Midspan Flatwise Motion % Error	Blade Midspan Edgewise Motion % Error	Tower Top In-plane Motion % Error	Tower Top Out-of-plane Motion % Error
1FA/1TO	0.643	1.56	1.56	1.56	1.56
1FS	0.674	0.15	-	-	-
1TI/1TO	0.711	1.55	1.55	1.55	1.55
1PR	0.940	-	0.74	-	-
1TO/1TI	1.149	1.39	1.39	1.57	1.57
2FA/1TO	1.694	0.35	0.35	0.35	0.35
2FS/2PR	1.694	0.35	0.35	0.35	0.35
2FA/1TO	1.786	0.78	0.78	0.78	0.78
3FS/2PR	2.850	-	0.60	-	-
3FA/2PR	2.953	0.47	0.47	0.47	0.47

A.4. Validation procedures

The beam element and OWENS finite element framework have been validated using experimental test data for the Sandia National Laboratories 34-meter VAWT test bed [4]. Validation procedures include comparison of parked modal analysis to experimentally observed natural frequencies and mode shapes. Furthermore, the availability of experimental data for the response of a rotating wind turbine was utilized to construct Campbell diagrams. Comparison of the experimental and predicted Campbell diagrams served as a validation exercise for the ability of OWENS to model a realistic, rotating structure.

A.4.a. Parked modal analysis

The predicted frequencies and mode shapes were compared to parked modal test results for the 34-meter VAWT as shown in Table A.21. Table A.21 also presents modal predictions from a previous, more detailed analysis of the parked test bed. Note that due to the prescribed boundary conditions tower modes are not predicted in initial analysis. Furthermore, more accurate models including mass and elastic axis offsets, concentrated mass terms, and more realistic boundary conditions are likely necessary to achieve better agreement with modal test results. Despite further refinement of the model, the OWENS Timoshenko implementation has a maximum difference of 8% for the 1st six modes, and the OWENS Euler-Bernoulli implementation has a maximum difference of 9.5%.

Timoshenko beam theory in general is more robust than Euler-Bernoulli beam theory, and appears to agree better with experimental results. However, Euler-

Bernoulli beam elements will likely yield sufficient accuracy for initial design studies.

Table A.21. Comparison of OWENS modal analysis frequencies (Hz) to parked modal tests for Sandia 34m VAWT

Mode	Modal Test	OWENS (T)	% Difference	OWENS (E-B)	% Difference	SNL [4]	% Difference
1 FA	1.06	0.99	6.20	0.96	9.51	1.05	0.94
1 FS	1.06	1.00	5.58	0.97	8.78	1.05	0.94
1 PR	1.52	1.58	4.06	1.62	6.63	1.56	2.63
1 BE	1.81	1.67	7.57	1.67	7.68	1.72	4.97
2 FA	2.06	2.04	1.21	1.98	3.83	2.07	0.49
2 FS	2.16	2.08	3.70	2.01	6.78	2.14	0.93

In an attempt to model guy-wires, boundary conditions on the top of the tower were removed and two linear springs were attached to account for the stiffening effect of guy-wires. The stiffness of these springs was tuned to the tower mode frequencies observed in experimental tests. Spring constants of 2.89×10^6 N/m in and out of the rotor plane were specified. The modal analysis predictions for the parked turbine with guy-wires (up to the first tower modes) are shown in Table A.22. Table A.22 also presents modal predictions from a previous, more detailed analysis of the parked test bed. For the most part, parked frequencies of blade modes do not change much from the pinned boundary condition at the turbine top, except for a rather drastic change of the 1st "butterfly" mode. Some "tuning" of the boundary conditions or structural properties to account could obtain better estimates of this modal frequency.

Table A.22. Comparison of OWENS modal analysis frequencies (Hz) to parked modal tests for Sandia 34m VAWT with guy wire modeling

Mode	Modal Test	OWENS (T)	% Difference	SNL [4]	% Difference
1 FA	1.06	0.99	6.20	1.05	0.94
1 FS	1.06	1.00	5.58	1.05	0.94
1 PR	1.52	1.58	4.06	1.56	2.63
1 BE	1.81	1.59	12.15	1.72	4.97
2 FA	2.06	2.00	3.00	2.07	0.49
2 FS	2.16	2.08	3.70	2.14	0.93
1 TI	2.50	2.50	0.00	2.46	1.60
1 TO	2.61	2.71	3.83	2.58	1.15

A.4.b. Rotating modal analysis

Rotating modal analysis of the SNL 34-meter VAWT was also conducted using the OWENS toolkit. Rotor speeds from 0 to around 50 RPM were considered, and stress stiffening effects were included. A static analysis under gravitational and centrifugal loadings was conducted to establish an equilibrium configuration about which modal analysis was conducted. This "spin-up" procedure incorporates pre-stress effects that result in a stiffening of the structure. Spin softening and spin stiffening effects compete as rotor speed increases, but typically spin stiffening effects are more dominant resulting in an increase in most natural frequencies of the system as rotor speed increases. Thus, the inclusion of stress-stiffening is critical in replicating behavior of actual rotating, flexible systems.

Figure A.38 shows the predicted Campbell diagram for the first 12 modes of the 34-meter VAWT for the rotor speeds considered. Experimental data obtained from edgewise and flatwise gauges are also plotted. Overall, the predictions are in good agreement with the trends of the experimental data, especially if one considers the

moderate resolution of the VAWT model. If one were to adjust the stiffness and mass distributions in the modeled VAWT better agreement may be achieved. Nevertheless, the model appears to be more than adequate for preliminary design considerations. It is notable that the tower mode is not predicted, but this mode is not possible due to the approximate boundary condition at the top of the tower. This boundary condition was prescribed to avoid modeling the guy wires of the actual turbine for initial validation efforts.

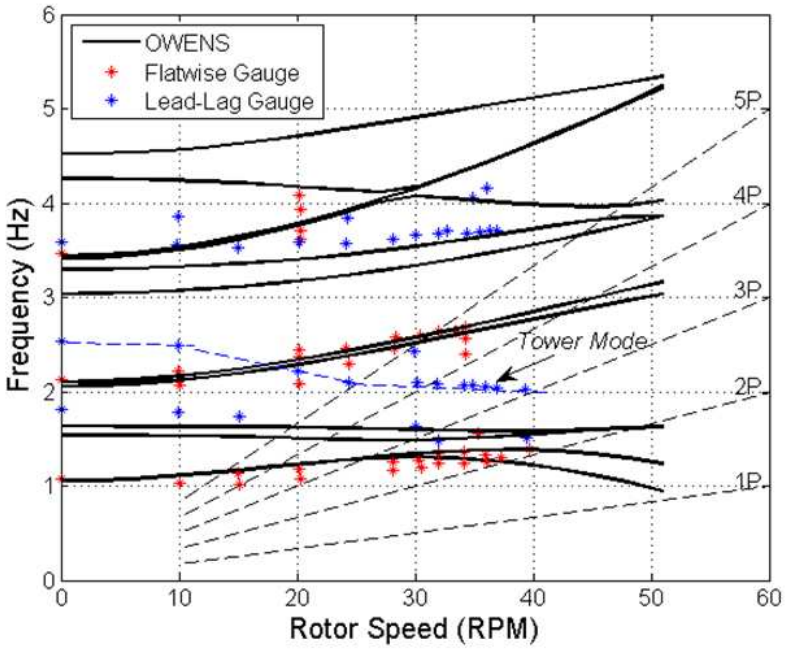

Figure A.38. Campbell diagram for the SNL 34-meter VAWT test bed (experimental data and numerical predictions)

As with the parked configuration, an approximate model of guy-wires was considered by removing the pinned boundary condition at the tower top and attaching

two linear springs. Although these springs are in the rotating hub-frame, the guy-wires provide a "transversely isotropic" stiffening about the axis of rotor rotation. Thus, the associated stiffness is the same regardless of rotor azimuth, and this modeling approach is acceptable. The Campbell diagram of the 34-meter VAWT with guy wires is shown in Figure A.39 and has visible improvement over the one generated with the pinned boundary condition in Figure A.38. Indeed, the first tower modes are captured with reasonable accuracy compared to experimental measurements. This is very encouraging for initial design studies and further improvement may be obtained by "tuning" boundary conditions and structural properties, but this is beyond initial validation exercises.

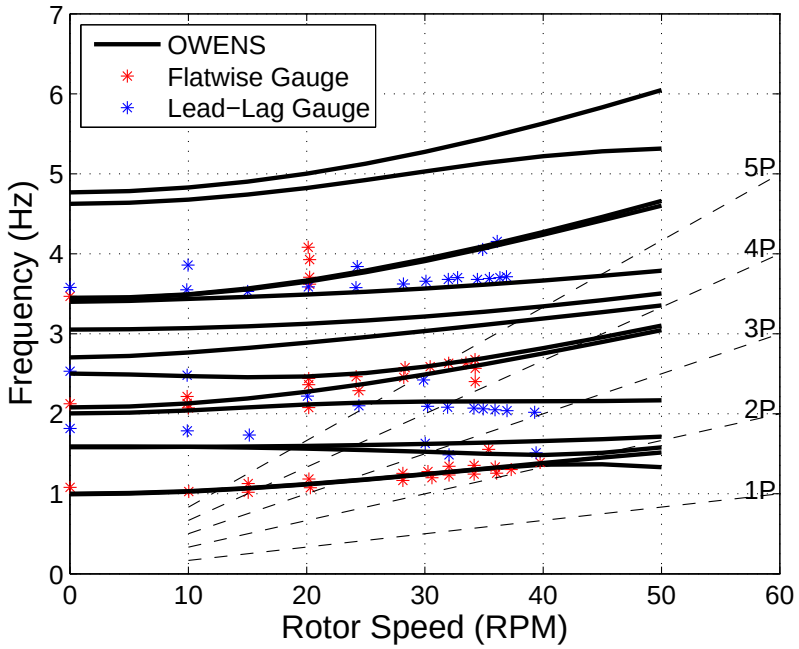

Figure A.39. Campbell diagram for the SNL 34-meter VAWT test bed with guy-wires (experimental data and numerical predictions)

A.5. Conclusions

A variety of verification procedures were considered for the OWENS toolkit. Verification exercises were conducted for Euler-Bernoulli and Timoshenko beam elements in addition to the overall finite element framework of OWENS. When possible, verification via analytical solutions was conducted. This included verification of free vibration of uncoupled modes of a beam as well as rotational or Gyric effects via an analytical solution for a "whirling shaft" configuration.

Extending verification procedures for more complicated configurations without known analytical solutions drew upon independent numerical methods for comparison. Verification procedures considered a code-to-code comparison between OWENS and commercial ANSYS finite element software. This served as an exercise to verify the ability of OWENS to model realistic VAWT structures. A number of advanced features of the code were verified against ANSYS, including concentrated mass, body forces due to acceleration and centrifugal loads, rotational effects, stress-stiffening, and pre-stressed modal analysis. An assumed modes method served to verify the implementation of numerous features including offset mass axes, arbitrary element orientations, and rotational effects outside of the whirling shaft configuration. Other numerical exercises verified the correct implementation of time integration methods by verifying consistency in frequency content between modal and transient predictions.

Validation procedures drew upon experimental data for the Sandia National Laboratories 34-meter VAWT test bed. Results of the procedure were very encouraging, with good agreement seen between OWENS analysis predictions and experi-

mental data. This is especially true considering the moderate level of detail used to model the 34-meter VAWT. Validation procedures indicated that the more robust Timoshenko beam element is better suited to predict motion of a realistic VAWT configuration, although the Euler-Bernoulli beam element may be adequate for initial design studies. Validation procedures confirmed the ability of OWENS to predict parked modes shapes and frequency of the 34-meter VAWT with reasonable accuracy. Modal analysis of a rotating VAWT at constant rotor speed also confirmed Campbell diagrams for experimental data and analysis predictions were in good agreement. Furthermore, this exercise also emphasized the importance of including stress stiffening effects to replicate the trends observed in experimental data for rotating VAWTs. It should be noted that better agreement with experimental data may be achieved by adjusting stiffness and mass properties (as well as boundary conditions) of the structural representation. These considerations, however, were considered beyond the scope of this validation exercise. Future work will continue to verify and validate aspects of the code as required by future analysis needs.

APPENDIX B

AN EXAMPLE DYNAMIC SYSTEM WITH A COMPLEX REPRESENTATION

To explore the ramifications of employing conventional structural dynamics analysis to a complex valued system, a simple example system with complex representation is considered. Consider the following familiar second order system:

$$M\ddot{x} + C\dot{x} + Kx = 0 \tag{B.1}$$

Here, M is a symmetric, real valued mass matrix. The matrices C and K are damping and stiffness matrices respectively. These matrices may be unsymmetric and may have a complex representation. For example, unsteady Theodorsen aerodynamics [23] will give rise to unsymmetric, complex representations in the form of aerodynamic damping and stiffness matrices.

Consider the diagonalization of M via a modal matrix, Φ. The modal matrix is composed of eigenvectors that are orthogonal with respect to the mass matrix. Thus, the diagonalized mass matrix, Λ is

$$\Lambda = \Phi^T M \Phi \tag{B.2}$$

Introducing the following relation

$$x = \Phi\eta \tag{B.3}$$

and pre-multiplying the governing equation by Φ^T results in the following system

$$\Phi^T M\Phi\ \ddot{\eta} + \Phi^T C\Phi\ \dot{\eta} + \Phi^T K\Phi\ \eta = 0 \tag{B.4}$$

$$\Lambda\ddot{\eta} + \Phi^T C\Phi\ \dot{\eta} + \Phi^T K\Phi\ \eta = 0 \tag{B.5}$$

Now, let a simplifying assumption be made that the off-diagonal elements of the transformed damping and stiffness matrices are small relative to diagonal components

$$\Phi^T C\Phi \approx \hat{C} \tag{B.6}$$

$$\Phi^T K\Phi \approx \hat{K} \tag{B.7}$$

Here, $\hat{C}$ and $\hat{K}$ are diagonal, complex matrices. Under these approximations, the system is

$$\Lambda\ddot{\eta} + \hat{C}\dot{\eta} + \hat{K}\eta = 0 \tag{B.8}$$

The resulting system is decoupled, resulting in multiple single degree of freedom scalar equations

$$\Lambda_j\ddot{\eta}_j + \hat{C}_j\dot{\eta}_j + \hat{K}_j\eta_j = 0 \tag{B.9}$$

Herein, let the index be dropped and a single degree of freedom scalar equation be considered. The complex representation of the damping and stiffness matrices can be emphasized in this equation as

$$\Lambda\ddot{\eta} + (c + i\ \tilde{c})\,\dot{\eta} + \left(k + i\ \tilde{k}\right)\eta = 0 \tag{B.10}$$

Suppose the following form of η is assumed

$$\eta = a\exp(\lambda t) \tag{B.11}$$

$$\dot{\eta} = a\lambda\exp(\lambda t) = \lambda\eta \tag{B.12}$$

$$\ddot{\eta} = a\lambda^2\exp(\lambda t) = \lambda^2\eta \tag{B.13}$$

Thus, the scalar equations of the decoupled system may be expressed as

$$\left\{\Lambda\lambda^2 + (c + i\ \tilde{c})\,\lambda + \left(k + i\ \tilde{k}\right)\right\}\eta = 0 \tag{B.14}$$

Solving for λ results in

$$\lambda = -\frac{\hat{C}}{2\Lambda} \pm \frac{1}{2}\sqrt{\frac{\hat{C}^2}{\Lambda^2} - 4\frac{\hat{K}}{\Lambda}} \tag{B.15}$$

$$\lambda = -\frac{c + i\ \tilde{c}}{2\Lambda} \pm \sqrt{\frac{(c^2 - \tilde{c}^2)}{4\Lambda^2} + i\frac{c\tilde{c}}{2\Lambda^2} - \frac{\left(k + \tilde{k}\right)}{\Lambda}} \tag{B.16}$$

Let the following expressions be introduced

$$A = \frac{(c^2 - \tilde{c}^2)}{4\Lambda^2} - \frac{k}{\Lambda} \tag{B.17}$$

$$B = \frac{c\tilde{c}}{2\Lambda^2} - \frac{\tilde{k}}{\Lambda} \tag{B.18}$$

Furthermore, let

$$\sqrt{A + \ iB} = a + i\ b \tag{B.19}$$

Therefore,

$$\lambda = \left(-\frac{c}{2\Lambda} \pm a\right) + i\ \left(-\frac{\tilde{c}}{2\Lambda} \pm b\right) \tag{B.20}$$

or

$$\lambda_1 = \left(-\frac{c}{2\Lambda} + a\right) + i\ \left(-\frac{\tilde{c}}{2\Lambda} + b\right) = \lambda_{R_1} + i\ \lambda_{I_1} \tag{B.21}$$

$$\lambda_2 = \left(-\frac{c}{2\Lambda_j} - a\right) + i\ \left(-\frac{\tilde{c}}{2\Lambda} - b\right) = \lambda_{R_2} + i\ \lambda_{I_2} \tag{B.22}$$

Note that $\lambda_{R_1} \neq \lambda_{R_2}$ and $\lambda_{I_1} \neq -\lambda_{I_2}$. Thus, in general for a complex representation complex conjugate eigenvalue pairs will not exist. Even for the specific case of no damping ($c = \tilde{c} = 0$) one may observe that

$$\lambda_1 = -\lambda_2 = a + i\ b \tag{B.23}$$

The lack of existence of complex conjugate pairs in a complex valued system is problematic in that the physical meaning of eigenvalues (and eigenvectors) is unclear and conventional techniques for extracting frequency, damping, and mode shapes may not be applied to systems with complex representations. For a real valued, damped system the governing differential equation is often expressed as

$$\ddot{x} + 2\xi\omega_n\dot{x} + \omega_n^2 x = 0 \tag{B.24}$$

Such that ω_n and ξ are the natural frequency and damping ratio of the system respectively. Assuming $x = x_0 \exp(\lambda t)$ allows the eigenvalues to be calculated

$$\lambda_{1,2} = -\xi\omega_n \pm i\ \omega_n\sqrt{1-\xi^2} \tag{B.25}$$

Inspecting this equation reveals that the eigenvalues of the real valued, damped system will occur in complex conjugate pairs. Indeed, inspection of the system presented in the previous section shows that the eigenvalues of the real valued system (setting $\tilde{c} = \tilde{k} = 0$) are complex conjugate pairs. As shown for the case of complex systems, complex conjugate pair eigenvalues do not exist in general. Therefore, extraction of frequency and damping information via the above expression is questionable for systems with complex representations.

APPENDIX C

RESONANCE OF RIGID BODY MODES OF A FLOATING WIND TURBINE

As shown in Chapter VIII, a floating wind turbine configuration introduces six rigid body modes to the system in addition to the flexible structural modes of the land-based configuration. Low frequency rigid body modes of a platform/turbine configuration are subject to excitations from the offshore environment (i.e. waves) and the reaction force at the turbine/platform junction. Wave excitation depends on the environmental conditions at the turbine siting location. The tower provides the connection between the floating platform and the turbine, and thus reaction forcing on the tower is related to the tower forcing. Therefore, the relations for frequency content of tower forcing are also applicable to the frequency content of the platform forcing due to the turbine reaction force.

Although potential resonance conditions for rigid body platform modes can be identified, the deployment of the platform in an offshore environment can lead to significant damping in rigid body modes. Consider the traditional second order structural dynamics system:

$$M\ddot{x}(t) + C\dot{x}(t) + Kx(t) = F(t) \tag{C.1}$$

Such that the degree of freedom vector $x(t)$ contains flexible degrees of freedom as well as rigid body degrees of freedom. Modal methods may be employed in an

attempt to diagonalize the system

$$\hat{M}\ddot{\eta}(t) + \hat{C}\dot{\eta}(t) + \hat{K}\eta(t) = \hat{F}(t) \tag{C.2}$$

$$x(t) = \Phi\eta(t) \tag{C.3}$$

$$\hat{F}(t) = \Phi^T F(t) \tag{C.4}$$

Furthermore, introducing a definition of damping force for the uncoupled mode

$$\hat{F}_{damp}(t) = \hat{C}\dot{\eta}(t) \tag{C.5}$$

and the equation of motion for a single uncoupled platform degree of freedom may be written as

$$\hat{M}\ddot{\eta}(t) + \hat{K}\eta(t) = \hat{F}(t) - \hat{F}_{damp}(t) \tag{C.6}$$

Therefore, for a particular rigid body mode, damping will overcome the forcing associated with a particular excitation so long as

$$\hat{F}_{damp}(t) > \hat{F}(t) \tag{C.7}$$

Damping force of rigid body platform modes is likely to be associated with the drag force of the rigid body moving through fluid. This, however, is dependent on fluid density, platform velocity, and more importantly, platform geometry. The "external forcing" $\hat{F}(t)$ is likely to come from wave excitation, aerodynamic loads on the turbine, or vibration of the turbine structure. Each of which, are dependent on environmental conditions or the turbine configuration. Therefore, it is difficult to predict if the rigid body damping will in general be sufficient to overcome potential resonant excitations. Transient analysis of such conditions with an accurate model of turbine and platform configurations, along with environmental conditions will likely yield greater insight for particular turbine/platform configurations.

APPENDIX D

APPROXIMATE TREATMENT OF RIGID BODY MODES IN MODAL ANALYSIS USING A GYRIC FORMULATION

This appendix presents and approximate treatment of rigid body modes in modal analysis using a Gyric formulation. First, an approach for treatment of rigid body modes in a conventional, non-rotating structure using an existing representation of the flexible structure is discussed. This is followed by extensions to Gyric systems for use in initial design studies of Gyric systems on flexible support structures with rigid body modes.

D.1. An approach for incorporating rigid body modes into an existing flexible structural dynamics framework

Support conditions are of potential interest in any structural dynamics study. For a conventional, non-rotating structure on a flexible foundation one may attempt to account for this support condition by simply modifying boundary conditions on an existing representation of the structure. For example, a finite element mesh of a flexible structure that once had a fixed boundary condition may be modified to allow for this boundary condition to be free instead. This would allow one to account for rigid body modes. Furthermore, for a flexible support foundation some compromise between the free and fixed boundary condition may be modeled by applying concentrated mass/inertia associated with the support to the node associated with the boundary condition. A similar approach may be taken with the support stiffness by

appending additional stiffness to this nodal location. This allows for the rigid body modes to be "tuned" to the desired frequencies. A simple schematic of this approach is shown in Figure D.1.

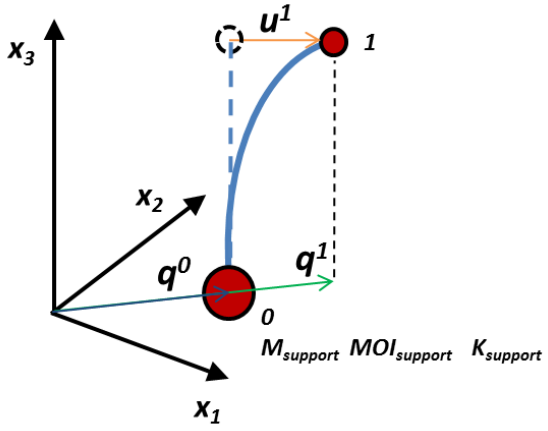

Figure D.1. Schematic of rigid body and flexible motion within a single frame

Under this approach, a single frame has been considered to model both rigid body motion and local deformation. This is a fairly straight forward method, and is easily employed in standard structural dynamics software packages without the need to consider multiple coordinate frames (one for rigid body motion and one for local deformation of a flexible structure). The resulting modal frequencies/damping for the system are valid and mode shapes may capture the coupling between rigid body and structural deformation. The degrees of freedom, however, in this approach represent absolute displacement. That is for a model with only translational displacements as degrees of freedom, the displacement vector of node i (q_m^i), is related to the

rigid body displacement vector q_m^0 associated with the node the support condition is being modeled at, and u_m^i is the flexible deformation associated with the node i (as illustrated in Figure D.1). Therefore, the absolute displacement vector is

$$q_m^i = q_m^0 + u_m^i \tag{D.1}$$

For a model with degrees of freedoms as both translational displacements and rotations (such as a model composed of beam elements) the absolute displacement q_m^i will be dependent upon rigid body translations, rigid body rotations, and flexible deformation. For example, the absolute displacement of a node under small angle approximations can be represented as

$$\begin{Bmatrix} q_1^i \\ q_2^i \\ q_3^i \\ q_4^i \\ q_5^i \\ q_6^i \end{Bmatrix} = \begin{bmatrix} I_{3\times3} & -\tilde{\chi}^i \\ 0_{3\times3} & I_{3\times3} \end{bmatrix} \begin{Bmatrix} q_1^0 \\ q_2^0 \\ q_3^0 \\ q_4^0 \\ q_5^0 \\ q_6^0 \end{Bmatrix} + \begin{Bmatrix} u_1^i \\ u_2^i \\ u_3^i \\ u_4^i \\ u_5^i \\ u_6^i \end{Bmatrix} \tag{D.2}$$

Here, the first three DOFs represent the translations associated with node i (or support node 0) in the x_1, x_2, and x_3 directions respectively and the last three DOFs represent rotations associated with node i (or support node 0) in the x_1, x_2, and x_3 directions respectively. The matrix $\tilde{\chi}^i$ is a skew-symmetric matrix constructed from the vector χ_m^i which contains the nodal coordinates of node i such that $\chi_m^i = [\bar{x}_1^i, \bar{x}_2^i, \bar{x}_3^i]^T$.

For simplicity in forthcoming developments, let the following definition be in-

troduced

$$\hat{T}^i = \begin{bmatrix} I_{3\times3} & -\tilde{\chi}^i \\ 0_{3\times3} & I_{3\times3} \end{bmatrix} \tag{D.3}$$

Thus, using this "node-by-node" transformation, the global DOF list for the system may be expressed as

$$\begin{Bmatrix} q_m^0 \\ q_m^1 \\ q_m^2 \\ \vdots \\ q_m^n \end{Bmatrix} = \begin{bmatrix} \begin{bmatrix} I_{3\times3} & 0_{3\times3} \\ 0_{3\times3} & I_{3\times3} \end{bmatrix} & [0_{6\times6n}] \\ \begin{bmatrix} \hat{T}^1 \\ \hat{T}^2 \\ \vdots \\ \hat{T}^n \end{bmatrix} & [I_{6n\times6n}] \end{bmatrix} \begin{Bmatrix} q_m^0 \\ u_m^1 \\ u_m^2 \\ \vdots \\ u_m^n \end{Bmatrix} \tag{D.4}$$

Here, $m = 1, 2, ..., 6$ for the local DOF numbering of a node. This transformation effectively separates rigid body and deformation degrees of freedom, thereby allowing the analyst to examine local structural deformation separately from rigid body motion. An inherent requirement in this transformation is that node 0 is modeling the support condition, and is nominally located at the origin of the coordinate system analysis is being performed in. An arbitrary system that has a different DOF ordering or nodal positions from this assumed form may simply be transformed accordingly before applying this transformation to decompose the system into rigid body and local deformation DOFs.

For simplicity, let the above equation be written compactly as

$$\vec{q}(t) = [\bar{T}]\vec{\bar{q}}(t) \tag{D.5}$$

Such that $\vec{q}(t)$ is the DOF listing of absolute displacements and $\vec{\bar{q}}(t)$ is the DOF listing decomposed into rigid body and local deformation displacements.

Accordingly, the original conventional structural dynamics system equation of motion shown below with absolute displacements

$$[M]\ddot{q}(t) + [C]\dot{q}(t) + [K]q(t) = 0 \tag{D.6}$$

may be transformed to separated rigid body and local deformation.

$$[\bar{M}]\ddot{\bar{q}}(t) + [\bar{C}]\dot{\bar{q}}(t) + [\bar{K}]\bar{q}(t) = 0 \tag{D.7}$$

Such that

$$[\bar{M}] = [\bar{T}]^T[M][\bar{T}] \tag{D.8}$$

$$[\bar{C}] = [\bar{T}]^T[C][\bar{T}] \tag{D.9}$$

$$[\bar{K}] = [\bar{T}]^T[K][\bar{T}] \tag{D.10}$$

For example, under this transformation, the mass matrix will have the following form

$$[\bar{M}] = \begin{bmatrix} \bar{M}_{oo} & \bar{M}_{oi} \\ \bar{M}_{io} & \bar{M}_{ii} \end{bmatrix} \tag{D.11}$$

Here $\bar{M}_{oo}$ represents the coupling between rigid body DOFs, $\bar{M}_{oi}$ and $\bar{M}_{io}$ represent the coupling between rigid body and flexible DOFs, and $\bar{M}_{ii}$ represents coupling between flexible DOFs. The damping and stiffness matrices ($[\bar{C}]$ and $[\bar{K}]$) of the transformed system may be expressed in a similar manner.

D.2. An extension of approach to Gyric system analysis

The previously described approach is a convenient way to incorporate the effects of a flexible support structure into the structural dynamics analysis of a conventional, non-rotating system. One may be inclined to extend the aforementioned approach

to account for rotating systems affixed to a flexible support condition by merely prescribing some rotation of the coordinate frame the system is represented in and considering the response of the system in a rotating frame. An example of such a system is a rotating vertical axis-wind turbine on a non-rotating, floating platform. Extending the aforementioned approach may be viewed as an acceptable modeling approximation if the support structure mass, stiffness, and damping properties do not vary significantly about the axis of prescribed rotation.

This simple extension, however, is problematic in that any rigid body motion relative to the prescribed axis of rotation will have Gyric effects applied to it. Indeed, Gyric effects should only be applied to local deformation of the system. For example, rigid body translation of the system should not experience the spin softening or Coriolis effects that a flexible deformation should. Herein, an approach is described to provide a correction for these effects, and extend a Gyric formulation to account for rigid body effects that may be suitable for initial design studies. More detailed analysis should consider the inherent periodicity of the system due to the time-varying system resulting from the addition of a non-rotating platform in a fixed frame.

Consider the transformed conventional system in the previous section with the addition of Gyric and spin softening matrices as shown below

$$[\bar{M}]\ddot{\bar{q}}(t) + [\bar{C} + \bar{G}]\dot{\bar{q}}(t) + [\bar{K} - \bar{S}]\bar{q}(t) = 0 \tag{D.12}$$

Now let the associated modal matrix ($[\bar{\Phi}]$) of the parked, undamped system ($[\bar{G}] = 0$, $[\bar{C}] = 0$, and $[\bar{S}] = 0$) be employed to represent the transformed system in modal

space such that

$$\eta(t) = [\bar{\Phi}]\bar{q}(t) \tag{D.13}$$

$$[\tilde{M}]\ddot{\eta}(t) + [\tilde{C} + \tilde{G}]\dot{\eta}(t) + [\tilde{K} - \tilde{S}]\eta(t) = 0 \tag{D.14}$$

Such that

$$[\tilde{M}] = [\bar{\Phi}]^T[\bar{M}][\bar{\Phi}] \tag{D.15}$$

$$[\tilde{K}] = [\bar{\Phi}]^T[\bar{K}][\bar{\Phi}] \tag{D.16}$$

$$[\tilde{C}] = [\bar{\Phi}]^T[\bar{C}][\bar{\Phi}] \tag{D.17}$$

$$[\tilde{G}] = [\bar{\Phi}]^T[\bar{G}][\bar{\Phi}] \tag{D.18}$$

$$[\tilde{S}] = [\bar{\Phi}]^T[\bar{S}][\bar{\Phi}] \tag{D.19}$$

Note that the following developments assume the first columns of the modal matrix are the eigenvectors (mode shapes) for the rigid body modes of the system. This will typically be the case for low frequency rigid body modes.

As before, the Gyric and spin softening matrices (now represented in modal space) may be represented in the following form.

$$[\tilde{G}] = \begin{bmatrix} \tilde{G}_{oo} & \tilde{G}_{oi} \\ \tilde{G}_{io} & \tilde{G}_{ii} \end{bmatrix} \tag{D.20}$$

$$[\tilde{S}] = \begin{bmatrix} \tilde{S}_{oo} & \tilde{S}_{oi} \\ \tilde{S}_{io} & \tilde{S}_{ii} \end{bmatrix} \tag{D.21}$$

Thus, the transformation procedures employed up to this point have sought to isolate the effect of rigid body modes on other rigid body modes as much as possible by transforming the system to modal space. To apply a correction to eliminate Gyric

effects on rigid body modes as a result of rigid body modes, let $\tilde{G}_{oo} = 0$ and $\tilde{S}_{oo} = 0$. The cross-coupling terms of $\tilde{G}_{oi}/\tilde{G}_{oi}$ and $\tilde{S}_{oi}/\tilde{S}_{oi}$ are retained to allow for Gyric coupling between rigid body modes and flexible modes. The $\tilde{G}_{ii}$ and $\tilde{S}_{ii}$ terms are also retained to allow for Gyric effects among flexible modes of the system.